THE UNIVERSITY *of* EDINBURGH

The investigation of blood cells migration in large stenosed artery

Anis Suhaila Shuib

Doctor of Philosophy

The University of Edinburgh

2012

ABSTRACT

Atherosclerosis is one of the main diseases responsible for the high global mortality rate involving heart and blood vessel disorders. The build-up of fatty materials in the inner wall of the human artery prevents sufficient oxygen and nutrients reaching the organs of the body. Atherosclerosis is a chronic, long term condition, which develops and progresses over time; however, the disease does not present any symptoms until an advanced stage is reached, which results in potential permanent debility and sometimes sudden death.

This thesis is concerned with the progression of atherosclerosis in an artery with mild stenosis that has resulted in a 30% reduction in its diameter. To this end, data on the low wall shear stress has been correlated with the atherosclerotic prone region. In a stenosed artery, this region corresponds to the separation zone that is formed distal to the lumen reduction. Atherosclerosis is a complex phenomenon, and not only involves wall shear stress, but also cellular interactions. Previous research has shown that even in the absence of wall biological effects, the blood cell distribution is strongly influenced by the hydrodynamics of the fluid.

The mechanisms of blood cell distribution and the dynamic behaviour of the blood flow were investigated by developing a physical model of the stenosed artery, and by using particles to represent the presence of the blood cells. Particle Image Velocimetry system was employed and the size of particles were the 10μm and 20μm.The flow field was characterised and the particle distribution was measured.

The characteristics of steady flow in the stenosed artery at Reynolds numbers of 250 and 320 revealed the importance of fluid inertia and the shear gradient distal to stenosis. Unequal distribution of the particles modelling the blood cells was observed, as more particles occupied the recirculation zones than the high shear region and central jet. The particle migration was found to depend on the particle size, particle concentration and fluid flow rates. The results suggested that the presence of similar effects in the real human arterial system may be significant to the progression of atherosclerotic plaques. At lower Reynolds number of 130, a particle depleted layer was observed at the wall region. In physiological flow the cell free layer will prevent the transport of oxygen and nitrogen oxide (NO) to the muscle tissues.

A numerical method was used to simulate the flow characteristics measured in the experiment. The numerical results revealed the importance of the hydrodynamic mechanism of particle migration. Drag and lift forces were found to affect the residence time of particles in the recirculation region.

The findings of this work have suggested that for a complex geometry like a large stenosed artery at physiological flow rates, hydrodynamic forces are important in cell migration in the flow separation zone. Even without biological forces, the cells migrate to the low wall shear stress region. For computational dynamics studies, this study has demonstrated the need for higher-order modelling at the cellular level in order to establish the particle migration mechanisms.

DECLARATION OF ORIGINALITY

I hereby declare that this thesis was composed entirely by myself, that the work contained herein is my own except where explicitly stated otherwise in the text, and that this work has not been submitted for any other degree or professional qualification except as specified.

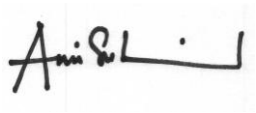

(Anis Suhaila Shuib)

ACKNOWLEDGEMENTS

I owe my deepest gratitude to my supervisors, Professor William Easson and Dr Peter Hoskins for their guidance, patience, support and encouragement. Their expertise, dedication and enthusiasm in research are always inspiring. The good advice and friendship has been invaluable on both an academic and a personal level, for which I am extremely grateful. I also thank Dr Prash Valluri for his teaching and advices on hydrodynamics.

I would like to thank Dr James Blake for his help in setting up the Particle Image Velocimetry system and his invaluable discussion on many subjects. Many thanks Siobhan Meagher for her help in developing the blood mimic fluid, Bobby Hogg for providing the laboratory technical support and SEE IT support team for dealing with the computing problems.

As a novice user for FLUENT simulation, I thank Dr David Hardman, Dr Yong Lu and Dr Salvador Vargas-Diaz for their advice and guidance in dealing with the interface. I also thanks other past research group members, Dr MingXiu Li, Dr Jason Beech-Brandt, Dr William Lee, Dr Kate Fraser, Dr Steven Hammer and Dr Pavel Stroev, who share the excitement of doing multidisciplinary research.

The completion of thesis would not have been possible without moral support and encouraging environment from postgraduate friends and departmental staff at Institute for Materials and Processes. For that I thank Avril Davies, Dr Susie Lakshmanan, Dr Rabah Mouras, Stephen Kwelle, Ruby Raheem, Muhanad AlMutaz and Hana Hussain.

I would like to knowledge the financial support from Universiti Teknologi Petronas Malaysia. I thank all staff at Chemical Engineering Department particularly Dr Shuhaimi Mahadzir for the understanding and patience.

Finally, I am grateful to my family for their everlasting love and warm-hearted support. This thesis is dedicated to my sons, Ikhwan and Imran.

DISSEMINATION

This work has been presented in several conferences and meetings, and has written in papers that have been published, given as follows.

Journal Paper

Shuib, A.S., P.R. Hoskins , W.J. Easson., Experimental investigation of particle distribution in a flow through a stenosed artery , Journal of Mechanical Science and Technology, vol. 25, no. 2, pp.357-364, 2011.

Conference Proceedings

Shuib, A.S., P.R. Hoskins , W.J. Easson., Flow regime characterization in a diseased artery model, Proceedings of the International Conference on Chemical and Biological Engineering, Penang, Feb 24-26, 2010.

Shuib, A.S., P.R. Hoskins, W.J. Easson., Flow visualization of a dilute particle suspension flowing in a physiological geometry. Proceedings of UK-Malaysia Engineering Conference 2008. University of College London, July 14-15, 2008.

Conference Oral presentations

Shuib, A.S., P.R. Hoskins , W.J. Easson., Particle distribution in a diseased artery model, UK-Malaysian-Ireland Engineering Symposium 2010, Queen's University, Belfast, June 23-25, 2010.

Shuib, A.S., P.R. Hoskins , W.J. Easson., Multiphase flow of blood in stenosis artery, International Conference on Chemical and Biomolecular Engineering, National University of Singapore, Jan 28-29, 2010.

Shuib, A.S., P.R. Hoskins , W.J. Easson., Expertimental investigation of particle dynamics in an arterial stenosis model. 21st Annual Scottish Fluid Mechanics Meeting. The University of Edinburgh, May 22, 2008.

Poster Presentations

Shuib, A.S., P.R. Hoskins , W.J. Easson., Two-phase flow in recirculation zone of a stenosis artery. Bioengineering 08. Imperial College London, Sept 18-19,2008.

Shuib, A.S., P.R. Hoskins , W.J. Easson., Particle accumulation in flow through physiological geometries. European Postgraduate Fluid Dynamics Conference. University of Birmingham, August 8-7, 2007.

Shuib, A.S., P.R. Hoskins , W.J. Easson., Viscosity characterisation of a blood mimic for use in studies on wall shear rate estimation in arteries. 4th physiological flow network meeting, University of Manchester. April 2-3,2007.

Shuib, A.S., P.R. Hoskins , W.J. Easson., Rheology of blood mimicking fluid. Non Newtonian Club Meeting, University of Nottingham, June 6, 2006.

CONTENTS

LIST OF FIGURES

LIST OF TABLES

NOMENCLATURE

List of Roman symbols

A	surface area
a	particle radius
$\boldsymbol{a}$	acceleration
C_D	drag coefficient
c	semi-empirical constant in blood rheology models
D	diameter of the inlet tube
D_0	minimum lumen or tube diameter
d	particle displacements
d_{diff}	diameter of the Airy disk
d_p	particle diameter
du/dr	axial velocity gradient
$du/dr_{,i}$	axial velocity gradient at inlet
dv/dr	radial derivative of flow velocity
F	force
F_{Bas}	Basset force
F_D	drag force
F_L	lift force
F_{LM}	Magnus lift force
F_{LS}	Saffman lift force
$F_{LSaffman\text{-}Mei}$	Saffman-Mei lift force
F_{PG}	pressure gradient force
F_{vm}	virtual mass force
f	focal length of the lens
$f\#$	f-number
g	gravitational acceleration
h	empirical constant in Power Law model
I	identity matrix
I'	local light intensity
$\hat{I}$	local mean light intensity
$\hat{I}_0$	mean light intensity at the inlet
k	Boltzmann's constant
k'	threshold ratio value of the highest signal peak to the second highest peak

L	length of the side of interrogation area
l	inlet length
M	magnification
m_p	mass of the particle
n	number of volume elements
Pe	Peclet number
p	pressure
p'	order of accuracy in Richardson extrapolation method
Q	volumetric flow rate
R	lumen or tube radius
Re	time-averaged Reynolds number
Re_g	Shear Reynolds number
Re_i	Reynolds number based on inlet velocity
Re_p	particle Reynolds number
Re_{throat}	Reynolds number at throat of stenosis
R'	convergence ratio
r	radial position
r/R	normalised radial coordinate
S	source term in Navier-Stokes equation
St	Stokes number
T	temperature
$t\text{-}t'$	time interval from the initiation of the acceleration
u	axial velocity component
u_{mean}	mean axial velocity component
u_{max}	maximum axial velocity component
u_p	axial velocity component of particle
u_∞	settling velocity
V	resultant velocity
V_{mean}	mean velocity
V_{max}	maximum velocity
V_p	instantaneous velocity of the particle
V_s	slip velocity
Vo	volume
Vo_p	particle volume
v	radial velocity component
v_p	radial velocity component of particle

Wo	Womersley number
x	axial coordinate
x/D	normalised axial coordinate
Z_0	distance between the lens and the particles
z	azimuth velocity component
z_0	distance between the image plane

List of Greek symbols

γ	shear rate
γ_c	critical shear rate
Δp	pressure gradient produced by hydrostatic pressure
Δs	displacement between elements
Δt	time between pulses
Δv	estimated velocity gradient within a cell
δz	depth of field
ϕ_m	particle concentration by weight
φ	volume concentration of particles
κ	degree of stenosis
λ	wavelength
μ	viscosity of fluid
μ_∞	asymptotic viscosity
μ_F	suspending medium viscosity of particulate suspension
ρ	density of the fluid
ρ_p	density of the particle
τ	shear stress
τ_w	wall shear stress
τ_y	yield stress
τ_{vel}	momentum response time of particle
τ_{col}	time between collisions
θ	flow property
Ω	vorticity
ω_p	particle rotation

List of abbreviations

2D	two dimensional
3D	three dimensional
CFD	computational fluid dynamics
CT	computed tomography
CVD	cardiovascular diseases
DMSO	dimethyl sulfoxide
FFT	fast Fourier transform
KSCN	potassium thiocyanate
LDL	low density lipoprotein
MRI	magnetic resonance imaging
NaCl	sodium chloride
Nd:YAG	neodymium-doped yttrium aluminium garnet
NS	Navier-Stokes
NO	nitric oxide
PIV	particle image velocimetry
PMMA	polymethylmethaacrylate
PRT	particle residence time
RBC	red blood cells
SIMPLEC	semi-implicit method for pressure-linked equations consistent
WBC	white blood cells
WHO	World Health Organisation
WSS	wall shear stress

Chapter 1

INTRODUCTION

1.1 Atherosclerosis

1.1.1 **Cardiovascular diseases and atherosclerosis**

Cardiovascular diseases (CVD) are the leading cause of death in the world. The World Health Organisation (WHO) divides CVD into several different main categories; coronary heart disease (that cause heart attack), cerebrovascular disease (also known as stroke), peripheral disease (that affects vessels in the arms and legs), vein thrombosis (blood clots), and rheumatic heart disease (that causes damage to heart muscle and heart valves). Statistics in Figure 1.1 indicate that the number of people who died because of CVD is larger than cancers and other diseases. Figure 1.2 shows the projected deaths for different diseases until 2030 using 2004 data.

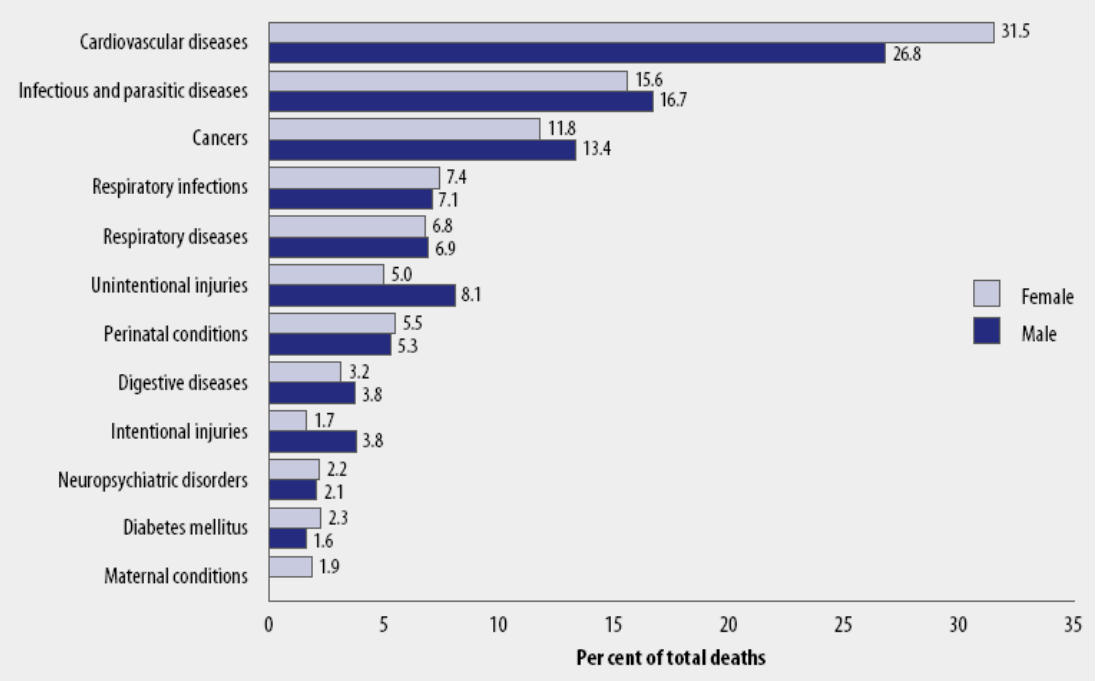

Figure 1.1 Distribution of death by leading cause group, male and female, 2004. Source: The Global Burden of Disease: 2004 update, WHO

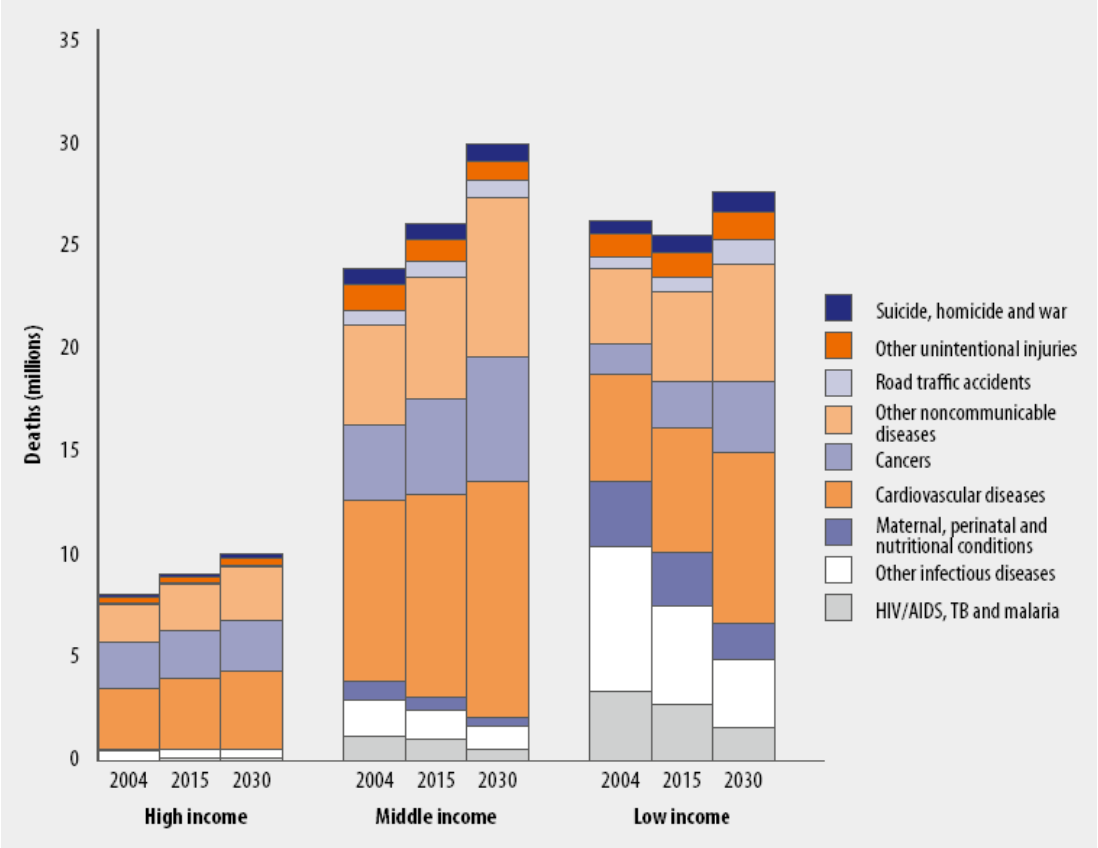

Figure 1.2 Projected deaths by cause for high-, middle- and low-income countries. Source: The Global Burden of Disease: 2004 update, WHO

Atherosclerosis is the build-up of fatty materials in the inner wall of the arteries. The narrowing of the arterial lumen is called a stenosis or plaque. If the degree of vessel occlusion is severe this prevents sufficient oxygen and nutrition reaching the distal tissues resulting in tissue damage and tissue death. In modern lifestyle smoking, unhealthy diet and lack of physical exercise are the major risk factors for cardiovascular diseases (WHO, 2002). The risk factors start as early as childhood life. Early lesions of atherosclerosis are most frequently encountered in children whose risk factors included smoking, obesity and high blood pressure.

The inflammatory process is triggered when blood containing a high level of low density lipoprotein (LDL) experienced an abnormal wall shear (Ku, 1997). LDL is a complex of numerous cholesterol molecules bound to a single protein carrier. LDL stimulates the recruitment of leukocytes (white blood cells) into the arterial wall (Weissberg, 2007). The leukocytes absorb LDL and transform into foam cells. At an early stage atherosclerosis is present as a fatty streak that consists of smooth muscle cells filled with lipid and macrophages. Early disease does not cause any symptoms, however over time with repeated

inflammation process, a fibrous plaque is formed. The last stage of atherosclerosis occurs when the plaque ruptures, exposing the cholesterol and the tissue underneath, and the chronic inflammatory reaction lead to thrombosis. Thrombosis is initiated by the adherence and accumulation of platelets at the inflamed site. The blood clot may cause lumen occlusion that within seconds to minutes ends with potential permanent debility and sometimes sudden death. The result is illustrated in Figure 1.3.

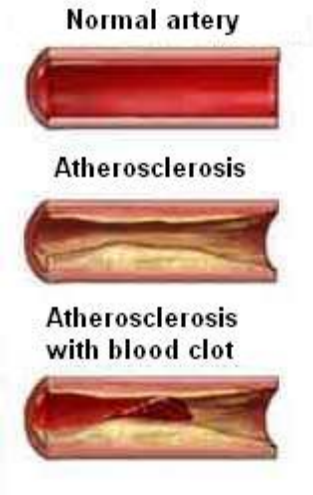

Figure 1.3 Atherosclerosis (Reprinted from http://www.medicalsymptomsguide.com)

It is recognized that the risk of rupture is also determined by the plaque composition. Vulnerable plaque is associated with a thin fibrous cap and a larger lipid pool, whereas stable plaque is associated with a thicker fibrous cap and a smaller or absent lipid pool (Libby et al., 2002).

Atherosclerotic lesions, which initiated in low wall shear stress region (Caro et al., 1971) grow over time and form a plaque with high concentration of lipid. For the established plaque, high wall shear stress is hypothesised to cause fibrous cap thinning, which leave the plaque at risk of rupture through high tissue stress (Slager et al., 1995; Slager et al., 1995). Arterial thrombus is usually found superimposed on the atherosclerotic plaque which has ruptured. Thrombi are found in the low shear region where the flow stasis and recirculation exist.

1.1.2 **Stenosed artery**

The human arterial system is shown in Figure 1.4. The artery system distributes oxygenated blood from the heart to the entire human body.

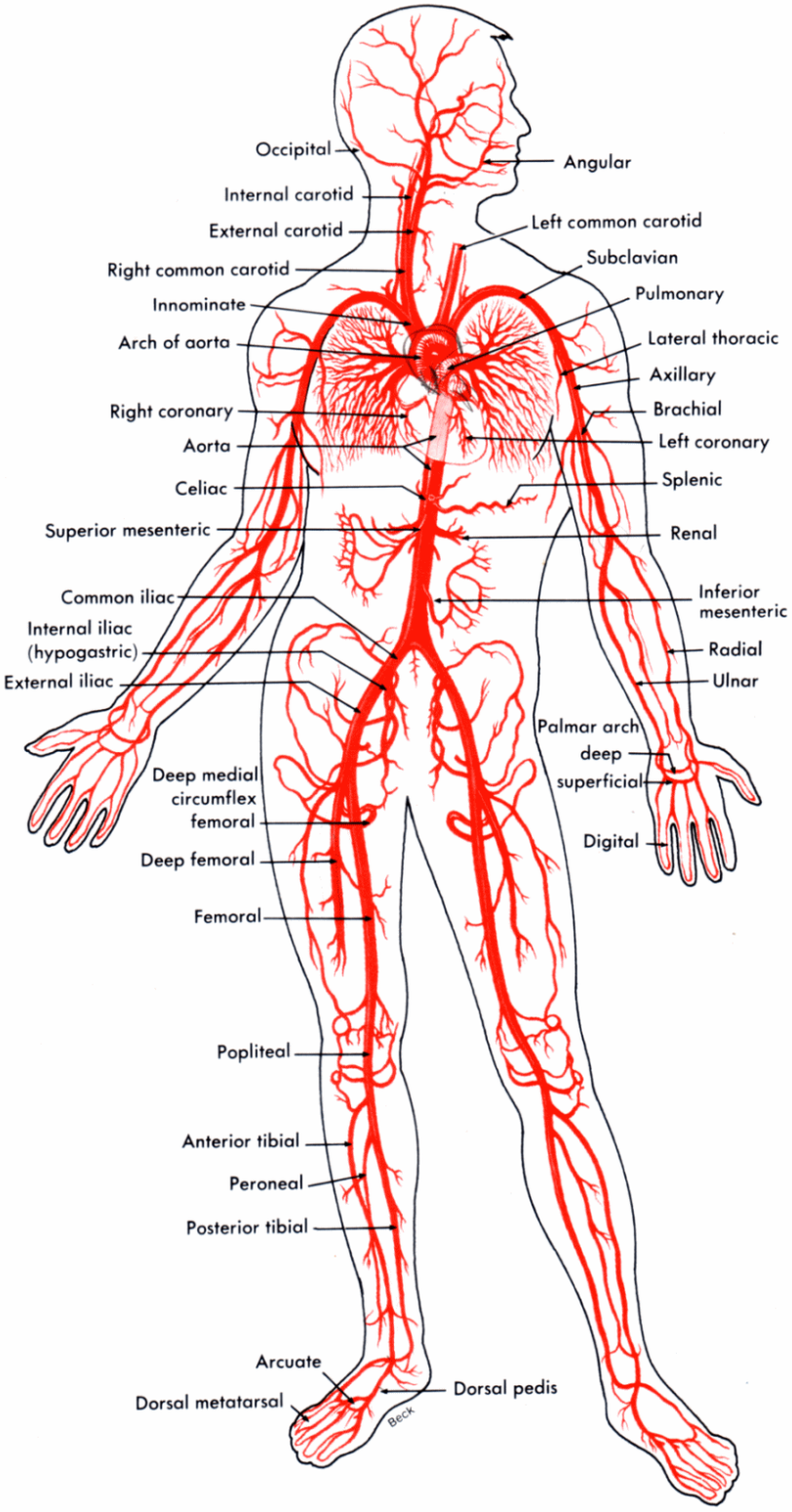

Figure 1.4 Artery system. (Reprinted from http://www.arthursclipart.org/medical/circulatory)

Table 1.1 presents the characteristic values of flow parameters within major healthy arteries (Hathcock, 2006) where the vessel mean diameter and the time-averaged Reynolds number, *Re* are tabulated. *Re* describes the ratio of inertial to viscous forces in fluid.

For comparison, the data for microcirculations, small arteries and arterioles are also included. These data are approximate by taking the averaged values compiled from Goldsmith and Turitto (1986), and Wootton and Ku (1999).

Table 1.1 Flow parameters in human arteries

Vessel	Mean diameter (mm)	*Re*
Ascending aorta	23-45	800-1600
Femoral artery	5.0	280
Common carotid	5.9	330
Internal carotid	6.1	220
Left main coronary artery	4.0	240
Right coronary	3.4	150
Small arteries	0.3	5
Arterioles	0.03	0.04

The sites of stenotic diseases are commonly found in the cereberal artery, the femoral artery, the abdominal aorta and the carotid bifurcation. The common features of these arteries include curvature and bifurcation where secondary flow and recirculation might develop and consequently change the fluid loading on vessel walls (Ku, 1997). An example of an angiogram image of a stenosed femoral artery is shown in Figure 1.5.

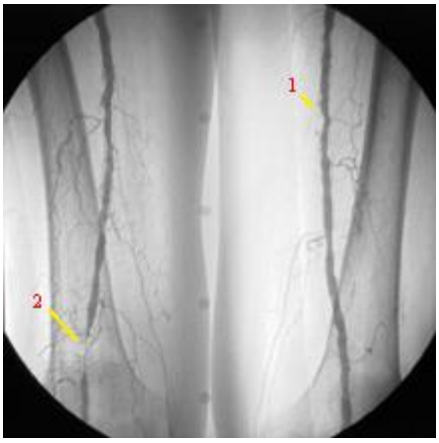

Figure 1.5 Angiogram image showing 1.Femoral artery 2. Stenosis of deep femoral artery (Reprinted from http://www.seattleavir.com/andp.html)

1.1.3 **Diagnosis**

Diagnosis of the location and extent of arterial disease is initially based on a clinical evaluation of the patient symptoms. Further clarification of the extent and degree of disease may be made using various types of imaging systems. Ultrasound and Magnetic Resonance Imaging (MRI) are non-invasive (ie. do not involve any damage or injury to the patient). X-ray techniques are invasive involving a radiation dose and often an arterial puncture.

X-ray angiography has been used for many decades. A contrast agent which shows up by absorbing the x-rays is injected into the blood to make it visible on the x-ray images. The x-ray images are usually taken using digital subtracts angiography to allow better visualisation of the vessels. Access to the blood vessel is through a guide wire or catheter. This invasive technique is associated with risk of bleeding, infection, pain and exposure to radiation. The risk of permanent neurological complications in angiographic procedures in cerebral arteries is between 1 to 4% (Hankey et al., 1990; Davies and Humphrey, 1993).

MRI is based on the resonance energy of the photons that depends on the magnetic field strength applied. An image can be constructed because the protons in different tissues return to their equilibrium state at different rates. By changing the parameters on the scanner this effect is used to create contrast between different types of body tissue or between other properties like blood. Even though MRI can give high resolution 3D images, signal loss may occur in a slow flow region and leads to inaccuracy in assessing stenosis artery images.

Computed tomography (CT) produces 2D and 3D cross-sectional images of an object from 1D X-ray images. Beams of X-rays are passed from a rotating device through the area of

interest in the body from different angles to create cross-sectional images, which then are assembled by the computer into a three-dimensional picture of the area being studied. CT produces detailed images of both blood vessels and tissues. Contrast agent could also be used to get clearer images. Although CT has been used in many clinical applications, blocked blood vessels make the images difficult to interpret. In application to the stenosed artery, this method is not yet reliable in imaging small tortuous arteries particularly coronary arteries in the rapidly moving heart (Kupeli et al., 2010).

Ultrasound is real-time, portable, inexpensive and safe imaging modality therefore it is widely used. Unlike the above methods ultrasound has no ionising radiation. Contrast agents could also be used. A high frequency beam of sound waves is transmitted into the body. The sound waves are emitted from the piezoelectric element that has been excited by electrical pulses. Several elements are arranged together to form a transducer. The wave travels into the body and comes into focus at a desired depth. The image is formed by the reverse of the process use to create the sound waves. The returning echoes to the transducer are converted by the elements into electrical signals and are then processed to form the image. The time taken for the echo to return back to the transducer will determine the location of pixels that form the image. The Doppler ultrasound technique has been used to evaluate blood flow in major arteries.

The above imaging method provides information on geometry and motion. A stenosed artery is characterised by the percentage of lumen diameter reduction that has resulted from plaque formed (Wootton and Ku, 1999).

1.1.4 **Treatments of atherosclerosis**

The purpose of atherosclerosis treatment is to reduce symptoms and prevent complications. These include life style change, medication and surgery. Life style changes include a low fat diet, weight loss and moderate exercise. Medication may be used to reduce fats and cholesterol in bloods (Steinberg, 2002). Medical therapy includes the prescription of cholesterol lowering drugs and anticoagulant to reduce risk of clot formation. In the case of carotid arteries, medical therapy is usually for mild to moderate cases while surgery is reserved for cases with severe stenosis (Strickman and Loyalka, 2005). However, nearly two thirds of the patients with acute coronary events were shown often to have <50% diameter narrowing before the clinical event (Alsheikh-Ali et al., 2010) . Though the decision to operate is based mainly on an assessment of the lumen reduction, it is addressed that the risk

of rupture is also determined by the plaque composition (Libby et al., 2002). Much research in imaging is devoted to the improvement of current diameter-base criteria, with the aim of identifying new biomarkers of plaque rupture non-invasively (Hoskins and Hardman, 2009).

There are several types of procedures to reduce or remove plaque for moderate to severe stenosed arteries. Balloon angioplasty is a procedure using a balloon-tipped catheter inserted through an artery to enlarge a narrowing in an artery (Figure 1.6). The balloon crushes the fatty deposits, so opening up the blood vessel to improved flow. The stent is inserted collapsed over a balloon and positioned at the stenosis, the balloon is inflated to expand the stent, and the balloon is deflated and withdrawn. Patients who undergo this treatment having risk of blood clot are normally given an anti-thrombosis medication. In bypass graft surgery, a vein usually obtained from the patient's leg (the saphenous vein) or a blood conduit fabricated from an artificial material, is grafted to the site of stenosis in such a way that the blood flow will bypass the occlusions. Endarterectomy is another invasive procedure; where the vascular surgeon makes an incision in the affected artery and removes the plaque or blood clot. There are risks related to operation procedure for instance the patient having coronary artery bypass graft are exposed to infection in the incision, loss of kidney function, brain complications and heart attack after the surgery.

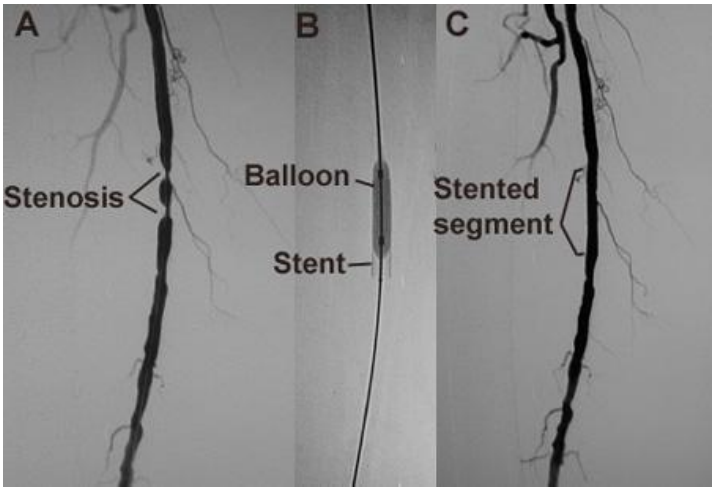

Figure 1.6 A. Preoperative angiogram showing stenosis of the femoral artery. B. Balloon and stent in place. C. Postoperative angiogram showing correction of the stenosis with a stent. (Reprinted from YourSurgery.Com®, http://www.yoursurgery.com).

1.1.5 **Summary**

Cardiovascular diseases associated to atherosclerosis have been introduced. The global death resulted from the diseased is anticipated to increase. The flow phenomena resulting from the stenosed geometry such as flow separation and recirculation are associated with atherosclerotic prone regions. During the diagnosis the stenosis artery is characterise according to diameter reduction that is due to plaque formation. The treatment of stenosis is decided based on the percentage of lumen occlusion whether it is mild, moderate or severe.

1.2 The role of fluid mechanics

Conventional diagnosis is based on lumen diameter, and relatively simple parameters such as the maximum blood flow velocity. It is however known that arterial disease progresses due to an interplay between local mechanical forces and local biology, and there is an opportunity to use more complex measurements related to the 3D velocity field, and measurements related to blood velocity such as wall shear stress, which currently are not used in diagnosis.

1.2.1 **Biomechanical forces**

When heart is pumping the blood to the vascular network, the artery wall is subjected to haemodynamic forces. The inner surface of the arterial wall, the endothelium, contains biological receptors that sense changes of these forces (Pritchard et al., 1995). The perpendicular forces resulting from the pressure pulse is responsible for arterial wall distension. The tangential stress exerted by the blood flow is the frictional force known as wall shear stress (WSS). Equation 1.1 states the relationship between wall shear stress τ_w, viscosity μ, and shear rate γ .

$$\tau_w = -\mu\gamma = -\mu\frac{\partial v}{\partial r} \tag{1.1}$$

The shear rate, γ is defined as the radial derivative of blood flow velocity ($\partial v/\partial r$). The WSS is evaluated using the velocity gradient at the wall. WSS is important in determining the endothelial cell function. The blood WSS modulates diameter adaptive responses, intimal thickening and platelet thrombosis (Wootton and Ku, 1999). For instance, if the artery senses an increase in flow, it will dilate and remodel with a larger diameter. The widening of blood vessels (vasodilation) is the result from the relaxation of smooth muscle cells. WSS

stimulates the release of endothelium –derived nitric oxide (NO) which will react with red blood cells that modulates the vascular function (Azarov et al., 2005). On the other hand, if low WSS is detected, an intimal thickening mechanism will be triggered to re-establish a normal WSS.

Early evidence suggested that mean wall shear stress was maintained constant in arteries in the region of 1-2Pa (Giddens et al., 1993). However recent evidence has suggested that there are variations in mean wall shear stress in different arteries. Cheng et al (2007) reported the values varied between 2 to 16 Pa. Under abnormal shear stress, endothelial dysfunction can occur (Shin et al., 2004). Disordered endothelial function triggers inflammatory response which contributes to the development of atheromatous plaque. Shear stress as low as 0.4 Pa was found to stimulate an atherogenic phenotype (Malek et al., 1999).

Low WSS has been correlated with atherosclerosis due to low mass diffusion of lipids away from the wall (Caro, 1978). Intimal plaque thickening was greatest at low WSS region. Fluid shear stress has been shown to regulate transcription by endothelial cells of adhesion molecules genes that attract leukocytes as well as transcription of growth factors such as platelet derived growth factor that simulate smooth muscle cells migration and proliferation (Slager et al., 1995)**.**

1.2.2 **Estimating wall shear stress**

As described in earlier, WSS is a frictional force between blood and endothelium which is a potential parameter to assist atherosclerosis diagnosis. The wall shear rate in Equation 1.1 can be estimated from imaging systems. However, it was found that there were difficulties in identifying the wall location in regions of low shear. In large arteries the assessment of WSS remains an approximation due to limited spatial resolution (Reneman et al., 2006). The in-vivo calculations for WSS are derived from Equation 1.2 where the stress is expressed in terms of volume flow rate by assuming fully developed laminar flow. The relationship (Hagen-Poiseuille equation) is given as

$$\tau = \frac{4\mu Q}{\pi R^3} \tag{1.2}$$

Where Q is the volumetric flow rate and R is the lumen radius. When the flow is assumed parabolic and viscosity is constant the expression for shear rate is reduced to

$$\dot{\gamma} = \frac{4V_{mean}}{R} = \frac{2V_{max}}{R} \tag{1.3}$$

The determination of WSS using simplification in Equation 1.3 requires the measurement of the vessel radius and either maximum or average flow velocity. However, the shear stress value calculated in this way poses an error as high as 50% (Reneman et al., 2006).

A more accurate method of determining the wall shear rate is by analysing the near vessel wall velocity gradient as in Equation 1.1 where the WSS is determined by multiplying the wall shear rate with blood viscosity. However, wall shear rate measurement is difficult by using imaging technique. Blood flow velocities have to be determined accurately close to the wall. In arteries, wall shear rate is assessed at a distance from the wall due to limited resolution of the ultrasound and MRI system. Extrapolation of shear rate data indicates that for shear rates values determined 250-300μm from the wall using the ultrasound technique, the shear stress at the wall is underestimated by 7-22% (Long et al., 2004; Blake, 2008).

1.2.3 **Image-guided modelling**

Image-guided modelling appeared to address many of the difficulties in obtaining reliable WSS values. Computational fluid dynamics (CFD) simulation is performed to estimate the blood flow velocities and hence the derived quantities including WSS. The processing chain for image guided modelling is shown in Figure 1.7.

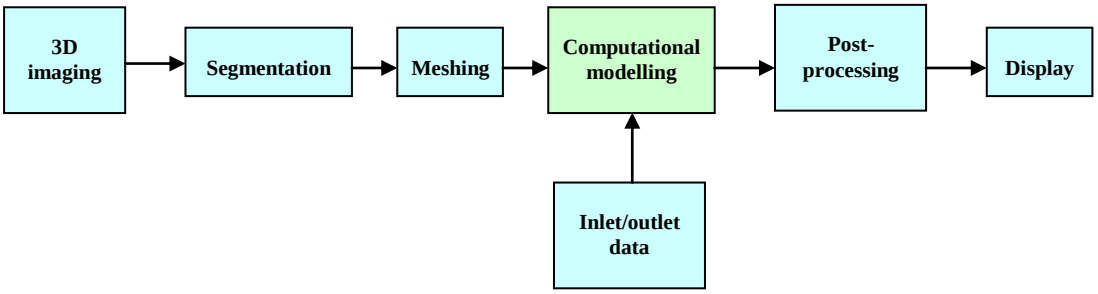

Figure 1.7 The process steps for image-guided modelling for displaying flow field data.

Simulations use true 3D geometry obtained from high resolution imaging techniques such as intravascular ultrasound (Chandran et al., 1996; Krams et al., 1997; Glor et al., 2005), MRI (Xu et al., 1999; Long et al., 2000; Glor et al., 2003), CT (Morris et al., 2005; Kagadis et al., 2008; Kim et al., 2008) and rotational angiography (Steinman et al., 2003; Cebral et al., 2005). Segmentation and meshing are performed to divide the arterial geometry into discrete finite elements. The governing mathematical flow equations are then solved over these volumes.

The accuracy of the CFD data is dependent on the mathematical modelling equation employed and the boundary conditions set. Hence, it is important to program the equations according to the physiological environment. Verification of the computational method and validation of mathematical models are needed before the models can be accepted into clinical decision making (Steinman and Taylor, 2005; Taylor and Steinman, 2010).

1.2.4 **Summary**

The WSS plays an important role on the development and progression of atherosclerosis. Low WSS has been correlated with plaque thickening. With current imaging techniques the assessment of the WSS are difficult and pose significant measurement error. CFD methods have been used to determine the WSS. Numerical models need to be validated against experimental models which are accepted as gold standard.

1.3 Blood models

Blood is a fluid transporting nutrients, oxygen, carbon dioxide and other essential components to the body. Whole blood consists of cells suspensions and plasma. The concentrated suspended blood cell elements include red blood cells (RBCs), white blood cells (WBCs) and platelets. In image-guided modeling, the blood properties have to be specified in the computational modeling. This section will first discuss the actual blood properties followed by the mathematical and physical models for blood used for WSS prediction.

1.3.1 **Blood composition**

The red blood cells themselves constitute 45% of blood volume. The volume fraction of RBCs in blood is also known as the haematocrit level. Other cells, such as leukocytes and platelets are only 1% of the total volume concentration. The remaining volume is the plasma which is mainly an aqueous solution containing organic and inorganic materials. Plasma consists of 90-92 % of water, 7% of proteins and remaining inorganic constituents. The blood composition and cell dimensions are summarised in Table 1.2. A schematic of cells in a blood vessel is further illustrated in Figure 1.8.

Table 1.2 Blood composition and cells dimension (Caro 1978)

Blood elements	Cell shape and dimension (μm)	Volume concentration
Plasma (Constituents: Water Proteins, Salts,hormones, glucose,metabolites, nutrients)	-	54 %
Red blood cells (Erythrocyte)	Biconcave disc 8 x 1-3	45%
White blood cells (Leukocytes)	Roughly spherical 7-22	1%
Platelets	Rounded or oval 2-4	

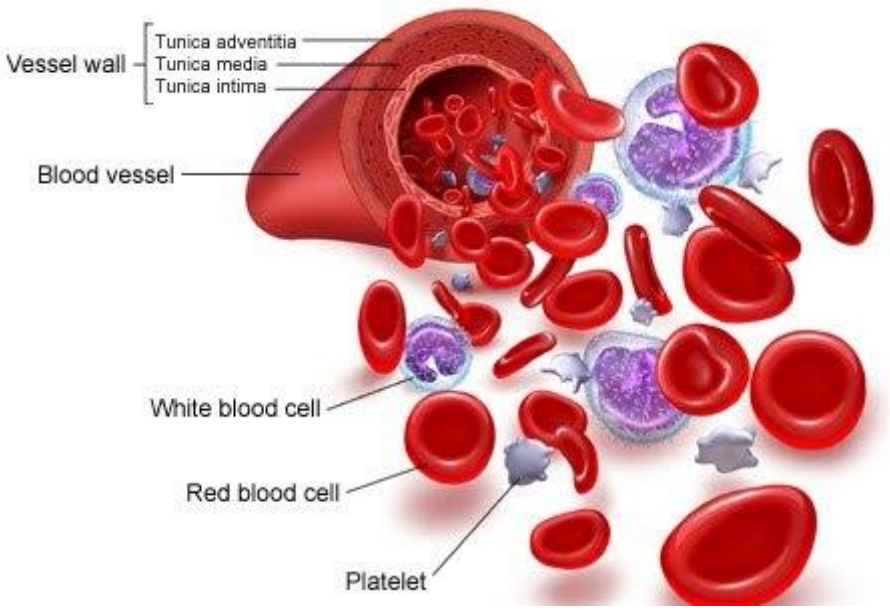

Figure 1.8 Blood vessel with cellular components (Reprinted from http://www.virtualmedicalcentre.com)

1.3.2 **Blood viscosity**

In general, the rheology of a fluid can be described by its viscosity. As described in Equation 1.1, viscosity is the ratio of the force that moves the fluid layers (shear stress) to the velocity gradient in the fluid, representing internal resistance between the fluid layers (Baskurt and Meiselman, 2003).

The suspended elements, mainly the RBCs which are the dominant cells that occupy blood volume, strongly influence the apparent viscosity. Plasma behaves like a Newtonian fluid with a constant viscosity of 1.2 mPas (Fung, 1993). However, in the presence of cellular components, the apparent viscosity is not constant, therefore the rheological behaviour is non-Newtonian. In viscometer measurements, whole blood shows a shear thinning property. At low shear rate of $23s^{-1}$ the viscosity of human blood at 37ºC is in the range of 8.4 to 5.6 mPas, and at a higher shear rate of $230s^{-1}$ viscosity is between 5.1-3.8 mPas (Wells and Merrill, 1962). At low shear, red cells form rouleaux that lead to high blood viscosity (Levick, 2003). At high mechanical shear rate typically $50s^{-1}$, the cells disaggregate (Pries et al., 1992). As the shear rate is increased, the rouleaux become progressively broken down in size by stretching and shearing forces acting during their deformation and rotation leads to decrease in viscosity. When shear rate reach $1000s^{-1}$, an asymptotic viscosity of 3.5mPas is reached and the blood behaves as a Newtonian fluid (Nichols and O'Rourke, 2005). The variation of viscosity and the presence of red blood cells in the blood suspension demonstrate the importance of cellular components on blood rheology. The shear thinning behaviour is described in Figure 1.9.

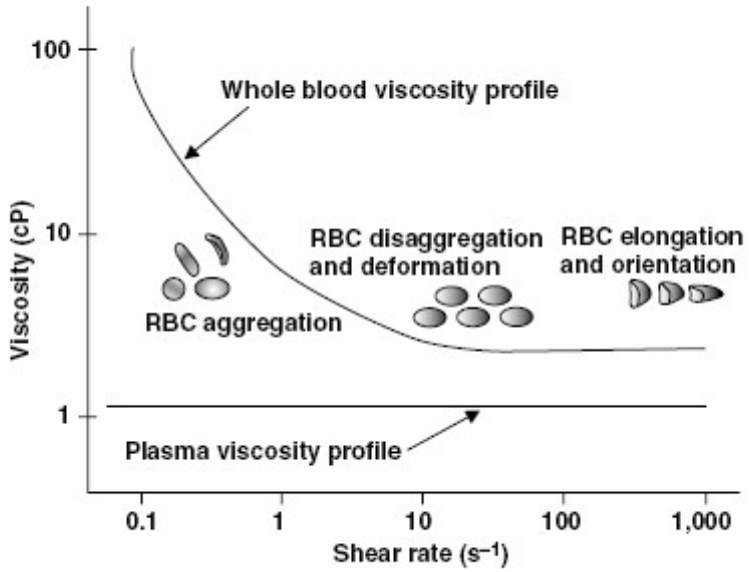

Figure 1.9 Blood viscosity (Reprinted from http://www.yashagrawal.com/2008/01/serum-or-whole-blood-viscosity.html)

1.3.3 **Computational rheological models in blood flow study**

CFD models have been developed extensively to simulate blood flows. In CFD, hemodynamic studies employed Newtonian (Beech-Brandt et al., 2005; Stroev et al., 2007) and non-Newtonian models (Neofytou and Drikakis, 2003; Hyun et al., 2004; Longest et al., 2004). For studies which assume blood is a Newtonian fluid, the viscosity is taken as a constant value, thus ignoring the shear-thinning behaviour of blood. The following discussion will explain the non-Newtonian blood models.

Common non-Newtonian blood constitutive equations employed are Casson, Power Law and Quemada models (Buchanan et al., 2000; Longest and Kleinstreuer, 2003a; Longest and Kleinstreuer, 2003b). Casson model (Ferziger and Peric, 1999) is given by

$$\begin{aligned} \sqrt{\tau} &= \sqrt{\tau_y} + \sqrt{\mu_\infty \gamma}, \quad |\tau| > \tau_y \\ \gamma &= 0 \qquad\qquad\qquad\quad |\tau| < \tau_y \end{aligned} \tag{1.4}$$

where τ_y is the yield stress and μ_∞ is the asymptotic viscosity. The difficulty of applying the Casson equation lies in its discontinuous character. Thus, several modified Casson equations have been proposed, so that the whole range of shear stress will be represented by one equation (Papanastasiou, 1987; Ishikawa et al., 1998)

A power law based model to represent blood is derived by Walburn and Schneck (1976). It is given by

$$\tau = c\gamma^{h} \tag{1.5}$$

This model takes into account the haematocrit and the total protein minus albumin (TPMA) in the parameters c and h. For blood with haematocrit 45% at 37˚C, c = 14.67 Pas and h = 0.7755. However, the application of this model is limited to 0.031 – 120s^{-1} (Easthope and Brooks, 1980).

In Quemada's model (Quemada, 1978), the shear rate is derived from the dependence of viscosity on shear rate and haematocrit in a concentrated disperse system. The correlation is given by

$$\tau = \mu_F \left(1 - \frac{1}{2} \frac{c_0 + c_\infty \sqrt{\gamma / \gamma_c}}{1 + \sqrt{\gamma / \gamma_c}} \varphi \right)^{-2} \gamma \tag{1.6}$$

where μ_F is the suspending medium viscosity at volume concentration of particles, φ. In blood flow, the suspending medium is the plasma and the volume concentration of particles refers to blood haematocrit, γ_c being the critical shear rate associated with relaxation time. c_0 and c_∞ are both semi-empirical intrinsic viscosities at $\gamma_r << 1$ and $\gamma_r >> 1$, respectively, where $\gamma / \gamma_c = \gamma_r$. For haematocrit at 45%, the μ_F = 1.2mPas, values of parameters are γ_c = 1.88 s^{-1}, c_∞ = 2.07 and c_0 = 4.33 (Neofytou, 2004). The Quemada model extends to a maximum shear rate of 256.7s^{-1} which is higher than Casson and Power Law boundary (Buchanan et al., 2000).

Other shear thinning models include Carreau-Yasuda (Cho and Kensey, 1991), Herschel-Bulkley (Sankar and Lee, 2008) and Cross (Chien, 1970). The details of these models applied in arterial flow is summarised by Johnston et al.(2004) and O'Callaghan et al. (2006).

1.3.4 **WSS and blood models**

In CFD studies comparing the WSS distribution of Casson, Power law and Quemada models in the same flow system across a stenotic vessel indicate an intense WSS variations (Neofytou and Tsangaris, 2006). Although the WSS distribution is similar, the peak values for WSS for every model throughout the cycle are markedly different. The haemodynamic parameters variation is also observed in other studies comparing different rheological models

disturbed flow (Buchanan et al., 2000; O'Callaghan et al., 2006). Table 1.3 compares the WSS of different computational models. The difference between Newtonian and non-Newtonian models are as small as few percent up to 160% depending on the geometry and the flow conditions.

Table 1.3 Comparison of peak WSS predicted from Newtonian and non-Newtonian models in CFD.

Authors	Geometry	Flow conditions	Peak WSS, Newtonian (Pa)	Peak WSS, non-Newtonian (Pa)	Difference
(Neofytou and Tsangaris, 2006)	50% asymmetric stenosis	Steady flow at inlet *Re* =300	10.2	Casson = 10.8 Power Law= 9.2 Quemada= 11.0	8-9%
(Buchanan et al., 2000)	50% axisymmetric stenosis	Pulse flow at mean *Re*=200, *Wo*=4.0	6.4	Power Law= 9.4 Quemada= 6.6	3-47%
(O'Callaghan et al., 2006)	Bypass graft anastomosis	Steady flow at inlet *Re*=273	2.5	Modified Cross = 2.7 Power Law= 2.5 Quemada= 2.6 Carreau=2.4	0-8%
		Steady flow at inlet *Re*=18	0.05	Modified Cross = 0.13 Power Law= 0.09 Quemada= 0.125 Carreau=0.125	80-160%

The assumption that blood can be modelled as Newtonian fluid is still in question. For instance, Perktold et al.(1991) assumed homogeneous Newtonian fluid in their carotid artery bifurcation model, bearing in mind the wall shear stress resulting from Newtonian and non-Newtonian model has 10% average difference. Blood is said to only have non-Newtonian properties when flowing in small arteries that have an internal radius less than 0.5mm, where the RBCs tend to aggregates (Levick, 2003; Nichols and O'Rourke, 2005). However, the rheological properties discussed above suggested the importance non-linear viscosity effects in disturbed flow of large artery. It can be concluded that choice of blood models has to be based on particular situations and cannot be treated as Newtonian/non-Newtonian in general. There is no single model can adequately describe the properties of blood under all circumstances (O'Callaghan et al., 2006).

In order to study the rheological implication in WSS measurement experimentally, various blood analogue fluids have been developed having similar properties to blood and tested

under physiologic experimental environment. Newtonian fluid experiment models normally use a water-glycerol mixture to mimic the viscosity of blood at 3.8-4 mPas (Deplano and Siouffi, 1999; Benard et al., 2003; Meagher et al., 2005). Meanwhile, for non-Newtonian fluid, various mixtures are employed. This include KSCN-Xanthan gum solution (Gijsen et al., 1999), polyacrylamide particle in DMSO solution (Walsh et al., 2003) and glycerine-Xanthan gum (Gray, 2002). Significant differences in velocity profiles relative to those measured with Newtonian fluid reported (Deplano and Siouffi, 1999; Gijsen et al., 1999; Gray, 2002; Walsh et al., 2003).

All of the non-Newtonian blood models employed in the computational modelling and experiment assumed blood as a homogeneous mixture. In other words, all blood models discussed treated blood as a single phase fluid. The deviation from linearity observed from non-Newtonian models is depending on the properties of the bulk fluid.

1.3.5 **Summary**

Blood composition and blood viscosity models have been discussed. There is a significant influence of the viscosity models on WSS determined from CFD and experimental work. Most of the blood rheological models in large arteries predicting WSS assumed blood as a homogeneous fluid which is not the case in in-vitro. From microscopic consideration, blood composed of cellular materials that could be rendered as particulates.

1.4 Multiphase nature of blood

In Section 1.3, the WSS measurements based on single phase blood models has been discussed. Blood is in fact a two-phase liquid. It can be considered a solid-liquid suspension if the cellular elements are regarded as solid particles. One of the factors responsible for non-Newtonian behaviour of whole blood is the presence of cell suspension (Pal, 2003). Although the blood cells are elastic, the properties were found insensitive to the velocity profile and WSS distribution in arterial geometry (Gijsen et al., 1998; O'Callaghan et al., 2006). Therefore, blood cells can be treated as solid particles. In this section, the cellular distribution observed in-vitro and the relationship with atherosclerosis will be discussed

1.4.1 **Inhomgeneity of blood cells in blood vessels**

In tube flow, RBCs tend to move towards the axis of the tube leaving a marginal plasma layer. This layer is relatively deficient of suspended particles. The cell free layer although

very thin has an important effect on haemodynamics (Fung, 1993). Butler et al. (1998) imposed a cell-free layer near the vessel wall in a simulation involving the scavenging effect of red cells on nitric oxide (NO) produced from endothelium, demonstrating that a cell-free layer was necessary for NO to have a vasodilator effect as is known to occur in-vivo.

Experimental observations made by Aarts et al.(1988) also demonstrated that platelets suspended in saline move radially and accumulate half way between the vessel centre and the vessel wall. However when suspended in a suspension of red cell ghosts at physiologic volume fractions (40%) the platelets were almost solely concentrated near the vessel wall.

Karino and Goldsmith (1977) studied the behaviour of blood cells and solid spheres flowing in the separation zone of a step expansion of a capillary-sized vessel. Blood cells and solid spheres with diameter less than 20μm migrated out of the vortex whilst larger cells and spheres remained in the recirculation region. Lima et al. (2008) found that RBCs dispersion in straight glass capillaries leads to unequal distribution of cells depending on the cell concentration and vessel diameter. Similar observations were obtained in small arteries where Jung and Hassanein (2008) reported RBC volume concentrations down to 5% near the vessel wall compared to average values in the human of 45%. Those observations supported the fact that cellular content of blood at different levels of circulatory system varies over wide range (Baskurt and Meiselman, 2003). These works provide the evidence that inhomogeneity of blood cells does occur in arteries and microcirculation.

1.4.2 **Cellular distribution and atherosclerosis**

Atherosclerotic lesion is not evenly distributed over the arterial system and is a geometrically focused disease. The lesion preferentially located at inner curvature of artery, near side branches and stenosis with complex flow pattern (Jung et al., 2006). Low WSS was reported under arterial flow phenomena where recirculation, stagnation, and secondary flow motion have been discovered at arterial branches, curves, bends and constriction (Sharma et al., 2004). Low WSS was associated to plaque-modulating factor (Krams et al., 1997). In the presence of LDL and low WSS the inflammatory process is triggered. The receptors at the artery wall will stimulate the recruitment of WBCs. The migration of WBCs at low shear region has been observed by Skilbeck et al. (2004). The migration of WBCs to the wall is triggered by inflammation mediators at the wall which involved free flowing WBCs exiting the central blood stream, interacting with RBCs and decelerating to initialise rolling. Rolling is mediated by adhesion molecules at the wall surface (Artoli et al., 2007). The adhesion of WBCs shows marked increase in the recirculation region of a disturbed flow (Karino and Goldsmith, 1979; Barber et al., 1998; Hinds et al., 2001). Even in the absence of wall

biological effects, the WBCs margination to the wall is strongly influenced by hydrodynamics (Pritchard et al., 1995).

In the case of thrombosis, increase in platelet accumulation is directly related to shear rate. Platelet accumulation may be explained in terms of a shear-link mechanism that involves platelet transport, platelet activation and embolisation (Ku, 1997). RBC motion and platelet concentration are the main factors that affect the rate of platelet interaction with thrombogenic surface (Aarts et al., 1988). Platelets were seen accumulated near the reattachment point in stenosis. Platelets may recirculate in a flow separation area long enough to allow activation and form aggregates (Bluestein et al., 1997).

Shear forces are not the only biomechanical factors that influence the vascular biology. Since the disease involves cellular interactions, we also need to look away from the wall and move to the bloodstream to understand vascular pathophysiology (Taylor and Steinman, 2010). Other than WSS, haemodynamic parameters related to blood cell interaction like flow residence time (Rayz et al., 2010) and near wall particle residence time (Longest et al., 2004) have been established.

1.4.3 **Summary**

Blood cell distribution is not uniform in the arterial network. Under low WSS, cellular interactions could lead to the onset of the inflammatory process and thrombosis. This suggest that particle parameters are important where the multiphase nature of blood could not be neglected.

1.5 The physics of cell migration

Migration and adhesion of blood cells in disturbed flow was reported in in-vitro experiments. In fluid mechanics blood cells can be regarded as particles. Whole blood is normally considered as a particle suspension.

1.5.1 **Particle migration in pipe flow**

In a dilute suspension of rigid spheres, the particles become concentrated in a thin cylindrical layer. They are moving at the same velocity and align themselves into a regular column parallel to tube axis. This observation appears when the particles travel a sufficient distance:

> "Two particles which happened to move along the same line attract each other, until they reach a minimum (not touching) distance. Then the repulsion predominates until by damped oscillations an equilibrium distance is found, and the particles form a stable pair. If the two particles were not initially aligned, a transverse displacement concomitant with this longitudinal rocking motion brings the particles into the same final configuration. This too, however, is final only if no other particle is found nearby, otherwise this also tends to align itself with the first two, and a group of three, equidistant particles is formed. And the process goes on, by capture of isolated spheres or by fusion of already formed groups, until all suspension is nothing more than a collection of nice, regular, long necklace" (Segre and Silberberg, 1961).

It was shown that a freely rotating neutrally buoyant sphere in a fluid undergoing Poiseuille flow reached a stable equilibrium radial position at $r=0.6R$ (Segre et al., 1962). The migration is independent of the initial point of release. Thus the overall migration leads to an accumulation of sphere in an intermediate annulus. This phenomenon is called the 'tubular pinch effect'. The physical mechanism is not fully understood but the Saffman lift force is shown to be one of the contributing the factors (Feng and Michaelides, 2003; Matas et al., 2004).

1.5.2 **Particle migration due to geometry expansion.**

Stenotic flow in an artery has a characteristic expansion on the distal (downstream) side. Previous studies on flow that developed recirculation or vortex zones have observed either particle depletion or accumulation depending on experimental conditions (Karino and

Goldsmith, 1977; Jin and Acrivos, 2004; Moraczewski et al., 2005; Moraczewski and Shapley, 2007). Table 1.4 summarises experimental work that has observed particle distribution in the recirculation region of the expansion geometry. Moraczweski et al. (2005) found a tendency for particles to migrate away or into the flow separation region in an abrupt axisymmetric 1:4 expansion depending on the tube-particle radius ratio, *R/a*, where *R* is the radius of the large tube. They concluded that a general pattern observed in their experiment as well as those of Altobelli et al. (1997) and, Karino and Goldsmith (1977) are

$$\begin{cases} R/a \le 17 & \textit{accumulation,} \\ 25 \le R/a \le 224 & \textit{depletion,} \\ R/a \ge 508 & \textit{accumulation.} \end{cases}$$

Table 1.4 Experimental conditions in the abrupt expansion geometry.

Expansion geometry	Particle	Mean Particle diameter (μm)	*R/a*	Initial particle concentration	*Re*	Authors
Axisymmetric pipe with ratio 1:4	Microparticles (PMMA* and Polystyrene)	85,255, 485	39, 75, 224	20%-50%	0.001 -3.2	(Moraczewski et al., 2005)
Axisymmetric pipe with ratio 1:4	Microparticles (PMMA*)	675,100	75,508	50%	0.007	(Altobelli et al., 1997)
Step expansion with ratio 1:3.3	RBCs, platelets, carbon microspheres, polystyrene latex spheres	3.6-50	10-194	1%-45%	0.5, 12.2, 37.8	(Karino and Goldsmith, 1977)
Axisymmetric pipe with ratio 1:2	RBC, microparticles	8,2	12.5-50	<20%	8.3-41.7	(Zhao et al., 2008)
Axisymmetric stenosis with ratio 1:1.6	WBCs	10	635	0.03%	100, 140	(Hinds et al., 2001)

*PMMA-polymethylmethaacrylate

Recent study by Zhao et al.(2008) disagreed with the correlation suggested. In their study RBC (*R/a*~12.5) and microparticles *(R/a*~50) were suspended together in blood plasma. The RBCs were found to escape the recirculation zone while the microparticles accumulated at the corner of the expansion zone.

Hinds et al. (2001) performed experiments at higher *Re* tracking the WBCs adherence to the wall of the expansion region. They found that the WBCs do not adhere to the inert wall of the flow separation zone at *Re* =100 and 140.

1.5.3 **Summary**

The observation of particle migration in tube flow has been put forward explaining the role of hydrodynamic force to the particle motion. Experimental investigation looking at particle migration phenomena in flows subjected to expansion has been discussed. The flow *Re* studied ranges from 0.001 to 140.

1.6 Critical gaps in the literature

The description of atherosclerosis, the diagnosis, treatment, prevention and management of the disease was reviewed in Section 1.1. The role of biomechanical forces, the WSS in plaque development and the methods to determine the forces were discussed in Section 1.2. With current imaging techniques, the estimation of WSS is challenging. Image-guided modelling is the emerging computational technique to predict the blood flow behaviour. Numerical data has been used but lacks verification and validation. In Section 1.3 the properties of blood and blood models were reviewed. Various computational modelling and experimental approaches have been performed where blood models often neglect the two phase nature of blood. In section 1.4 the evidence of particle inhomogeneity has been put forward where the concentration of blood cells varied. Other than WSS, the blood cells localisation is also the contributing factor to the initiation and progression of the disease. Even though atherogenesis and atherothrombosis strongly influenced by WSS and cells-wall interaction, the correlation between blood cells concentration distribution at low WSS region that occur at atherosclerotic lesion was not fully understood. Section 1.5 relates the physics of cell migration and the atherosclerotic prone region. The study on migration of blood cells and micro-particles in the recirculation region of expansion geometry was reviewed.

1.6.1 **The need of understanding the particle migration in stenosed artery**

At cellular level there are many variables can influence the flow field hence, the WSS. The blood cells morphology such as the size and the shape as well as the concentration in plasma may affect the hydrodynamic behaviour. The question here is: to what extent do cell-plasma cell-wall and cell-cell interactions have an influence on the flow field? Unfortunately, a hydrodynamics mechanism has not been established due to difficulties in separating these

variables (Davies et al., 2005). Responding to this gap, this study will look at the basic factors that influence the migration of blood cells to the region prone to the disease progression.

1.6.2 **The need for micro-scale measurements for large arteries**

With present imaging techniques, the estimation of WSS is limited to macro estimation where the level of accuracy is in questioned. Near wall cellular interaction that influences surrounding velocity field is at micro scale. In-vivo estimation sometimes has limited spatial resolution that does not allow accuracy down to this scale.

In computational studies, most viscosity models employed are not a function of blood cells interactions. The blood cells are assumed homogeneous with rheological models either Newtonian or non-Newtonian.

The cellular interaction for microcirculation has been established and for large arteries this factor is often neglected. It has been shown that the cells distribution in a recirculation region is a function of cell size and vessel diameter (Matas et al., 2003; Moraczewski et al., 2005; Lima et al., 2008). Hence, the dynamics may differ between microcirculation and large arteries.

Particle migration behaviour as summarised in Table 1.3 is limited to a low *Re* below large artery physiological flow rates. In arteries the mean *Re* spans from 160 to 1600 (Table 1.1). Considering large arteries with diameter range of 3-8mm, the tube-particle ratio, *R/a* are within 150 to 4000. At the moment all experimental studies looking at particle migration have the *R/a* up to 675 and maximum *Re* of 140. It is important to see the particle migration behaviour at the recirculation zone at much higher Reynolds number, where the inertial effect is significant.

1.7 Outline of the thesis

This study focuses on the hydrodynamics forces that affect cell distribution in the flow separation region of a diseased artery model where WSS are low. A physical experiment is conducted to investigate the particle distribution and computational simulation is performed to analyse the forces involved. In the experiment, a blood mimic solution is prepared by suspending micro-particles in fluid. The concentration of micro-particles prepared is dilute so that the flow field can be measured. Steady flow is used so that the involvement of variables due to transient effects is minimised. This work focuses on dilute particle suspensions where the concentration is less than 1%.

1.7.1 **Aim**

The aim of the thesis is to investigate the particle migration behavior through a stenosed artery model. The influence of particulates suspension on the stenotic flow field is examined.

1.7.2 **Objectives**

The objectives of the thesis are

- To characterize the flow through the stenosis geometry model using particle image velocimetry method.
- To characterize the particle distribution distal to stenosis at physiological flow rates
- To study the effect of particle sizes, particle concentration and flow rates on the particle distribution
- To perform computer simulation to study quantitatively the motion of particles and the forces influencing the particle distribution

1.7.3 **Thesis structure**

The work is focused on the influence of particulate suspension on the flow field of a stenosed artery.

Chapter 2 presents the principles of fluid mechanics in order to describe the flow of particle suspension. The single-phase flow of Navier-Stokes equation is first described followed by two-phase flow principles. The hydrodynamic forces involved in particle-fluid and particle-particle are discussed.

Chapter 3 explains the experimental approach in measuring the flow velocities of a stenosed artery model. This chapter describes the utilization of Particle Image Velocimetry (PIV) system to physically measure the flow field.

Chapter 4 presents the essential characterisation of flow field in a stenosed artery model. The velocity is determined by PIV method and the velocity gradient is calculated. Flow dimensionless parameters were assessed to understand the flow behaviour.

Chapter 5 examines the particle distribution in the recirculation region of a stenosed artery model. The influence of particle sizes, particle distribution and flow rates are reported.

Chapter 6 deliberates a computational approach to validate the flow field measured in Chapter 4. The flow is treated as single phase. The reattachment length and the central vortex are compared.

Chapter 7 presents the study employing computer simulation method to investigate the particle dynamics. The effect of hydrodynamic forces such as drag and lift forces on particle migration is discussed. The WSS in the recirculation region in the presence of particles is compared with the WSS for single-phase condition.

Chapter 2

ESSENTIAL THEORETICAL CONSIDERATIONS

The understanding of biofluid dynamics like blood flow in artery relies on analytical fluid mechanics. The relations between blood plasma and cellular components play a role in understanding the mechanisms that leads to the initiation and progression of diseases. This chapter presents relevant fluid dynamics principles related to the particle migration behaviour. Dynamic similarity parameters are discussed and these parameters will be used consistently in the thesis. Single phase flow governed by the Navier-Stokes equations and the flow in a straight tube are reviewed. The overview is followed by multiphase consideration where the fundamental principle of solid-liquid flow is discussed. With that, the basic understanding is established for reference in the discussion of subsequent chapters.

2.1 Dynamic similarity

2.1.1 **Introduction**

Dynamic similarity is important in fluid mechanics because it gives the benchmark to describe and compare flows under different conditions. In the case of flow in a human artery, the physical experimental model and computational model can be referred to the same dynamic parameters. These parameters are dimensionless where the magnitude of the hydrodynamic forces is expressed as a ratio to another force. In other words, the ratio of magnitude of any two forces in real human artery must be the same as the magnitude ratio of the corresponding forces in the laboratory measurement in physical model. For particle-fluid system investigated here, the relevant dimensionless flow parameters are the Reynolds numbers, Stokes number and Peclet number.

2.1.2 **Reynolds numbers**

The Reynolds number, *Re,* is proportional to the magnitude of the inertia force to the viscous force. A *Re* can be based on flow of fluid, particle suspended in the fluid and the shear acting on the particles in the fluid (Saffman, 1965). In general the flow *Re* of fluid in the cylindrical pipe is given as

$$Re = \frac{\rho D V_{mean}}{\mu} \tag{2.1}$$

where ρ is density of the fluid, D is the diameter of the inlet, V_{mean} is the mean velocity of the fluid and μ is the viscosity of the fluid. The mean velocity could be expressed in terms of the velocity magnitude, axial component, u or radial component, v. As shown in Table 1.1, blood flow Re in large arteries ranges from 160 to 1600.

The particle Reynolds number, Re_p is based on particle diameter, d_p instead of pipe diameter, D.

$$Re_p = \frac{\rho d_p V_s}{\mu} \tag{2.2}$$

where V_s is the slip velocity which is the difference between the fluid velocity and particle velocity. Since the blood cells in the range of micron size, the Re_p was commonly taken as approaching zero (Kleinstreuer, 2006).

Shear Reynolds number, Re_g is important when the flow of particles in fluid is subjected to shearing stress. It expressed as

$$Re_g = \frac{a^2 \rho}{\mu} \frac{du}{dr} \tag{2.3}$$

where a is the particle radius and du/dr is the axial velocity gradient across the particle. In most of the study modelling blood cells behaviour, the assumption of $Re_g << 1$ was normally made (Buchanan et al., 2000; Hyun et al., 2000; Kleinstreuer, 2006) .

2.1.3 **Stokes number**

Stokes number, St, is an important parameter to described particle laden flow. It is the ratio of the particle inertial force to the fluid inertia force and is given as

$$St = \frac{\rho_p d_p^2}{18\mu} \frac{du}{dr} \tag{2.4}$$

where ρ_p is the density of the particle. If the $St << 1$, the fluid hydrodynamics interaction is dominant and the particle will tend to follow the fluid path. On the other hand, when $St >> 1$ the fluid velocity changes will have little effect on the particle trajectory. For cell suspension in blood flow, the St is known to be smaller than unity (Hyun et al., 2004; Kleinstreuer, 2006).

2.1.4 **Peclet number**

The Peclet number, *Pe*, expresses the ratio of the hydrodynamic shear forces and diffusive Brownian forces acting on the suspended particles.

$$Pe = \frac{6\pi\mu a^3}{kT}\frac{du}{dr} \tag{2.5}$$

where k is the Boltzmann's constant and T is the temperature. The Brownian forces tend to bring the suspended particles back to their equilibrium configuration, which is continuously disturbed by the hydrodynamic shear forces acting on the particle. Large *Pe* indicates the system is non-Brownian and the particle motion is govern by hydrodynamic shear.

The suspension rhelogy relationship between Re_g and *Pe* is shown in Figure 2.1 (Stickel and Powell, 2005). The correlation suggests that the shear thinning behaviour is important where the $Pe < 10^{-3}$. For large *Pe* the particulate suspension has a Newtonian behaviour.

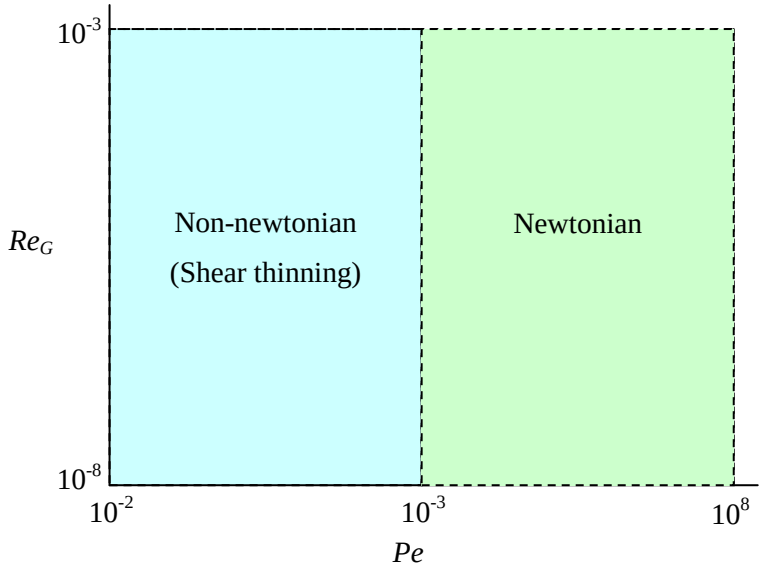

Figure 2.1 Phase diagram for suspension rheology based on Re_g and *Pe* (Stickel and Powell 2005)

The diffusion of blood cells was not widely investigated. To the best of author's knowledge, the relationship of the cells microstructure in blood flow that relating *Pe* and Re_g was not established.

2.1.5 **Summary**

In particulate suspension flow, the motion of particles in fluid can be analysed by referring to the dimensionless numbers. For flow subjected to shear gradient *Re*, Re_p, Re_g, *St* and *Pe* will be essential parameters to describe the flow behaviour.

2.2 Single phase flow

2.2.1 **Introduction**

In many studies, fundamental work investigating blood flow commonly assumes blood as a single phase fluid where the flow system is considered as a homogenous mixture (Perktold et al., 1991; Buchanan et al., 2000; Johnston et al., 2004; Longest et al., 2004; Li et al., 2007; Stroev et al., 2007). The equations of motion of a single phase fluid derived from the conservation of mass and conservation momentum. Conservation of mass is also known as continuity equation meanwhile the momentum conservation is the Navier-Stokes(NS) equations.

2.2.2 **Governing Equations**

Mass conservation equation or continuity equation is given as

$$\frac{\partial \rho}{\partial t} + \nabla \cdot (\rho V) = 0 \tag{2.6}$$

where V is the velocity and ρ is the density of the fluid . For incompressible flow where the density is constant,

$$\nabla . V = 0 \tag{2.7}$$

In Cartesian coordinate system, the continuity equation is given by

$$\frac{\partial u}{\partial x} + \frac{\partial v}{\partial y} + \frac{\partial w}{\partial z} = 0 \tag{2.8}$$

The Navier-Stokes (NS) equations describe the motion of fluid derived from principles momentum conservations equations. NS equations assume the fluid is continuous and not made up of discrete particles. The general equation is expressed as

$$\rho \frac{DV}{Dt} = -\Delta p + \mu \nabla^2 V + \rho S \tag{2.9}$$

The term on the left represents the total derivative consisting of the temporal and convective acceleration terms. The term on the right hand side represents the pressure gradients, the forces due to the viscosity of the fluid, and the body acting forces, *S* respectively. The expressions in terms of x, y and z component are

$$\rho\left(\frac{\partial u}{\partial t}+u\frac{\partial u}{\partial x}+v\frac{\partial u}{\partial y}+w\frac{\partial u}{\partial z}\right)=-\frac{\partial p}{\partial x}+\mu\nabla^2 u+S_x \tag{2.10}$$

$$\rho\left(\frac{\partial v}{\partial t}+u\frac{\partial v}{\partial x}+v\frac{\partial v}{\partial y}+w\frac{\partial v}{\partial z}\right)=-\frac{\partial p}{\partial y}+\mu\nabla^2 v+S_y \tag{2.11}$$

$$\rho\left(\frac{\partial w}{\partial t}+u\frac{\partial w}{\partial x}+v\frac{\partial w}{\partial y}+w\frac{\partial w}{\partial z}\right)=-\frac{\partial p}{\partial z}+\mu\nabla^2 w+S_z \tag{2.12}$$

2.2.3 **Hagen-Poiseuille flow**

The flow in a straight, infinite cylindrical pipe is known as Hagen-Poiseulle flow (Figure 2.2). It was established by solving NS equation across a circular tube and can be applied to describe the flow across a healthy artery.

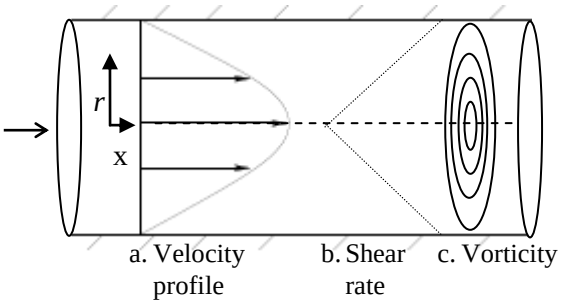

Figure 2.2 The interpretation of Hagen-Poiseuille Flow.

The velocity profile for the laminar regime is given as

$$V = V_{max}(1 - r^2/R^2) \tag{2.13}$$

where R is the pipe radius and V_{max} is the maximum velocity is at $r = 0$. The shear stress distribution, τ is expressed as

$$\tau = \mu \frac{du}{dr} \tag{2.14}$$

In Poiseuille flow, the shear field is non-uniform. The velocity distribution and variation of the rate of shear are functions of the radial distance *R* from tube axis, as illustrated in Figure 2.2 a. and b. The shear rate varies linearly with the radial distance from the tube axis and the velocity profile is parabolic.

Vorticity, Ω measures the rotation of small fluid elements. A fluid element has vorticity when it spins on its axis as it moves along its path. Mathematically, vorticity is the curl of the fluid velocity

$$\Omega = \nabla \text{x } V \tag{2.15}$$

In Hagen- Poiseuille flow, vorticity can be described as a series of rings of varying circulation (Figure 2.2 c). At any point along the pipe, the vorticity is azimuthally and distributed linearly over the cross section with a maximum at the wall and falling to zero as it approach the radial axis.

2.2.4 **Summary**

The governing equations for single-phase flow and the Hagen-Poisuille flow characteristic are discussed. The flow behaviour will be referred as basis to evaluate any deviation observed in stenosis flow in the following discussion.

2.3 Solid-liquid flow

2.3.1 **Introduction**

Multiphase flow can be divided into four categories; gas-liquid, gas-solid, solid-liquid and three-phase flows (Crowe et al., 1998). Solid-liquid flows consist of flows in which solid particles are carried by the liquid. As discussed in Chapter 1, biofluids like blood could also be rendered as a particulate suspension or termed as a solid-liquid system where the blood particles are regard as solid (Kleinstreuer, 2006).

2.3.2 **Particle motion of spherical particle in fluid.**

The equation of motion for a particle is fundamentally derived from Newton's laws where the resultant of all the forces, ΣF acting on a mass of particle, m is proportional to the

acceleration, a of the particle and each action has a reaction equal in magnitude, but opposite in direction.

$$\Sigma F = m\boldsymbol{a} \tag{2.16}$$

The equation of particle motion of a spherical particle in a fluid where the particle-particle interactions are neglected is given as (Crowe et al., 1998):

$$m_p \frac{dV_p}{dt} = m_p\left(1-\frac{\rho}{\rho_p}\right)g + F_{PG} + F_D + F_L + F_{vm} + F_{Bas} \tag{2.17}$$

where m_p is the mass of the particle, V_p is the instantaneous velocity of the particle and g is the body acceleration. The term on the left hand side describes the particle inertia, and the terms on the right-hand side are forces caused by particle-fluid interaction. F_D is the drag force, F_L is the lift force generated by rotation of particle and fluid shear, F_{PG} is the force that exists in the absence of the particle due to acceleration of the fluid and the hydrostatic pressure gradient, F_{vm} is defined as a virtual mass force accounts for the work required to change the momentum of the surrounding fluid as the particles accelerates and F_{Bas} is the unsteady drag force or Basset force which accounts for temporal development of the viscous region of the vicinity of the particles.

2.3.3 **Pressure gradient force**

The effect of local pressure gradient gives rise to a force in the direction of the pressure gradient. F_{PG} is the force due to pressure gradient in the fluid surrounding the particle and is described as:

$$F_{PG} = -Vo_p \Delta p \tag{2.18}$$

Where Vo_p is the particle volume and Δp is the pressure gradient produced by hydrostatic pressure.

2.3.4 **Drag force**

F_D is the drag force required in order to move a particle in a constant fluid velocity and pressure field.

$$F_D = \frac{1}{2}\rho C_D \frac{\pi d^2}{4} V_s \tag{2.19}$$

where C_{D} is the drag coefficient, d is the particle diameter and V_s is the relative velocity between fluid and particle. Stoke's Drag where the $Re_p << 1$ is given as (Stokes, 1845)

$$C_D=24/Re_p \tag{2.20}$$

The studies by Oseen (1910) extended the Stoke's Drag for condition valid at finite and small , Re_p <1 to

$$C_D=\frac{24}{Re_p}\left(1+\frac{3}{8}Re_p\right) \tag{2.21}$$

The C_D proposed by Schiller and Naumann (1935) is valid at intermediate Re_p where

$$C_D=\frac{24}{Re_p}\left(1+0.15Re_p^{\,0.687}\right) \quad 0.1<Re_p\le 1000 \tag{2.22}$$

$$C_D=0.44 \qquad Re_p>1000 \tag{2.23}$$

Morsi and Alexander (1972) proposed an expression for the drag coefficient for all ranges of Re_p up to Re_p >10000.

$$C_D=a+\frac{b}{Re_p}+\frac{c}{Re_p^{\,2}} \tag{2.24}$$

$$a,b,c\begin{cases}0,24,0 & 0<Re_p<0.1\\ 3.690,22.73,0.0903 & 0.1<Re_p<1\\ 1.222,29.1667,-3.8889 & 1<Re_p<10\\ 0.6167,46.50,-116.67 & 10<Re_p<100\\ 0.3644,98.33,-2778 & 100<Re_p<1000\\ 0.357,148.62,-47500 & 1000<Re_p<5000\\ 0.46,-490.546,578700 & 5000<Re_p<10000\\ 0.5191,-1662.5,5416700 & Re_p\ge 10000\end{cases} \tag{2.25}$$

However, realistic Re_p for blood cells suspended in plasma are known to be less than unity (Hyun et al., 2000; Longest and Kleinstreuer, 2003c; Hyun et al., 2004; Longest et al., 2004). Hence a low Re_p drag model is more appropriate for blood flow systems.

Yilmaz and Gundogdu (2009) compare of drag models available in the literature (Schiller and Naumann, 1935; Morsi and Alexander, 1972; Barnea and Mizrahi, 1975; Ishii and Zuber, 1979; Kumar and Hartland, 1985) at Re_p<1 and conclude that C_D exponentially decreases with Re_p. To date, data for drag correlation of blood cells was unavailable hence a general drag correlations discussed above were referred.

2.3.5 **Lift force**

Lift forces on a particle are due to particle rotation in which the rotation may be caused by a velocity gradient or fluid vorticity. There are two important lift forces which are known as Magnus lift force, F_{LM} and Saffman lift, F_{LS} force.

Saffman lift (Saffman, 1965) is developed due to pressure gradient acting on particle induced by a velocity differential at the top and bottom of the particles or shear gradient. The illustration of lift forces due to fluid velocity gradient is presented in Figure 2.3. The transverse force is given as

$$F_{LS} = 1.615\mu d_p \left(Re_g\right)^{1/2}\left(V_s\right) \tag{2.26}$$

The above expression is valid for $Re_p << Re_g^{1/2}$, $Re_p << 1$, $Re_g << 1$. McLaughlin (1991) extended Saffman lift forces to eliminate the $Re_p << Re_g^{1/2}$ restriction and, Mei and Adrian (1992) relaxed the above constraint with a correlation for a greater range of of Re_p ($0.1 \leq Re_p \leq 100$). Saffman-Mei lift model $F_{LSaffman\text{-}Mei}$ is written as

$$\begin{aligned} F_{LSaffman\text{-}Mei} &= F_{LS}\left[\left(1 - 0.3314\beta^{0.5}\right)exp\left(-\frac{Re_p}{10}\right) + 0.3314\beta^{0.5}\right] \quad Re_p \leq 40 \\ &= F_{LS}\left[0.0524\left(\beta Re_p\right)^{0.5}\right] \qquad\qquad\qquad\qquad\qquad\quad Re_p > 40 \end{aligned} \tag{2.27}$$

where

$$\beta = \frac{d_p}{2|V_s|}\left|\frac{du}{dr}\right| \qquad\qquad 0.005 < \beta < 0.4 \tag{2.28}$$

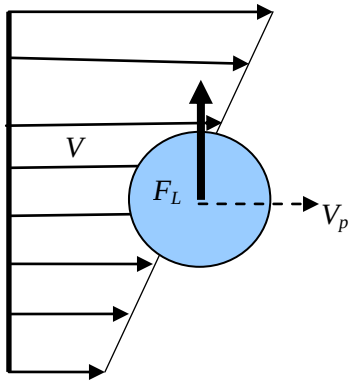

Figure 2.3 A particle in a shear flow.

Magnus lift is related to the particle rotation caused by a pressure differential between both sides of the particle as shown in Figure 2.4. The Magnus force for Re_p in the order of unity is derived by Rubinow and Keller (1961) and given as

$$F_{LM} = \frac{\pi}{8} d_p{}^3 \rho \left[\left(\frac{1}{2} \nabla \times V - \omega_p \right) \times V_s \right] \tag{2.29}$$

where ½ ∇xV is the local fluid rotation and ω_p is the particle rotation.

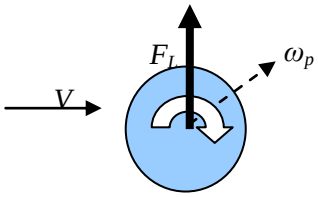

Figure 2.4 Magnus lift on particle rotating in a fluid

Lift models are often neglected in simulating blood particles (Buchanan et al., 2000; Hyun et al., 2000; Longest and Kleinstreuer, 2003c). The number of study in developing lift models at wider range of shear flow is very limited (Yilmaz and Gundogdu, 2008).

2.3.6 **Unsteady Forces**

F_{vm} and F_{Bas} are the forces developed due to the acceleration of the relative velocity. The F_{vm} arises, when a body is accelerated through a fluid and there is a corresponding acceleration of the fluid which is at the expense of work done by the body. This additional work relates to the virtual mass effect. F_{vm} is also known as added mass force. This force has a tendency to keep the particle from being accelerated in any direction. In other words, the force accounts for the form drag due to the acceleration.

$$F_{vm} = \frac{\rho V o_p}{2} \left(\frac{dV}{dt} - \frac{dV_p}{dt} \right) \tag{2.30}$$

where $\left(\frac{dV}{dt} - \frac{dV_p}{dt} \right)$ is the relative acceleration of the fluid with respect to particle acceleration.

The Basset force (F_{Bas}) is associated with the viscous effect which causes temporal delay in the boundary layer development as the relative velocity changes with time. This is also often referred to as the Basset history term as it relates to the past movements of the particle

$$F_{Bas} = \frac{3}{2} d_p{}^2 \sqrt{\pi \rho \mu} \int_0^t \frac{\left(dV/dt\right) - \left(dV_p/dt\right)}{\sqrt{t-t'}} dt' \qquad (2.31)$$

where *t-t'* is the time interval from the initiation of the acceleration.

In numerical multiphase simulation of the red blood cells in plasma, the unsteady forces was found negligible (Jung et al., 2006; Srivastava and Srivastava, 2009). In both studies the red blood cells were treated as a continuous phase and not as a cluster of individual cells. Numerical simulation performed by (Srivastava and Srivastava, 2009) used a simple flow geometry of healthy artery and the geometry employed by (Jung et al., 2006) was an idealised curved human coronary artery.

Works by Buchanan et al.(2000) and, Longest and Kleinstreuer (2003a, 2003b,2003c) that used Lagrangian approach neglected the Basset history term and virtual mass with the basis of very low blood particle relaxation time (10^{-6}s) and because the density of blood cell and blood plasma are nearly equal. The velocity of the particles is assumed similar to the velocity of blood plasma, hence the slip velocity is zero.

2.3.7 **Summary**

The governing equations for solid liquid flows have been presented where the forces involved in particle-fluid interactions that relevant to blood flow system have been discussed. The Re_p in blood flow is less than unity and general low drag coefficient is accepted. The lift forces F_{LM} and F_{LS} depend on velocity gradient and vorticity of blood plasma as well as the cell rotation. The transient forces F_{vm} and F_{Bas} have been taken not to have significant effect in blood flow.

2.4 Particle-particle interactions of dilute and dense system

Due to mass transfer or momentum exchange there are always interactions between particles. Particle suspensions are considered dilute when there are no particle-particle collisions which implies particles are far apart and fluid flow forces are unaffected. However, the pressure gradient around the particles induces a stress field which may influence the local flow field. In dilute flows particle motion is controlled by hydrodynamic forces such as drag and lift. On the other hand, dense flow describes the situation where the particle motion is controlled by particle-particle collisions.

For any given system, the particle concentration and particle size greatly determine the probability of inter-particle collisions. If the $\rho_p / \rho > 10^{-3}$ the flow is dilute where average particle distance is very much larger than the particle diameter (Kleinstreuer, 2006).

The question whether the system is dilute or not can be classified by comparing the ratio of momentum response time of particle, τ_{vel} to the time between collisions, τ_{col}. Momentum response time relates to the time required for a particle to respond to velocity changes.

$$\tau_{vel} = \frac{\rho_p d_p^2}{18\mu} \tag{2.32}$$

$$\tau_{col} = \frac{1}{f_{col}} \tag{2.33}$$

where f_{col} is the collision frequency. The flow can be considered dilute if $\tau_{vel} / \tau_{col} < 1$, because the particle has sufficient time to respond to local fluid dynamic forces before next collision. In turn the flow is dense, if $\tau_{vel} / \tau_{col} > 1$, the particle does not have sufficient time to completely respond to the fluid dynamic forces before the next collision. In this work, the solid suspension concentration was less than 1% and the $\rho_p / \rho \sim 0.95$ where it can be classified as a dilute suspension. In continuum fluid mechanics the pressure drive the fluid flows. For dilute particle concentration the kinetic pressure due to particle velocity fluctuations or collisions is neglected.

2.5 Summary

This chapter provide the description of cellular flow in blood from fluid mechanics point of view. The relevant of dimensionless parameters and the governing equations for single phase (liquid) and two-phase (solid-liquid) flows have been presented. For two-phase considerations, the forces involved in particle-fluid have been discussed. The particle-particle interactions have been pointed out but for the case dilute suspension, the interactions normally neglected.

Chapter 3

EXPERIMENTAL EQUIPMENT AND TECHNIQUES

This chapter discusses the design of the model stenosis and the measurement technique. Particle image velocimetry (PIV) has been employed to carry out the velocity measurements. Hence the materials and methods to develop the flow system were designed to suit the PIV environment.

3.1 Introduction

Flow field visualization and characterization is important to obtain essential information of a particular flow system. The velocity of the flow system is the main parameter to analyse the flow behavior such as the wall shear stress, turbulence and vorticity. Several in-vitro techniques for velocity measurement in arterial systems have been employed including Laser Doppler Anemometry (Gijsen et al., 1997; Lei et al., 2001; Liepsch, 2002), Ultrasound (Meagher et al., 2007; Hoskins, 2008), MRI (Taylor et al., 2002; Morbiducci et al., 2009) and Particle Image Velocimetry (Lima et al., 2006; Raz et al., 2007). PIV is the technique that not only quantifies the velocities but also allows visualization.

PIV is a measurement method for obtaining instantaneous whole field velocity vectors. By using this technique, high spatial resolution images can be recorded and the velocity information can be extracted out of these images. In general, the spatial resolution is large and velocity could be measured at a suitable temporal resolution. The temporal resolution for PIV is limited compared to other velocimetry technique. A compromise between spatial resolution and velocity dynamic range are sought through technical setting to ensure the smallest velocity structures are measured.

The principle used by PIV is to measure velocity as the distance over time of a large number of particles in the flow field. The fluid is seeded with particle tracers and the motion of the tracer is captured on camera at short time intervals. The seeded particles must be able to follow the flow without disturbing the flow structure. The general description of the PIV set-up is illustrated in Figure 3.1. The experimental set-up of PIV comprised of four sub-systems; a test section with flow seeded with tracers, flow illumination system, image acquisition and a computer interface. The test section must be optically transparent to allow a

laser sheet to pass through the models and illuminate the particle seeding. The light scattered by the particles was recorded on a sequence of frames. The displacement of the particles between light pulses was determined through the evaluation of the images recorded. Each image was subdivided into small interrogation areas. It was crucial to ensure the size of interrogation area was set as small as possible so that the smallest velocity structure was captured. Velocity range for artery with mild stenosis was in the range of 0.001m/s to 1.000 m/s (Blake et al, 2009). Appropriate particles seeding concentration was essential to yield accurate estimates of the velocity vectors. The movement of the particles in interrogation area between the time intervals should be short enough to avoid particles with out-of-plane velocity. A detailed description of PIV is given by Raffel et al.(1998), Adrian et al.(1991) and Santiago et al.(1998).

As indicated in Table 1.1, the *Re* in large arteries ranged from 150 -1600 and for severely stenotic artery the maximum *Re* could be up to 1000. This work focused on characterizing a steady flow in a mild stenosed artery model with *Re* ranging from 180 to 320, With relatively slow flow in a simple geometry, an appropriate size of interrogation area and a suitable time interval could be set using the PIV method. Details of technical settings to ensure appropriate temporal and spatial resolution are discussed in the following chapter.

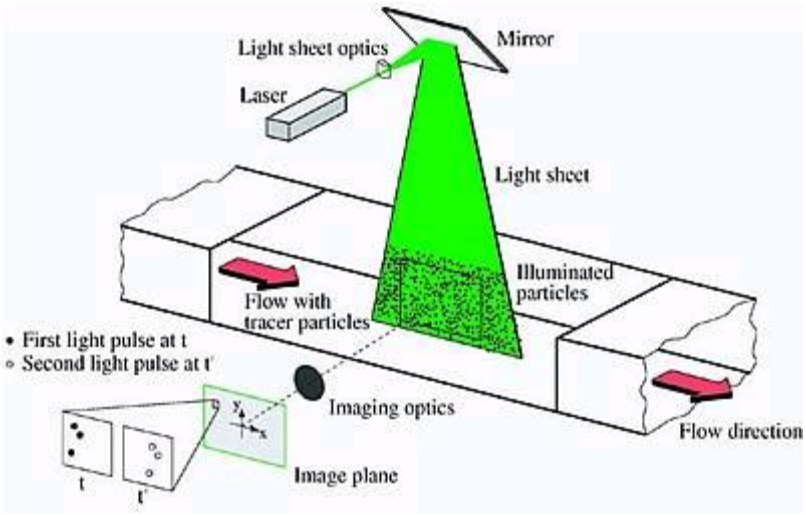

Figure 3.1 A typical PIV set-up (Reprinted from http://www.dlr.de).

3.2 Stenosis artery model

The geometry of an idealised stenosed artery was constructed according to an axisymmetric model used by Ahmed and Giddens (1983). The constriction follows a cosine curve define by the following equation

$$r(x) = \frac{D}{2}\left\{1 - \frac{1}{2}\kappa\left[1 - \cos\left(\frac{x\pi}{D}\right)\right]\right\} \tag{3.1}$$

r(x) is the radius as a function of axial distance *x* and D is the inlet diameter. κ is the degree of stenosis which given as (Ku, 1997)

$$\kappa = 1 - \frac{D_0}{D} \tag{3. 2}$$

where D_0 is the minimum lumen diameter. In this work, the D was 8mm and D_0 was 5.6mm, hence κ was 0.3 for 30% diameter occlusion. Figure 3.2 shows the constriction shape with central coordinate at the radial axis and middle of stenosis throat.

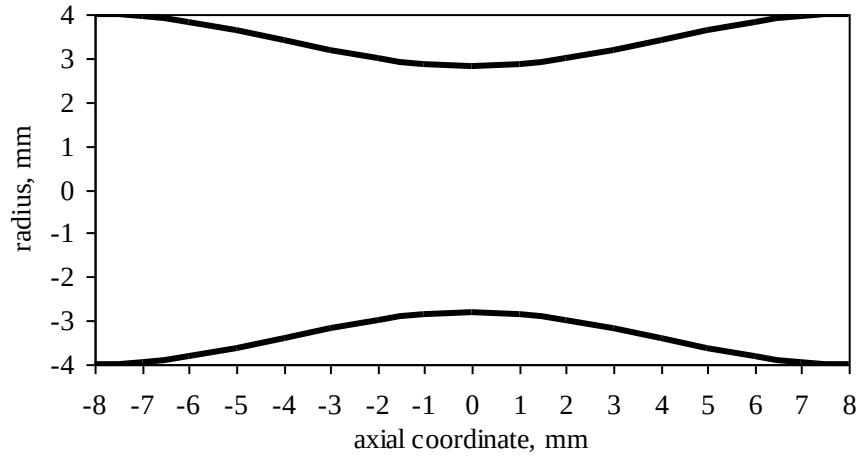

Figure 3.2 The constriction shape with 30% diameter occlusion.

In order to construct the model, an 8mm diameter brass rod was machined on a computer controlled lathe to according to the above shape. The rod was manufactured by Pentland Precision Engineering Ltd (Edinburgh, UK). The rod was constructed in two sections with the throat of the stenosis forming the join between the halves. A steel pin in the stenosis throat reinforced the junction between each half as illustrated in Figure 3.3.

Figure 3.3 Two sections of rods that formed the stenosis throat.

A ‘lost core’ technique was used to manufacture the stenosis model where the rod was placed in a rectangular casing. The casing walls were made from Perspex with connectors fitted to holes cut in either end, through which the stenosis rods extended both into and out of the casing. An optically clear silicon rubber liquid (Sylgard 184, Dow Corning, Barry, UK) was prepared and poured into the case. When the silicon had cured and hardened, the Perspex walls were removed and the rod was withdrawn as shown in Figure 3.4. Finally the completed flow phantom was a continuous lumen inside the transparent model (Figure 3.5). The refractive index of the silicone was reported as 1.4100 (Blake, 2008).

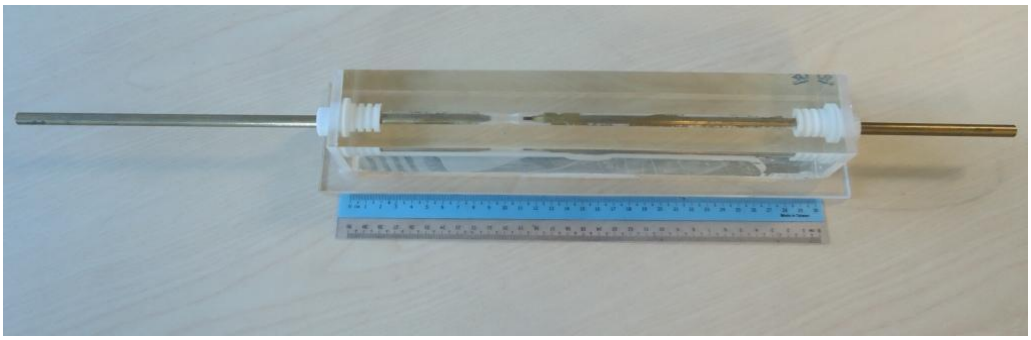

Figure 3.4 The rods were withdrawn to create stenosed lumen.

Figure 3.5 The completed model.

3.3 Blood analogue fluid

In order to ensure the fluid is optically transparent, a blood mimicking fluid was prepared. The fluid consists of particle suspension in liquid where the particles acted as the tracer for flow field measurement. Three main criteria must be adhered which were to ensure the particles were neutrally buoyant in the fluid, the tracer particles must be able to scatter light efficiently and the refractive index of the fluid matched the stenosed artery model. The recipe was adapted and slightly modified from Blake et al. (2009). The main reason for modification was the difference of particle density. The fluid composition for both studies

were identical and the refractive index of the liquid used in this study,1.41, matched the silicone model. The fluid was a mixture of glycerol-water-NaCl solution. The composition is summarised in Table 3.1.

The particles chosen in this work were spherical rigid particles made from polyamide material (Orgasol, Elf-atochem, France). The density of the particle quoted was 1030kg/m^3. The settling velocity under gravity is evaluated according to Stokes' law

$$u_\infty = \frac{g\, d_p{}^2 \left(\rho - \rho_p\right)}{18\mu} \tag{3. 3}$$

where u_∞ is the settling velocity, d_p and ρ_p are the particle diameter and density respectively, and μ and ρ are the fluid viscosity and density respectively. The density of the blood mimic fluid was 1080kg/m^3 and therefore the calculated settling velocity was in the range of 4-20x10^{-7} m/s which was negligible compared to the fluid velocity in the recirculation zone. Hence it was considered that the particles were neutrally buoyant.

Two different particles sizes were used in these experiments; 20±2μm and 10±2μm diameter. The chosen particle sizes were in the range of blood-borne elements (Caro, 1978). The weight of particles was measured and then mixed with glycerol-water-NaCl solution. Particle concentrations, ϕ_m investigated in this study were 0.04%, 0.07% and 0.14% by weight. The particle suspension was stirred for 30 minutes and filtered to remove remaining clumps. The distribution of particles in the solution was observed under a microscope (Zeiss, Germany) to ensure particles were not aggregated. The temperature was kept constant at 20˚C controlled by an air conditioning system. The temperature in the room was monitored using a mercury thermometer.

The viscosity of the solution is determined by using a rheometer (Haake Mars, Germany). It was a rotational rheometer where the samples were rested on between two metal discs. The top disc was rotated at a controlled speed. The shear stress was determined from the torque applied and the geometry of the disc. The shear rate is proportional to the rotational movement. The viscosity was determined by dividing the shear stress with the shear rate. The viscosity for all particle concentrations, ϕ_m which were 0.04%, 0.07% and 0.14% by weight are plotted in Figure 3.6. The viscosity at the beginning of the measurement was higher where the metal discs started to rotate. The viscosity approaches an asymptotic value at a shear rate greater than 70s^{-1}. The average asymptotic viscosity of all liquid solutions was 6.23±0.01 mPas. The density of the fluid was measured by dividing the weight with corresponding volume which yielded 1.080±0.05 g/ml. The fluid and particle properties used in this study are summarized in Table 3.1 and Table 3.2.

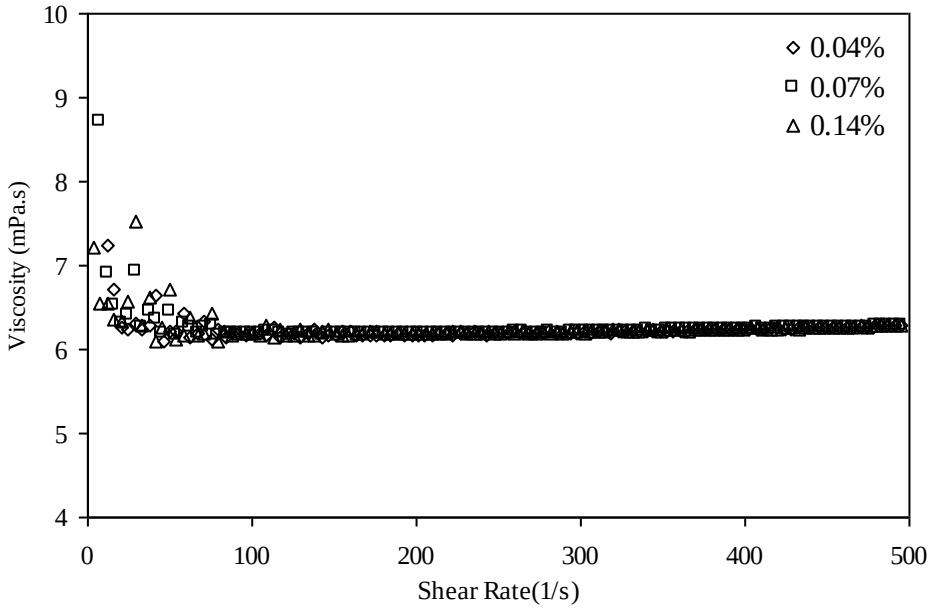

Figure 3.6 Viscosity measured by rheometer at shear rate from zero to 500s^{-1} for particle concentration at 0.04%, 0.07% and 0.14% by weight.

It is important to note that the concentrations prepared in this study were dilute compared to the red blood cells composition. An attempt was made to increase the concentration of particles.Unfortunately the solution lost its transparency and too much light was scattered. The velocity information was irretrievable because the resulted images were all glared.

Table 3.1 Fluid properties.

Fluid properties	
Composition (w/w%)	Glycerol = 37.1
	Water = 47.9
	NaCl = 15.0
Viscosity, μ	6.23 ± 0.01 mPas
Density, ρ	1080 kg/m^3

Table 3.2 Particle properties

Particles properties	
Material	Polyamide (Orgasol)
Shape	Rigid, roughly sphere
Diameter, d_p	20±2 μm, 10±2 μm
Density, ρ_p	1030 kg/m^3
Concentration, ϕ_m	0.14%,0.07%,0.04%

3.4 The flow system

The flow of the fluid was steady and driven by a peristaltic pump (Masterflex L/S, Cole-Parmer Instrument, Illinois, USA) through a pulse dampener (Cole-Parmer, Illinois,USA) before entering the stenosis artery model. Fluctuations in flow were eliminated in a pulse dampener resulting a steady and smooth flow. An extension of pipe was attached to the inlet of the stenosis model when necessary to allow a sufficient entrance length for fully developed flow to establish. A Perspex pipe with the same internal diameter as the inlet stenosis model fitted snugly into the connector. The fluid exiting the stenosis model was collected in a reservoir where it entered the flow cycle again. The continuous flow loop is shown in Figure 3.7.

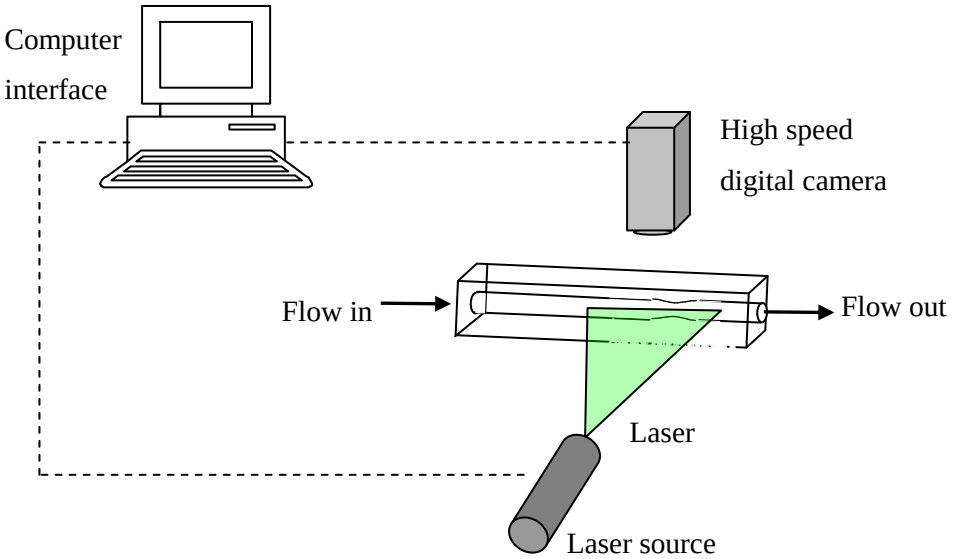

a. PIV set-up

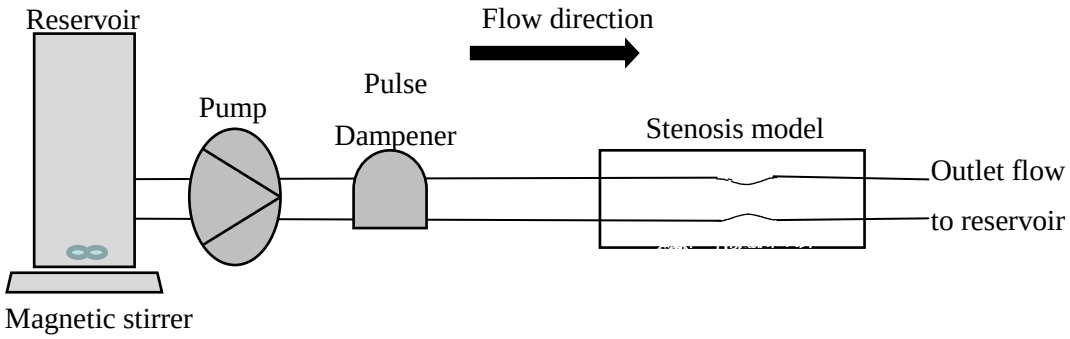

b. Flow loop

Figure 3.7 The flow system.

The flow rate was set by controlling the pump speed. Volumetric flow rates were measured by collecting the volume of the fluid within a specified time. The range of volumetric flowrates studied was 5.5ml/s to 12.0ml/s.

3.5 Illumination system

The flow field under investigation was illuminated and the light scattered by the particles was recorded. The illumination system consisted of laser source and some optics to produce a thin laser light sheet. A laser was normally used for PIV because of its capability to produce intense, bright, short pulses of light. A laser consists of three main components, laser material, pump source and mirror arrangement. The laser material could be a gas, semiconductor or solid material. The pump source will excite the laser material by electromagnetic or chemical energy and finally the mirror arrangement allows an amplifying oscillation within the laser material.

The laser light was generated using neodymium-doped yttrium aluminium garnet (Nd:YAG) solid. The beam is generated by Nd^{3+} with YAG crystal acted as host material and pumped with white lights. The laser used had two Nd:YAG cavities (New Wave Solo 200XT, Dantec Dynamics, Bristol, UK) with a green wavelength, λ of 532nm .The repetition rate of the two pulses is within a range of 8 to 21Hz with energy of 0.120J each. Due to the twin cavities, the pulse separation is infinitely variable.

The laser beam light is converted into a light sheet by passing through a two lens configuration. Two cylindrical lenses were used where the light was first passed through a diverging lens (80x62 module, Dantec Dynamics, Bristol, UK). This lens spread the light beam into one plane. The second lens was a converging cylindrical lens (80x63 module, Dantec Dynamics, Bristol, UK) which reduces the thickness of the resulting sheet by focusing the laser beam in the vertical plane. The illustration from top view and side view are drawn in Figure 3.8.

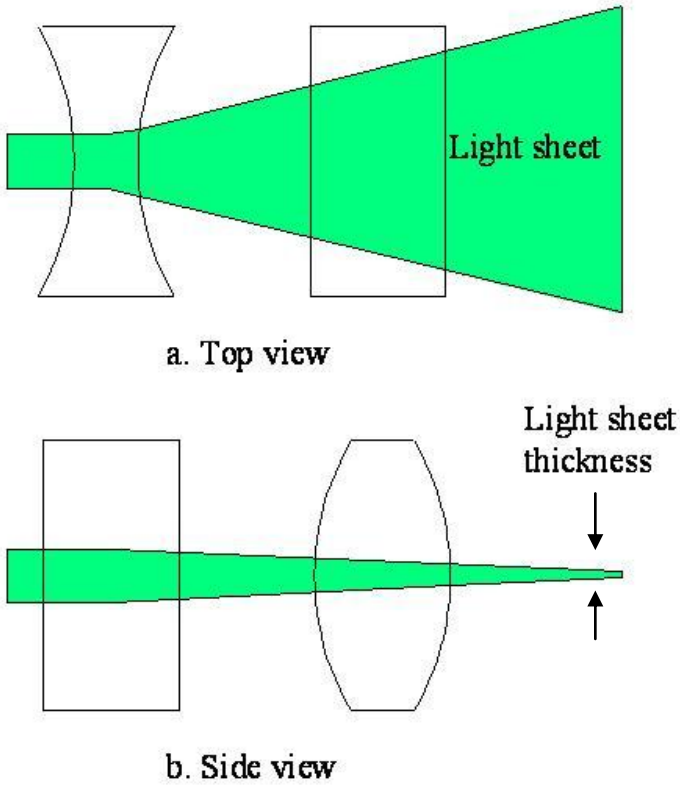

Figure 3.8 Lenses arrangement to form the light sheet.

The alignment of the laser system used can be controlled by a flexible light guide called an optical head. The light sheet thickness could be adjusted by moving the lens focus adjuster. In this experiment a 0.5mm light sheet thickness was the minimum and set throughout the measurement. The maximum width was approximately 400mm.

3.6 Image acquisition

In the PIV system, digital image recording was employed to acquire images of light scattered by particles. The images of the illuminated flow field between laser pulses were collected as pair of images in the acquisition system. The distance configuration for a camera lens is governed by equation

$$\frac{1}{f} = \frac{1}{z_0} + \frac{1}{Z_0} \tag{3. 4}$$

Where f is the focal length of the lens, z_0 is the distance between the image plane and the lens, Z_0 is the distance between the lens and the particles scatterer. The correlation is illustrated in Figure 3.9.

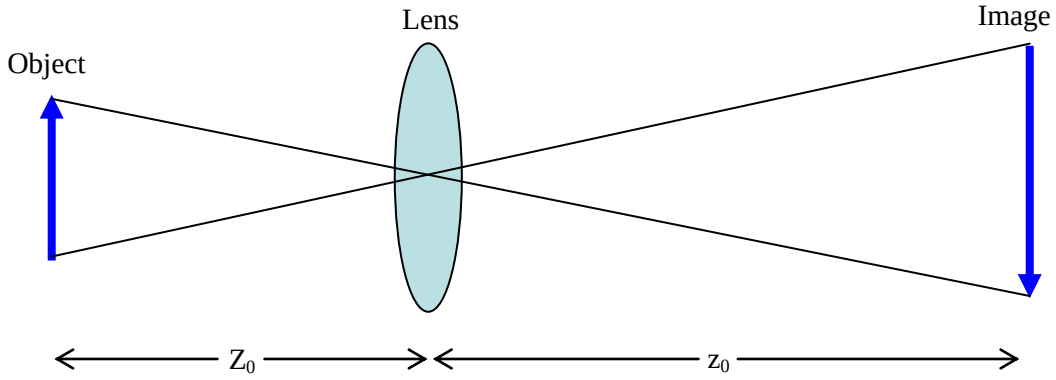

Figure 3.9 Image construction.

The magnification factor M is defined as

$$M = \frac{z_0}{Z_0} \tag{3. 5}$$

The diameter of the Airy disk, d_{diff} represents the smallest particle image that can be obtained for a given imaging configuration and given as

$$d_{diff} = 2.44 f\#(M+1)\lambda \tag{3. 6}$$

where λ is the laser wavelength . $f\#$ is defined as

$$f\# = \frac{f}{D} \tag{3. 7}$$

where D is the diameter of the aperture. The d_{diff} were found smaller than the size of all particles employed in the experiment by 5-12µm.

The depth of field, δz is the region on the object plane where the image were in-focus and must be smaller than light sheet thickness. δz is given as

$$\delta_z = \frac{2 f\# d_{diff}(M+1)}{M^2} \tag{3. 8}$$

The calculated δz for all magnifications (16µm and 30µm) and particle diameters used (10µm and 20µm) were less than laser sheet thickness (500µm).

In this experiment the pair of images was acquired using a high speed digital camera (Kodak Megaplus ES1.0, Dantec Dynamics) and recorded on an electronic charge-coupled device (CCD) sensor. The CCD sensor converts lights into picture elements (pixel). The size of the sensor is 9.1mm horizontal x9.2mm vertical. A Nikor 50mm lens (f = 50mm) was used to focus the image on the CCD sensor. The position of the lens could be adjusted by having a photographic bellow (Cameratics, Edinburgh, UK) so that the z_0 could be extended hence the magnification, M could be increased. The depth of field, δz could be determined prior setting up the measurement. The movement of the camera in the axial direction of the flow and vertically could be adjusted by fitted the camera on a traverse (LG Motion Limited, Basingtoke,UK). The Z_o could be varied by controlling the vertical height and the measurement location along the model were changed by moving the camera horizontally.

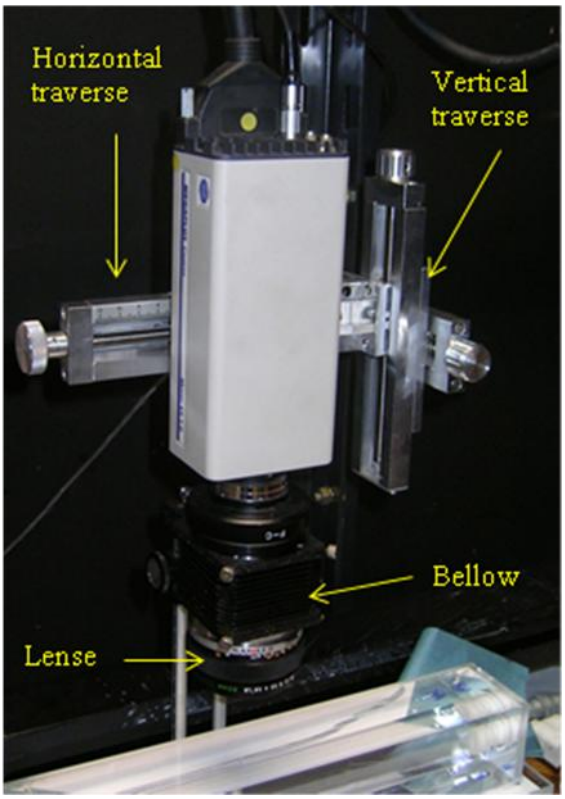

Figure 3.10 High speed camera (15 Hz).

Two image examples acquired in these experiments are shown in Figure 3.11. The first image recorded the whole diameter of the model and the second image was zoomed to focus on the recirculation zone. The image of whole diameter with M=1.1 is used in Chapter 4 and

the latter (M=2.5) is used in Chapter 5. The settings for both magnifications are summarized in Table 3.3.

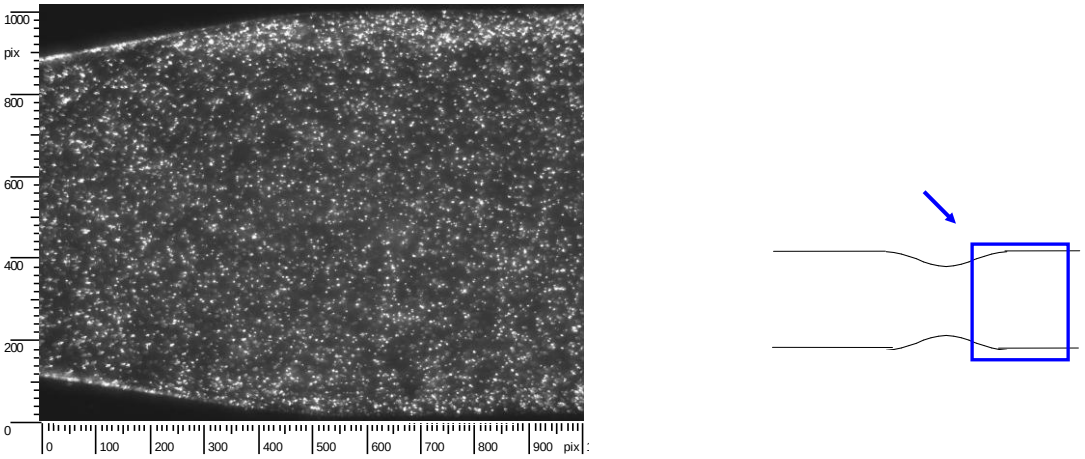

a. M = 1.1. Set-up for measurement in Chapter 4.

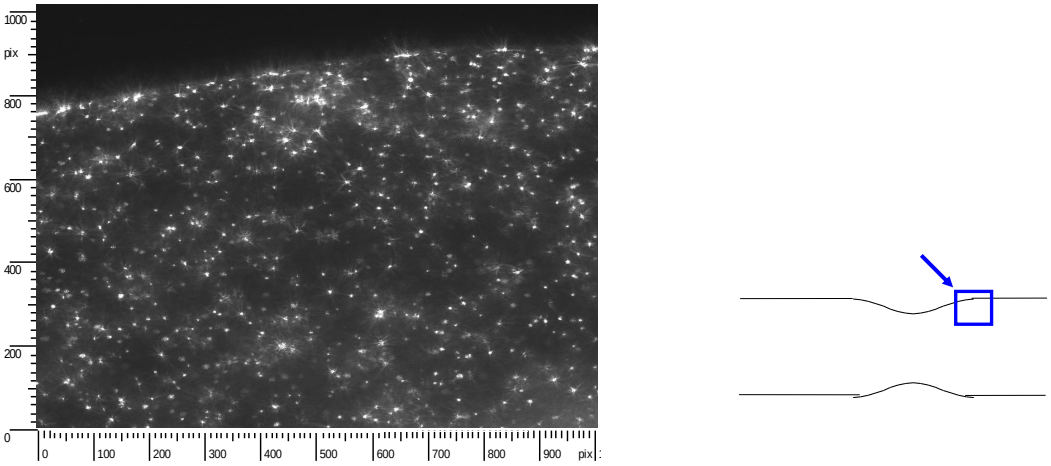

b. M = 2.5. Set-up for measurement in Chapter 5

Figure 3.11 Image magnifications.

Table 3.3 Camera setting to focus the object on CCD imager.

Optic settings parameter	Image a.	Image b.
M	1.1	2.5
f ,mm	50	50
$Z0$,mm	100	74
$z0$,mm	110	185
$f\#$	1.8	1.8
d_{diff},mm	4.89×10^{-6}	8.15×10^{-6}
δz,mm	3.05×10^{-5}	1.64×10^{-5}

3.7 Velocity field characterization

The computer was the FlowMap system (Dantec Dynamics Ltd., UK) which synchronised the laser illumination, camera recording and user interface. FlowManager software installed in the computer provided mechanism for system integration and communication between FlowMap system and the operator.

Input buffer in the FlowMap processor read image map from CCD camera, stored the image map and sent the images to the correlation software. For each velocity measurement, at least 200 image pairs were recorded. Each image was subdivided into small interrogation areas. There were at least five particles within each interrogation area in order to ensure high signal-to-noise ratio (Willert and Gharib, 1991).

The time delay between each image pair at various flow rates was inspected and optimized. The main criteria was that the in-plane displacement should be less than one-quarter of the interrogation area (Westerweel, 1997). For each pair of images recorded in the two frames, the time between pulses, Δt was specified through FlowManager software.

The pair of illuminated particles images represented the shift position information. Hence, the two components of instantaneous velocity vector in the plane of the laser light sheet could be measured as briefly illustrated in Figure 3.12.

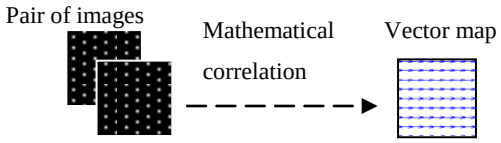

Figure 3.12 Velocity vector correlation.

The pair of images was correlated using a correlation function to find the mean distance the particles moved within the time duration based on a basic relationship of particle velocity, V_p and particle displacements, d

$$V_p = \frac{d}{M\ \Delta t} \tag{3.9}$$

where M is the magnification and Δt is the time between images captured. Each interrogation area yielded one velocity vector. PIV was based on determining the displacement of a group of particles using the Fast Fourier Transform (FFT) correlation technique. The correlation function was determined on an interrogation area of 32 x 32 pixels or 64 x 64 pixels depending on the particles concentration. This is to ensure that at least five particles were present in one interrogation area, hence the size of interrogation the area was smaller for fluids with more particles.The particles in the interrogation area were identified and the algorithm was used to match the initial and final position. Near the interrogation area edges there was a possibility of either the initial or final particle position being outside the area. To avoid loss of pairs, each interrogation area was overlapped with its neighbour by 50%. This yielded a sufficient number of vectors to demonstrate the flow pattern within the region of interest. The FFT function estimated the relative displacement of particles in the interrogation area.

3.7.1 **Flow measurement set-up**

Measured velocity in mild stenosis artery ranged from 0.001 to 1.000 m/s (Blake et al., 2009). In order to set up appropriate Δt, assessment on the size of interrogation area and particle velocity was made. The size of image was 1008x1016 pixels and the interrogation area was 32x32 pixels. For measurement described in Figure 3.11a (experiment set-up for Chapter 4), each of the side of interrogation area correspond to a length, L of 0.262mm. Maximum Δt estimated from equation 3.9 was 238.18μs, where the maximum velocity was taken as 1.000m/s and displacement of 0.262mm. For cross correlation method, maximum displacement recommended was less than one-quarter of interrogation area. This yield an optimum Δt of 59.54μs. For a velocity of 0.001m/s, Δt required was 59.54ms. Therefore the

range of Δt for the flow was approximately from 60μs to 60ms. Optical arrangement described in Figure 3.11b (for experiment in Chapter 5) addressed the improvement for small velocity measurement. The interrogation area of 32x32 pixels was equal to 0.115mm x 0.115mm length. To capture the velocity scale down to 0.001m/s, a Δt in the range of 10ms is required.

Homogeneous flow within interrogation area is desired in the measurement. Generally, cross correlation method tolerates large velocity gradients. The estimation of the actual velocity gradients, Δv within each cell can be made based on particle diameter d_p which given as $(M\Delta v\Delta t)/L < d_p$ (Keane and Adrian,1992). The Δv yielded for both set-ups based on the smallest Δt were $1165s^{-1}$ and $6.95s^{-1}$ respectively. In order to preserve a well-defined correlation peak, the Δv should not exceed 3-5% (Keane and Adrian,1992). For experiment with M=1.1, the acceptable velocity gradient was after the throat region where the anticipated values were less than $1200s^{-1}$. In experimental set-up for Chapter 5, the estimated maximum velocity gradient is $10s^{-1}$ which is more than 5% tolerance. Therefore the set-up in Chapter 4 gave more reliable velocity measurements in the post stenosis region where the velocity gradient in a cell can be neglected.

The seeding particles within the interrogation area were ensured to be more than 5 particles per interrogation area. Particles tend to distribute in heterogeneous manner after the stenosis. This present a challenge on deciding the number of particles seeded. Seeding at more than 0.07% weight concentration was found able to give sufficient number of particles. However, at Re_i less than 130, the particles was found escaped certain region. Thus, the velocity information in this region was not able to be measured.

3.7.2 **Correlation technique**

The average motion of small groups of particles can be correlated using auto-correlation or cross-correlation method. The first technique has disadvantages that it cannot resolve particle displacements smaller than particle image diameter and the direction of the displacement could be misleading when reversed flow exists. As the flow system in this study investigated disturbed flow condition the latter technique was selected. Details on the correlation methods are discussed in Adrian (1991) and Prasad (2000).

Figure 3.13 outlines the displacement function. The function was expressed as a linear signal processing model. The function *f (m, n)* represents the light intensity within the interrogation area recorded at time t, whereas the function *g (m, n)* represents the light intensity recorded at time $t+\Delta t$. The output of an image transfer function *s (m, n)*, takes *f (m, n)* as input, with

the noise function *d (m, n)* added. *F(u,v), G (u,v)* and *S(u,v)* functions are the Fourier transforms of the corresponding light intensity functions where *(u, v)* are coordinates in the spatial frequency domain. *s (m, n)* is directly related to the flow and the time between the two recordings, while the noise function *d (m, n)* is a result of seeding particles moving into or out of the interrogation area in the period between the two recordings. The estimation of the spatial shifting function *s (m, n)* is on the basis of known values of *f (m, n)* and *g (m, n)*. Spatial cross-correlation function predicted the *s (m, n).*

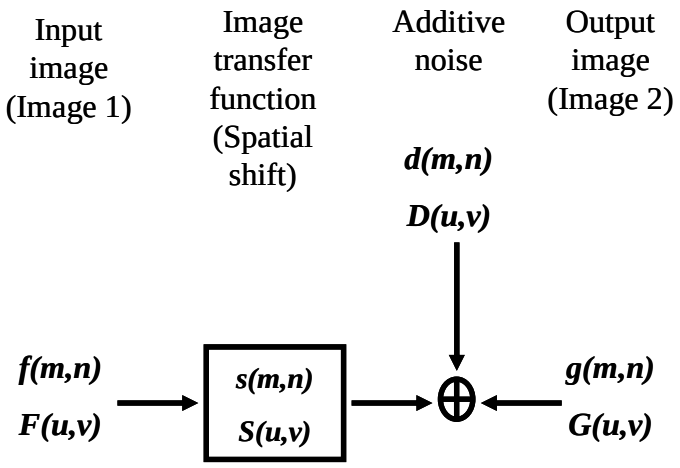

Figure 3.13 Image displacement function.

A high cross-correlation value was observed, where many particles match up with their corresponding spatially shifted partners. The highest correlation peak can be considered to represent the best match between the functions *f (m, n)* and *g (m, n)* when the number of matching particle pairs is large. Small cross-correlation peaks were observed when individual particles matched up with other particles. The location of the correlation peak in the correlation plane corresponds directly proportional to the average particle displacement within the interrogation area investigated. The correlation function was computed sequentially over all interrogation areas. With known displacements, the velocity vectors of the flow field were generated. The cross-correlation method is described in Figure 3.14.

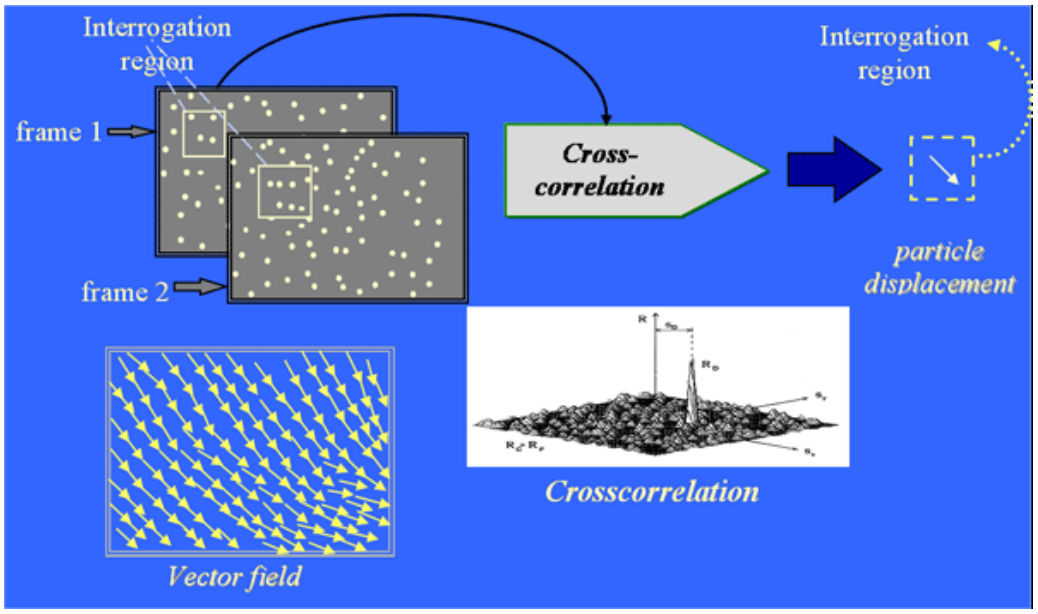

Figure 3.14 Correlation steps to determine the vector field (Reprinted from www.tsi.com).

3.7.3 **Vector field validation**

Measurement errors had been minimized by careful selection of experimental conditions, however PIV is an instantaneous measurement base on correlation of particles. Particle images may not belong to the same pair. Other sources of error were the recording noise, computing error and error due to approximating local Eulerian velocity from Lagrangian motion of seeding particles. The flow field may contain false or spurious vectors and it was necessary to validate vectors from the raw image map in order to remove the outlier contribution from the noise of instantaneous spatial information (Westerweel, 1997).

In this experiment, the flow rates studied were relatively slow such that the flow was streamlined with negligible velocity fluctuation. Since most of the outliers lay in the core flow region where the flow direction is unlikely to change, a moving-average validation was employed. This technique iteratively validated vectors based on a comparison between neighbouring vectors. The method was described in detail by Host-Madsen and McCluskey (1994). A typical unvalidated and validated flow field at the inlet is given in Figure 3.15.

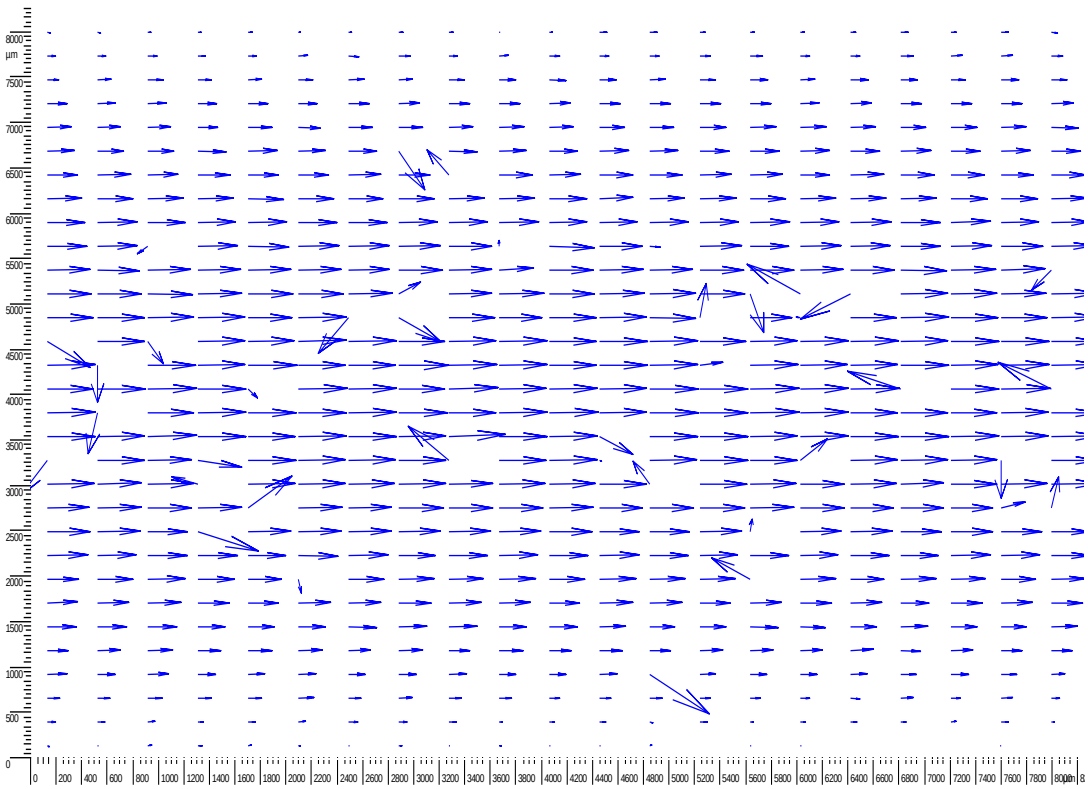

a. Raw vector field

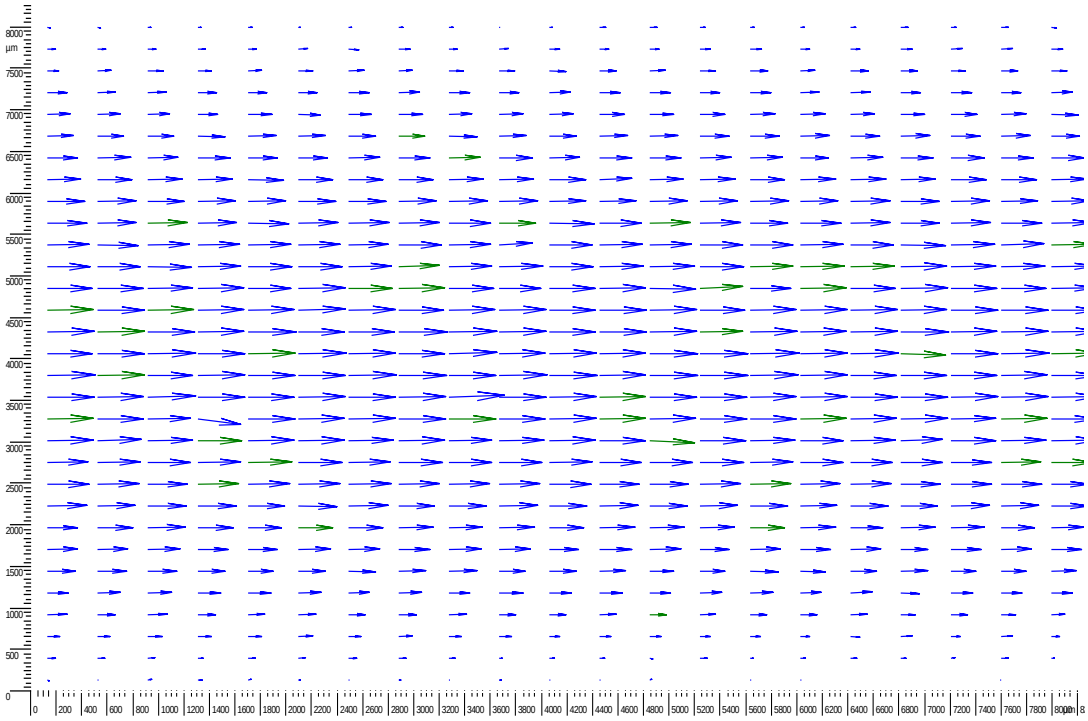

b.Validated vector field. Green vectors are the substituted vector resulted from moving average validation method

Figure 3.15 Vector field validation.

3.7.4 **Near wall and curved surface boundary**

It was problematic to define the boundary for the near-wall velocity field. The geometry curved at the wall, but the interrogation area was square in shape, as shown in Figure 3.16. Therefore, the velocity data from the interrogation area at the boundary was not considered. In MATLAB, this data were assigned with Not a Number (NaN) values. When velocity gradient is determined in this region, the values at the boundary may introduce error.

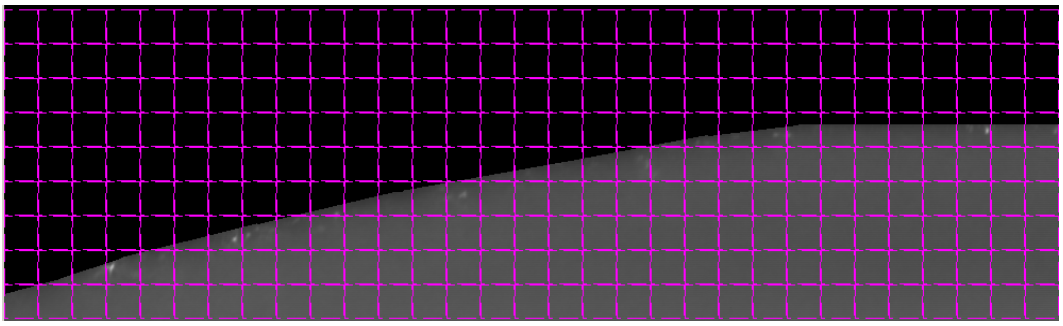

Figure 3.16 The interrogation boxes drawn on the PIV image of the recirculation zone.

3.8 Particle concentration distribution measurement

The distribution of particles during the flow was analysed from the images acquired by the high speed camera. For each experiment 750 images were acquired and mean light intensity was determined. The total recording time was 15minutes. All recordings began after steady state was obtained. Steady flow was validated by analyzing the inlet velocity profile to ensure it was parabolic and constant.

10μm and 20μm particles at concentration 0.07% and 0.14% were used in this study. The power used to illuminate an equivalent fluid suspension with 10μm particles was smaller than the power required to illuminate fluid with 20μm particles, since the number of particles is inversely proportional to the cube of the diameter, whilst the scattering is proportional to the square of the diameter. Furthermore, when the seeding particle density was increased, a lower laser power had to be used to reduce the glaring effect due the presence of more particles. Due to this variation, it was found necessary to optimize the light intensity so that the chosen power level suited each measurement. In these experiments the same laser power was then maintained for each set of measurements with the same particle size and concentration.

The light intensity in the region of interest, I' was normalized by dividing the local mean pixel values, $\hat{I}$ with the mean light intensity at the inlet , $\hat{I}_0$ i.e.

$$I' = \frac{\hat{I}}{\hat{I}_0} \tag{3.10}$$

Images from PIV system were exported into MATLAB r2009a (The Mathworks, MA, USA) to analyse the pixels value using Image Processing Toolbox.

3.9 Summary

A method of construction of a stenosed artery model and the preparation of a blood analogue fluid that suits PIV measurement has been presented. The technique to measure the velocity field and particle concentration distribution using PIV has been described.

Chapter 4

FLOW FIELD CHARACTERISATION IN THE STENOSIS MODEL

This chapter presents the experimental measurements of the flow field in the stenosed artery model. The velocity is determined by the PIV method and the velocity gradient is calculated. Flow dimensionless parameters were assessed to understand the flow behaviour.

4.1 Introduction

There is a correlation between low wall shear stress (WSS) and sites where atherosclerosis develops. This can happen when a vessel is curved or bifurcated, or when there is a sudden change in geometry. Stenoses in the arterial network are varied and complex, thus a simplified axisymmetrical constriction in a cylindrical tube is often used to investigate flow behaviour. Both theoretical and computational methods have been employed in order to gain a greater understanding of stenotic flow.

Stenotic flow has been extensively studied over a wide range of flow conditions. The Reynolds number, *Re* has ranged between 1800~2300 (Giddens et al., 1993) and 15000 (Deshpande and Giddens, 1980). Ahmed and Giddens (1983) have performed studies in the range of 500 to 2000. Physiological flows for medium-size arteries have *Re* values well below this range: normally between 100 and 2000 (Caro, 1978). The mean flow *Re* in the carotid artery was around 300 (Long et al., 2001).

The importance of quantifying blood flow velocity in the diagnosis, treatment and management of atherosclerosis was discussed in Section 1.4. In this chapter, we will discuss the flow behaviour of the blood mimic through a mildly stenosed artery by first obtaining the flow velocity. Dimensionless flow parameters were assessed from the velocity information, in order to describe the behaviour. The characterisation used the PIV technique described in Chapter 3. It is important to note that the PIV flow measurement principle was based on single-phase and homogeneous assumptions.

4.2 Method

4.2.1 **Flow measurement**

The PIV system was used to measure two dimensional (2D) velocity field data. Further details of the measurement method were provided in Section 3.1. To obtain the flow velocity field, the fluid was seeded with particles whose diameter was 20μm at weight concentration, ϕ_m of 0.04%. Two flow rates were studied, with a mean of Re_i=250 and Re_i=320. This corresponded to the mean axial velocity at the inlet. The inlet length, l required for fully developed laminar flow is calculated from the relationship of l/D=0.06Re_i (Caro, 1978). The calculated inlet length required is 15D and 19D. The inlet velocity profiles for both rates were measured further downstream at 158mm or equivalent to 20D from the inlet (4D from stenosis throat), hence, at the measured position, the flow is fully developed. The inlet flow rates, Re_i and the entrance length required are summarised in Table 4.1.

Table 4.1 Inlet flow parameters at pump volumetric flowrates of 8.94ml/s and 11.83ml/s.

Flow parameters	Volumetric flow rates, ml/s	
	8.94	11.83
Maximum velocity measured u_{max}, m/s	0.36	0.46
Mean velocity calculated u_{mean}, m/s	0.18	0.23
Re based on inlet u_{mean}, Re_i	250	320
Inlet length required l, mm	120 (15D)	154 (19D)

The profiles were plotted and compared with the parabolic Poiseuille relationship for laminar flow. The Poiseuille equation is given as:

$$u = u_{max}(1 - r^2/R^2) \tag{4.1}$$

As shown in Figure 4.1, the curves fit the parabolic equation. The regression equations for flow at Re_i=250 and Re_i=320, were u=0.363-0.361$(r/R)^2$ and u=0.463-0.453$(r/R)^2$, respectively. The respective regression equations in the form of Equation 4.1 yield u=1.0055$[u_{max}(1 - r^2/R^2)]$ and u=1.0220$[u_{max}(1 - r^2/R^2)]$. Both factors were close to 1.0000 and complied with the parabolic Poiseuille relationship for laminar flow.

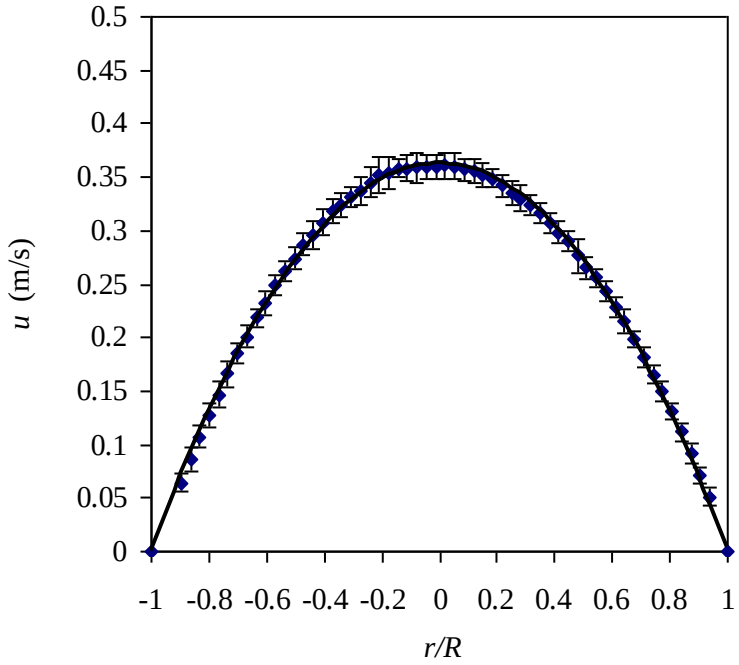

a. Re_i = 250.The regression equation : u=0.363-0.361$(r/R)^2$

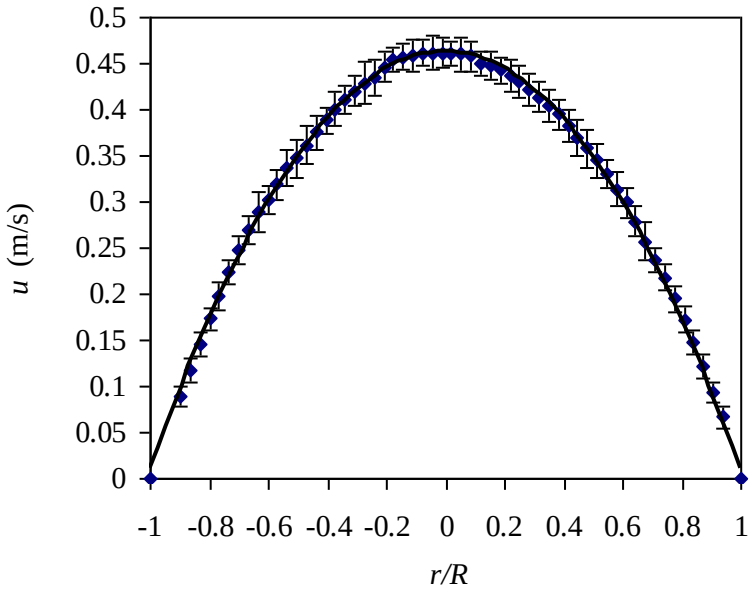

b. Re_i=320. The regression equation : u=0.463-0.453$(r/R)^2$

Figure 4.1 Parabolic curve fit for inlet flow at Re_i =250 and Re_i =320.The error bars represent the standard deviation of the root mean squared velocity of 200 images.

The measurement field of a selected region covered the diameter of the duct. Each image dimension was equivalent to 1008x1016 pixels. One pixel corresponded to 8.19μm, and 200 pairs of images were recorded. The interrogation area was 32x32 pixels (0.262x0.262mm) and each overlapped with its neighbour by 50%. The images were evaluated using the cross-correlation method presented in Section 3.1.4. At Re_i = 250, the time delay, Δt between the pulse pairs was 150μs; at Re_i=320, the time interval was 180μs. The preliminary selection of Δt was presented in Section 3.1.1. It is important to note that by setting the Δt between 150μs to 180μs, the particles exceeded one-quarter distance of interrogation area but still displaced within the interrogation area.

As indicated in Figure 4.2, the measurement regions were: proximal stenosis, distal stenosis, and the stenosis throat. Region A shows the inlet field, region B the entrance. The image of the stenosis throat was acquired 201mm from region B. Two regions of images were captured distal to the stenosis. One started at 204mm and the other at 206mm, as indicated by regions C and D, respectively. The point where the diameter reduction ended was equal to the inlet diameter, and served as a reference point to identify the coordinates. In regions C and D, this point was captured, hence there was an apparent overlap.

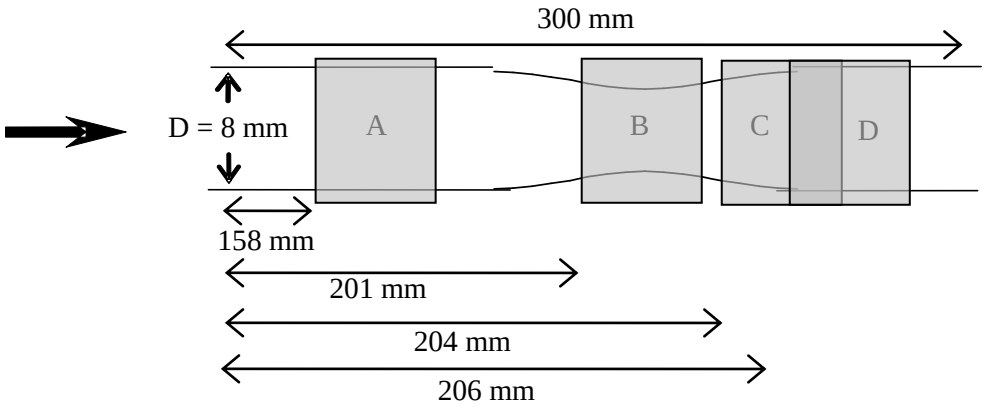

Figure 4.2 Measurement locations (not to scale).

In each region, local coordinates were translated into global coordinates; see Figure 4.3. The radial coordinate was normalised by the inlet geometry radius, *R* (4mm) and the axial coordinate by the diameter, *D* (8mm). The coordinates' reference point (0,0) lay in the central coordinate of the throat region.

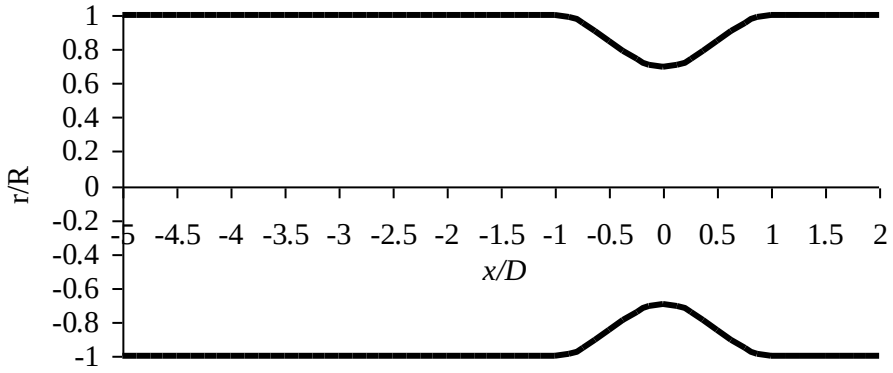

Figure 4.3 Normalised scale for measurement area.

4.2.2 **Dimensionless flow parameters**

The flow behaviour was evaluated using dimensionless numbers (discussed in Section 2.1). Table 4.2 summarises the numbers calculated from the velocity field data.

Table 4.2 Dimensionless numbers considered.

Numbers	Equations
Flow Reynolds number	$Re = \frac{\rho D u}{\mu}$ (4.2)
Shear Reynolds number	$Re_g = \frac{a^2 \rho}{\mu} \frac{du}{dr}$ (4.3)
Peclet number	$Pe = \frac{6\pi\mu a^3}{kT} \frac{du}{dr}$ (4.4)
Stokes number	$St = \frac{\rho_p d_p^2}{18\mu} \frac{du}{dr}$ (4.5)

Nomenclature: ρ - density of the fluid, ρ_p -density of particle, D - diameter of the inlet, d_p - particle diameter, a - particle radius, u - axial fluid velocity, v - radial fluid velocity, μ - viscosity of the fluid, du/dr - axial velocity gradient, k -Boltzmann's constant, T - temperature and g - gravitational acceleration

4.3 Results

4.3.1 **Flow visualisation from PIV measurement**

As discussed in Section 3.1.2, the resulting raw vector maps were validated to remove spurious vectors. Peak validation method was performed followed by moving average validation. Due to the large amount of data, a threshold ratio value of the highest peak to the second highest peak, *k'* was set. By using this method, the highest peak is taken as the signal and the second highest peak is noise. The vectors was rejected if the value of *k'* is less than the threshold value. A good quality recordings was reported when *k'* was in the range 1.0 to 1.5 (Adrian,1991). In order to determine the threshold value, the average peak width in the correlation plane was ensured to have values between 3 to 6 pixels as recommended by Westerweel, (1997). For this reason the histogram for validated data was inspected for each set where the optimised *k'* value was taken at 1.2.

The valid vectors was further analysed by using moving average validation. Moving average validation is a whole flow field validation where the vectors representing small interrogation area are compared with its neighbours and the difference is analysed. The vectors which deviated by exceeding a certain percentage of the velocity difference will be rejected and replaced. Iteration approach was adopted and detail algorithm is explained by Host-Madsen and McCluskey (1991). The total percentage of invalid vectors of the whole field vectors was ensured to be not more than 5% from the raw vectors as indicated by Westerweel (1997). The substituted vectors were mainly in the core flow where the velocity was relatively high. Most of the valid vectors towards the wall including in the recirculation zone were the raw vectors. These vectors were not undergone any rejection or substitution during vector validation process.

The flow was investigated at the inlet Reynolds number Re_i of 250 and 320. The velocity vectors at regions A, B, C and D are super-imposed onto the images in Figure 4.4 and Figure 4.5, the background image corresponds to the average light intensity of 200 images. In this frame size, 1008x1016 pixels equalled 8.2x8.3 millimetres. The vectors' reference scale was equivalent to 0.5m/s. In general, the flows at Re_i =250 and Re_i =320 were laminar through distal and proximal to the stenosis. For the velocity field in region C, there was relatively high scattered light intensity near the wall. The intensity near the wall at Re_i=320 was lower than that observed at Re_i=250.

The near wall flow in region C is enlarged in Figure 4.6, and the vectors clearly indicate flow recirculation. It was difficult to determine the reattachment point precisely, as it involved

accurate velocity characterisation at the wall boundary, and the velocity here was approaching zero. The reattachment point was decided based on the direction of the velocity vector close to the wall boundary (indicated in Figure 4.7). The reattachment points at Re_i=250 and Re_i=320 were x/D=1.63 and x/D=1.93, respectively. However, the estimation was subject to error, partly due to the particles' movement in the interrogation area. Near the wall, the particles' movement in the interrogation area were non-uniform and had significant gradients. At the reattachment point, the surrounding particles moved in different directions. The size of the interrogation area was too large to describe the detail of the flow, and the velocity took the average of the particle movement.

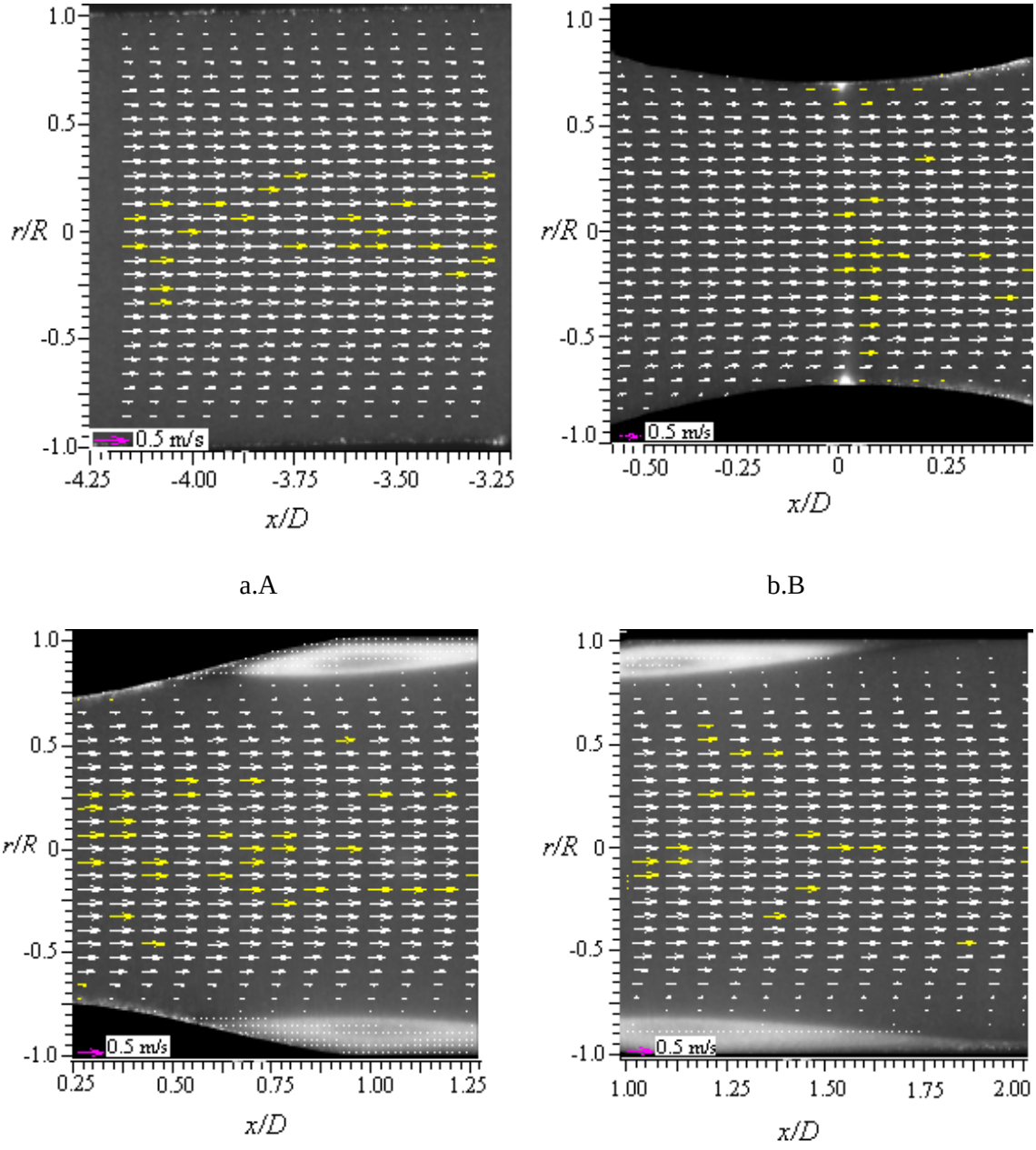

Figure 4.4 Velocity vector map at Re_i =250 at locations A, B, C and D. White vector is the valid vector and yellow is the substituted vector.

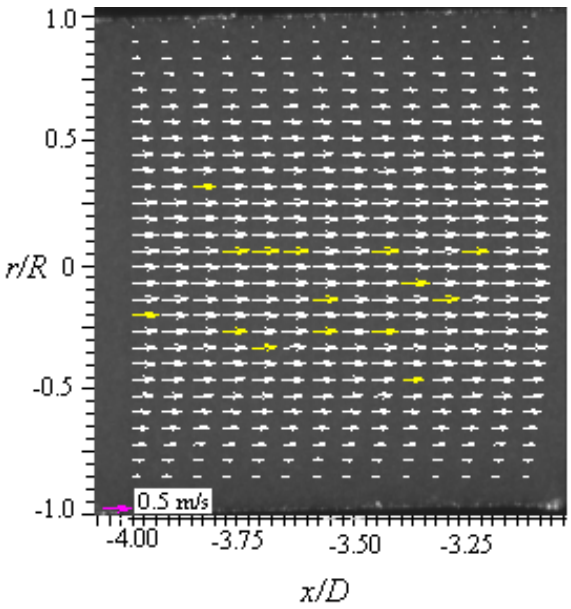

a. A

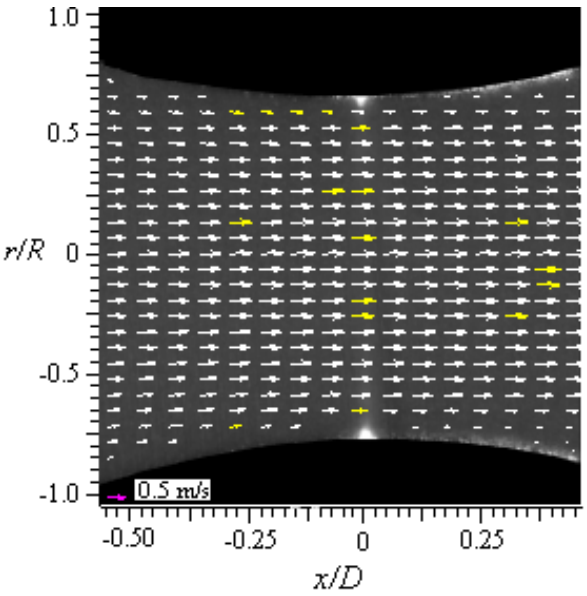

b. B

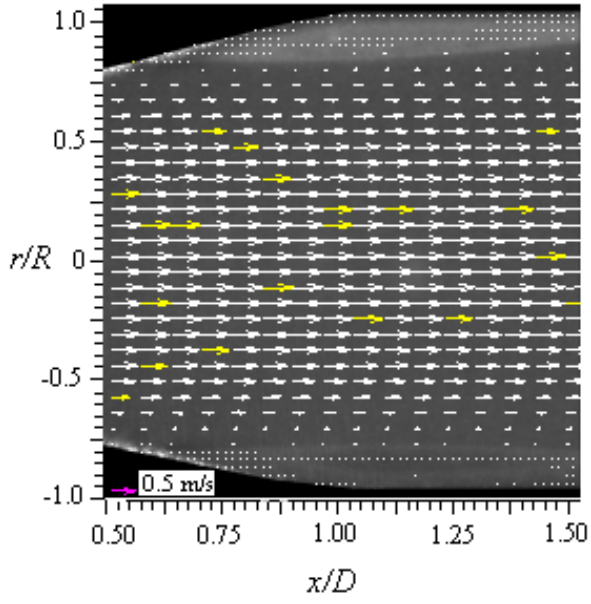

c. C

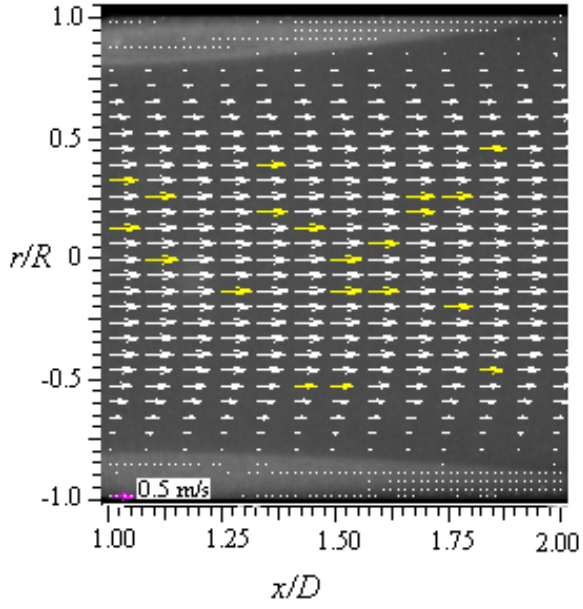

d. D

Figure 4.5 Velocity vector map at Re_i =320 at locations A, B, C and D. White vector is the valid vector and yellow is the substituted vector.

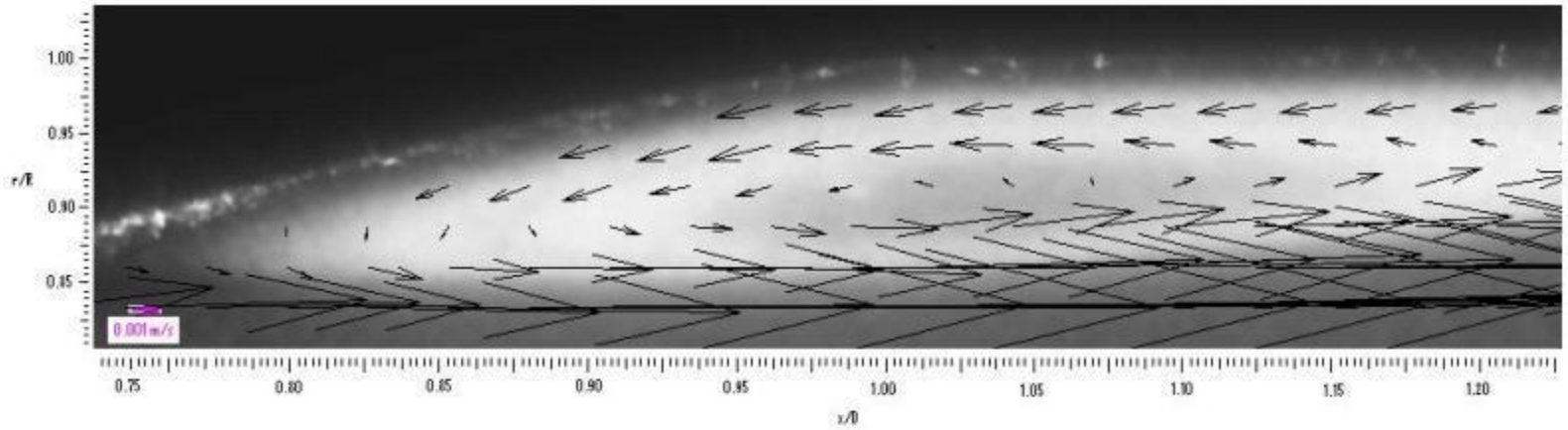

a. Re_i=250

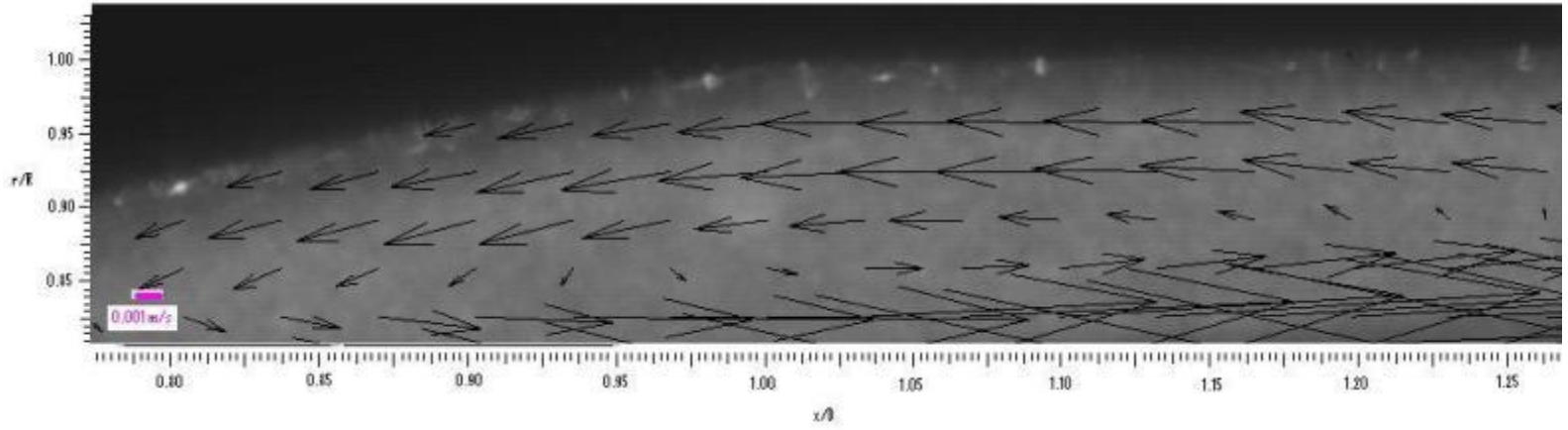

b.Re_i =320

Figure 4.6 Flow recirculation in region C. All vectors are the valid vectors without any substituition.

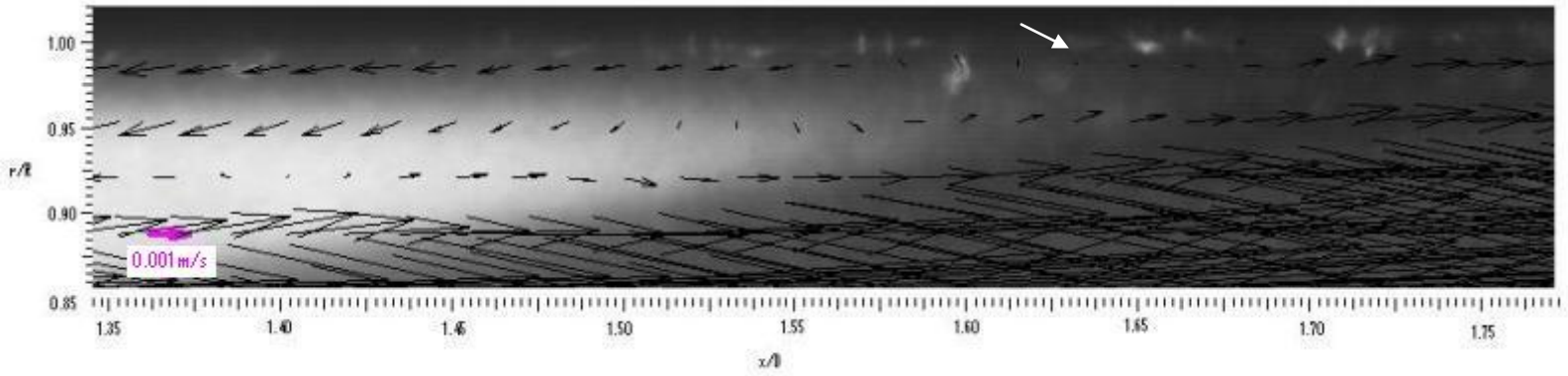

a. Re_i=250 with the reattachment point at x/D=1.63

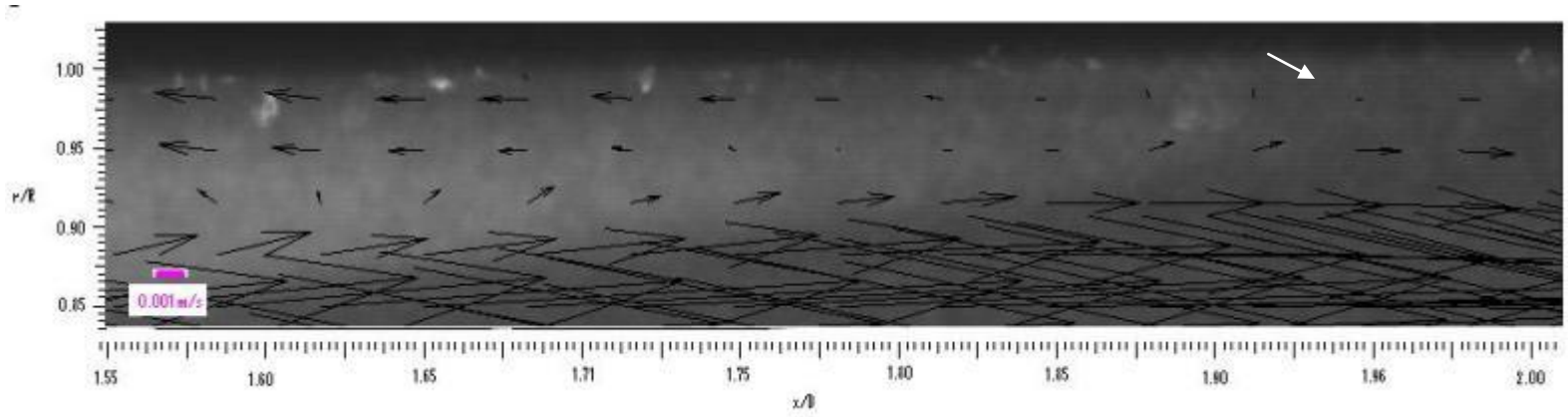

b. Re_i =320 with the reattachment point at x/D=1.93

Figure 4.7 Reattachment-point estimation in region D: the arrow indicates the reattachment point near the wall.

4.3.2 **Error analysis**

The standard deviation of the 200 velocity vectors in each measurement is analysed. The errors were normalised based on the local velocity. The comparison of the measurement errors between Re_i=250 and Re_i=320 at x/D=1 is shown in Figure 4.8. Within the core flow up to r/R=0.50, the error range was 3.5±1.0%. From this point to r/R=0.65 the errors gradually increase to a maximum of 17%. At r/R=0.80 the maximum errors were around 25%. The errors were increased towards the wall. The deviation error for measurement at Re_i =320 with location x/D=-4, x/D=1 and x/D=1.5 is compared in Figure 4.9. The errors at the inlet (x/D=-4) are smaller than that the errors distal to stenosis.

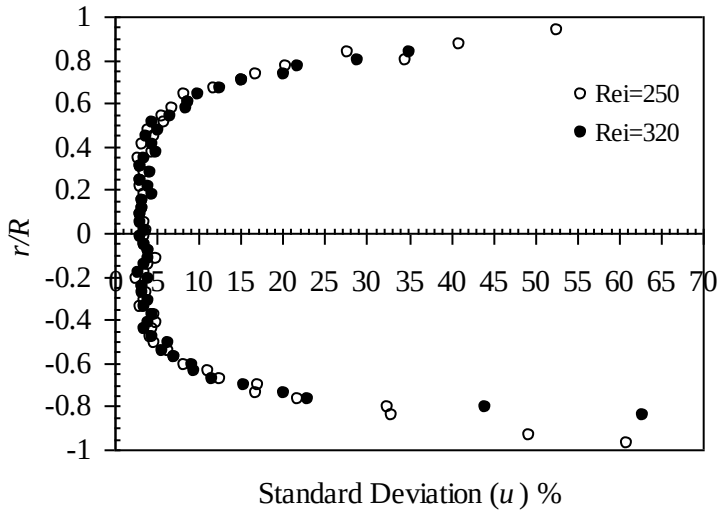

Figure 4.8 Errors at x/D=1 for Re_i =250 and Re_i =320

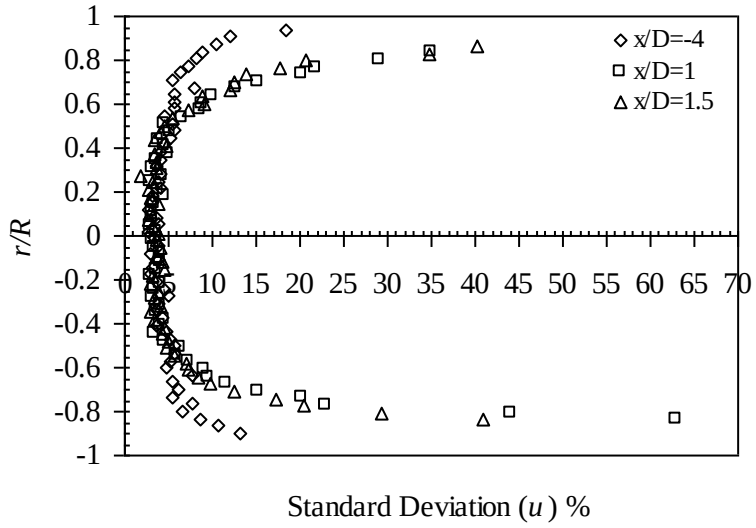

Figure 4.9 Standard deviation of axial velocity data at *x/D*=-4, *x/D*=1 and *x/D*=1.5 for Re_i=320

The accuracy of the PIV measurement depended on the uncertainty of the measurements of particle displacement. These errors come from varying sources which were random error arising from noise, bias error due to the process of computing the signal to sub-pixel accuracy, gradient error resulting from deformation of flow within the interrogation area, tracking error due to the inability of a particle to follow the flow and acceleration error caused by local Eulerian velocity approximation for Lagrangian motion of tracer particles (Prasad, 2000). As seen from the image map for region C and D, the particles were not scattered homogeneously. This explains why the errors at the distance 30% from the wall in the expansion region were significantly large. This observation corresponds to the difficulty in the definition of the wall boundary and the wall curvature effect during PIV measurement. When the data is extracted, the location of *x/D*=0 and *x/D*=1 were the reference point to measure other coordinate. The uncertainties to define the wall boundary were half of the interrogation area which was equal to ±16 pixels or ±0.13mm.

4.3.3 **Velocity magnitude**

The velocity magnitude is shown in Figure 4.10 and Figure 4.11, where the axial velocity of each region is plotted. Proximal to the stenosis region, the highest velocity was in the throat area (region B), slightly beyond x/D=0. The centreline velocity u_{max} at x/D =-4, 0.2, 1 and 1.5 is given in Table 4.3. In both flow rates, the maximum velocity at the throat region was 40% higher than at the inlet. Downstream of the stenosis a jet is found which indicating the velocity spread for several directions. Distal to stenosis the velocity was not immediately returned to laminar fully developed flow.

Table 4.3 Centreline velocity

	Re_i=250				Re_i=320			
x/D	-4	0.2	1	1.5	-4	0.2	1	1.5
u_{max}(m/s)	0.36	0.51	0.48	0.48	0.46	0.65	0.63	0.62
$u_{max}/u_{max,i}$	1	1.4	1.3	1.3	1	1.4	1.3	1.3

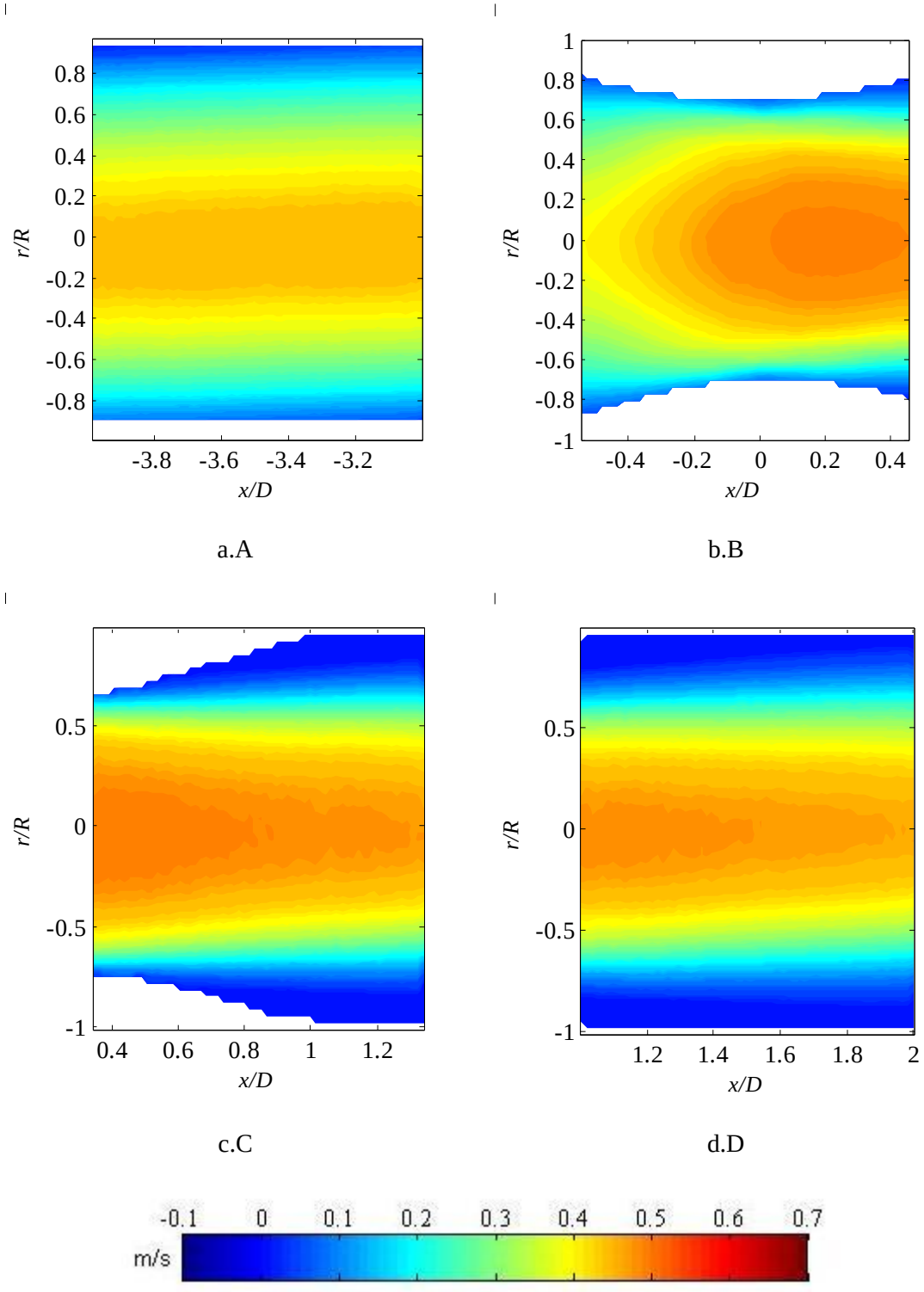

Figure 4.10 Velocity magnitude at Re_i =250.

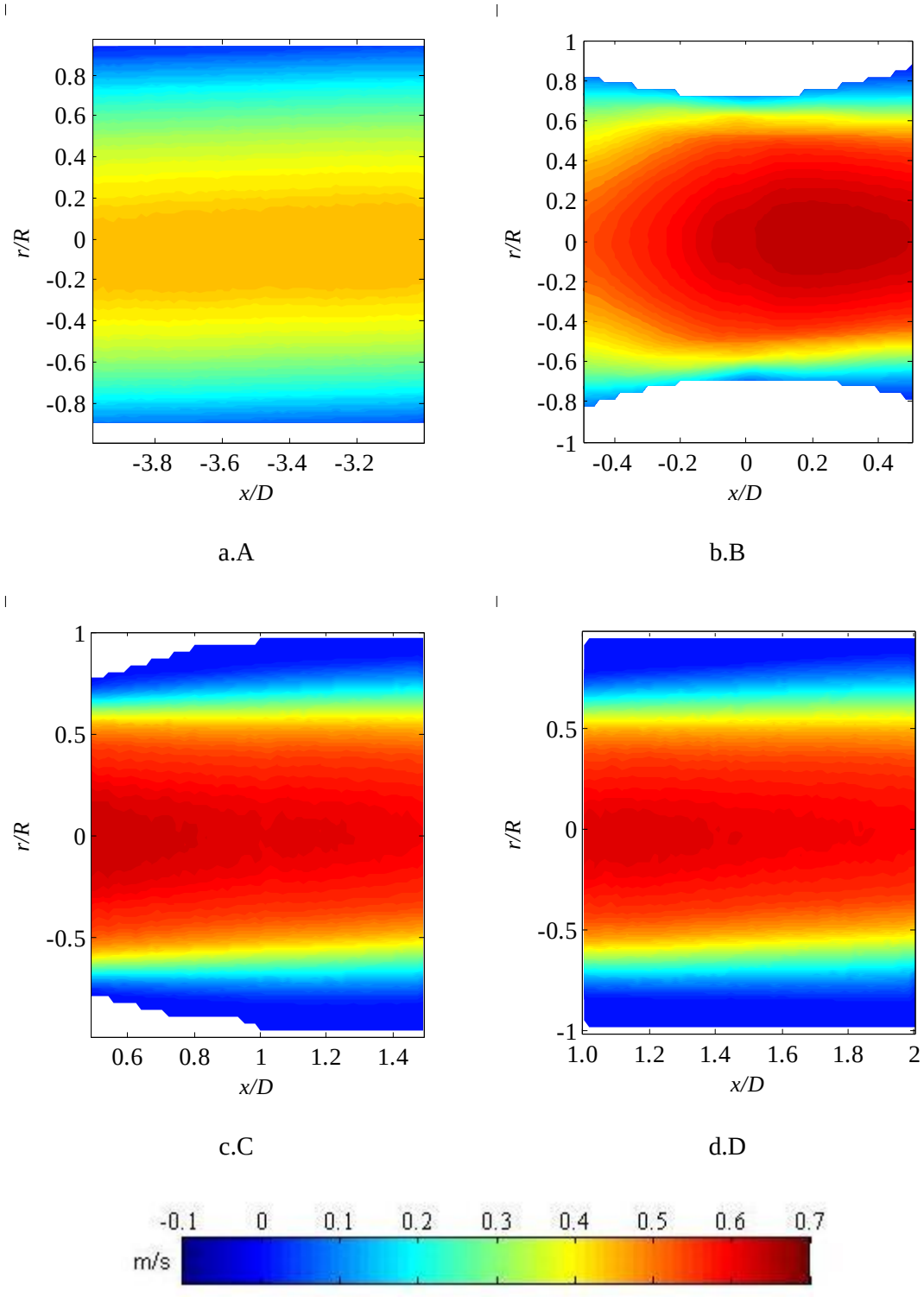

Figure 4.11 Velocity magnitude at Re_i =320.

4.3.4 **Velocity gradient**

Figures 4.12 and Figure 4.13 depict the velocity gradient *du/dr*.At the centreline, this is always zero. At the inlet, the gradient increased towards the wall. The highest velocity gradient occurs at the wall of the throat region. The gradient of the flow separation region is lower than the maximum shear gradient of the inlet. In region C, the velocity gradient between *r/R* =0.5 and 0.7 is higher than that of the recirculation region. As the flow moves downstream to region D, these gradients decrease.

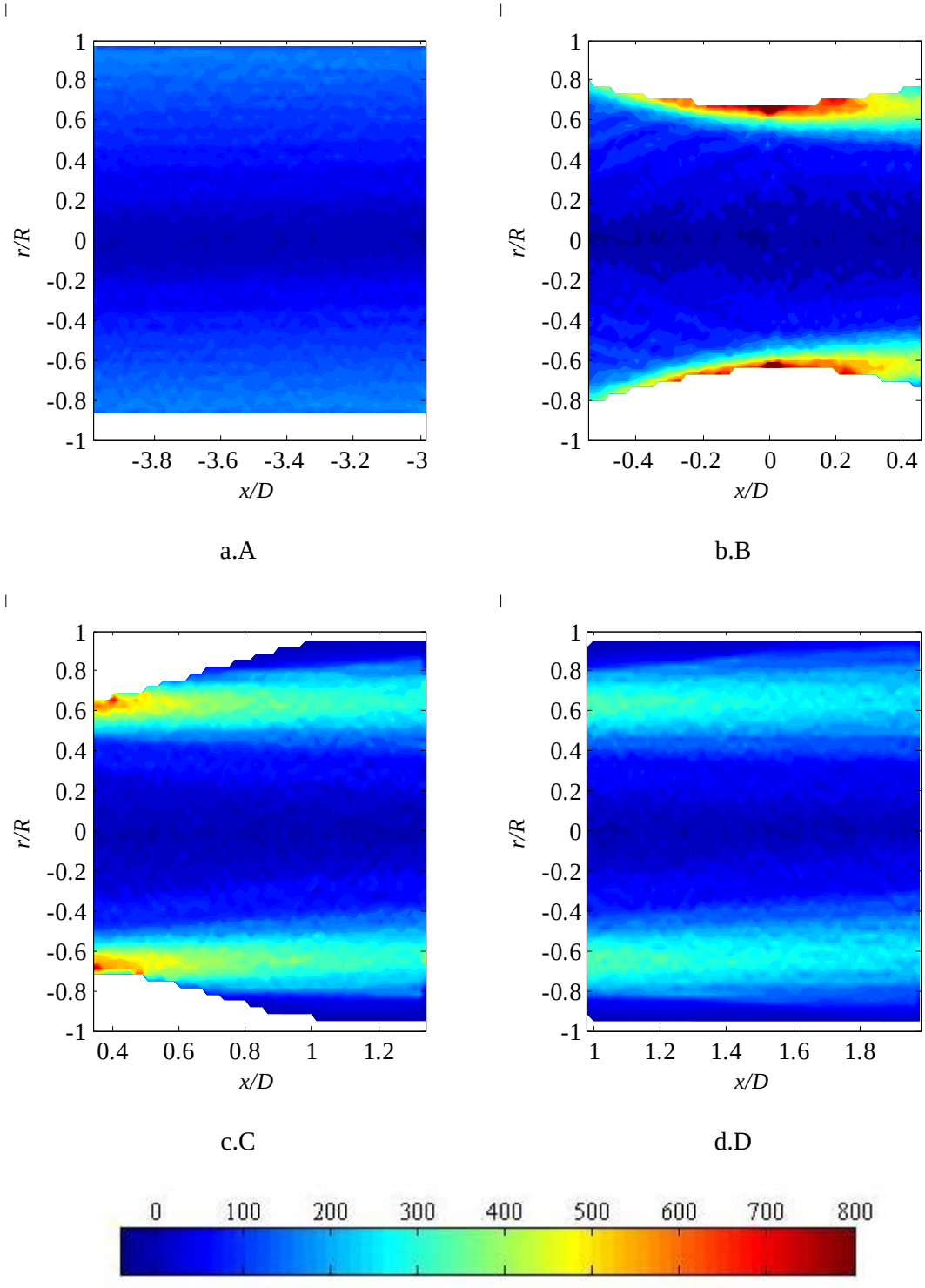

Figure 4.12 *du/dr* for Re_i =250.

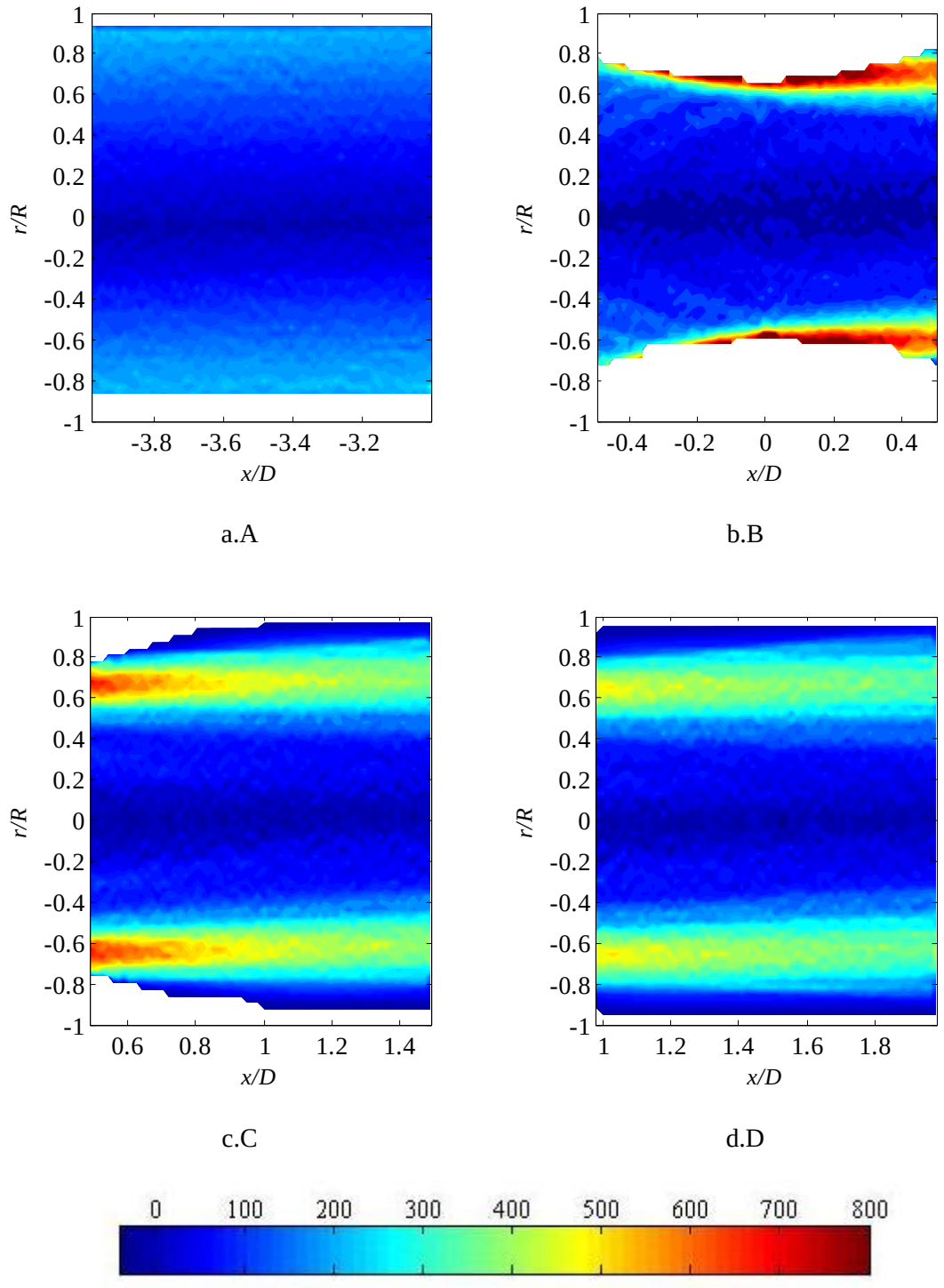

Figure 4.13 *du/dr* for Re_i =320.

Table 4.4 summarises the *du/dr* at *x/D* = -4, 0.5, 1 and 1.5 with radial position of *r/R*=0.7. These local *du/dr* at this radial position are within the high shear zones distal to stenosis. The ratio of local shear gradient to the inlet at Re_i=250 and 320 is plotted in Figure 4.14. The falling of shear gradient from the throat region to the downstream suggested an exponential drop.

Table 4.4 Maximum velocity gradient *du/dr* at *r/R*=0.6

	Re_i=250				Re_i=320			
x/D	-4	0.5	1	1.5	-4	0.5	1	1.5
du/dr (s^{-1})	120	550	350	275	150	800	500	400
$du/dr/\ du/dr_{,i}$	1.00	4.58	2.92	2.29	1.00	5.33	3.33	2.67

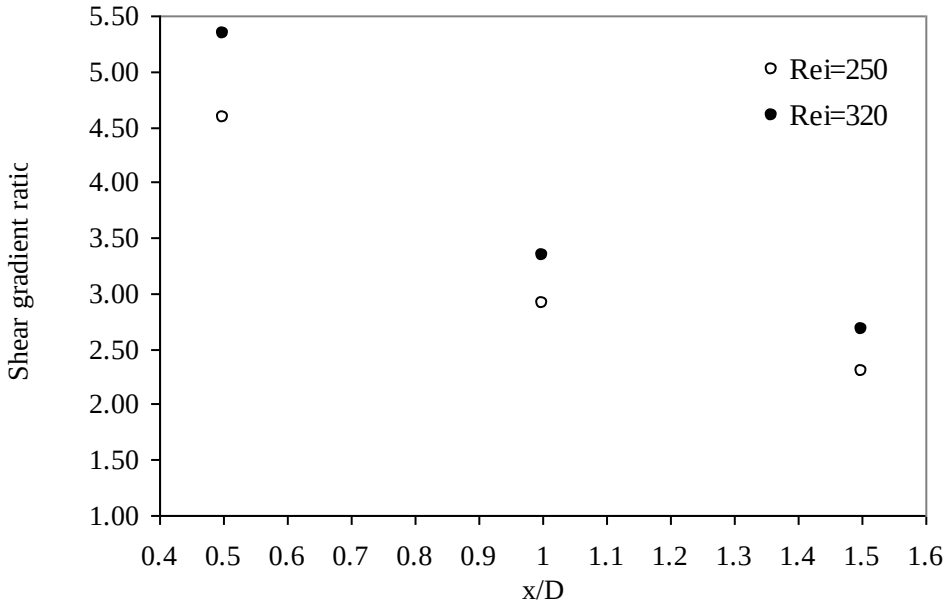

Figure 4.14 The shear gradient ratio distal to stenosis at Re_i =250 and Re_i =320

The gradient Reynolds number Re_g (Equation 4.3), the Peclet number *Pe* (Equation 4.4) and *St* (Equation 4.5) are all functions of the shear gradient: therefore, they follow its contours.

As discussed in Section 2.3.4, the characterisation of the lift models was based on Re_g (Saffman, 1965; Mei and Adrian, 1992; McLaughlin, 1993). From the plot in Figure 4.15 and 4.16, the Re_g were in the range of 10^{-3} to 10^{-2}.

Pe expresses the ratio of the hydrodynamic shear forces to the diffusive Brownian forces. The latter acted to return the suspended particles to their equilibrium configuration which is continuously disturbed by the shear forces. The magnitudes are plotted in Figure 4.17 and 4.18 which indicates the *Pe* for the system in the region of 10^7.

The Stokes number, *St* compares viscous relaxation time scale to the fluid characteristics time scale. Fluid characteristic time scale equals to the inverse of the velocity gradient $(du/dr)^{-1}$ which makes the *St* proportional to the *du/dr*. From Figure 4.19 and 4.20, the *St* was found in the range of 10^{-3}.

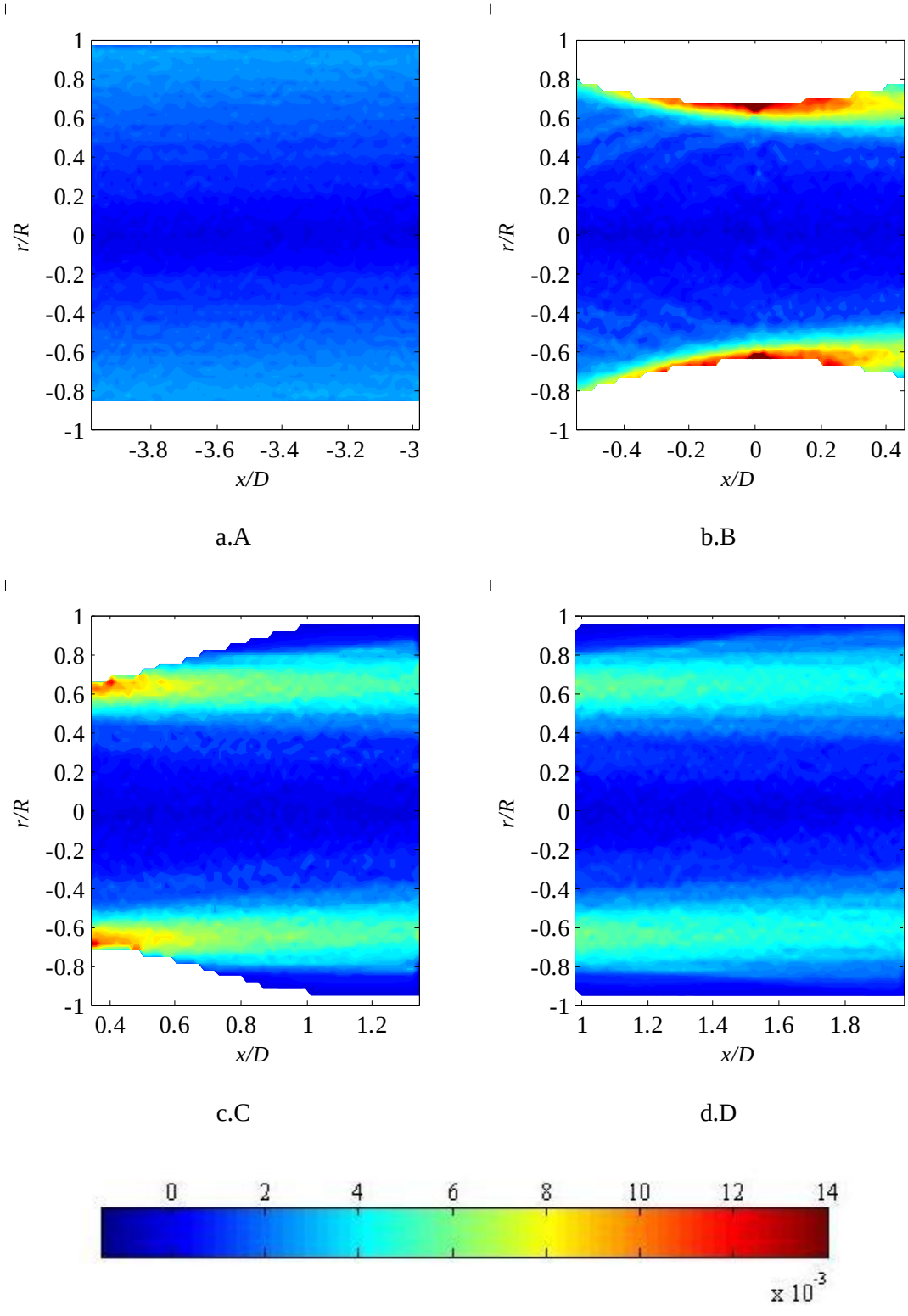

Figure 4.15 Shear gradient Reynolds number Re_g for Re_i =250.

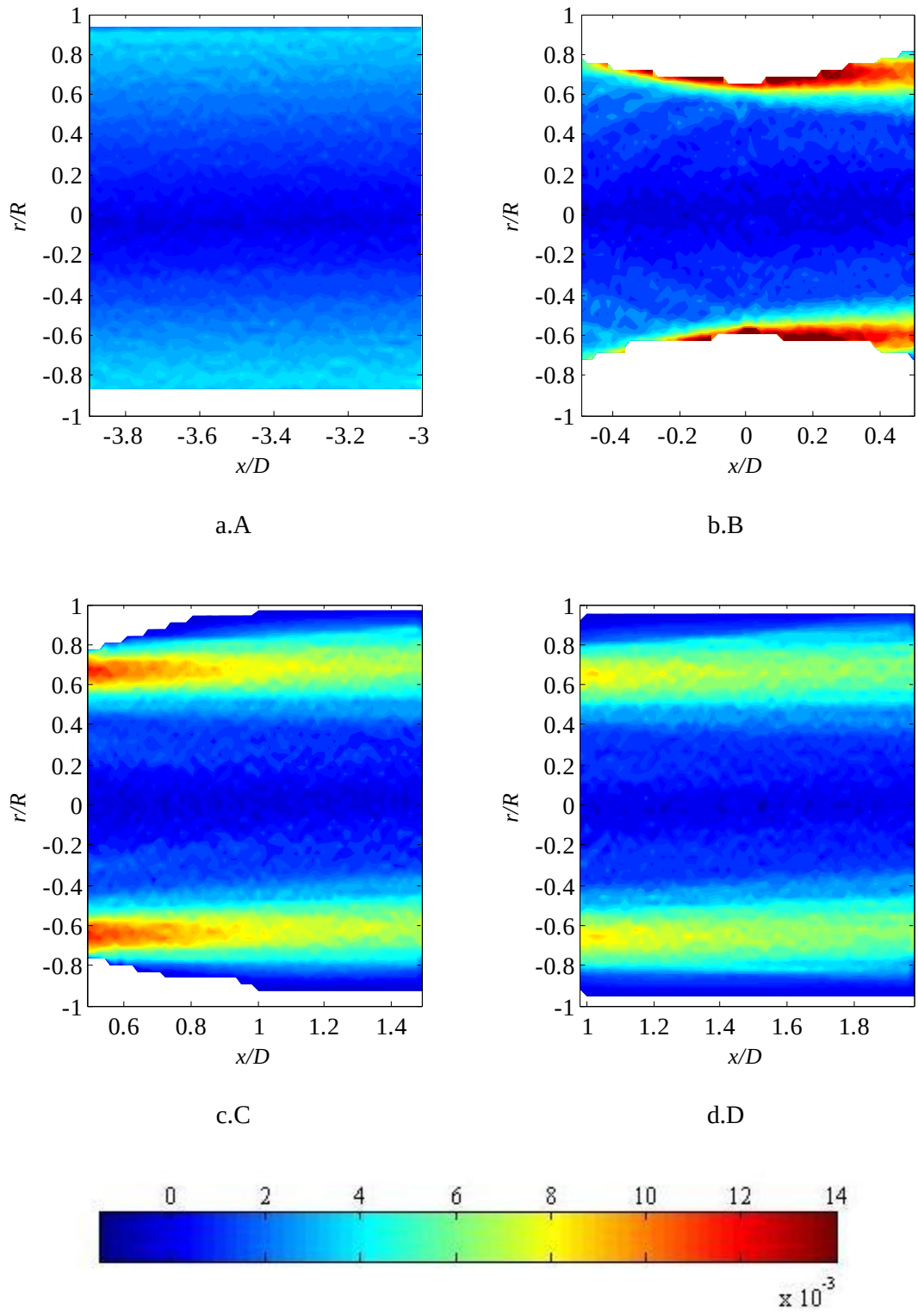

Figure 4.16 Shear gradient Reynolds number Re_g, for Re_i =320.

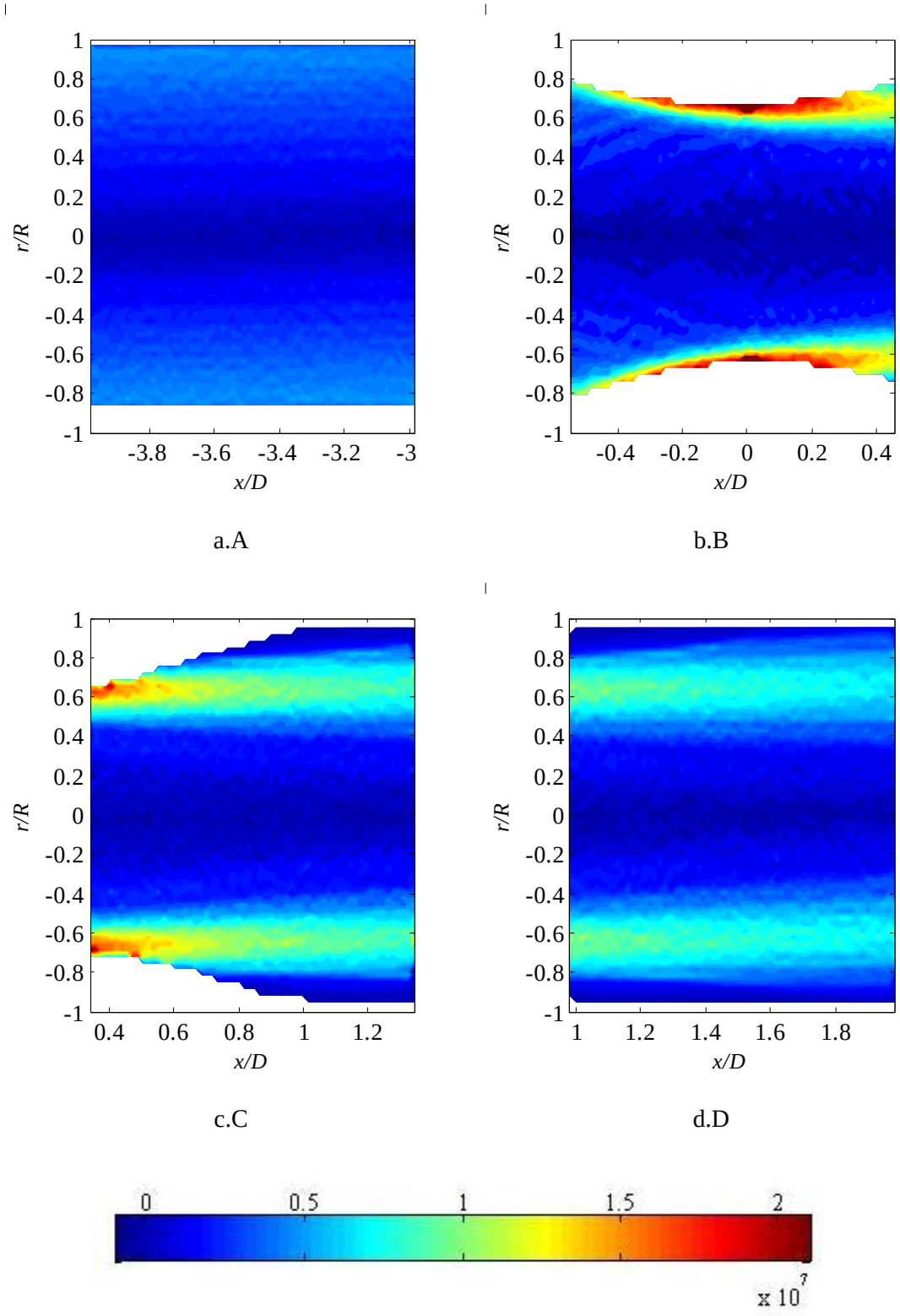

Figure 4.17 Peclet number *Pe* for Re_i =250.

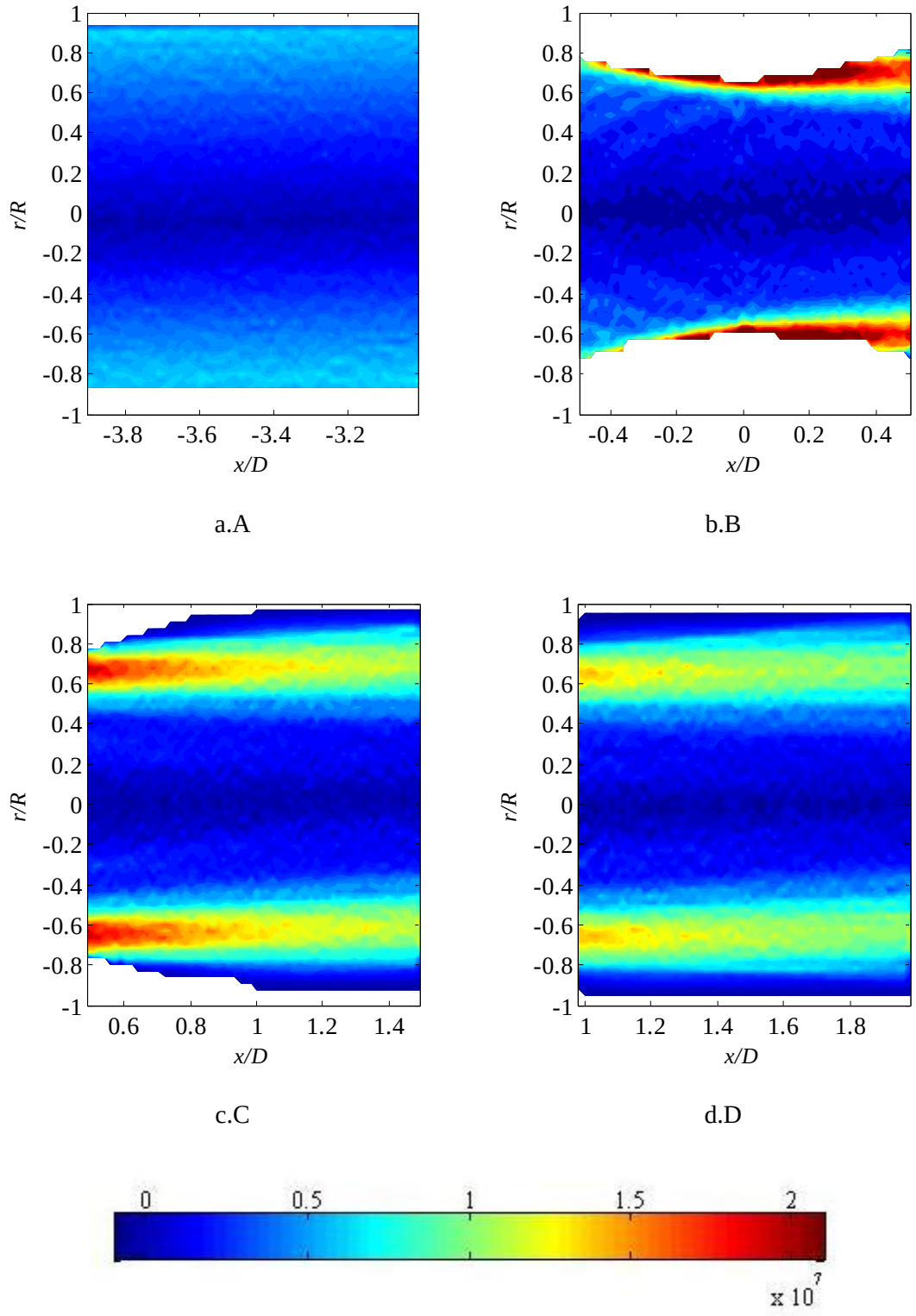

Figure 4.18 Peclet number *Pe* for *Rei* =320.

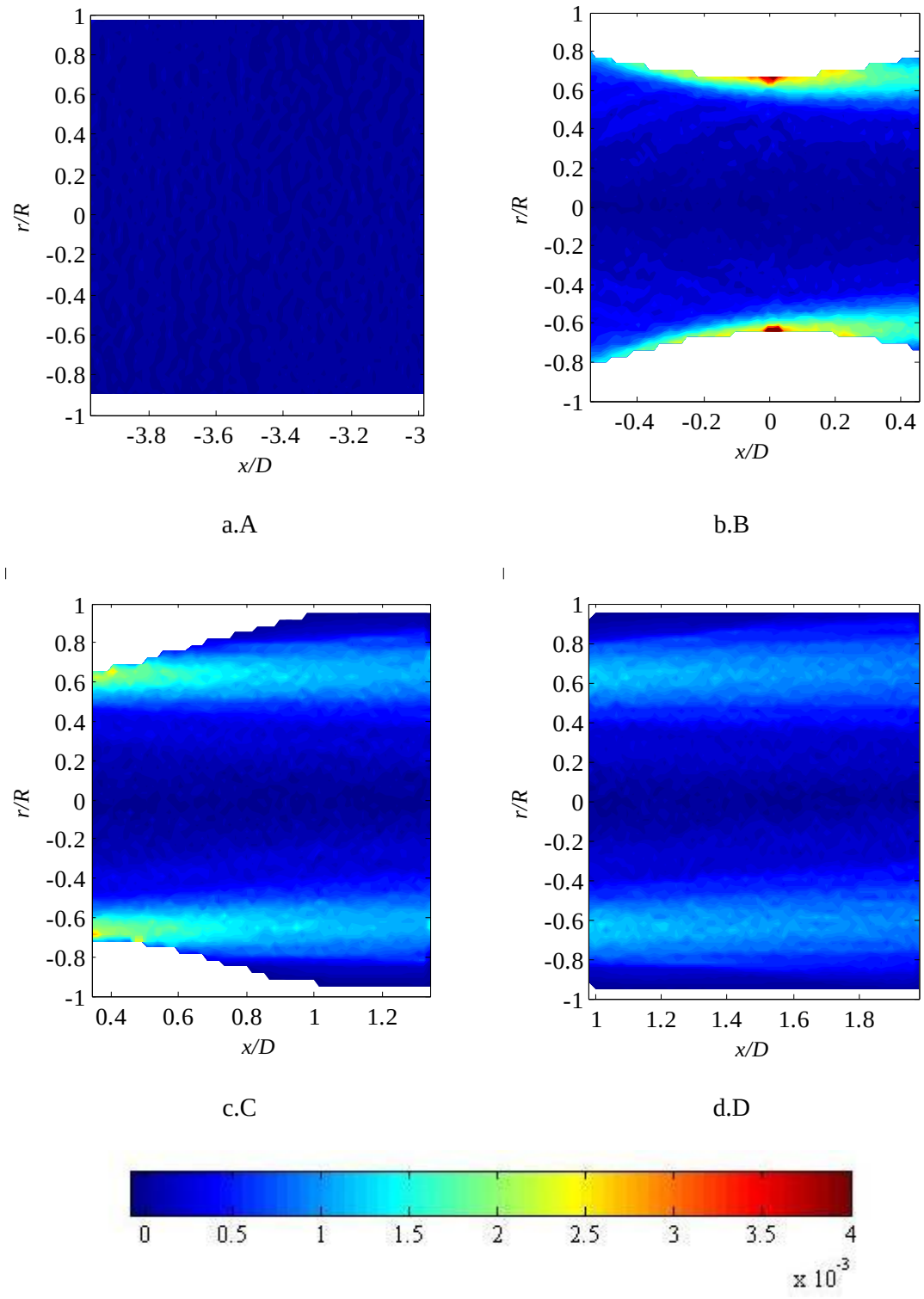

Figure 4.19 Stokes numbers for Re_i =250.

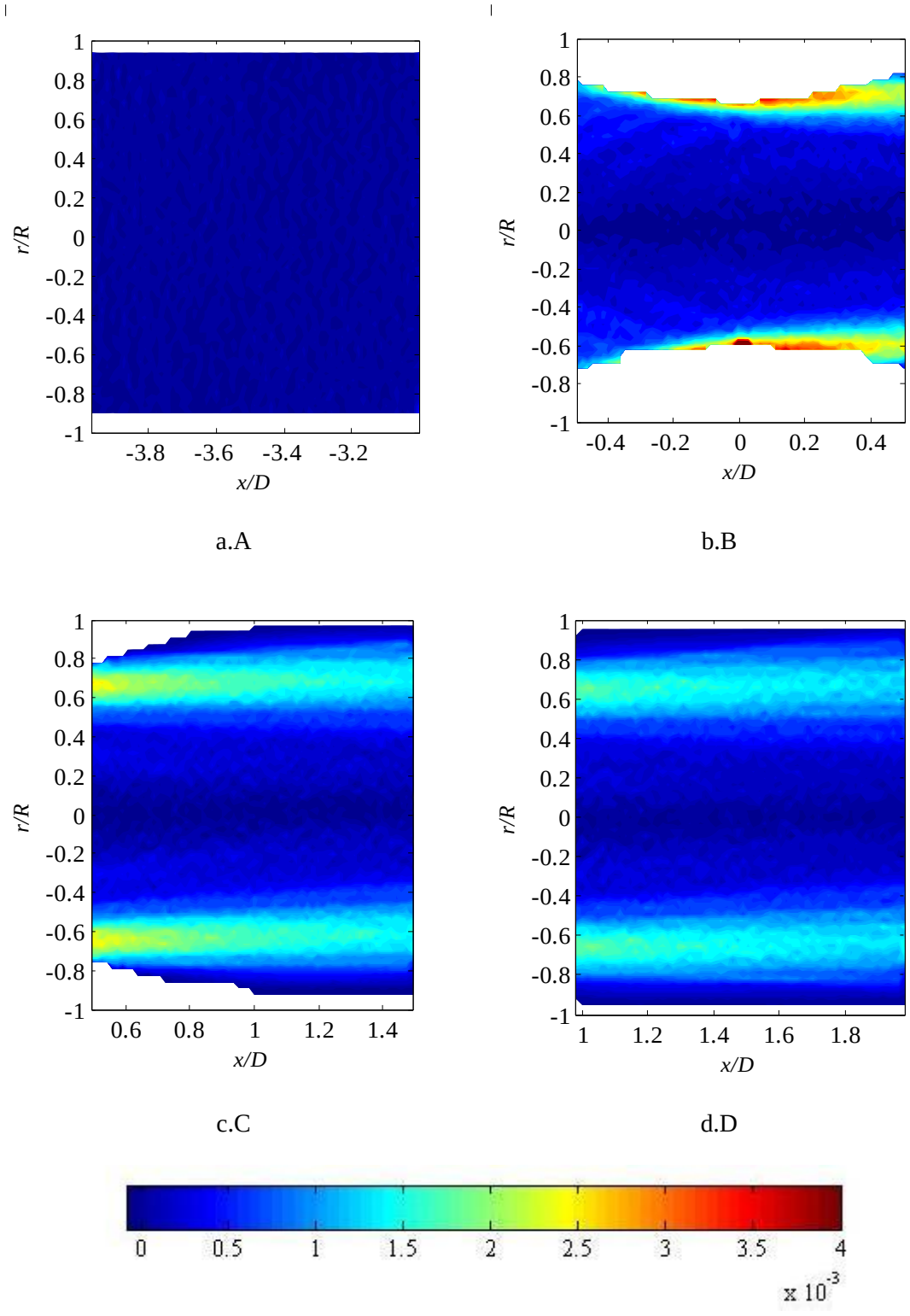

Figure 4.20 Stokes numbers for Re_i =320.

4.4 Discussion

The flow behaviour in the stenosis geometry is typical venturi flow. Due to the sudden change in the cross-sectional area at the throat of the stenosis, the velocity increased and the pressure dropped at a faster rate. This was accompanied by a jet formation. The flow *Re* here was 40% higher than at the inlet. In the expansion section, the decrease in velocity was accompanied by an increase in static pressure in the direction of motion. The adverse pressure tended to retard the flow. In the mainstream, the inertia opposed the retardation but close to the wall, the fluid velocity and inertia were smaller. The fluid lost momentum due to viscous friction; hence, it was decelerated by the adverse pressure gradient and the direction of flow was reversed. Boundary-layer separation occurred and fluid recirculation was observed between the jet and the wall: this site produced most of the lost pressure, thus creating additional viscous loss. The results of the experiment agree well with the observations of Ku (1997), Berger and Jou,(2000), and Wootton and Ku (1999).

The flow visualisation in Figure 4.4 and Figure 4.5 indicates that the flow was streamlined. The particle concentration in the flow separation region indicated by the light intensity was significantly higher. The reattachment point increased with the flow rates, in agreement with the theoretical Navier-Stokes equation. Gach and Lowe (2000) characterise stenotic flow regime according to the length of the separation region, concluding that the flow is laminar for Re_i<250. A transition region was observed up to Re_i <1500. This suggests that at Re_i=250 and Re_i=320, the regime may fall within a boundary of laminar and a transition phase in which the flow became unstable.

There was a large variation of velocity gradient in the system (Figure 4.16 and Figure 4.17). At the core flow of the inlet, the shear gradient was zero and this increased as it approached the wall. The maximum shear gradient occurred near the wall at the throat of the stenosis. In the literature, the maximum gradient was slightly before the throat (Long et al., 2001; Li, 2006). The discrepancies were due to the masking procedure to define the wall boundary at the wall curvature. This experimental error is discussed in Section 3.7.3. Downstream of the stenosis, relatively high shear was observed between the core flow and the separation region. In contrast, the shear gradient in the recirculation region was the lowest. As discussed in Section 2.3.4, the characterisation of the lift models was based on Re_p and Re_g (Saffman, 1965; Mei and Adrian, 1992; McLaughlin, 1993). The Re_g were in the range of 10^{-3}, however the Re_p is not excatly known. Thereby the Saffman lift model that requires the $Re_p << Re_g^{1/2}$cannot be verified at this stage.

At the inlet and the throat, *Pe* was greater than 10^3 and Re_g was in the range of 10^{-3} (Table 4.5) . In the recirculation region, *Pe* was around 10^3 and Re_g between 10^{-6} to 10^{-3} (Table 4.6). Based on a phase-diagram of suspension rheology which as function of *Pe* and Re_g decribed in Figure 2.1, these ranges show that the flow behaved as Newtonian (Stickel and Powell, 2005). The Peclet number ranged from 10^3 to 10^7, indicating that the system was non-Brownian and that hydrodynamic shear force was dominant.

In all cases, calculated Stokes numbers (Figure 4.19 and 4.20) were less than unity in the region of 10^{-4} to 10^{-3}. Although Brownian diffusion was neglible, the particle diffusion may have been the result of the hydrodynamic shear (Leighton and Acrivos, 1987) .Shear-induced dispersion is the migration of particles across the streamlines (daCunha and Hinch, 1996). It arises from the random motion of particles that occurs as the suspension is sheared (Tiwari et al., 2009). The self-diffusion coefficient is proportional to $du/dr\ a^2\phi$ (Abbas et al., 2009). In the region of $St<1$, the particle diffusivity is related to the particulate velocity fluctuations occuring after multiple particle encounters (Abbas et al., 2009). In the limit of dilute suspension, theoretical prediction was due to three-body hydrodynamic interaction, where the symmetry of two particles' interaction was broken (Acrivos et al., 1992). While surface roughness may significantly modify the microstructure, it plays no role in the random walk in a dilute susupension (Zarraga and Leighton, 2002). Asmolov (2008) reports that self-diffusion mechanisms in wall-bounded flow are due to large-scale fluctuations in particle concentration and fluid velocity. Even a small concentration inhomogeneity can result in significant diffusivity growth near the walls. Based on this argument, self-diffusion is high where there is a high shear gradient. Therefore, the particle inhomogeneity in recirculation zone may have resulted from the particle diffusion from the boundary with the jet. Thus the motion of the particles can be described using an advection-diffusion equation. The advection term accounts for the particle velocity arising from the drag exerted by the macroscopic flow and the external forces; the diffusion term describes the effect of the microscopic hydrodynamic interaction of the particles.

4.5 Conclusions

A steady flow at Re_i=250 and Re_i=320 across a stenosis with 30% diameter reduction was characterised using particle image velocimetry (PIV). The flow was streamlined and the reattachment point increased in accordance with the flow rates. At these rates, the flow behaviour was close to the transition regime. Moderate *Re* and $St < 1$ indicated that the fluid inertia was important. High shear region was observed at the throat, which extended to the

beginning of the expansion section in the direction of the flow; meanwhile, the minimum shear was in the recirculation area. Very large *Pe* and $Re_g<10^{-3}$ indicate that the particles were non-Brownian and that the suspension rheology was Newtonian. The existence of shear gradient in the flow may also have induced self-diffusion in the dilute suspension, due to inter-particle interaction.

Chapter 5

PARTICLE DISTRIBUTION IN THE RECIRCULATION REGION

As an extension from Chapter 4, this chapter examines the particle distribution in the recirculation region of the stenosed artery model. The influence of particle sizes, particle distribution and flow rates are reported.

5.1 Introduction

Flow separation and recirculation are frequently encountered in an arterial network (Ku, 1997; Wootton and Ku, 1999). Experimental flow systems have been used to investigate the flow patterns in models of diseased arteries (Gijsen et al., 1997; Gijsen et al., 1999) , and to examine the relationship between local haemodynamics and local vascular biology; however, these techniques assume that the blood is a homogeneous fluid. A physical understanding through experimental work has been developed in several geometries, producing flow separation through a backward-facing step (Karino and Goldsmith, 1977) and a tapered artery (Hinds et al., 2001), but their flow Reynolds numbers were very low. Karino and Goldsmith (1977) study the behaviour of blood cells and solid spheres flowing in the separation zone of a step expansion of a capillary-sized vessel at Reynolds numbers between 12 and 110. Blood cells and solid spheres with diameters less than 20μm migrated out of the vortex, whilst larger cells and spheres remained in the recirculation region. Hinds et al.(2001) investigate the adhesion of white blood cells at mean *Re* of 100 and 140 in the recirculation zone, examining the biological activity on the vessel wall. In both of these studies, the flow rates are below large artery conditions.

Lima et al. (2008) find that the dispersion of red blood cells in straight glass capillaries of 50 and 100μm diameters leads to an unequal distribution of cells, depending on their concentration and the vessels' sizes. Similar observations were obtained in small arteries, where Aarts et al. (1988) and Jung and Hassanein (2008) report red blood cell volume concentrations down to five percent near the vessel wall compared to average values in the human of 45%. Aarts et al.(1988) also demonstrate that platelets suspended in saline move radially and accumulate halfway between a vessel's centre and its wall. However, when in a suspension of red cell ghosts at physiologic volume fractions (40%), the platelets were almost solely concentrated near the vessel wall. Aarts et al. (1988) also demonstrated that

platelets suspended in saline move radially and accumulate half way between the vessel centre and the vessel wall. However when suspended in a suspension of red cell ghosts at physiologic volume fractions (40%) the platelets were almost solely concentrated near the vessel wall. Butler et al. (1998) imposed a cell-free layer near the vessel wall in a simulation involving the scavenging effect of red cells on nitric oxide (NO) produced from endothelium, demonstrating that a cell-free layer was necessary for NO to have a vasodilator effect as is known to occur in-vivo. These papers provide the evidence that inhomogeneity of blood particles does occur in small arteries and microcirculation. However, the effect in larger arteries, typically in the recirculation region, where there is a high risk of atherosclerosis progression, has mostly been ignored. Moraczweski et al.(2005) found that the tendency of particles to migrate away or into the flow separation region depends on the tube-particle radius ratio *R/a*. Therefore, the dynamics of particle cells may differ in capillaries and arteries. The results suggested the cells in capillary-sized vessel escaped the separation zone but in large artery, the cells tend to accumulate.

This chapter establishes a fundamental understanding of particle distribution in a disturbed flow. This includes a physical investigation of particle inhomogeneity in a large arterial stenosis model, at physiological Reynolds number values, with particular attention paid to the particle distribution in the separation zone of a stenosed geometry. The effect of varying flow rates (Re_i = 130, 250 and 320), particle sizes (d_p = 10μm and 20μm) and particle concentrations (ϕ_m = 0.07% and 0.14%) on the flow field and particle distribution was investigated using a particle image velocimetry (PIV) system: this required the particle suspension to be dilute for the reasons given in Chapter 4.

5.2 Flow measurement set-up

5.2.1 **PIV**

The PIV system, discussed in Chapter 4, was used in this study. The image size remained the same, but the magnification increased by 2.5, as described in Section 3.6. The image magnification and the optical setting for it are presented in Figure 3.10 and Table 3.3.

5.2.2 **Fluid suspension**

The preparation of the fluid suspension was described in Section 3.3. Two different particles sizes were used in these experiments: their diameters were 20±2μm and 10±2μm. Two particle concentrations ϕ_m were prepared, 0.07% and 0.14% by weight for each diameter.

5.2.3 **Image recording and post-processing**

The velocity information in the flow was obtained from the fluid with seeding particles diameter of 10μm at weight concentration ϕ_m of 0.07% (see Section 3.7 for a detailed description of the method). The interrogation area was 32x32 pixels (0.115 mm x 0.115 mm) and each overlapped with its neighbour by 50%: this yielded a sufficient number of vectors to demonstrate the recirculation pattern within the region of interest. Time between pulses, Δt was set at 10ms. The selection of Δt was discussed in Section 3.7.1.

The light intensity of the images was analysed, in order to determine the particle distribution. The method was described in Section 3.8, where the light intensity, I', in the region of interest , averaged over 750 images, was normalised by dividing the local mean pixel value, $\hat{I}$ by the mean light intensity at the inlet $\hat{I}_0$ i.e.

$$I' = \frac{\hat{I}}{\hat{I}_0} \tag{5.1}$$

5.3 Results

5.3.1 **Flow velocity in the recirculation region**

The velocity vectors in the separation zone at Re_i=130, Re_i=250 and Re_i=320 are plotted on their image, as shown in Figure 5.1, Figure 5.2 and Figure 5.3, respectively. For Re_i=130, there was a particle-free region near the wall where no velocity information could be obtained. The resulting streamlines were plotted for Re_i=250 and Re_i=320. This aided in finding the vortex centre: for Re_i=250 this was at (x/D=1.022, r/R=0.89) and for Re_i=320 at (x/D=1.063, r/R=0.87).

The shear gradient is plotted in Figure 5.4 to Figure 5.6. The contour at the boundary has been removed, due to radial gradient discrepancy at the wall. The key observation is that the velocity gradient measured in the recirculation zone was less than $10s^{-1}$ which yields a WSS below 0.06Pa.

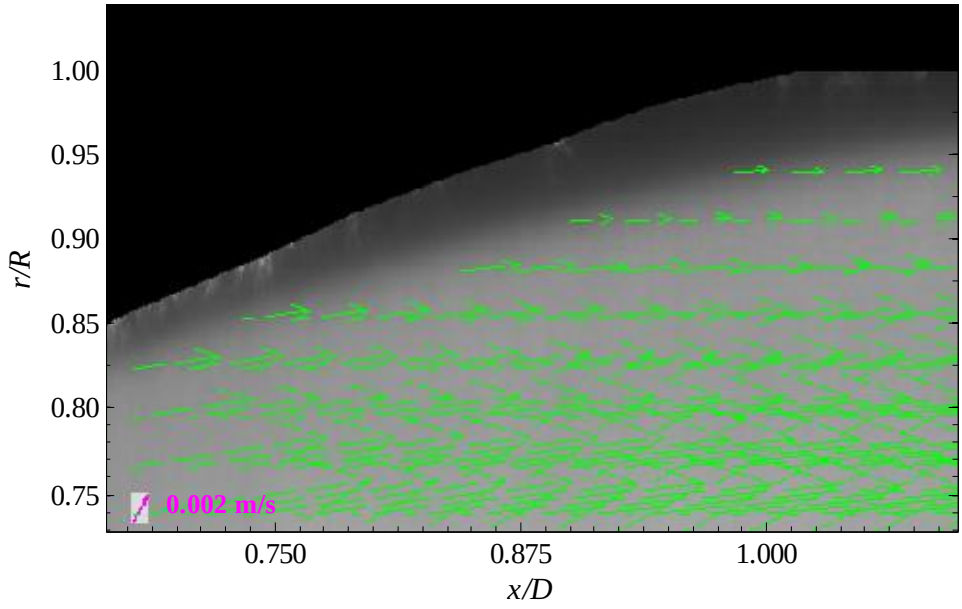

Figure 5.1 Velocity vector at Re_i=130

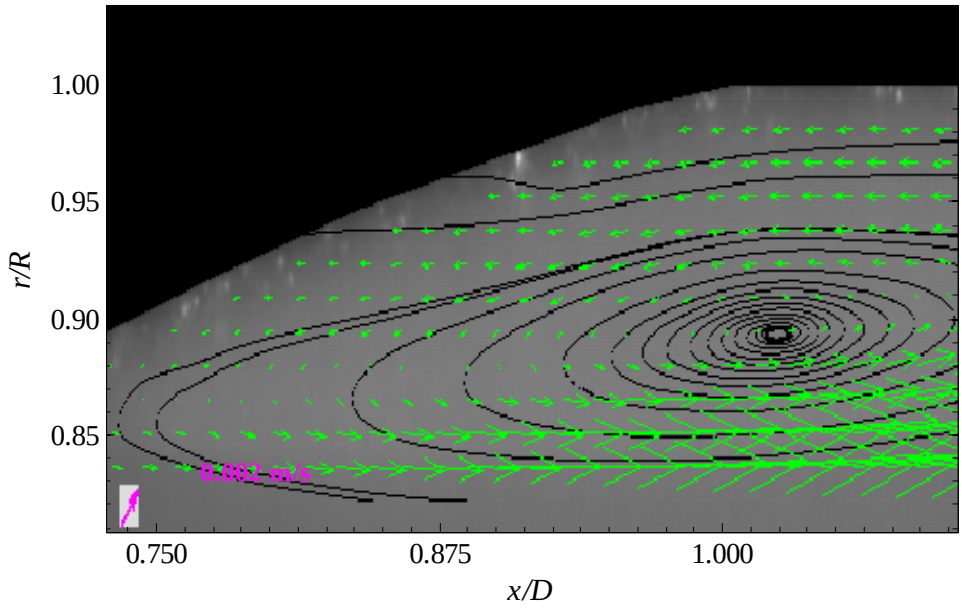

Figure 5.2 Velocity vector and streamlines at the corner of the post-stenotic region for Re_i=250

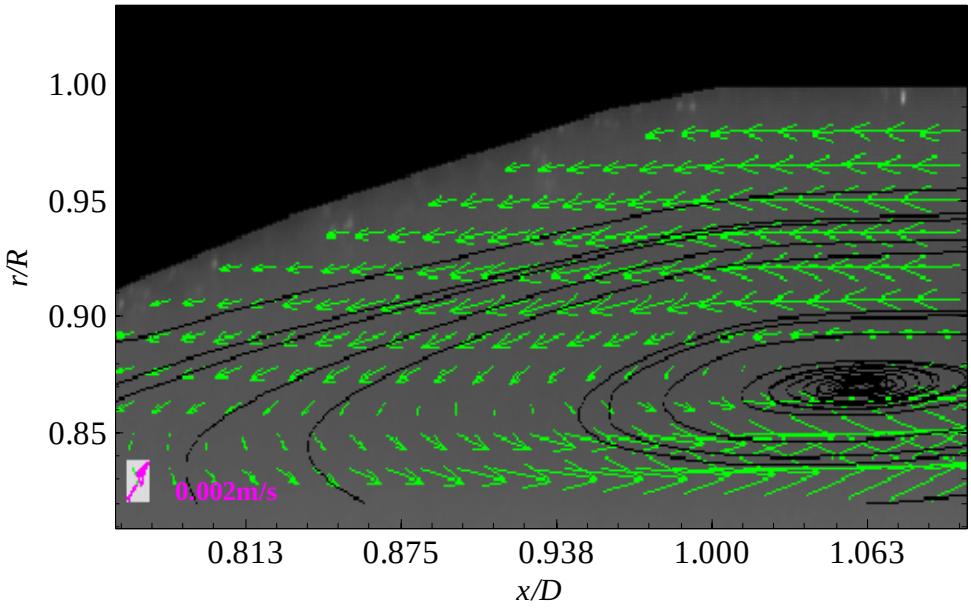

Figure 5.3 Velocity vector and streamlines at Re_i=320

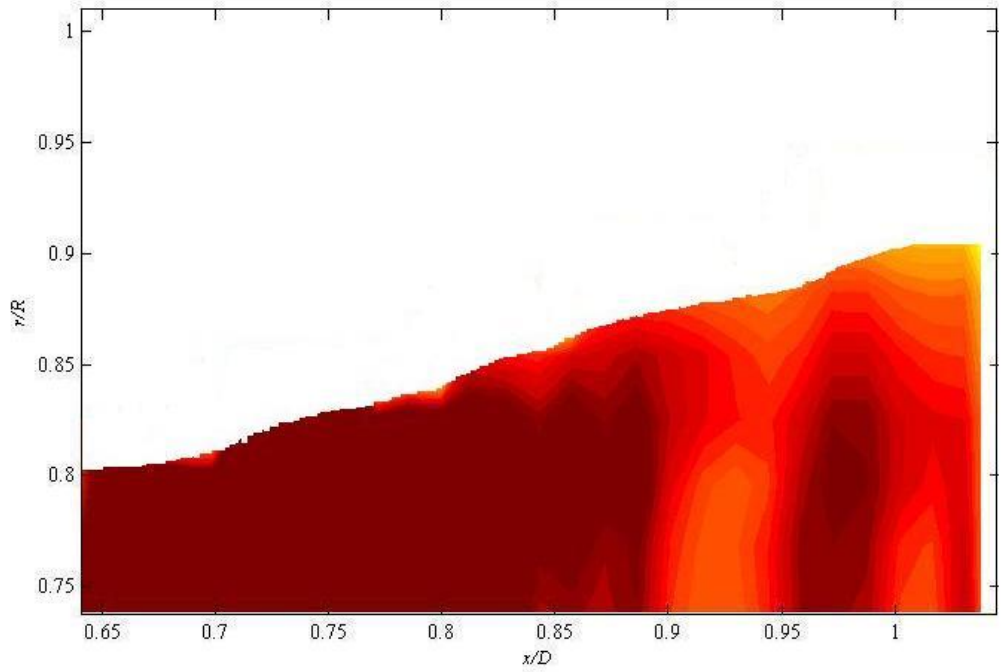

Figure 5.4 Velocity gradient at Re_i=130

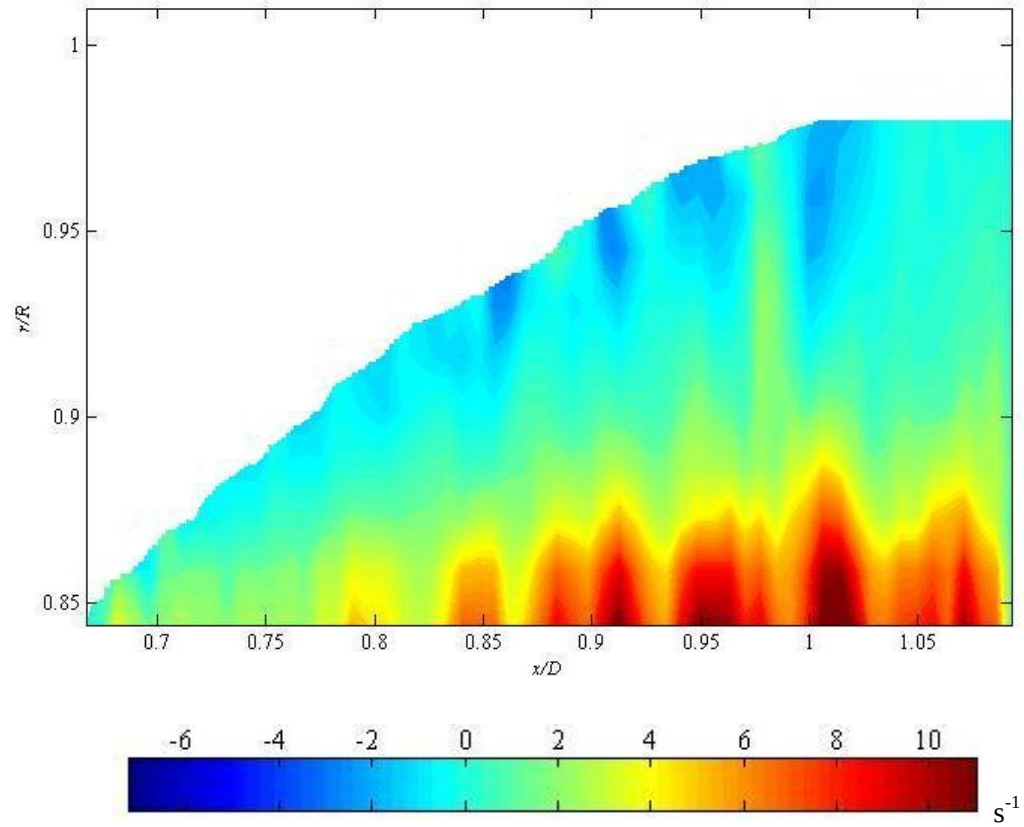

Figure 5.5 Velocity gradient at Re_i =250

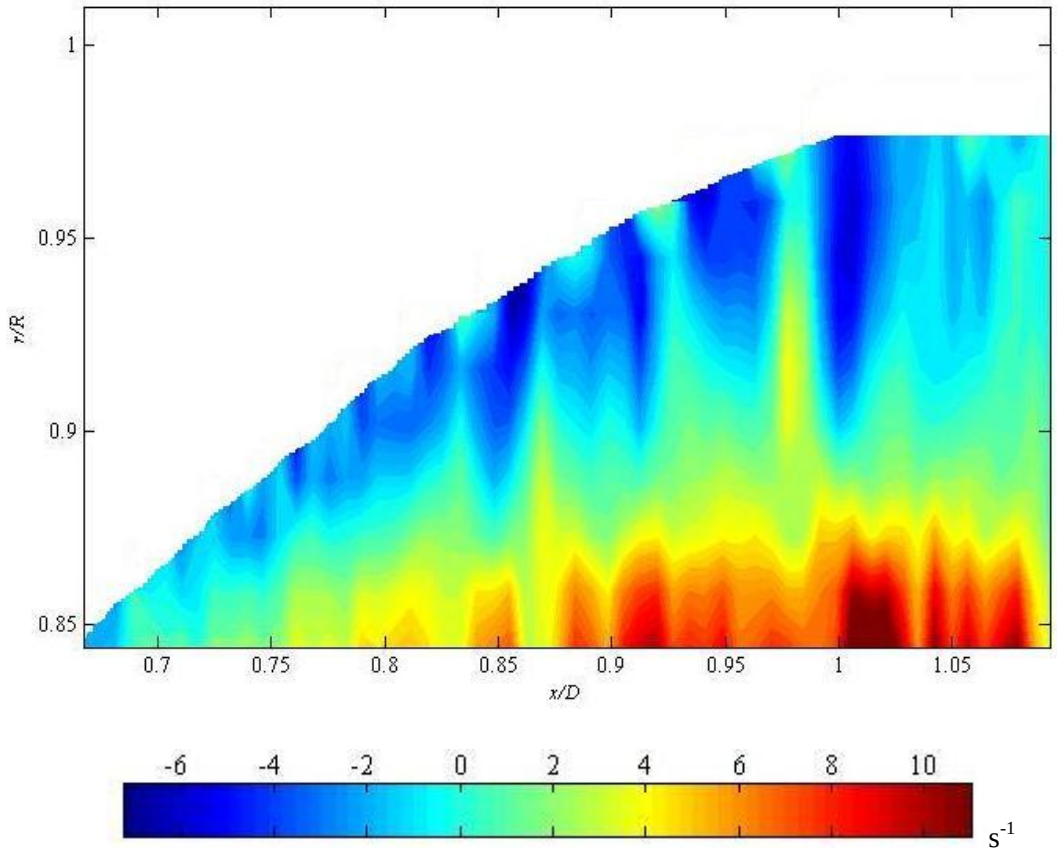

Figure 5.6 Velocity gradient at Re_i=320

5.3.2 **The influence of particle size on particle distribution**

Figure 5.7 compares the normalised light intensity *I'* of images for flows with different particle diameters. It shows the images for 10μm and 20μm particles at Re_i=250 with weight concentration ϕ_m=0.07%. The intensity is plotted on horizontal (*AB*) and vertical (*CD*) lines crossing the centre of the recirculation orbit beneath each image. The vortex centres for 10μm and 20μm seeding particles are at (*x/D*=1.022, *r/R*=0.89) and (*x/D*=1.024, *r/R*=0.89), respectively. For 10μm particles, the intensity along AB is almost constant at 1.1±0.01 from *x/D*=0.840 onwards, where no significant variation in distribution was observed. The intensity dropped below 1.0 when approaching the wall, indicating a lower particle concentration in this region. Along the vertical line *CD*, *I'* slightly increased before plateauing between *r/R*=0.87 to 0.90 and dropping to a value of less than 1.0 near the wall.

In contrast, for flow with 20μm diameter particles and the same concentration (Figure 5.7b), a clear inhomogeneous *I'* distribution in the recirculation orbit forming an elliptical shape is observed. *I'* peaks twice along the line *AB*, once at the centre and the other at an outer orbit (*x/D*=0.790). Similarly, two peaks exist along the line *CD* at the vortex centre and at *r/R*=0.985. In both cases, the magnitude of the peaks approaching the wall is less than at the central peak. At the vortex centre, the peak has an intensity value that was slightly greater than 3.0. Approaching the wall, *I'* reduces but is still greater than 1.0. Therefore, in flows with larger diameter particles the particles tended to migrate to the middle of the vortex and to form a stable equilibrium in the recirculation region: in flows with smaller particles they are almost homogeneously distributed.

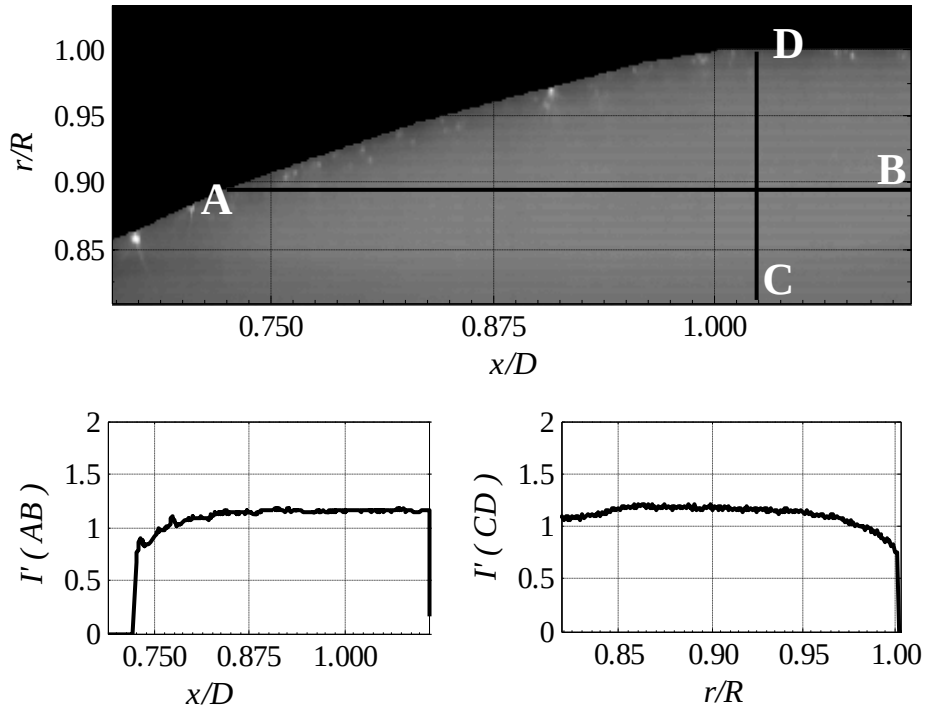

a.10μm

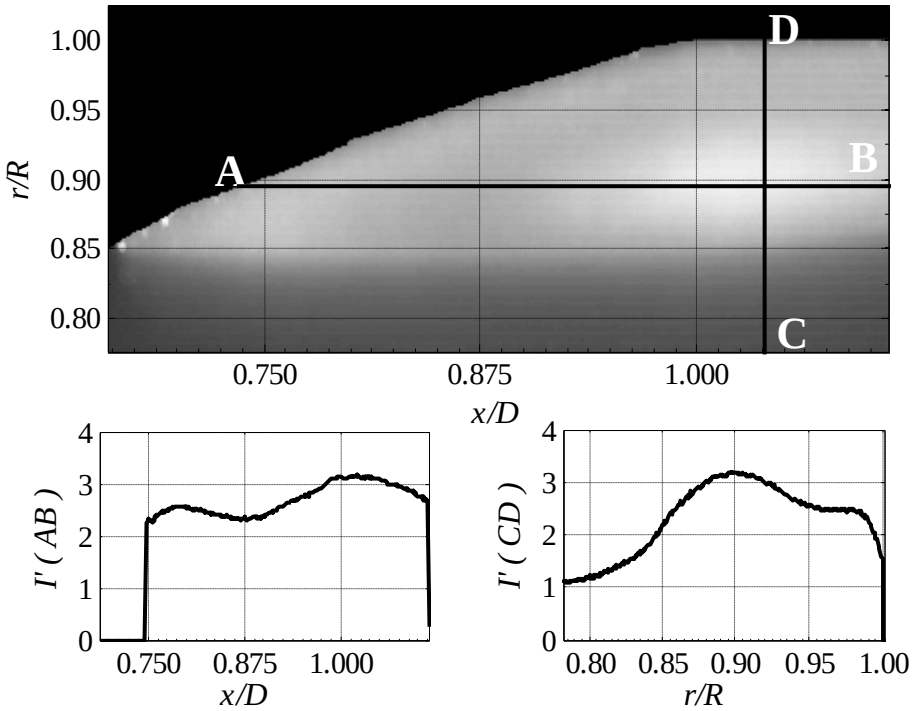

b. 20um

Figure 5.7 Normalised light intensity at Re_i=250 with particle concentration 0.07 weight % and particle size d_p: a. 10μm, b. 20μm

5.3.3 **Flow rate variation**

Figures 5.8 to 5.10 enable a comparison of the flow images at Re_i=130, 250 and 320, respectively, for the larger particle diameter of 20μm with ϕ_m=0.14%.

The intensity at Re_i=130 along AB at *x/R*=0.97 is below 0.4. The intensity along CD at *x/D*=1.000 drops steeply as it approaches the wall at *r/R*=0.93. The layer thickness measured from here corresponding to the sudden decrease in particle concentration was around 0.35mm (0.04*D*). The very low *I'*, in the range of background noise near the wall, suggests that a particle-free layer was established.

At Re_i=250 (Figure 5.9) and Re_i=320 (Figure 5.10), the variations in intensity in the form of elliptical orbits are more apparent. The vortex centres are at (*x/D*=1.013, *r/R*=0.91) and (*x/D*=1.041, *r/R*=0.88), respectively. For flow at Re_i=250 (Figure 5.9), the maximum in *I'* is in the vortex centre, indicating the highest concentration of particles. The position of the maximum concentration is (*x/D*=1.013, *r/R*=0.91), slightly different from the vortex centre measured from the PIV images for ϕ_m=0.07% (Figure 5.7b). Plots of the intensity along the lines AB and CD, as shown in Figure 5.9, clearly indicate that the highest particle concentration at the centre, surrounded by an annulus of normal concentration, and then a second annulus containing a high concentration of particles. Towards the wall, the intensity decreases monotonically to around 50% of the normalised value. The thickness of the particle-reduced layer from the second annulus to the wall is 0.17mm.

When the flow rate increases to Re_i=320 (Figure 5.10), two peaks remain, but there is a higher concentration at the annular position than in the centre and a smaller variation in intensity. The central maximum occurrs at (*x/D*=1.041, *r/R*=0.88), and the intensity plots are shown through this point. Again, near the wall, the intensity decrease indicates fewer particles. The particle-depleted layer thickness is 0.15mm for the reduction of *I'* from 1.0 to 0.5.

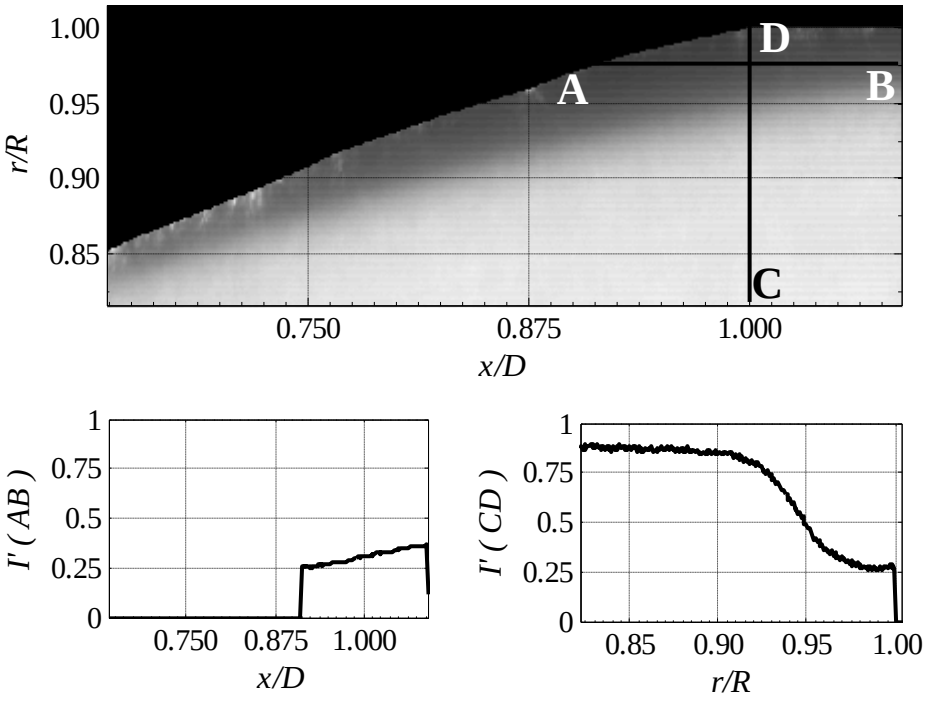

Figure 5.8 Normalised light intensities at Re_i=130 with ϕ_m =0.14 weight %

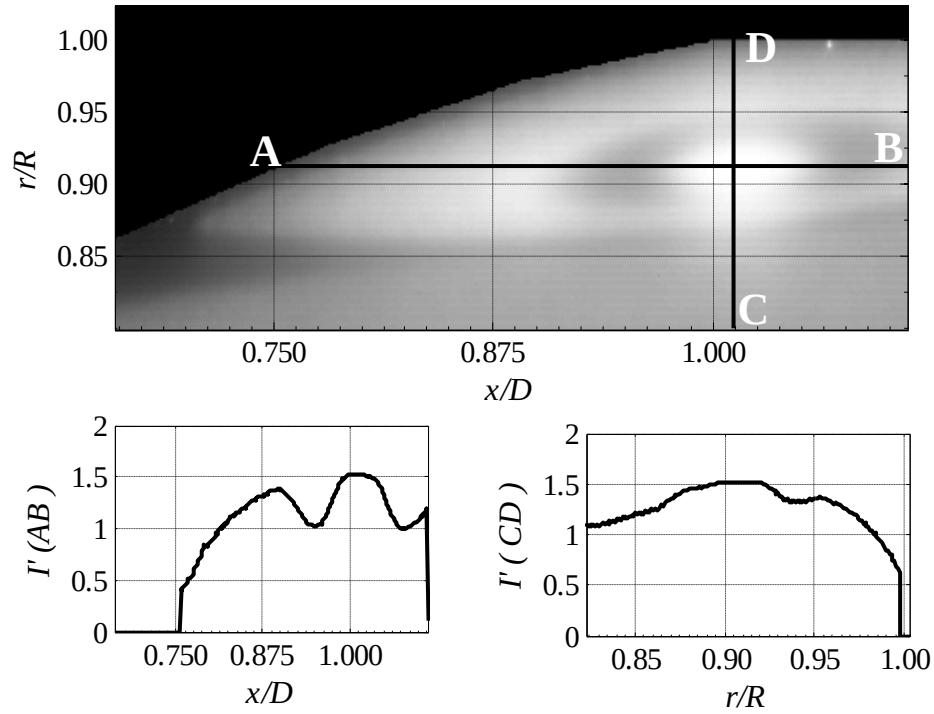

Figure 5.9 Normalised light intensities at Re_i =250 with ϕ_m=0.14 weight %

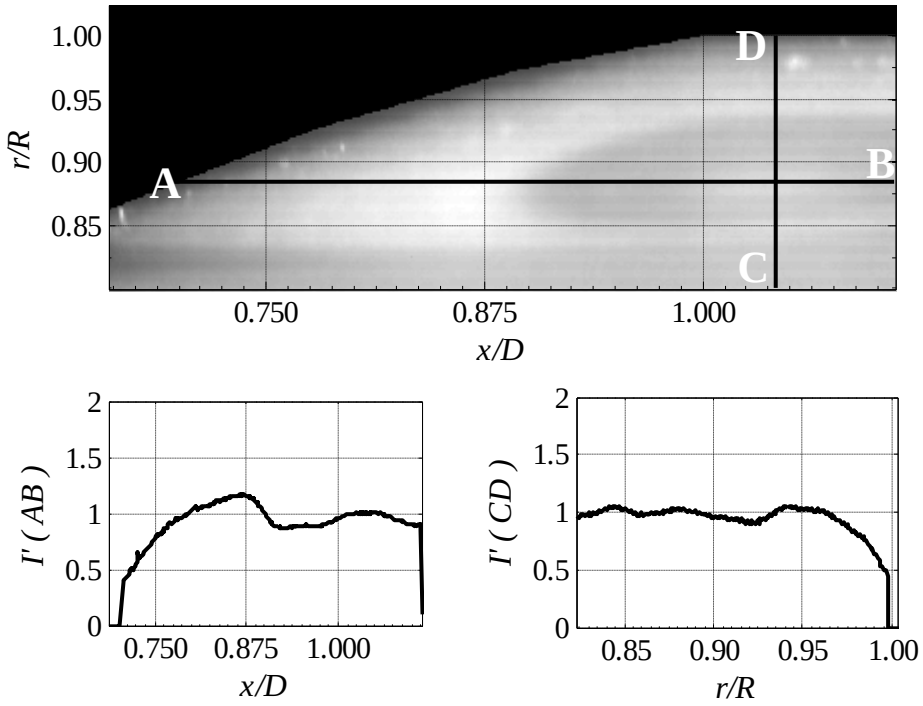

Figure 5.10 Normalised light intensities at Re_i =320 with ϕ_m=0.14 weight %

5.3.4 **The effect of particle loading on its distribution**

Figure 5.7b and Figure 5.9 enable a comparison of the effect of increasing ϕ_m from 0.07% to 0.14% for the same size of particle at the same flow rate. Both results were at Re_i=250, employing a 20μm particle diameter. In both cases, the particles accumulated at the vortex centre and had a high concentration in an elliptical orbit. However, at the higher particle concentration (Figure 5.9), the orbital peak was almost as great as at the central peak. For the weaker concentration, where ϕ_m=0.07%, the overall magnitude of the light intensity distribution was larger. The relative peak intensity in the vortex centre was double that of ϕ_m=0.14%, indicating more particles had migrated here.

5.3.5 **Vortex centre**

Table 5.1 shows the position of the vortex centre under the flow conditions studied.

Table 5.1 Vortex centre position, (x/D, r/R) at Re_i=250 and Re_i=320

Seeding properties	Vortex central position	
	Re_i=250	Re_i=320
d_p=10μm, ϕ_m=0.07%	x/D=1.022±0.007 r/R=0.89±0.007 (Figure 5.2)	x/D=1.063±0.007 r/R=0.87±0.007 (Figure 5.3)
d_p=20μm, ϕ_m=0.07%	x/D=1.024±0.200 r/R=0.89±0.05 (Figure 5.7)	No data
d_p=20μm, ϕ_m =0.14%	x/D=1.013±0.145 r/R=0.91±0.05 (Figure 5.9)	x/D=1.041±0.270 r/R=0.88±0.04 (Figure 5.10)

For seeding with d_p=10μm and ϕ_m=0.07%, the position was determined from the streamlines' plot, while the others were obtained from the light intensity results. When the flow rate increased from Re_i =250 and Re_i =320, the vortex moved slightly downstream. The position hardly changed as the particle diameter doubled and was within the measurement error. The variations of the vortex centre with particle concentration were well within the measurement error.

The particle distribution in the vortex is indicated by I'. For comparison of particle distribution in vortex centre and outer orbit, the I' at the centre and the maximum I' along line AB is summarised in Table 5.2.

Table 5.2 *I'* at vortex centre and maximum *I'* at the outer orbit along line AB for Re_i =250 and Re_i =320

Seeding properties	Re_i =250		Re_i =320	
	I' at vortex centre	*I'* at outer orbit	*I'* at vortex centre	*I'* at outer orbit
d_p=10μm, ϕ_m=0.07%	1.2 (Figure 5.7a)	1.2 (Figure 5.7a)	-	-
d_p=20μm, ϕ_m=0.07%	3.2 (Figure 5.7b)	2.5 (Figure 5.7b)	-	-
d_p=20μm, ϕ_m=0.14%	1.5 (Figure 5.9)	1.4 (Figure 5.9)	1.0 (Figure 5.10)	1.2 (Figure 5.10)

Particle distribution was uniform for d_p=10μm at ϕ_m=0.07% in the recirculation zone at Re_i=250. For larger particle having twice diameter, d_p=20μm at similar concentration, the particles accumulated 28% more in the vortex centre than the orbit. Upon increasing the particle concentration from 0.07% to 0.14% for d_p=20μm, the *I'* at the recirculation zone dropped by 47% at the centre and 56% at the outer orbit. At higher flow rates, Re_i=320 more particles leaved the vortex centre giving the *I'* 20% larger than the centre.

5.4 Discussion

Velocity gradient within the recirculation region in the range of $10s^{-1}$ resulted in a low WSS (<0.06Pa). Healthy WSS levels for arteries was reported to vary between 2 to 16 Pa (Cheng et al., 2007). Malek et al.(1999) found WSS as low as 0.4Pa triggers biological inflammatory process which leads to the development of atheromatous plaque. As discussed in Section 1.2.1, low WSS has been correlated with atherosclerosis due to low mass diffusion of lipids away from the wall.

In this experiment, the mean light intensity scattered by seeding particles was correlated to particle distribution. The light intensity was taken as proportional to the number of particles. The light intensity was normalised by the intensity at the inlet. It is important to note that the intensity at other points in the illuminated field may not be exactly the same as that at the inlet. When the velocity is varied, the intensity at the inlet may not consistent. With particles present in the reference window, the normalised intensity may have carried a small degree of error due to noise. These variation was assumed negligible when the flow is varied between Re_i = 130 to 350.

The distribution of particles in the separation zone of an ideal, symmetrical stenosis depends on the flow rate. At the lowest flow rate investigated (Re_i=130), a particle-depletion layer exists near the wall region and at the corner of the stenosis. The maximum thickness of this is 0.35mm. In microcirculation studies where the artery size was <100 μm, the presence of a particle-free layer of 3-4μm thickness adjacent to the wall was observed (Bitsch et al., 2003; Sugii et al., 2005). In larger arteries, this effect was assumed to be negligible due to the relative size of the particles and the artery's diameter (Caro, 1978). However, this study demonstrates the existence of a particle-depleted layer present in the recirculation region of a large stenosed artery model. The layer thickness is dependent on the flow rate, where at a lower velocity a particle-free or depleted layer is more likely to occur than particle accumulation. The cell free layer in an artery has physiological implications such that the layer may become a diffusion barrier for oxygen transport to the muscles tissues due to low oxygen solubility in plasma (Kim et al., 2009). As discussed in Section 1.2.1, NO is an important mediator in blood vessel dilation. The scavenging of NO by red cells during vessel diameter modulation was found affected by the presence of cell-free layer. Increasing the cell-free layer width would decrease the scavenging effect hence, the reduction of NO diffusivity to the smooth muscle cells will interrupt the vasodilatory activity (Azarov et al., 2005).

At higher flow rates, the particle distribution in recirculation orbits depends on particle size and concentration. At Re_i =250, it was found that the particles formed a stable equilibrium position at the vortex centre and in an outer orbit. When the flow rate was increased to Re_i=320, the particles in the centre depleted, leaving only one equilibrium position in the outer orbit. In both cases, particle distribution dropped to about 50% near the wall.

Karino and Goldsmith investigate the particle dynamics of the separation zone of a step expansion from 151μm to 504μm diameter at low Reynolds numbers (Karino and Goldsmith, 1977). From their observations, at Re_i < 10 blood cells and latex spheres with diameter < 20μm particles migrated spirally outwards of the vortex joining the core flow and after a certain time, the vortex was emptied, whereas larger aggregates remained in the central orbit. At 70< Re_i <110, they find that, regardless of their size, the particles all stayed in the vortex and circulated in the equilibrium orbits. Furthermore, upon increasing Re_i to 120, more particles stayed in the vortex . Although our dimensions and flow rate are beyond theirs, the particle size is in the same range. In addition, the earlier study's sudden expansion caused an immediate transition to separation at the corner of the inlet tube, at all but the very lowest Reynolds numbers, whereas the gradual expansion used here has a separation point which moved upstream as Re_i increased. At a steady state with 20μm and 10μm particle diameters, we observed a small, almost empty wall region at Re_i =130. The concentration of particles at both concentrations (0.07% and 0.14%) was less than 25% of those studied by Karino and Goldsmith (1977). For higher Reynolds numbers, the particles remained in the vortex region (Re_i=250 and Re_i=320).

We have observed that a stable equilibrium position is dependent on particle concentration. Higher loadings favoured stable equilibrium positions at the vortex centre and outer orbit but at lower particle concentrations the particle distribution was more spread out. Matas et al. (2004) measure particle concentration in a long tube, extending the work of Segre and Silberberg (1962). They find two concentration peaks, one at the so-called Segre-Silberberg radius and another closer to the axis of the flow. It is possible that the observations presented in our observation are due to the interaction of wall-effect and higher order gradients in the flow field. However, inter-particle interaction may play a major role where interaction within orbits may change the trajectories of neighbouring particles, leading to an increase in the stability of the regions of high concentration.

Jung and Hassanein (2008) perform a computational simulation of red and white blood cells flowing in a sudden expansion geometry and a human right coronary artery (RCA) model with volume concentrations of 45% and 0.5%, respectively using Eulerian mehod. The

diameters were 8.2μm for the red cells and 18μm for the white. There was a higher concentration of white cells in the vortex at the corner of the expansion region, while the composition of red cells was lower here. Similar behaviour was observed in the stenosis area of the RCA geometry. In this work, we observed a similar trend, as 20μm particles tended to accumulate in the vortex while 10μm particles were homogeneously distributed. This suggests that even for dilute concentrations, particles that are larger than red cells will occupy the vortex in the recirculation zone. Particle diameter may play an important role in the migration mechanism.

The particles with 20μm diameter at weight concentration of 0.07% migrated to the central recirculation vortex. The particles were having a diameter within the range of the size of white blood cells, the monocytes (Caro, 1978). The volume fraction of monocytes was 0.0643% or equivalent to 0.0688% by weight (Skalak and Chien, 1987) was close to concentration used in the experiment. Since the particles used having similar physical properties with monocytes, the results for particles distribution in Figure 5.7b can suggest the monocytes behaviour when flowing distal to stenosis.

The progression of atherosclerosis could be the result of the interaction between blood cells, low density lipoproteins and muscle cells in an artery. Fluid shear stress triggers an inflammatory response that causes white blood cells and platelets to adhere to the endothelium (Kamm, 2002). The smooth muscle proliferates and migrates to the inner layer in response to the cellular interaction of platelets and foam cells (Weissberg, 2000). Hence the mechanism triggering atherosclerosis plaque build-up might be enhanced where the concentration of blood cells is inhomogeneous while orbiting in the recirculation zone.

5.5 Conclusions

This study has shown that in the post-stenotic region, under flow conditions similar to those found in major arteries and for particle sizes relevant to white and red cells, particle inhomogeneity can exist, although the effect is dependent on *Re* and particle diameter. The presence of similar effects in the arterial system may be significant in plaque evolution. In selecting numerical simulation models to predict the development and progression of stenosis in arteries, two-phase properties must be considered where flow recirculation exists.

Chapter 6

SINGLE PHASE SIMULATION

Computational fluid dynamics (CFD) is a practical tool for investigating local haemodynamics. It can be used to simulate blood flow and vessel dynamics, test hypotheses under controlled conditions, and evaluate potential clinical treatments that have not yet been implemented. This chapter considers a computational approach to simulate the flow field measured in the experiments. The flow is treated as a single phase and therefore, the Navier-Stokes (NS) equations were solved by taking the blood as pure incompressible fluid. The simulation is performed at Re_i= 130, 250 and 320 similar to the experimental conditions. The velocity field, flow separation boundary and shear gradient simulated are compared.

6.1 Introduction

Generally, CFD method replaced the continuous flow domain with discrete domain using grid. The full un-simplified partial differential equations describing flow phenomena (equations of continuity, momentum and particle transport) in three dimensions cannot be solved analytically. Hence, a numerical solution is sought. In order to obtain a numerical solution, the discretisation method approximates the differential equations by a system of algebraic equations that can be solved using a computer.

In particle suspension, single-phase simulation provides macroscopic information about the bulk flow. It is assumed that the existence of particles has a negligible effect on the flow. However, the influence of velocity and shear environment on haemodynamics, vessel dynamics, geometry, rheologic and wall mechanical variables can be identified. The transport of blood-borne elements, such as red cells, white cells, lipoprotein and platelets, is primarily determined by the macroflow behaviour.

The level of detail in CFD allowed more sophisticated indicators of disturbed flow. The blood-flow field uses a single-phase approach to investigate several biomechanical variables, for instance predicting the wall shear stress (WSS). In artery intervention, CFD methods have been use to examine haemodynamic condition in surgical procedures. For example acute and long-term graft patency depends on the flow field, as thrombosis and intimal hyperplasia are associated with disturbed flow (Lemson et al., 2000; Lei et al., 2001). Numerical simulation is a valuable tool to study haemodynamic parameters that might trigger abnormal biological processes.

In this chapter, we discuss performing a single-phase modelling to simulate the flow field observed in the experimental study. Steady flow at Re_i= 130, 250 and 320 were simulated The flexibility in assessing the flow parameters in CFD enables more information to be gleaned from the macroscopic flow behaviour.

6.2 Simulation method

The simulations were carried out using FLUENT 6.3.26, a finite-volume method that uses an integral form of conservation equations. The solution domain was divided into a finite number of control volumes. A computational node was at the centroid of each control volume, at which the variables values were calculated.

6.2.1 **Mathematical models**

The Navier-Stokes equations govern single-phase blood flow. As discussed in Chapter 2, they are derived from the conservation laws of mass and momentum. The former is given as:

$$\frac{\partial \rho}{\partial t} + \nabla \cdot (\rho V) = 0 \tag{6.1}$$

where v is the velocity vector and ρ the density of the fluid. For an incompressible fluid like blood, where ρ is constant, the equation reduces to:

$$\nabla \cdot V = 0 \tag{6.2}$$

The law of momentum conservation equation in 3D for incompressible Newtonian fluid can be written as:

$$\rho\left(\frac{\partial u}{\partial t} + u\frac{\partial u}{\partial x} + v\frac{\partial u}{\partial y} + w\frac{\partial u}{\partial z}\right) = -\frac{\partial p}{\partial x} + \mu\nabla^2 u + S_x \tag{6.3}$$

$$\rho\left(\frac{\partial v}{\partial t} + u\frac{\partial v}{\partial x} + v\frac{\partial v}{\partial y} + w\frac{\partial v}{\partial z}\right) = -\frac{\partial p}{\partial y} + \mu\nabla^2 v + S_y \tag{6.4}$$

$$\rho\left(\frac{\partial w}{\partial t} + u\frac{\partial w}{\partial x} + v\frac{\partial w}{\partial y} + w\frac{\partial w}{\partial z}\right) = -\frac{\partial p}{\partial z} + \mu\nabla^2 w + S_z \tag{6.5}$$

where u,v,w are the respective velocity components, p the pressure and S the source terms of gravitational and other external body forces. Relating to Newton's second law of motion, the left-hand side is the inertial term balanced by the pressure gradient, convective viscous term, and other external forces. In the case of steady (time-independent) flow, the acceleration term vanishes; hence the momentum conservation can take the following form:

$$\rho(v \cdot \nabla v) = -\nabla p + \mu \nabla^2 v + S_v \tag{6.6}$$

6.2.2 **Solution domain**

For the control volume to achieve a numerical solution, the solution domain was divided into volume element meshes. As depicted in Figure 6.1, the volume elements consisted of a face, an edge and a node.

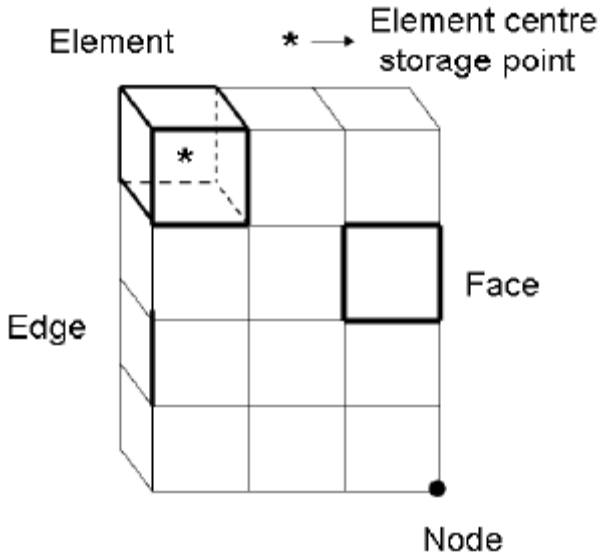

Figure 6.1 Volume elements

The flow domain used a three-dimensional (3D), axisymmetric model. The geometry of the stenosis artery model was constructed using Gambit 2.0.4 with hexahedral volume elements (Figure 6.2). The stenosis geometry was constructed in a similar manner to the experimental model. The stenosis was described by the cosine function: this is discussed in greater detail in Chapter 3. The inlet length was shorter to reduce the computing time. To enable this, a fully developed velocity profile calculated by Equation 6.7 was introduced to the inlet flow.

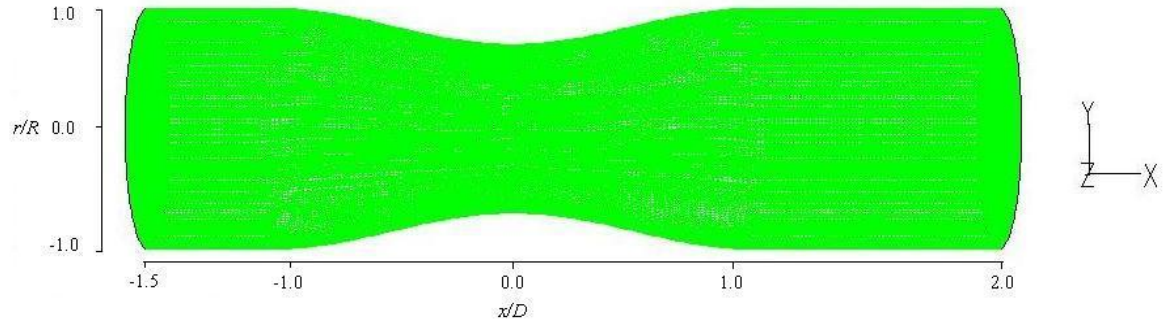

Figure 6.2 Geometry of the stenosed artery: flow from left to right

$$u = u_{max}(1 - r^2/R^2) \tag{6.7}$$

It is important to note that the plane measured in the experimental study was two-dimensional (2D). The previous results' discussion on the radial location of *r/R* was taken on the azimuthal plane, according to the position of the laser light sheet, illustrated in Figure 3.6a. Therefore, the equivalent radial location, *r* in 2D geometry, was the *z* coordinate in the 3D view. In the subsequent section in this chapter, *r* will correspond to the location of *z*.

6.2.3 **Discretisation**

The transport equation was integrated in a control volume, yielding a discrete equation. The integral governing equations were solved for each volume element. The integral forms of steady state continuity and the momentum conservation equation over an element's surface area can be written as:

$$\oint \rho V \cdot dA = 0 \tag{6.8}$$

$$\oint \rho VV \cdot dA = \oint pI \cdot dA + \oint \mu \cdot \nabla V \cdot dA + \int_V S_v dVo \tag{6.9}$$

where V is the velocity vector, Vo is the element volume, A is the surface area vector, I is the identity matrix, and S_v is the source of V per unit volume – i.e, gravity per unit volume, ρg.

The variables stored at the elements' centres were used to calculate the variable values at the elements' nodes. The variables' values at the surface were interpolated from the nodes' values. The discretisation of the spatial component for the continuity and momentum conservation equations are represented in the following equations, respectively:

$$\sum_{f}^{N_{faces}} \rho_f V_f \cdot A_f = 0 \tag{6.10}$$

$$\sum_{f}^{N_{faces}} \rho_f V_f \cdot A_f = \sum_{f}^{N_{faces}} pI \cdot A_f + \sum_{f}^{N_{faces}} \mu \cdot \nabla V_n \cdot A_f + S_v Vo \tag{6.11}$$

where the subscript *f* refers to the face of the volume element.

A second-order upwind scheme was used, where the discretised equation for any flow property θ can be written as:

$$\theta_f = \theta_{centre} + \nabla \theta_{centre} \cdot \Delta s \tag{6.12}$$

Where, $\nabla \theta_{centre}$is the gradient between the volume element centre and the immediate element upstream, and Δs is the displacement vector between the respective elements.

6.2.4 **A pressure-velocity solution**

In the governing equations, the pressure term and the velocity are interrelated, whereas the continuity and momentum equation are solved sequentially. During this process, the continuity equation is used to introduce the pressure, but the pressure term does not appear explicitly in the equation. Therefore, an algorithm for pressure-velocity coupling was employed, using the relationship between velocity and pressure correction to enforce momentum conservation and to obtain the pressure field. The iteration between both fields is required until the NS equation is satisfied: therefore, the Semi-Implicit Method for Pressure-Linked Equations Consistent (SIMPLEC) algorithm, which is suitable for laminar flow, was deployed. A more detailed explanation of this algorithm can be found in (Patankar, 1980).

6.2.5 **Material parameters and boundary conditions**

The material parameters from the experimental model in Section 3.3 were set-up. The properties of the fluid simulated were the properties of blood analog fluid where the fluid density measured was 1080kg/m^3 and the measured viscosity 6.23mPas.

The boundary conditions were set to match the fluid's properties in the experimental model. A velocity for the inlet boundary condition used the Poiseuille (parabolic) flow profile as in Equation 6.7.

PIV measured the centreline velocity, u_{max}. The maximum velocities from the experimental study were 0.19m/s, 0.36m/s and 0.46m/s for Re_i=130, 250 and 320, respectively. The inlet velocity profiles were introduced at the inlet of the flow domains, as user-defined function was written in C language. The walls were treated as rigid, no-slip and no-penetration boundary conditions were applied.

6.2.6 **Mesh-independence study**

The number of volume elements in the flow domain geometry determines the accuracy of the simulation. However, the smaller the mesh elements the more computational effort is involved. Therefore, there had to be a balance between the size of the volume element and the computational cost, in order to yield accurate results. To resolve the number of elements required, different mesh densities were tested to ensure the flow solution was grid-independent. The number of volume elements of the stenosis geometry created were n_1=829980, n_2=1467060 and n_3=2129160. The solution criterion was the reattachment point, which indicates the length of flow separation distal to stenosis. The reattachment point was the position at the wall where the axial velocity gradient was zero. The position yielded by each mesh was analysed to determine grid independence.

Figure 6.3 presents the shear gradient at the wall boundary for mesh densities of n_1, n_2 and n_3, from x/D=1.5 to 1.6. The negative shear gradient indicates backflow velocity and moved towards zero values. The reattachment point was where the velocity gradient at the wall was zero. Above this point, the velocity direction followed the mainstream velocity and had positive values. Figure 6.4 tabulates the mesh size and the reattachment position. The values were rounded to three decimal places with an uncertainty of 0.001: n_2 and n_3 that resulted in an asymptotic value of reattachment point at x/D=1.357. The uncertainty of 0.001 corresponds to a distance of $1x10^{-6}$m, which in the range of the smallest cell distance at the wall boundary of the recirculation region ($3.2x10^{-6}$m).

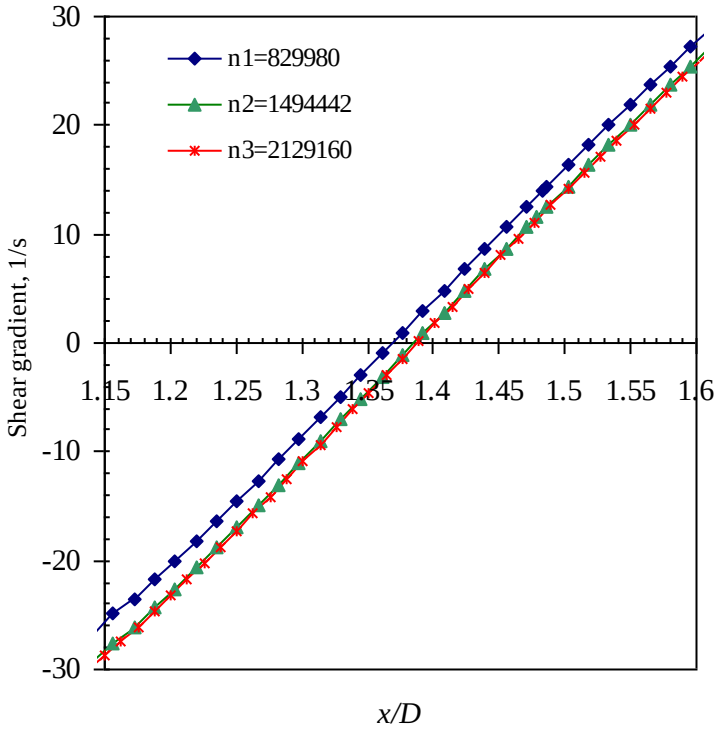

Figure 6.3 Shear gradient along the wall downstream of the stenosis for different mesh densities

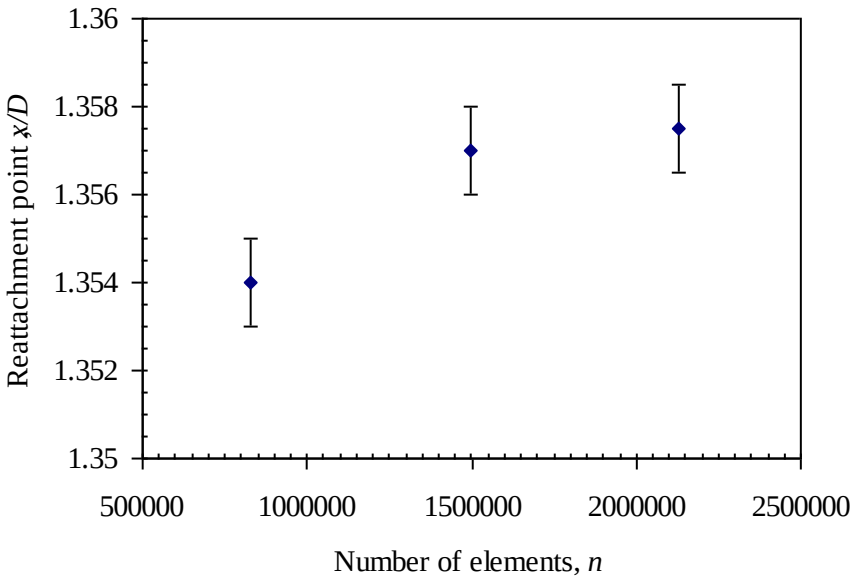

Figure 6.4 The reattachment point at different mesh elements.

A more stringent test is performed using Richardson extrapolation (Richardson and Gaunt, 1927) where the reattachment value is estimated at the grid size tended to zero ($1/n \rightarrow 0$). The extrapolation method calculate a higher order estimate of the flow fields from a series of lower discrete reattachment values (f_1, f_2,…,f_n). Roache(1994) generalised Richardson extrapolation by introducing the p^{th}- order method;

$$f_{exact} \approx f_1 + [(f_1 - f_2)/(r^p - 1)] \tag{6.13}$$

In this study, the grid refinement ratio, r is taken as the average of n_2/n_1 and n_3/n_2 which gave $r = 1.609$. The p^{th}- order of accuracy can be estimated by using the following equation;

$$p' = \frac{ln(\varepsilon_{32}/\varepsilon_{21})}{ln\, r} \tag{6.14}$$

$$\varepsilon_{i+1,i} = f_{i+1} - f \tag{6.15}$$

The resulted extrapolation from Richardson method, n_r is plotted in Figure 6.5.

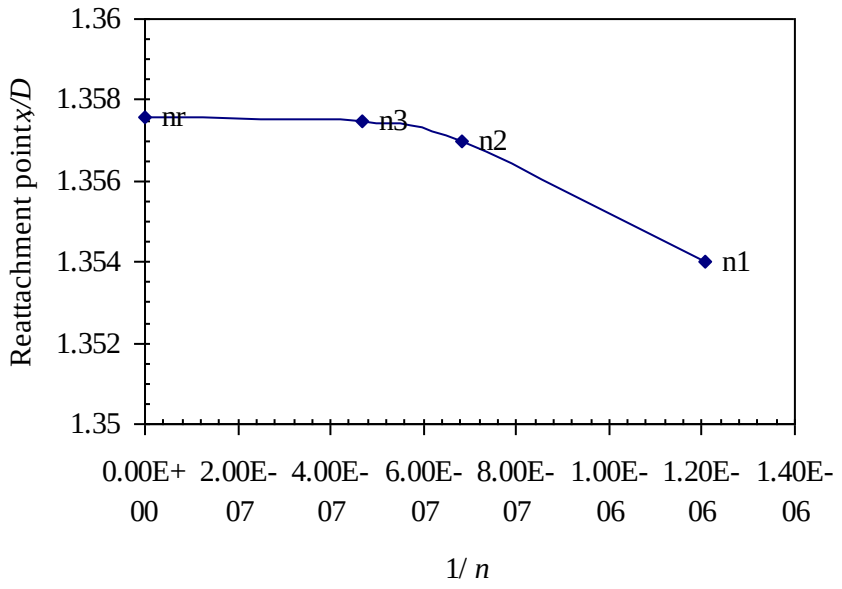

Figure 6.5 Richardson extrapolation for n_3, n_2 and n_1.

To evaluate the extrapolated value from these solutions, the convergence conditions must be first determined. The three possible convergence conditions are; 1. Monotonic convergence; $0<R'<1$, 2. Oscillatory convergence; $R'<0$ and 3. Divergence; $R'>1$, where

$$R' = \frac{\varepsilon_{21}}{\varepsilon_{32}} \tag{6.16}$$

Table 6.1 summarise the accuracy for reattachment point. The convergence ratio *R'* indicate convergence condition was monotonic.

Table 6.1 Order of accuracy for reattachment point

ε_{32}	ε_{21}	p	R
0.003	0.0005	3.77	0.167

Mesh with grid density n_2=1 467 060 was selected for further simulation. The main reason for selection is computing time, costs and acceptable accuracy achieved from the Richardson extrapolation. The simulation time for n_2 was five days.

6.2.7 **Simulation**

Although the flow under investigation was steady, there may be some degree of instability in the stenosis. Therefore, it was useful to set the flow condition under unsteady-state mode. The simulation was carried out on the School of Engineering's computing server. The convective time scale which defines as the time required to be convected through a small distance was calculated. The minimum length in *x*-direction of the mesh element is divided with the maximum axial velocity yield $3.3\text{x}10^{-3}$s, hence, the time step size Δt set was at $1\text{x}10^{-3}$ s. Convergence criterion for continuity equation was set at $1\text{x}10^{-9}$, and for momentum equation; criteria for *x, y, z* velocities were set at $1\text{x}10^{-6}$, $1\text{x}10^{-9}$ and $1\text{x}10^{-9}$ respectively. The number of timesteps was set at 250. Maximum time step per iteration was 200. The convergence time depended on the mesh density and ranged between two to seven days. The residual plot at the end of the simulation time of the flow domain for transient simulation with mesh element of n_2 is shown in Figure 6.6. The solutions for 250 timesteps were converged to residuals of less than 10^{-8}.

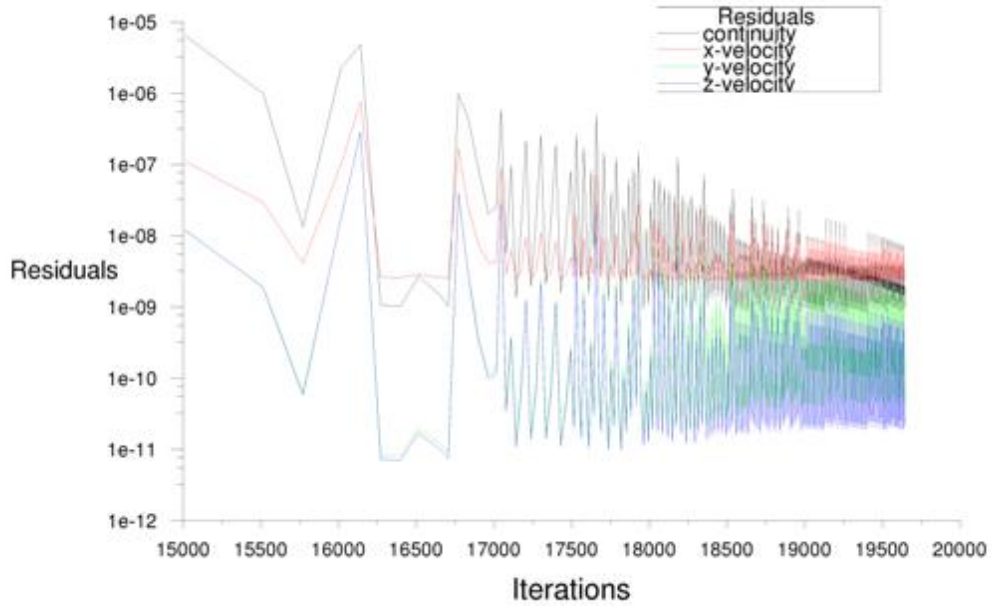

Figure 6.6 Residuals at the end of simulation time of 250 timesteps.

6.3 Results

6.3.1 **Comparison of flow simulation at different flow rates**

The flow field description comparing the flow rates at Re_i=130, Re_i=250 and Re_i=320 was assessed by considering the velocity magnitude, vorticity contours and axial velocity gradients.

The velocity magnitude was compared in Figure 6.7. The maximum velocity in all cases was slightly downstream of the throat of the stenosis at x/D=0.18. The peak velocity at the throat region at all flow rates were generally 40% higher than the centreline velocity at the inlet. The results was verified from conservation of mass principles which conclude that for 30% degree of stenosis, Re_{throat}=1.4Re_i.

Figure 6.8 presents the contours of the vorticity magnitude. Vorticity measures a fluid's tendency to spin: if the vorticity is non-zero, the flow is rotational. There was a vorticity of varying strength in the flow of interest. The peak vorticity was in the constriction region of the throat and increases with the flow rates.

The axial velocity gradient (du/dz) is shown in Figure 6.9. Negative values indicate the opposite velocity direction below the radial axis. The vorticity and velocity gradient contours

had a similar behaviour where the maximum was slightly upsteam of the throat. The velocity gradient and vorticity region distal to stenosis were between the recirculation zone and the central jet. The maximum vorticity and velocity gradients are compared in Figure 6.10, showing both magnitudes increased linearly with Re_i. The rotation of fluid element was caused by the shear gradient formed downstream of the stenosis.

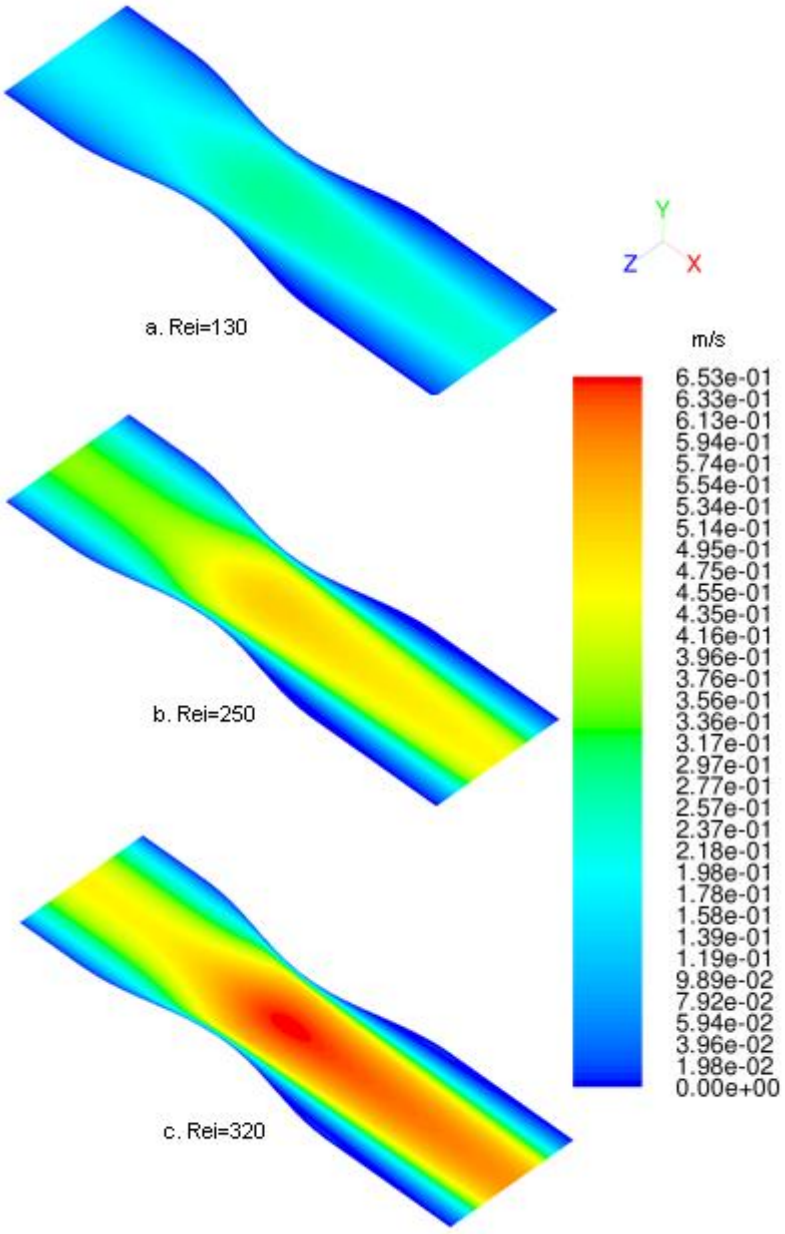

Figure 6.7 Velocity magnitude.

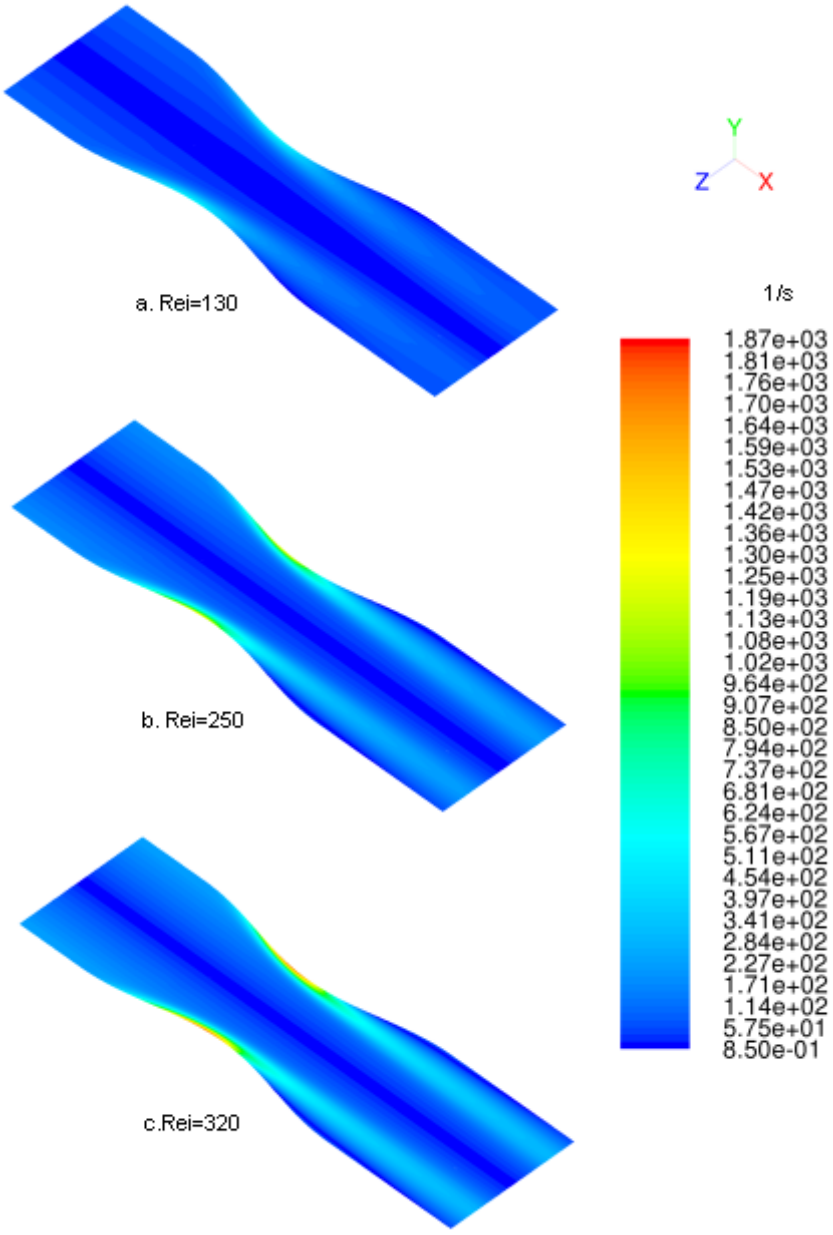

Figure 6.8 Vorticity contour.

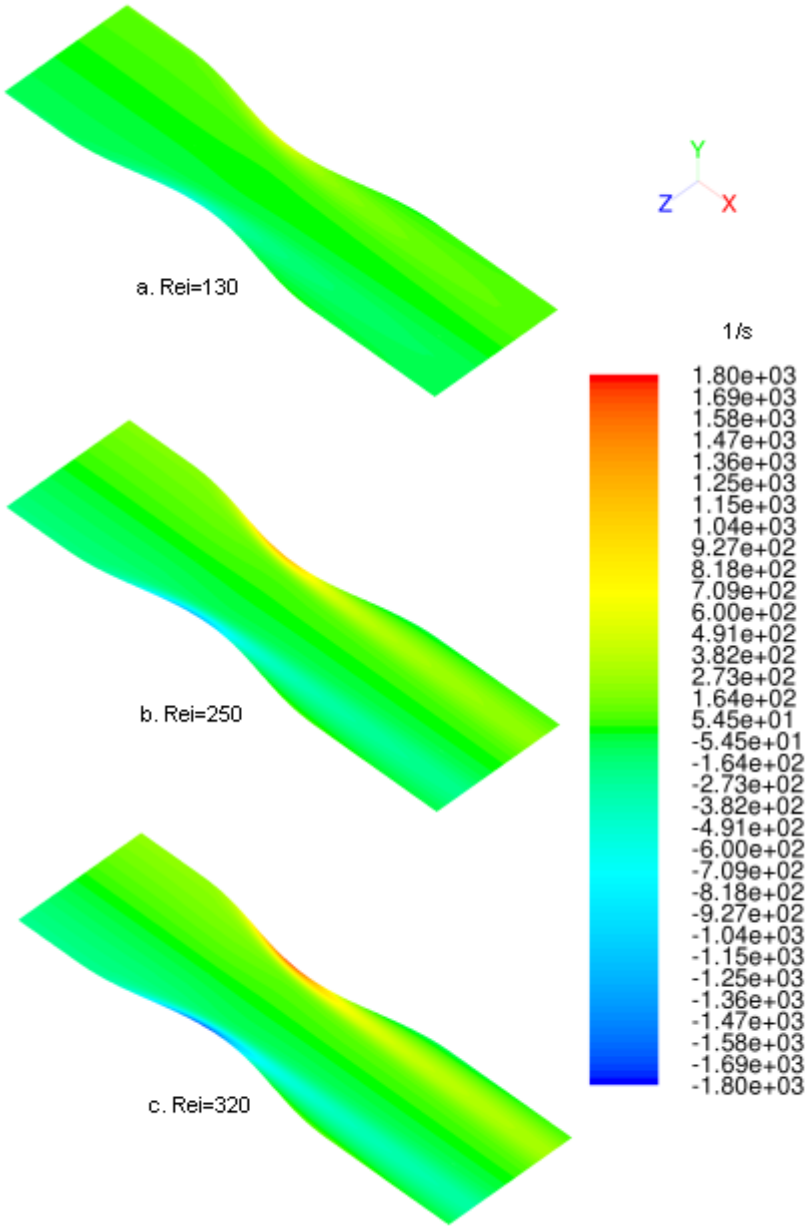

Figure 6.9 Radial velocity gradient.

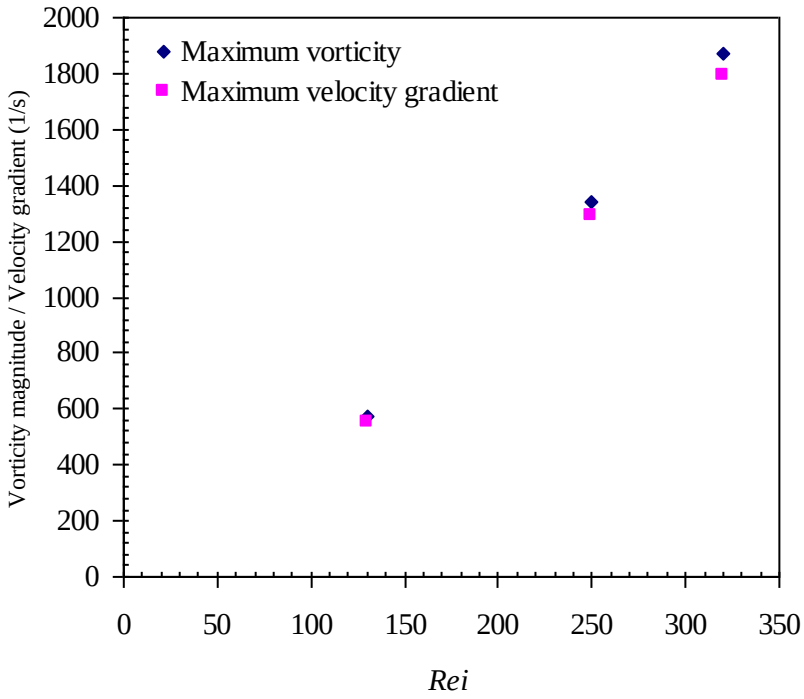

Figure 6.10 Maximum vorticity and velocity gradient against bulk Reynolds number.

The vorticity information from PIV measurement was limited to 2-dimensional measurement. Therefore the interpretation of vorticity components can be assessed further from the simulated results. The 3-dimensional representation of simulated vorticity magnitude at Re_i=250 is shown in Figure 6.11. As observed in previous section, the vorticity behaviour at the inlet was the Hagen-Poiseuille vorticity: maximum at the wall and approaching zero towards the centre radius. The simulated results clearly show that the vorticity at the wall grew as the flow entered the stenosis zone, and was maximum at slightly before the middle throat. Distal to stenosis, the vorticity was relatively high between the recirculation area and the core flow. As indicated earlier, the vorticity close to the wall was lower than at the inlet.

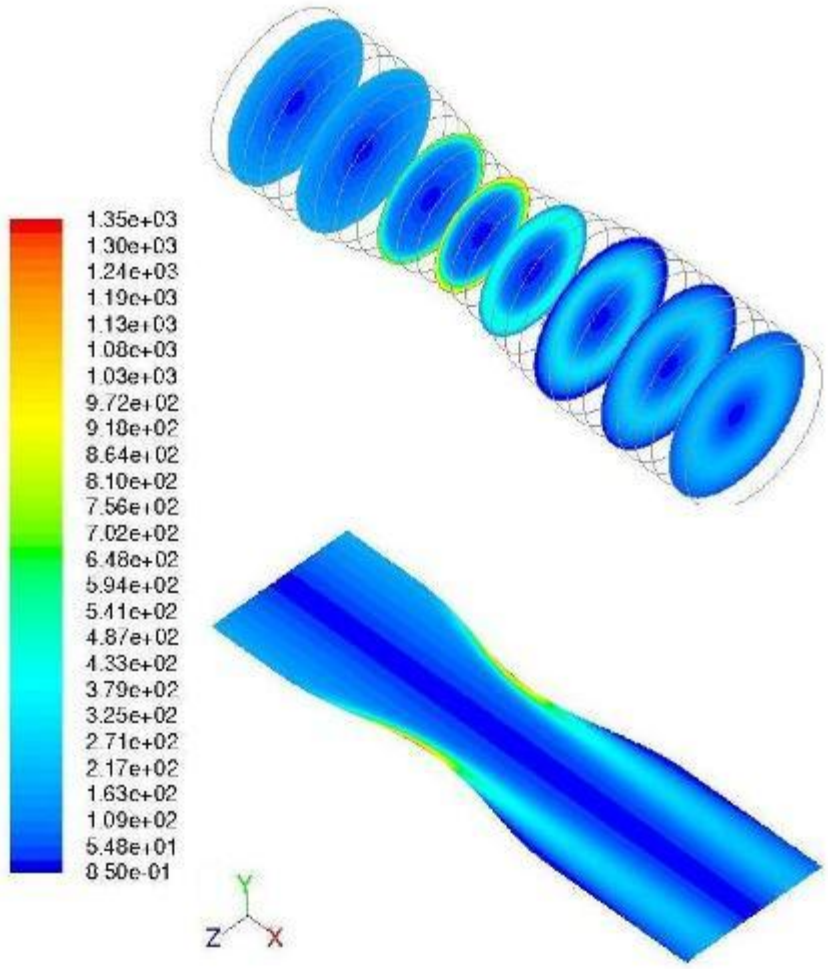

Figure 6.11 The contour of simulated vorticity magnitude (1/s) in *y-z* plane and *x-z* plane views (bottom). For the *y-z* plane, the *x/D* locations from the inlet are -1.375, -0.875, -0.375, 0, 0.375, 0.875, 1.375 and 1.875.

The vorticity component for *x*, *y* and *z* is described as $\Omega_x = \frac{\partial w}{\partial y} - \frac{\partial v}{\partial z}$, $\Omega_y = \frac{\partial u}{\partial z} - \frac{\partial w}{\partial x}$ and $\Omega_z = \frac{\partial v}{\partial x} - \frac{\partial u}{\partial y}$. The vorticity components at *x/D*=1 is shown in Figure 6.12. The peak vorticity was mainly depended on the *y* and *z* vorticity component. The streamwise vorticity was small and this explains that the fluctuation in the axial direction was not significant.

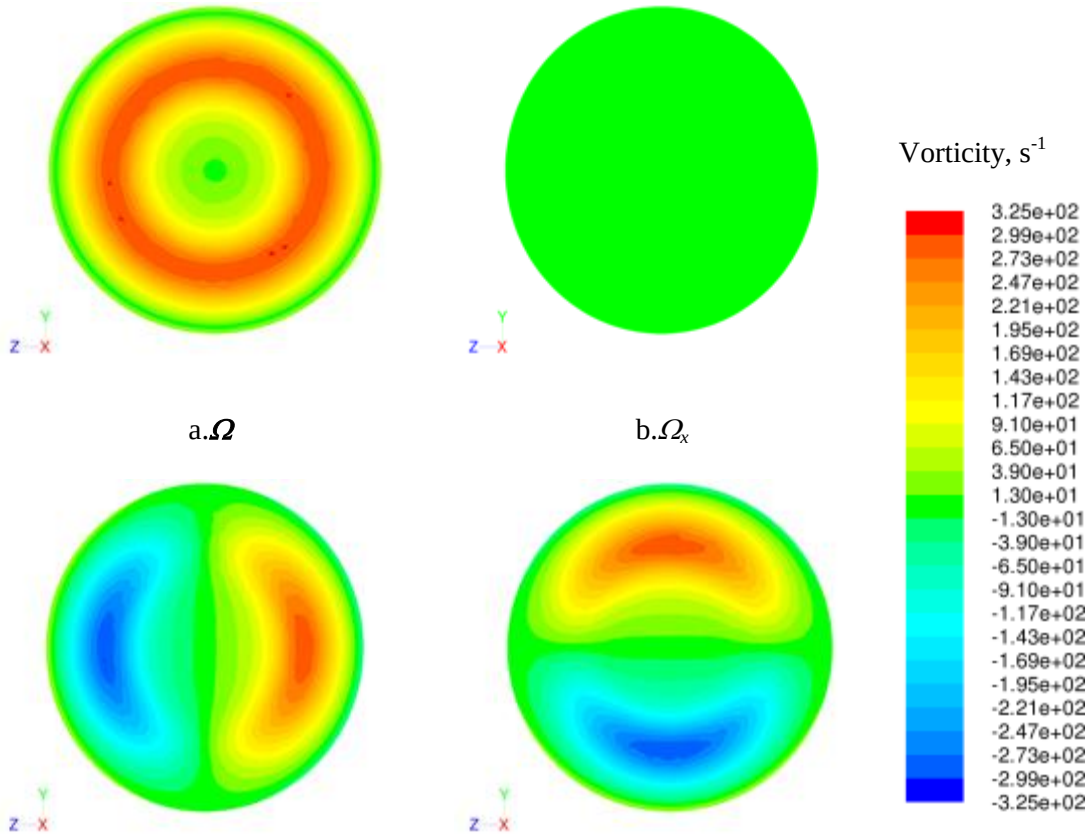

a.Ω b.Ω_x

c.Ω_y d.Ω_z

Figure 6.12 The simulated vorticity magnitude and the components at *x/D*=1

6.3.2 **Wall shear stress and flow separation boundary**

Wall shear stress (WSS) is a key haemodynamic parameter and a linear function of shear gradient. Figure 6.13 presents its contours showing that the peak stress increases with the flow rates. The WSS was high upon entering the stenosis throat: for example at Re_i=250 a maximum of 9Pa, compared to the inlet which was 1.5Pa. The axial location of the highest stress was x/D= -0.1625. From this position, the stress on the wall gradually decreased until it reached a minimum value where the flow separated. The low WSS region for Re_i=250 is illustrated on a smaller scale in Figure 6.14. The region experienced stress of less than 1Pa, from x/D =0.3243 to x/D=2. The WSS decreased from the throat and reached zero at x/D=0.5047, where the flow was first separated. In the recirculation region, the stress increased beyond the detachment point and returned to zero at x/D= 1.3570. At this location, the flow attached to the mainstream.

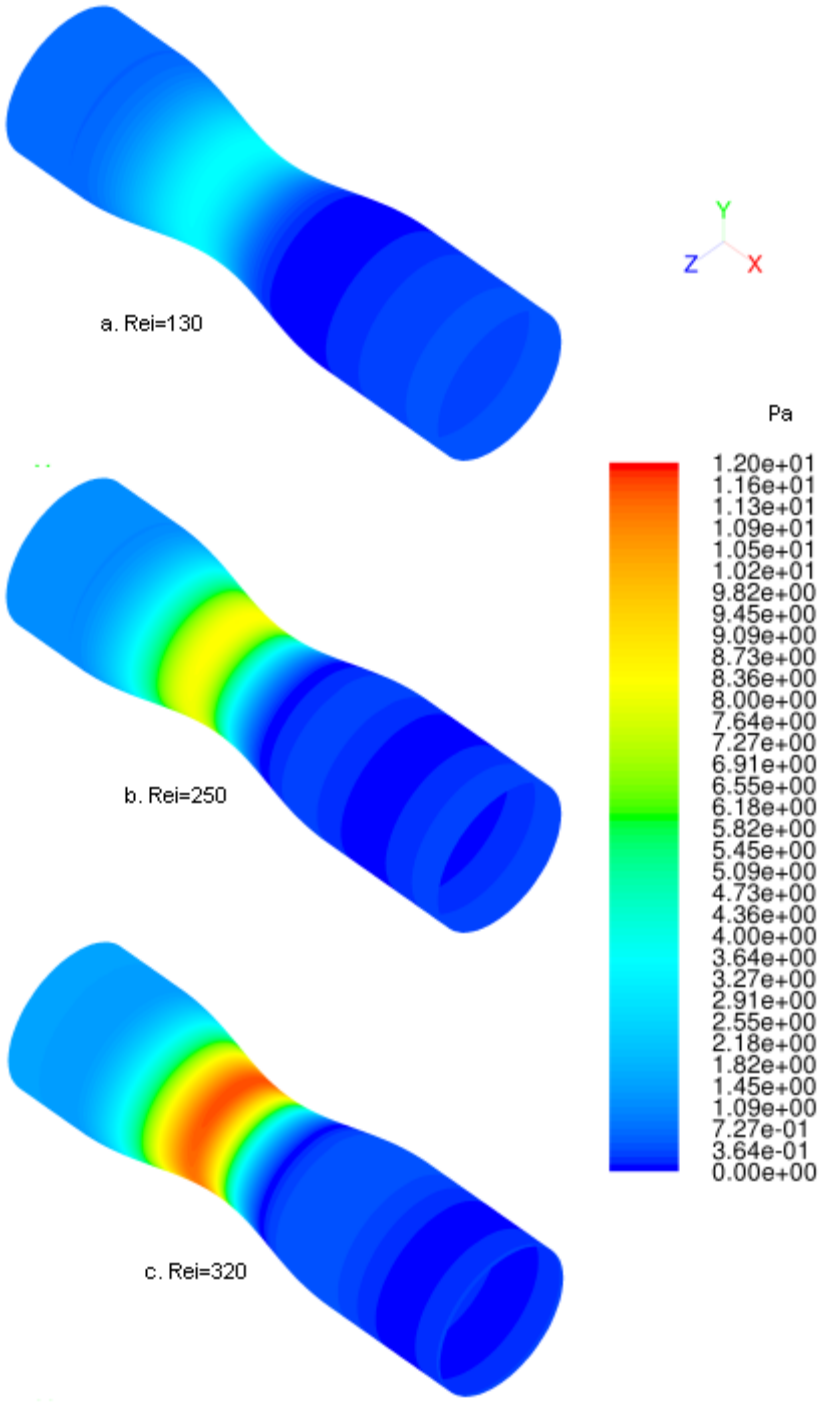

Figure 6.13 WSS

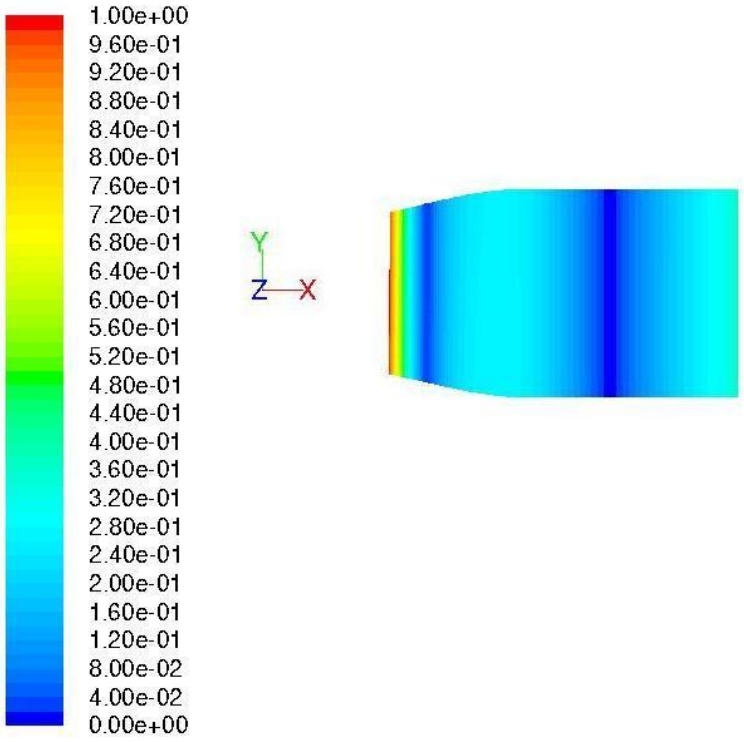

Figure 6.14 Low WSS (Pa) region at Re_i=250 at the downstream of stenosis observed at the wall. The WSS was less than 1Pa.

The variation of the WSS at the flow separation region is compared in Figure 6.15 where the WSS is plotted along the axial direction. The detachment point of the flow separation for Re_i=250 and 320 is marked by the location where the WSS first reaches minimum. The detachment points are x/D=0.5047 and x/D=0.47075, respectively. The reattachment point is where the second minimum WSS read x/D=1.3570 and x/D=1.6258, respectively.

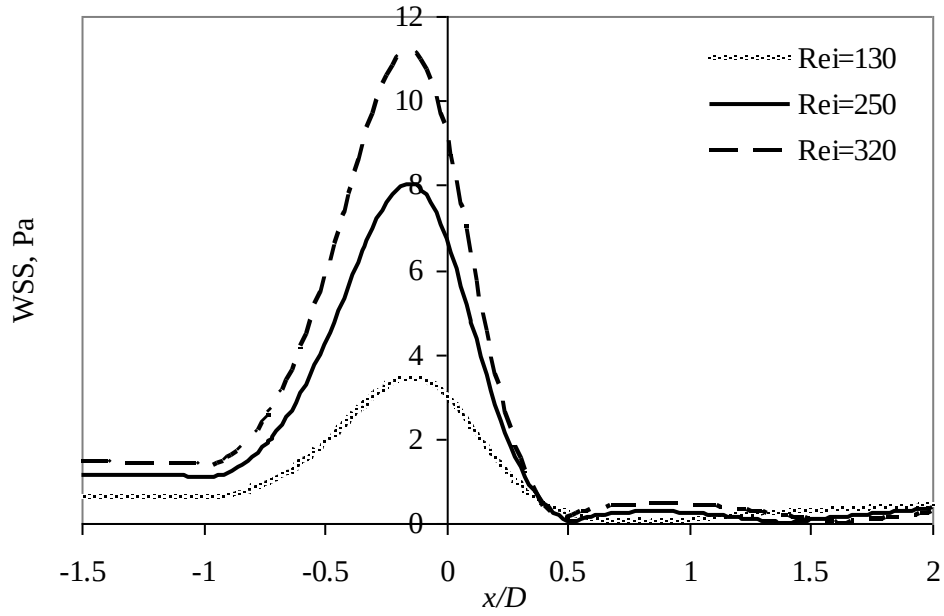

a. WSS

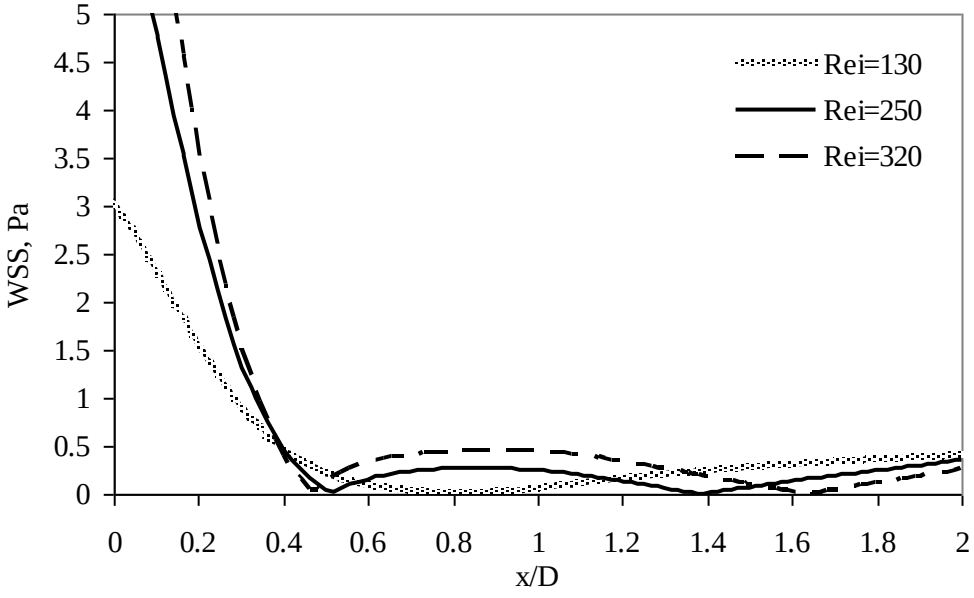

b. WSS from the middle of the throat ($x/D = 0$) to the outlet. WSS first reaches minimum at the detachment point and secondly, at the reattachment point.

Figure 6.15 Comparison of WSS along the axial location.

The flow separation boundary for all Re_i can be seen from the velocity field distal to the stenosis presented in Figure 6.16. Unlike the flows at Re_i=250 and 320, the recirculation flow does not exist in the flow at Re_i=130. Backflow velocity, indicating the recirculation region, was observed at the downstream corner of the stenosis for Re_i=250 and 320. The streamlines in Figure 6.17 demonstrate that the flow separation zone at Re_i=320 is larger than at Re_i=250. The coordinates of the middle vortex, G at Re_i=250 and 320 are (x/D=0.9187, r/R=0.9075) and (x/D=0.9476, r/R=0.8900), respectively. The detachment and reattachment point is indicated as E and F, respectively.

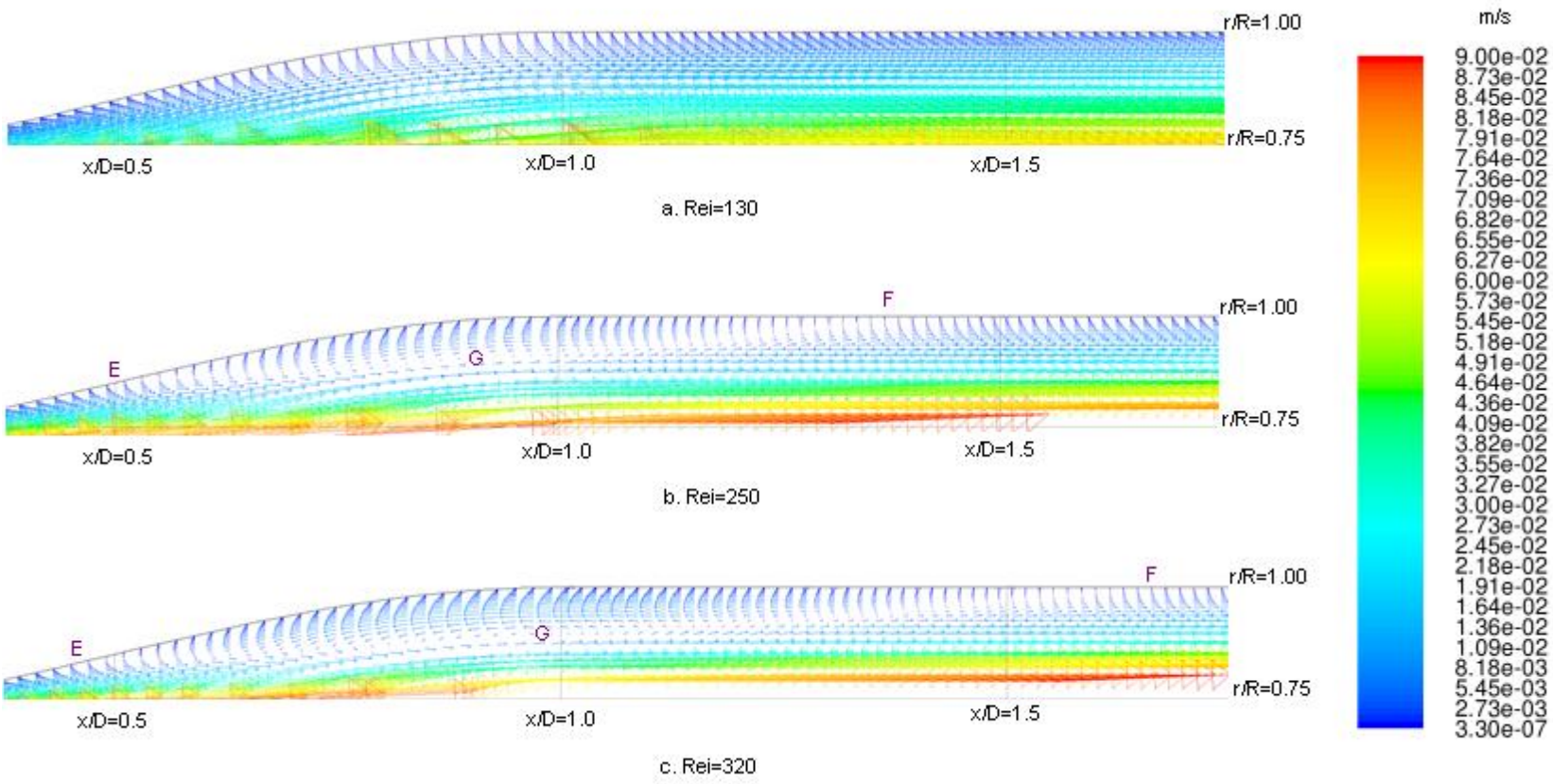

Figure 6.16 Velocity vector fields in the recirculation region. E is the flow detachment point, F is the reattachment location and G is the middle vortex.

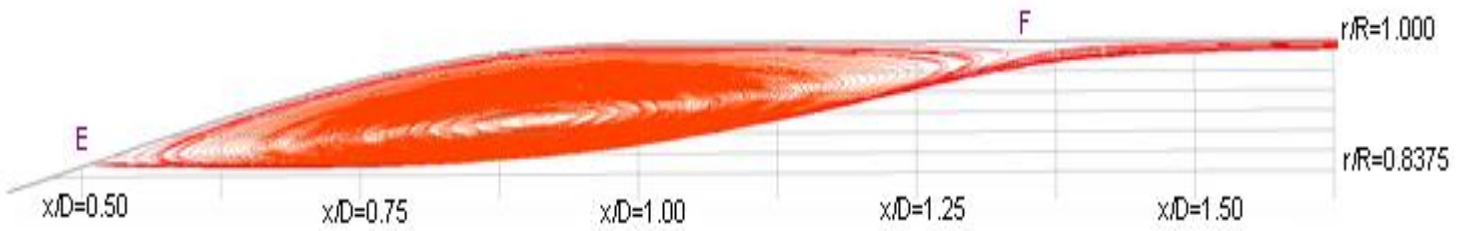

a. Rei=250

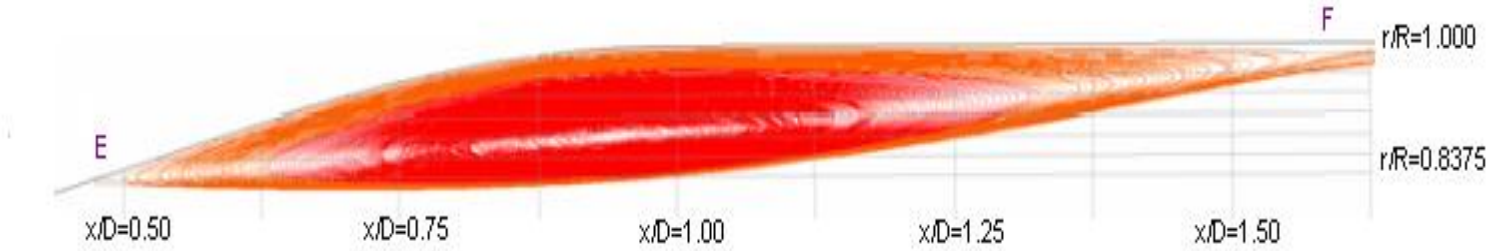

b. Rei=320

Figure 6.17 The streamlines of the flow in the recirculation region

6.4 Discussion

6.4.1 **Comparison with PIV measurements**

In Chapter 4, the flow field was characterised at selected downstream locations covering the stenosis diameter. This section will compare flow field measured by PIV and simulated results at Re_i=250. In Figure 6.18, the axial velocity profile is compared. The inlet velocity for the plotted experimental results was measured at *x/D*=-3.5, and for simulated results the location was *x/D*=-1.5. The axial position for the rest of the compared profile was at *x/D*=-0.5, 0, 0.5, 1.0 and 1.5. In general, the velocity profiles for both methods agree, although asymmetry has been observed in the experimental results.

The experiment performed in Chapter 5 zoomed into the recirculation region by altering the optics of the PIV system to increase the resolution. The image was magnified to 2.5 times and more velocity vectors could describe the flow. The results at *r/R*> 0.8 were compared to the simulated data shown in Figure 6.19. The axial locations were *x/D*= 0.75, 0.8125, 0.875, 0.9375, 1, 1.0625 and 1.125. The broken green lines act as the axis where the axial velocity behind the line was negative, which indicates backflow velocity. The axial velocities in the recirculation region were all negative in the near-wall region. As the vectors approached the inner radial axis, the values crossed the green line. The point where the profile crossed the line suggested the zero axial velocity. Beyond this point, the direction followed the mainstream velocity. The radial positions for zero velocity in the experiment differed from those found in the simulation. The magnitude for the positive velocity measured in the experiment was smaller than in the simulation. The velocity gradient at *r/R*<0.91 measured in the experiment agreed with the simulations results but towards the inner flow, the experimental velocity gradient were smaller. Marked difference were seen at *x/D*<0.9375 where the simulated results were as large as 18 times higher than the measured velocity gradient.

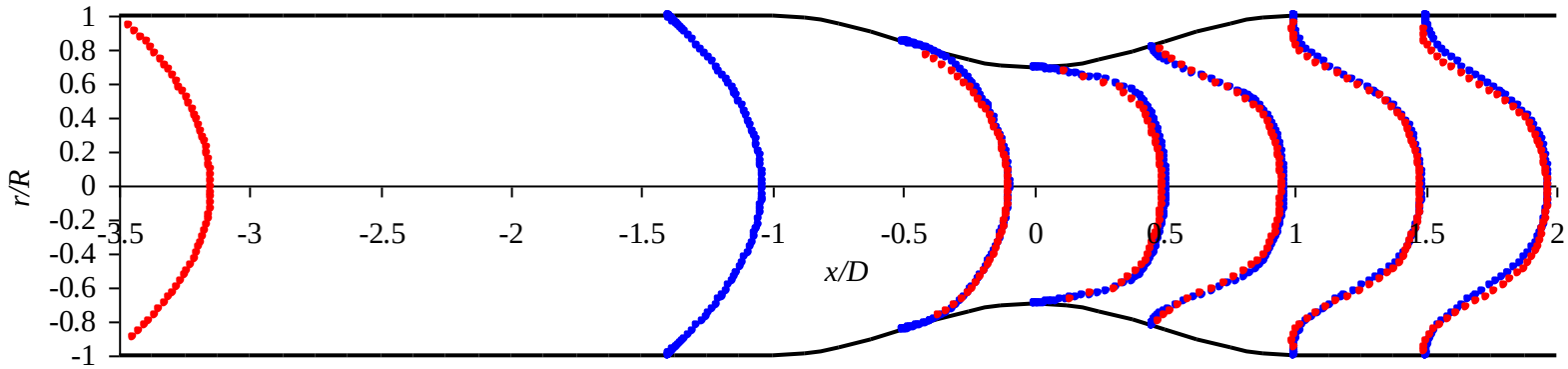

Figure 6.18 Axial velocity profiles of experimental data measured in Chapter 4 (red) and the simulation results (blue).

.

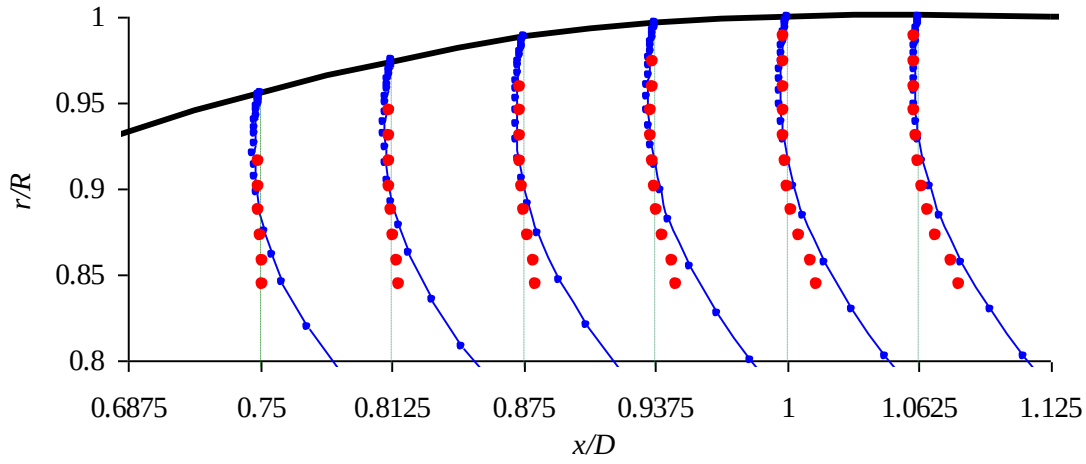

Figure 6.19 Axial velocity, *u* profiles in the recirculation zone measured by PIV (red) in Chapter 5, and the simulation results (blue)

The vorticity measured from experiment and calculated from simulation are compared. It is important to note that the measurements in PIV are two-dimensional whereas the geometry used in the simulation is three-dimensional. Therefore, instead of quantifying the vorticity component, the magnitude was taken into account. In Figure 6.20, the vorticity before entering the stenosis throat was experimentally measured at x/D=-3.5. In the simulation the inlet of the geometry is at x/D=-1.5. The vorticity was zero at the flow axis and linearly increased towards the wall correspond to Hagen-Poiseuille vorticity. Both results agreed with the maximum difference between the simulated and experimental results of 1%. The maximum vorticity at the wall of the inlet region was 186 s^{-1}.

At the throat of the stenosis (x/D=0), the results at the flow axis matched. In the experiments, the points very near to the wall were not considered because geometry imperfection of the joints at the wall. There was an abrupt increase of vorticity at r/R=0.5.The simulated results showed that the maximum vorticity at the wall of the middle throat was 6 times higher than that of the wall inlet. The flow constriction at the throat resulted in a significant vorticity growth at r/R>0.5.

Vorticity profile at x/D=1.5 showed the agreement of the experiment and the simulation profile. The results of vorticity gradient from r/R=0 to r/R=0.3 was similar to the gradient observed at the throat and the inlet. Beyond this radial position, the vorticity increased to a peak value at r/R=0.6 with a steeper gradient. Experiment result shows the peak vorticity was higher than the simulated results with a difference of 15%. The simulated peak vorticity

at this axial location was 20% of the maximum vorticity at the throat (x/D=0) and 30% greater than the maximum vorticity at the inlet. At location r/R>0.6, the vorticity decreased to a minimum of 9 s^{-1} near the wall.

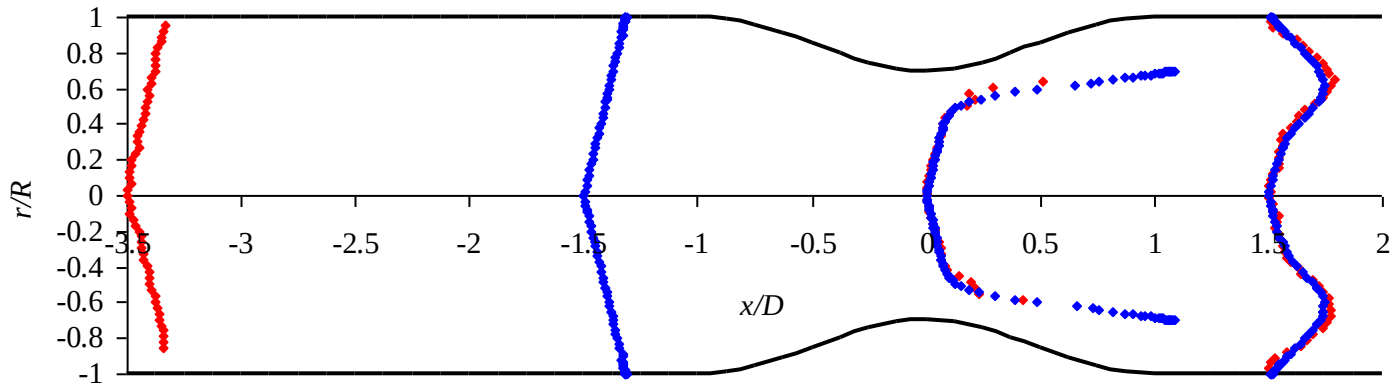

Figure 6.20 The vorticity profiles of experimental data measured in Chapter 4 (red) and the simulation results (blue).

6.4.2 **Comparison of the flow separation boundary**

The experimental results were compared with the CFD simulation. The flow separation zone boundary for both cases at Re_i=250 and Re_i=320 is shown in Table 6.1. The size obtained in the experiment was slightly different from the simulated results, in which the reattachment point obtained from PIV measurement were further downstream. At both flow rates, the reattachment points measured were around 2mm ($\Delta x/D$=0.25) further. The central vortex observed in the experiment was within 1mm ($\Delta x/D$=0.125) away from the position observed in the numerical simulation. There was 16.7% and 15.8% difference between experiment and simulation results for reattachment points which mainly due to the masking effect at the wall boundary. As discussed in experimental method in Section 5.2.3, the vectors yielded within 0.3mm from the wall (r/R>0.07) were discarded. Furthermore, the cell size in the simulation domain was in the range of 3μm to 100μm which was smaller than the size of interrogation area in PIV measurement (115μm and 262μm). The order of error for PIV measurements was comparable with errors published in the literature where Zhang et al. (2008) reported an error ranged from 12% to 47%.

Table 6.2 Comparison between recirculation sizes in the experiment and the simulation.

Flow rates		Experiment	Simulation	% difference
Re_i = 250	Wall detachment point (E)	No data	x/D=0.5047	-
	Wall reattachment point (F)	x/D= 1.63±0.016 (Figure 4.7)	x/D=1.3570 (Figure 6.20)	x/D =16.7%
	Middle vortex (G)	x/D=1.022±0.007 r/R=0.89±0.007 (Figure 5.2)	x/D=0.9187, r/R=0.9075 (Figure 6.20)	x/D=10.1% r/R=1.9%
Re_i = 320	Wall detachment point (E)	No data	x/D=0.4707	-
	Wall reattachment point (F)	x/D= 1.93± 0.016 (Figure 4.7)	x/D=1.6250 (Figure 6.20)	x/D=15.8%
	Middle vortex (G)	x/D=1.063±0.007 r/R=0.87±0.007 (Figure 5.3)	x/D=0.9476, r/R=0.8900 (Figure 6.20)	x/D=10.8% r/R=2.2%

6.5 Conclusions

CFD simulation was performed by considering the blood mimic as a single phase fluid. The flow fields in the PIV measurements were compared with numerical simulation results. Simulation at Re_i=130 proved that the flow was not separated as observed in the experiment. Simulation results confirmed that the flow was streamline and recirculation region were formed at Re_i=250 and Re_i=320. The peak velocity was in the throat region. The vorticity followed the velocity gradient contour where the peaks were also at the throat but before the expansion section. The peak vorticity and velocity gradients at the narrowest geometry increased with the flow rates. Similar to experimental results, the size of the recirculation zone increase with flow rates. However, the reattachment point and the central vortex simulated were shorter by 16-17% and 10-11% respectively. The small discrepancy was due to the experimental errors in PIV measurement where the range was within the errors reported in the literature.

Chapter 7

PARTICLE DYNAMICS SIMULATION

The single-phase simulation performed in Chapter 6 provides macroscopic information about the bulk flow; however when considering two-phase-flow, particle-fluid interactions can be modelled. This chapter presents the application of CFD methods to investigate the particle dynamics. The movement of the particles in fluid is simulated. The paths of the particles are tracked where the effect of hydrodynamic forces, such as drag and lift on particle migration is discussed.

7.1 Introduction

Generally, there are three approaches to modelling blood cell dynamics (Hund and Antaki, 2009): the discrete model, the fluid continuum model, and the dilute-phase model. Each of these will be discussed in more detail in turn.

In discrete models, the microstructure of the blood is explicitly represented by considering an individual particle or a group of particles, known as the Lagrangian model. This model has been applied to the simulation of blood cell flow in capillaries and arterioles (Kuharsky and Fogelson, 2001; Guy and Fogelson, 2002; Fogelson and Guy, 2004). However, its application in larger flow domains, such as in larger blood vessels that involve the transport of trillions of blood cells, has become computationally intensive.

The second approach employs a fluid-continuum model that assumes that the particle cells comprise of a distinct continuum mixed with plasma carrier fluid (Jung et al., 2006; Jung et al., 2006; Jung and Hassanein, 2008). Red blood cells (RBC) can be modelled sensibly, but the white blood cells (WBC) and the platelets are too dilute for the classical definition in continuum mechanics. These cells are therefore not considered influential for the flow of plasma.

The third approach uses the dilute-phase model, which is governed by convection-diffusion theory. Blood is modelled as a single continuum, whereby the dilute species are the WBC and the platelets (Wootton et al., 2001; Jordan et al., 2004; Hund and Antaki, 2009). The influence of the RBC is accounted for by the mass conservation equation, where the

diffusivity of the dilute phase is a function of RBC concentration (Hund and Antaki, 2009). The RBC profile was prescribed from experimental data from multiphase simulation.

In this work, we have considered the dilute cellular species that are within the range of the white blood cell properties, specifically the monocytes. During the inflammatory process, when the vessel wall sensed a low shear stress, monocytes in the bloodstream migrated to the wall and subsequently initiated the plaque formation that promotes atherosclerosis (Slager et al., 1995). The formation of atherosclerosis has been discussed in Section 1.1.1. Since the particulate suspension system under investigation is at a low concentration, individual particle motion was simulated in this study using the first approach, the discrete-phase model.

The aim of this chapter is to perform a simulation to investigate the particle dynamics that are responsible for the particle accumulation observed in the experiments. In Chapter 5, it was observed that the particles with a 20μm diameter at a weight concentration of 0.07% migrated to the central recirculation vortex. The particles simulated had a diameter within the range of the size of white blood cells, the monocytes (Caro, 1978). The volume fraction of monocytes was 0.0643%, which is equivalent to 0.0688% by weight (Skalak and Chien, 1987), and was close to the concentration used in the experiment. Since the particles used had similar physical properties to the monocytes, the results for the particle distribution can suggest the monocytes' behaviour when flowing distal to the stenosis. The simulations performed were used to investigate the influence of lift force on the particle migration phenomena.

7.2 Simulation method

The geometry and mesh used in the single-phase simulation described in Figure 6.2 was employed as the domain for modelling the particle flow. In addition to the single-phase flow simulation, the equations of particle motion were solved. The equations for particles and the simulation technique are discussed in this section.

7.2.1 **Governing equations**

The physics of solid-liquid flow were presented in Chapter 2. The equation of particle motion is rewritten here and described in Equation 7.1.

$$m_p \frac{dV_P}{dt} = m_p \left(1 - \frac{\rho}{\rho_p}\right) g + F_{PG} + F_D + F_L + F_{Vm} + F_{Bas} \qquad (7.1)$$

where m_p is the mass of the particle, V_p is the instantaneous velocity of the particle, ρ and ρ_p are the density for fluid and particle respectively, and g is the body acceleration. The term on the left hand side describes the particle inertia, and the terms on the right-hand side are forces caused by particle-fluid interaction.

The first inertial term is the gravitational force. F_{PG} is the force that exists in the absence of the particle due to the hydrostatic pressure gradient;

$$F_{PG} = -Vo_p \nabla p \tag{7.2}$$

where Vo_p is the particle volume and ∇p is the pressure gradient produced by hydrostatic pressure.

F_D is the drag force, and is given by:

$$F_D = \frac{1}{2}\rho C_D \frac{\pi d^2}{4} V_s \tag{7.3}$$

where C_D is the Stoke's drag coefficient, d is the particle diameter and V_s is the relative velocity between the fluid and particle.

F_L is the lift force generated by the rotation of the particle and fluid shear. As shown in the experimental results in Chapter 4, the shear gradient has been found to be significant in the post-stenotic region, therefore shear generated lift forces are of interest. The Saffman-Mei lift model (Mei, 1992) was used in this analysis. This force has been discussed in detail in Section 2.3.5, and the lift model is written as:

$$\begin{aligned} F_{LSaffman\text{-}Mei} &= F_{LS}\left[\left(1 - 0.3314\beta^{0.5} \right) exp\left(-\frac{Re_p}{10} \right) + 0.3314\beta^{0.5} \right] && Re_p \le 40 \\ &= F_{LS}\left[0.0524\left(\beta Re_p\right)^{0.5} \right] && Re_p > 40 \end{aligned} \tag{7.4}$$

where

$$\beta = \frac{d_p}{2|V_s|}\left|\frac{du}{dr}\right| \qquad 0.005 < \beta < 0.4 \tag{7.5}$$

F_{Vm} is defined as a virtual mass force, and it accounts for the work required to change the momentum of the surrounding fluid as the particle accelerates.

$$F_{Vm} = \frac{\rho Vo_p}{2}\left(\frac{dV_p}{dt} - \frac{dV}{dt}\right) \tag{7.6}$$

where $\left(\frac{dV_p}{dt} - \frac{dV}{dt}\right)$ is the relative acceleration of the fluid with respect to the particle acceleration.

F_{Bas} is the unsteady drag force or Basset force, which accounts for the temporal development of the viscous region in the vicinity of the particles.

$$F_{Bas} = \frac{3}{2} d_p{}^2 \sqrt{\pi\rho\mu}\int_0^t \frac{\left(dV_p/dt\right) - \left(dV/dt\right)}{\sqrt{t-t'}} dt' \tag{7.7}$$

where *t-t'* is the time interval from the initiation of the acceleration.

As the system under investigation is steady, virtual mass, F_{Vm} and Basset force, F_{Bas} are neglected in the simulation. Even in pulsatile flow, Buchanan et al. (2000) states that F_{Vm} is insignificant for solid-liquid flow or for a colloidal (such as blood suspension) where the densities are similar. Longest and Kleinstreuer (2003c) neglected the Basset term with the argument that the blood particle relaxation time is in the range of 10^{-6}, which is small for blood-borne transport in plasma. Similar assumptions were made in this simulation. Hence, Equation 7.1 is reduced to;

$$m_p \frac{dV_p}{dt} = m_p\left(1 - \frac{\rho}{\rho_p}\right)g + F_{PG} + F_D + F_{LSaffman-Mei} \tag{7.8}$$

The body force due to gravity was negligible because the density of the fluid (ρ = 1080 kg/m^3) and the particle (ρ_p= 1030 kg/m^3) were nearly equal. The pressure gradient force, F_{PG} is the particle volume multiplied by the hydrostatic pressure gradient. Since the F_D and $F_{LSaffman-Mei}$ are a function of slip velocity (V_p-V), the effects of the flow field on particle trajectory are mainly dependent on these forces.

7.2.2 **Simulations**

The discrete phase model in the ANSYS FLUENT 12.1.4 simulation package, which follows the Euler-Lagrange approach, was used for the simulation. The continuous fluid was solved according to the Navier-Stokes equation and the suspended solid by tracking the individual

particles through the calculated fluid-flow field. As the solid concentration was less than 1%, which was considered as a low-volume fraction, each particle computation was solved at time intervals during the fluid-phase calculations.

Trajectory equations are solved by stepwise integration over discrete time steps. The integration of time in Equation 7.8 yielded the velocity of the particle at each point along the trajectory.

7.2.3 **The number of particles tracked**

The Lagrangian method solved the trajectory of individual particles in this analysis. Therefore, the more particles that were introduced, the more equations there were to be solved. An initial attempt was made to track particles travelling in a plane in which there was one particle in every mesh element. There were 1 467 060 mesh elements and 7485 particles at the inlet plane in the direction flow. With this number of particles to be tracked up to the outlet, the computation processing and the memory requirements exceeded the computer's capability. Hence the number of particles and the length of paths tracked had to be reduced and optimised as the computer system, as it could only support fewer particles. In this simulation, a maximum of 220 particles was tracked at any one time.

7.2.4 **Boundary conditions**

Similar to the boundary conditions used in the single phase simulation, the fully developed flow achieved in the experiment was specified at the inlet. As this study incorporates a rigid wall, the inclusion of pressure boundary conditions was not necessary. The inlet boundary conditions will create the pressure differential required to drive the flow.

The particles simulated had a diameter of 20μm, which was in the range of the size of white blood cells, the monocytes (Caro, 1978). Having computing limitations on simulating the actual numbers of particles in the flow suspension, the number of particles introduced to the domain was far less than in reality, as large arteries transport billions of white cells per second (Hund and Antaki, 2009). As discussed in the previous section, the particles tracked in this simulation are less than 220 to account for computational limitations.

7.2.5 **Particle modelling method**

The simulations were carried out to investigate the path and residence time of the particles. Two type of particle treatment method were considered;

i. The equations for fluid flow and particle motion were solved simultaneously. The particle motion equations in this section were solved with the fluid motion under an unsteady condition, which is known as unsteady particle injection.

ii. The equations for the fluid, which were the equations for single-phase flow in Chapter 6, were solved first. The equations for particle motion were then introduced into the domain to track the particle path.

There was a momentum exchange between the particles and the fluid, and therefore generally the first approach is more robust than the second method; however the computing time and cost for the former is higher.

7.3 Unsteady particle tracking

This section provides the simulation detail and results for the first particle modelling method, where the equations for the particles were solved simultaneously with the fluid. The particle motion equations in this section were solved with the fluid motion under an unsteady condition. The equation of motion 7.8 was solved with the Navier-Stokes equation. The particles were released from an initial point within a certain time duration, and the final positions were located.

7.3.1 **Variables of interest**

The drag force, F_D, and $F_{LSaffman\text{-}Mei}$ in the equation of particle motion are a function of the slip velocity, which is the difference between the fluid and particle velocity, $V_s=(V_p-V)$. The velocity of the particles, V_p and the slip velocity V_s were then analysed in this simulation. The slip velocity is expressed as particle Re_p.

$$Re_p = \frac{\rho d_p V_s}{\mu} \tag{7.9}$$

where ρ and μ are the fluid density and viscosity respectively.

7.3.2 **Simulations performed**

The particles introduced at the inlet (x/D=-1.5) and distal to the stenosis (x/D=0.5) at Re_i=250 were tracked simultaneously. The particles were introduced on a single line on the z-plane. There was one particle in each mesh element, equating to 109 particles in the line. The particle time step was $1x10^{-4}$ s and it ran for 280 time steps. The total iterations for the flow time of up to 0.028s were 21,625, which is approximately equal to 1392 hours (60

days). The convergence criterion for the continuity equation was set at $1x10^{-9}$, and for the momentum conservation equation at $1x10^{-6}$. The residual plot is shown in Figure 7.1, and the solution was converged. An attempt to introduce more than single-line particles in order to illustrate 3-D behaviour was unsuccessful, due to memory limitations and longer simulation time.

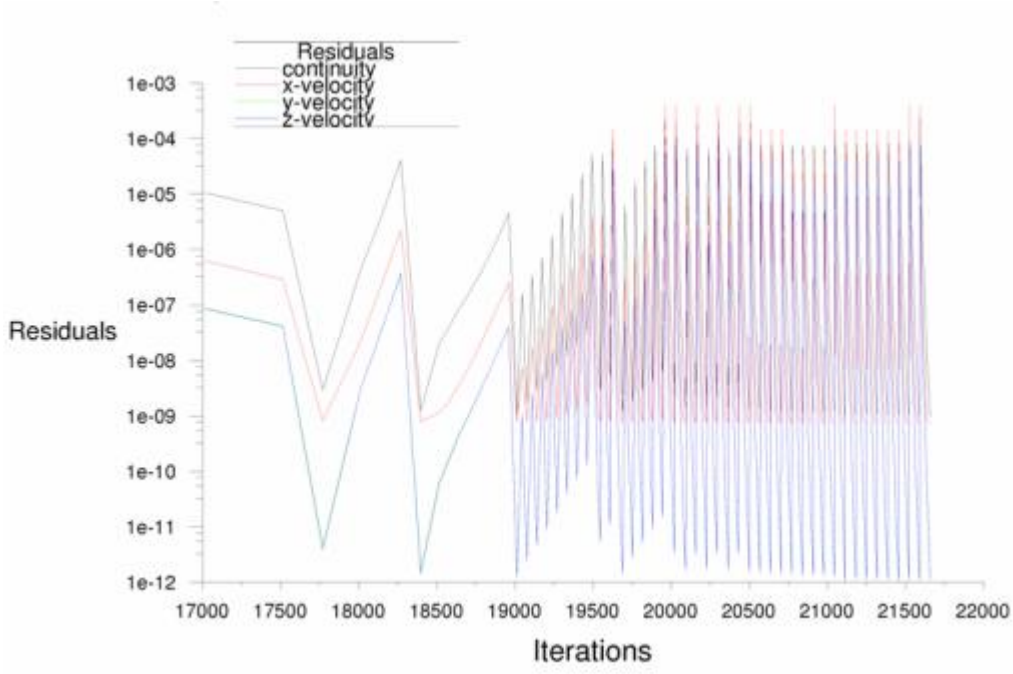

Figure 7.1 Residuals plot at the end of simulation time of 0.028s.

7.3.3 **Results and discussion**

The particles' trajectories and final positions are presented in Figure 7.2. Note that the sizes of the particles do not geometrically represent the actual diameter, but they have been enlarged for data visibility. For the particles injected at *x/D*=0.5, the maximum axial distance reached was *x/D*=1.3420. The reattachment point determined from Chapter 6 was *x/D* =1.3574 indicated by point F. Hence, the particles near the wall were in the region of recirculation. As shown in Figure 7.2a, the resultant velocities of the flow injected from the inlet were fully developed, but the parabolic velocity profile for particles injected at *x/D*=0.5 were flattened and the velocity magnitude was reduced. The axial and radial velocity component of particles injected at *x/D*=0.5 are shown in Figure 7.2b and c respectively. There was high radial velocity component for particles in the recirculation zone which indicates radial migration from high to low shear region.

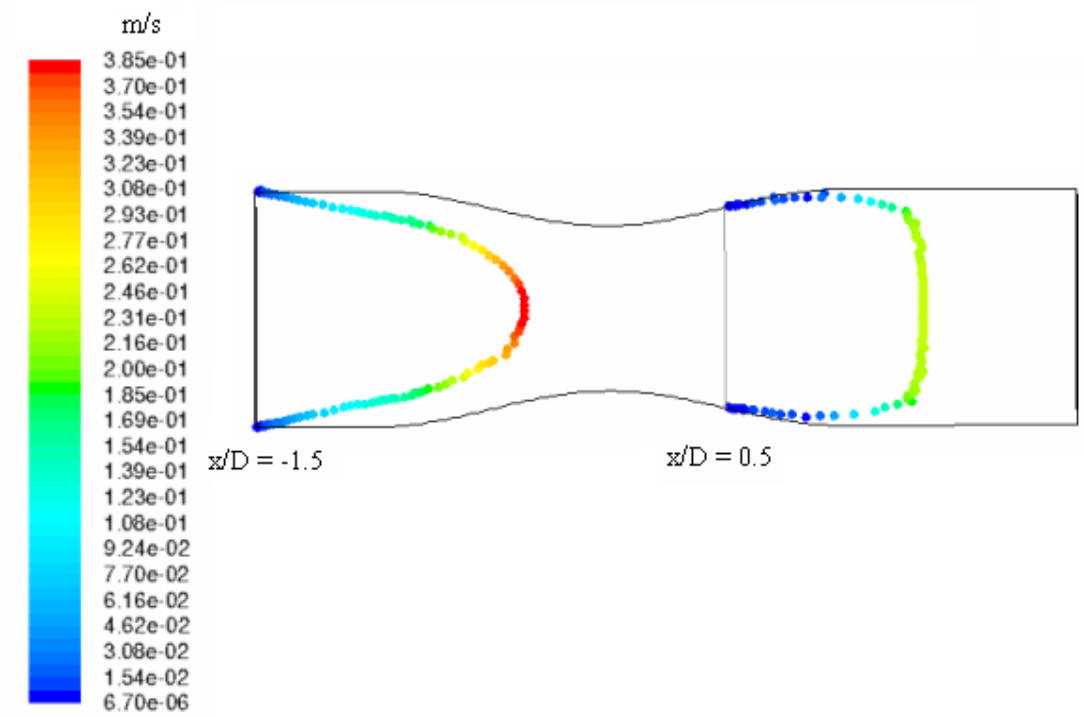

a. Particles' velocity magnitude, V_p

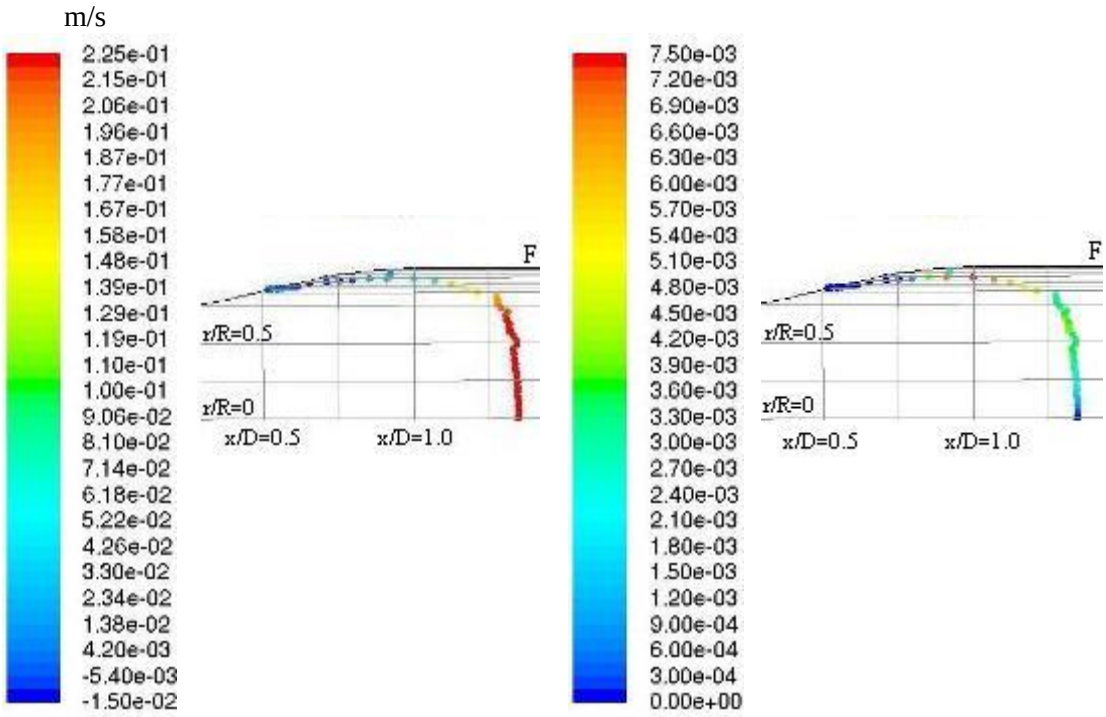

b. axial velocity of particles, u_p c. radial velocity of particles, v_p

Figure 7.2 Final location of tracked particles from inlet and x/D=0.5. The colour scale represent a. the particle velocity, V_p, b. axial velocity component, u_p and c. radial velocity, v_p

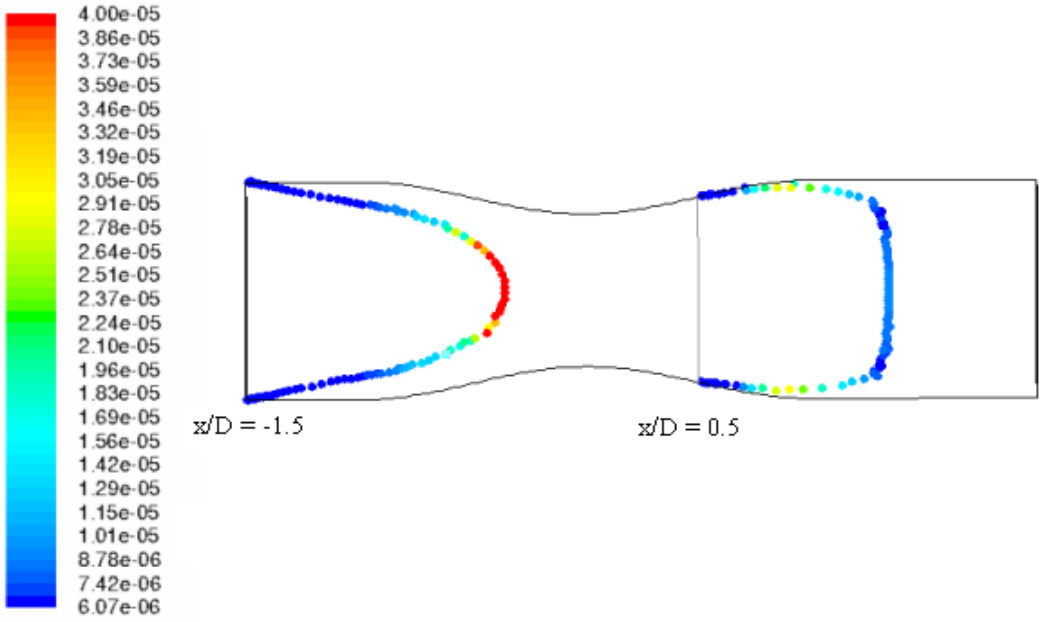

Figure 7.3 Final location of tracked particles from inlet and x/D=0.5. The colour scale represent the particles Reynolds number, $Re_p = \rho d_p(V_p - V)/\mu$

Figure 7.3 shows the Re_p which is a function of slip velocity (V_p-V). There was a smaller Re_p value for the particles introduced at x/D=0.5 than at the inlet. For particles introduced at x/D=0.5, Re_p values were higher in the recirculation zone compared to those in the mainstream. This means even though the particle velocity in the recirculation region is small, the particle inertia is significant. It was determined that particles did not follow the fluid velocity exactly. These particles may leave the fluid velocity path and resides in the recirculation zone longer.

7.3.4 **Conclusions**

Particles flowing in the post stenosis region migrated to the recirculation zone. The radial velocity component of particles was higher in this region. The particle Re_p in the recirculation zone was relatively higher than the mainstream. This indicates that the slip velocity which is linearly proportional to particle Re_p was also higher in the recirculation zone. Hence, the particle inertia in this region was significant. The particles entered recirculation zone having high tendency to remain in that region.

7.4 Particle tracking in steady fluid flow

This section presents the results from the second method employed in tracking the particles' motion. The main reason behind performing steady particle tracking is due to very long time required for particle modeling under an unsteady mode. The Navier-Stokes equation of the background fluid was first solved to obtain the momentum and direction of the flow field, which in turn is used to calculate the particle motion. The time step for the background fluid was discussed in Chapter 6 where the time scale was set at $1x\ 10^{-3}$s.

7.4.1 **Variables studied in the simulation**

The particles were not introduced from the inlet but from their initial point directly to the region of interest, i.e. the recirculation zone. The particles' physical properties were set as described in Chapter 4. The initial velocity of the particles was set to follow the local fluid velocity.

The simulations were carried out to investigate the path and residence time of the particles. The particle residence time is defined as the time taken by a particle to reach a particular position (Kunov et al., 1996). The particle residence time does not indicate how much time they spend in each location along their path.

The following factors were taken into account:

i. The influence of the Saffman-Mei lift force was investigated by running the simulation with and without the equation. Saffman-Mei lift force is a function of shear rate and slip velocity. From previous experimental and simulation results, shear rate and slip velocity were significantly higher in the expansion region. The particles were introduced to the region with a high velocity gradient and to the recirculation zone. There was a comparison of the path and residence time of each particle.

ii. As indicated in Chapter 5, the flow rates affected the particle distribution. Simulations were performed to compare the particle residence time at Re_i =250 and Re_i =320. The particle residence time for both flow rates was evaluated.

7.4.2 **The effect of lift forces on particles from high vorticity regions**

The particles travelling from high vorticity regions were tracked. The particles' diameter was set at 20μm. The movement of five particles from an initial radial position close to the wall

at *x/D*=0.125 were monitored for 0.763s. The particles' positions are summarised in Table 7.1 and their paths shown in Figure 7.4. The paths were tracked both with and without Saffman-Mei lift force as discussed. Figure 7.4a presents the particles' paths and residency times up to the drag force only. Figure 7.4b shows the results with the Saffman-Mei lift force included.

Table 7.1 Radial position of particles injected at *x/D*=0.125.

Particle point	Radial coordinates, *r/R*
H	0.500
I	0.625
J	0.600
K	0.650
L	0.700

In both cases, the particles deflected towards the wall, and the particles close to the mainstream flow travelled faster than those near the wall. In both cases, the tracks were identical but the residence times were slightly different. The maximum particle residence time (PRT) of each particle is summarised in Table 7.2. A longer PRT means that the particle travelled more slowly than one with a shorter residence time in the same domain. Particles with shorter residence times escaped the flow domain earlier than the other particles.

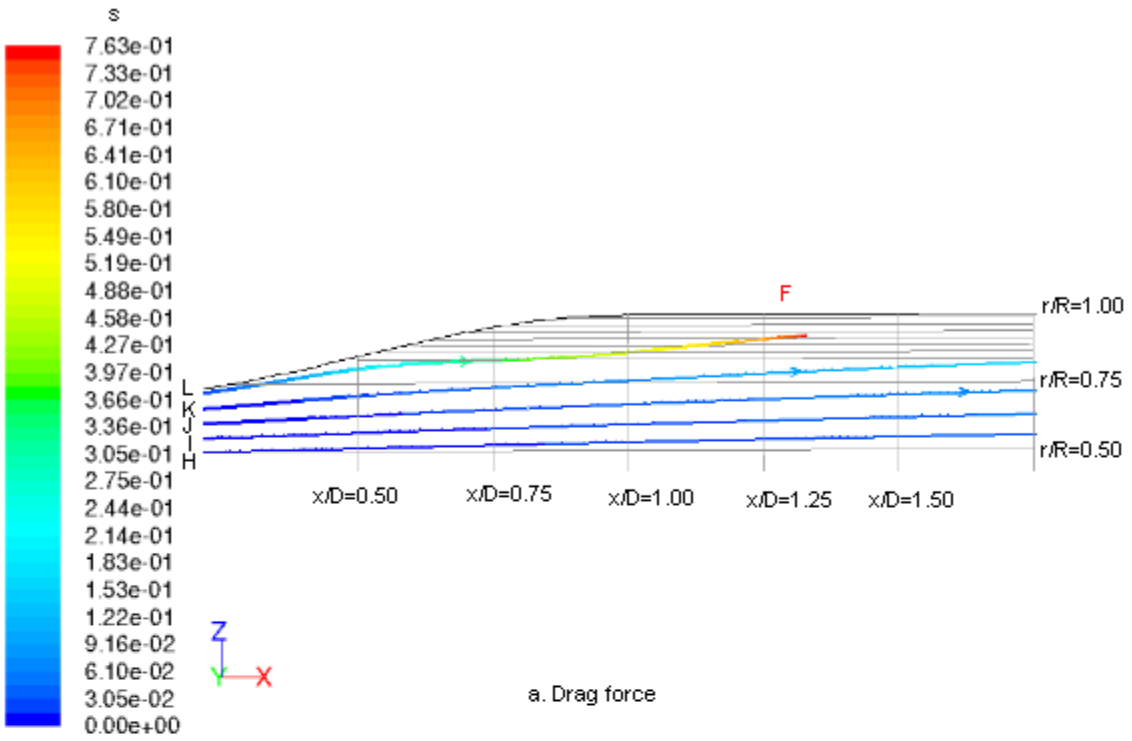

a. Drag force

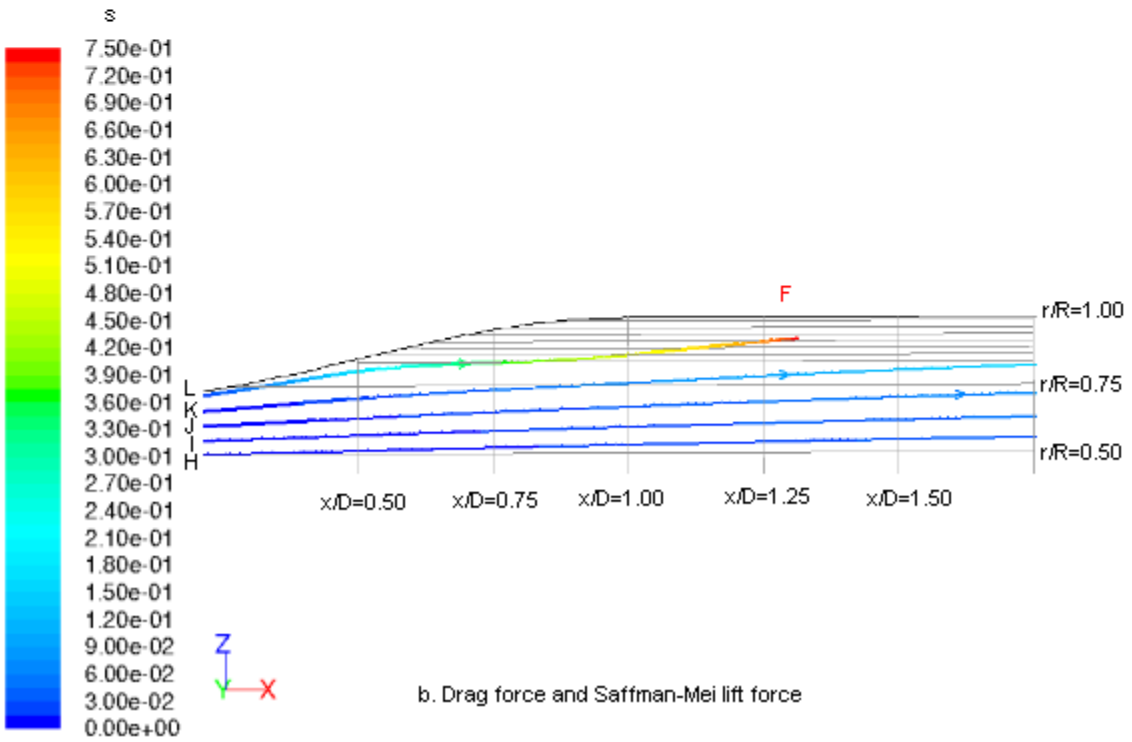

b. Drag force and Saffman-Mei lift force

Figure 7.4 The particle path and the residence time tracked with a. drag force and b. drag and lift force. F indicates the reattachment point.

Table 7.2 PRT (millisecond) for each particle location.

Particle initial point	PRT with drag force and Saffman-Mei lift force, ($PRT_{drag+lift}$)	PRT with drag, (PRT_{drag})
H	46.8	46.8
I	59.7	59.6
J	90.6	90.5
K	195	194
L	750	763

The ratio between the PRT of both cases ($PRT_{drag+lift}$: PRT_{drag}) is plotted in Figure 7.5. The residence time for Particle L (with a radial initial position at *r/R*=0.7) decreased by 1.8% when the Saffman-lift force was considered. The additional lift force decreased the particle's residence time. However, for Particle K, at the initial position of *r/R*= 0.650, the residence time increased where the lift force reduced the particle's velocity by 0.5%. Unlike near-wall particles, PRTs at locations nearer the flow axis were dominated by the drag force.

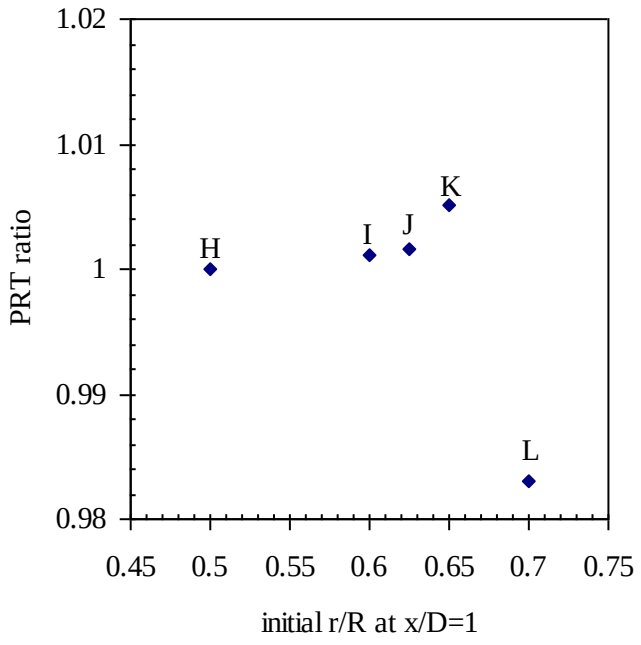

Figure 7.5 The ratio of $PRT_{drag+lift}$: PRT_{drag}.

7.4.3 **The effect of drag and lift forces on particles from a flow separation boundary**

The paths of particles were tracked from the boundary between the flow recirculation region and the high shear region, along r/R=0.850 and r/R=0.855. The Re_i was at 250. The initial positions are summarised in Table 7.3 and are marked as N, O, P, R, S and T in Figure 7.6, which represent the particles' paths travelled within a time of 4.230s. Particles M and Q were stagnant and remained at their initial position (not shown). The drag and Saffman-lift forces were considered in this case, for particles N, O and P with the radial position r/R=0.850, which escaped the recirculation zone. The initial position for the particles along r/R=0.855 (R, S and T) was closer to the separation zone. Particle T, the farthest to the right, escaped the separation zone and the other particles orbited inside the vortex.

Table 7.3 Initial positions of the particles at the flow separation boundary.

Particle initial point	*r/R*	*x/D*
M	0.850	0.500
N	0.850	0.625
O	0.850	0.750
P	0.850	0.875
Q	0.855	0.500
R	0.855	0.625
S	0.855	0.750
T	0.855	0.875

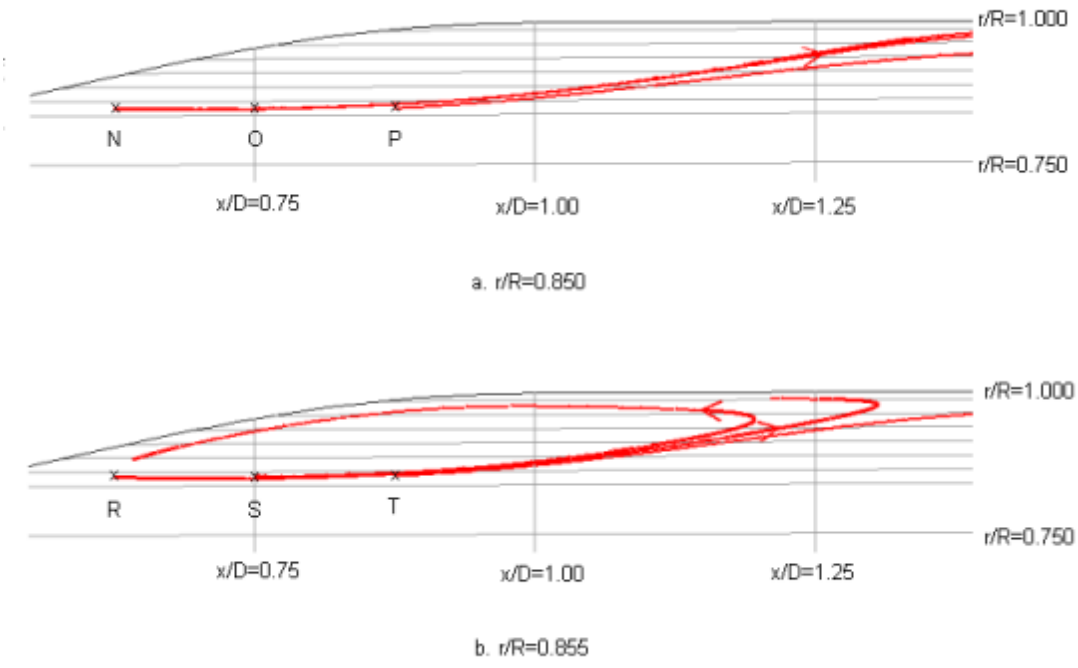

Figure 7.6 Particles' paths at the boundary of the separation zone. N, O, P, R, S and T indicate their initial position.

The residency time for particles R and S, which orbited inside the recirculation region, is shown in Figure 7.7. R' and S' denote the final positions at the end of the time they are tracked. Particle R orbited at a larger orbit diameter than Particle S.

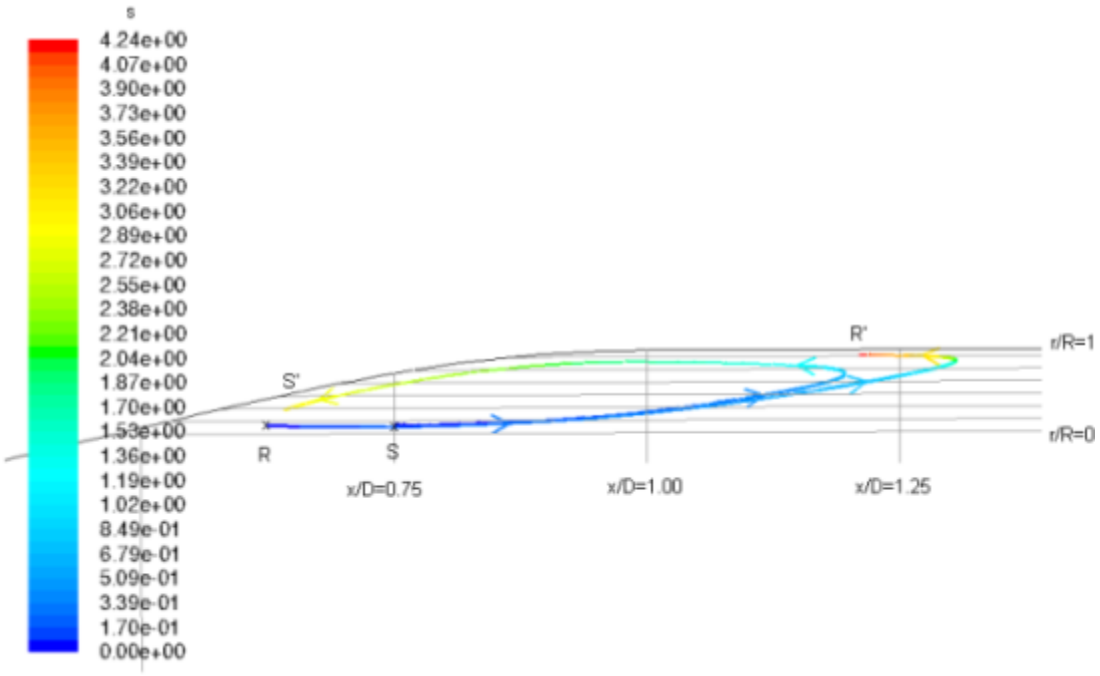

Figure 7.7 Path of Particles R and S at total residence time of 4.24s.

In Figure 7.8, Particles R and S were tracked over longer paths, with a total residence time of 14.8s. Particle R completed one orbit before escaping the separation zone, and particle S proceeded to orbit in the separation zone, stopping at the final location with a PRT of 8.13s.

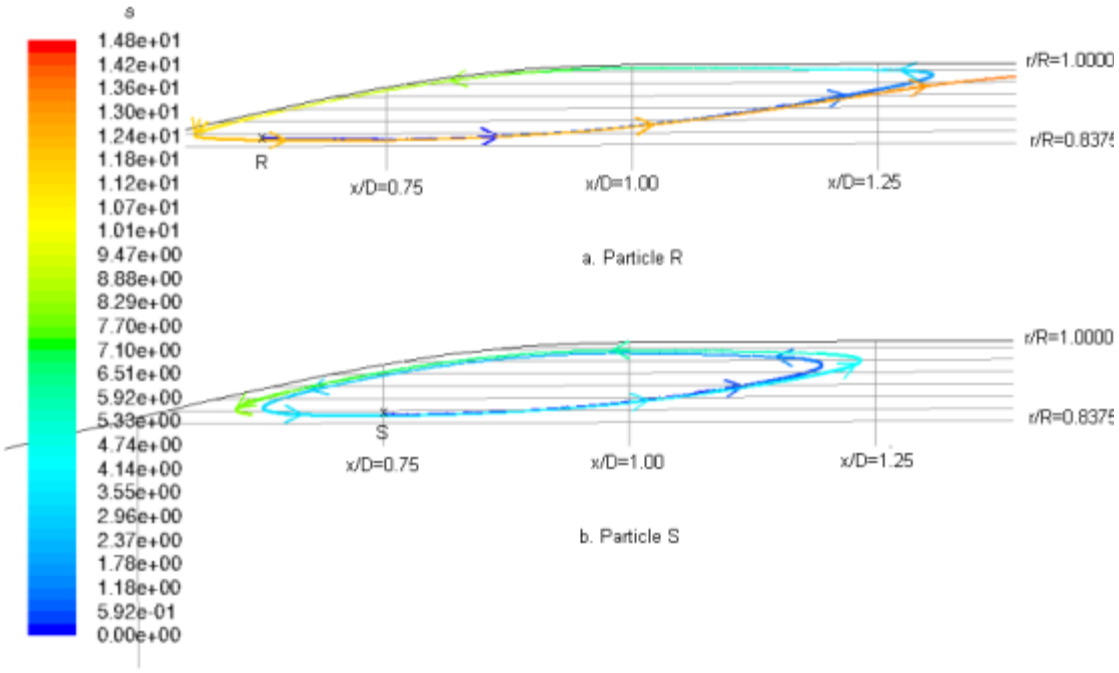

Figure 7.8 Residence time for Particles (a.) R and (b.) S with a total residence time of 14.8s.

Particle S was tracked for a longer time period, until the particles left the separation zone; the PRT is shown in Figure 7.9a. After completing one orbit, the particle circulated with a larger diameter for the next orbit. Particle S orbited three times and then travelled out of the separation zone, which took 21.12s. The velocity magnitude of Particle S is shown in Figure 7.8b. This particle moved faster at the mainstream boundary, with a velocity in the range of 10^{-2}m/s compared to the near wall velocity of around 10^{-4}m/s.

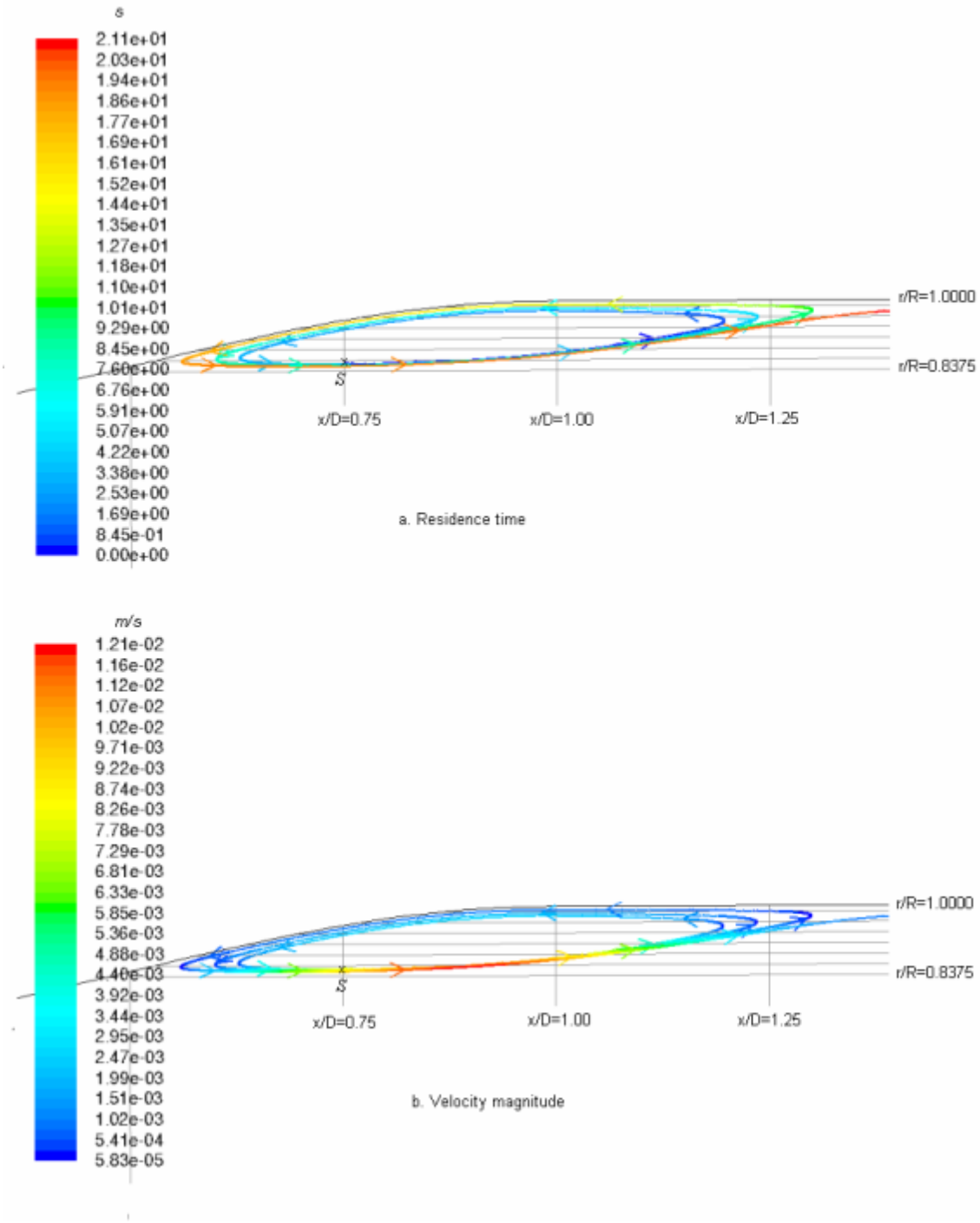

Figure 7.9 Residence time and velocity magnitude for Particle S with Saffman-Mei lift force, for the longer integration time of 21.12s.

The lift-force effect on the residence time of Particle S was considered by calculating the ratio of the residence time with and without the Saffman-Mei lift force. The particle path and PRT without accounting for Saffman-Mei is shown in Figure 7.10, and the PRT with lift is

obtained from Figure 7.9a. The total difference in residence time was 0.008s, which yielded value of $PRT_{drag+lift}$:PRT_{drag} = 0.996. It can be concluded that the inclusion of the lift force in the simulation resulted in a slightly shorter residence time. The time ratio was close to unity, suggesting that the lift had little effect on the particle path in the recirculation region.

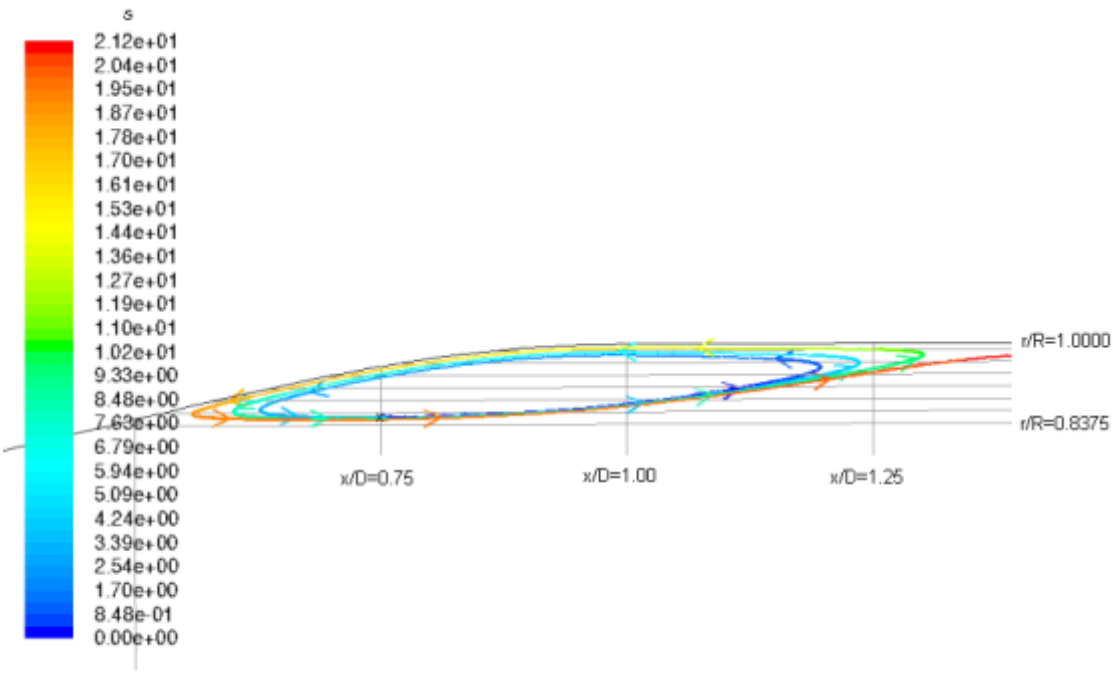

Figure 7.10 Residence time for Particle S without the Saffman-Mei lift force for integration time of 21.12s

It can be concluded from the simulation that, when the Saffman-Mei lift force is applied to particles in the recirculation zone, the particle residence time is not increased. The $PRT_{drag+lift}$:PRT_{drag} ratio is close to unity, indicating that the lift force can be neglected. However, Particle K travelling from a high shear area to the boundary of the separation zone did not manage to enter the recirculation region (Figure 7.4), having a longer residence time when Saffman-Mei lift force was applied.

7.4.4 **Residence time of particles in the post-stenotic region**

The particles from the central vortex, high vorticity region and flow separation boundary were tracked for 78,890s. Table 7.4 shows the coordinates, and the particles' diameter was 20µm as discussed. In addition to the particles simulated earlier; the particles at the boundary separation region are denote (N, O, P, R, S and T) and the particles travelling from the high

vorticity region are (H, I, J, K, L). Particle W is introduced at the central vortex and Particle X is from the flow axis.

Figure 7.11 presents the residence time of all of the particles. Particle X from the flow axis left the flow domain within 0.3s. Particle W from the central vortex travelled outwards and completed 30 orbits before leaving the separation zone within 78.87s. The PRT for particles orbiting in the flow separation region was about 260 times longer than in the mainstream.

Table 7.4 The coordinates of the tracked particles

Region	Particle point	*r/R*	*x/D*
Central vortex	W	0.9075	0.9187
Flow axis	X	0.000	1.000
Flow separation boundary	N	0.850	0.625
	O	0.850	0.750
	P	0.850	0.875
	R	0.855	0.625
	S	0.855	0.750
	T	0.855	0.875
High vorticity	I	0.625	1.000
	J	0.600	1.000
	K	0.650	1.000
	L	0.700	1.000
	H	0.500	1.000

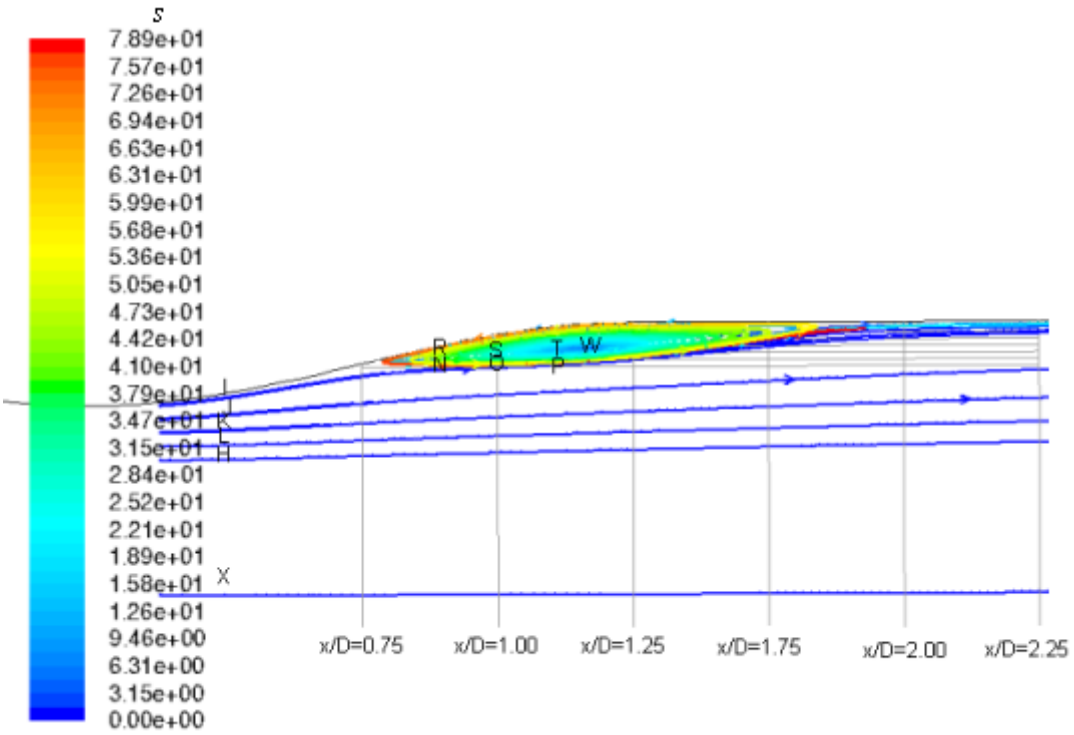

Figure 7.11 Trajectory of particles; the initial location of each particle is labelled as H, I, J, K, L, N, O, P, R, S, T, X and W, as described in Table 7.4 .The total particle residence time is 78.87s.

7.4.5 **The effect of fluid flow rates on particles in the recirculation zone**

In order to investigate the influence of the flow rate on the PRT, the paths for the particles travelling from the central vortex were tracked for fluid at Re_i=250 and Re_i=320. Particles W and Y marked the initial position at the central vortex at the respective fluid flow rates. The residence time for particles orbiting in the recirculation zone until they left the area and reached an axial position of x/D=1.60 is plotted in Figure 7.12. As reported earlier, for fluid with Re_i=250, particle W orbited 30 times and the final residence time was 78.87s. For a higher flow rate, with Re_i=320, particle Y travelled out of the central vortex in 40 orbits, taking a time of 40.60s. Although the particles suspended in regions of higher fluid flow rates (Re_i =320) completed more orbits, the residence time was almost half of that for the particles suspended in lower fluid flow rates (Re_i =250).

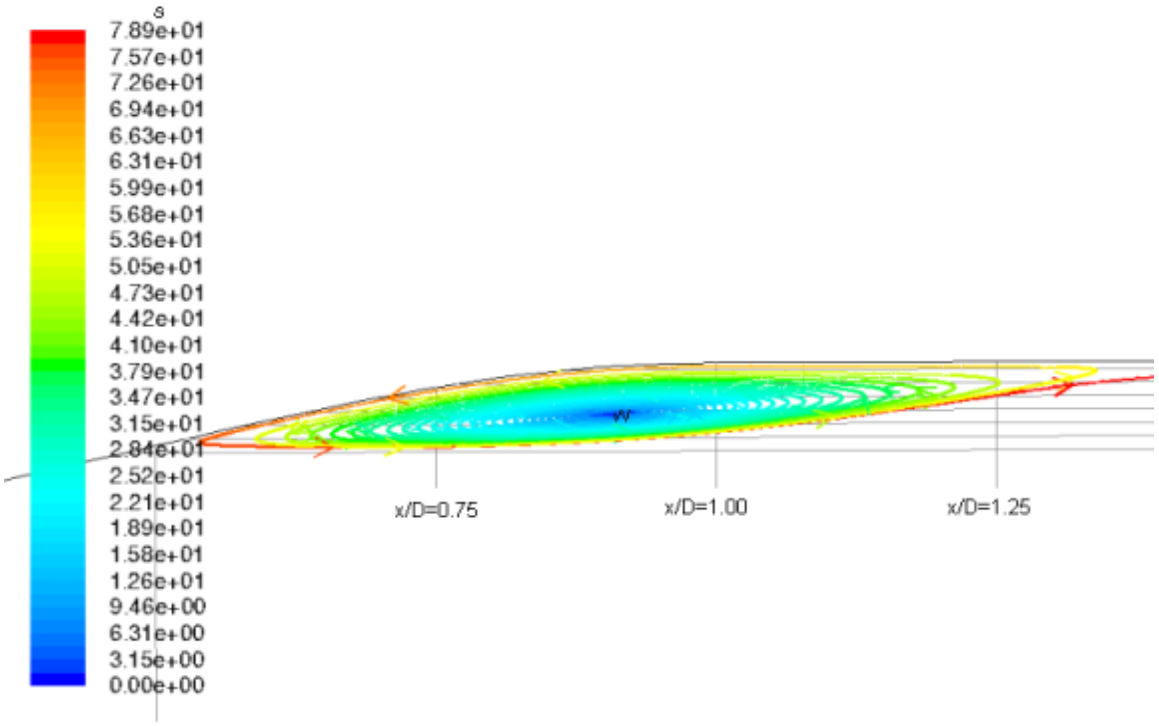

a. Re_i =250. The total PRT is 78.87s. Number of orbits is 30.

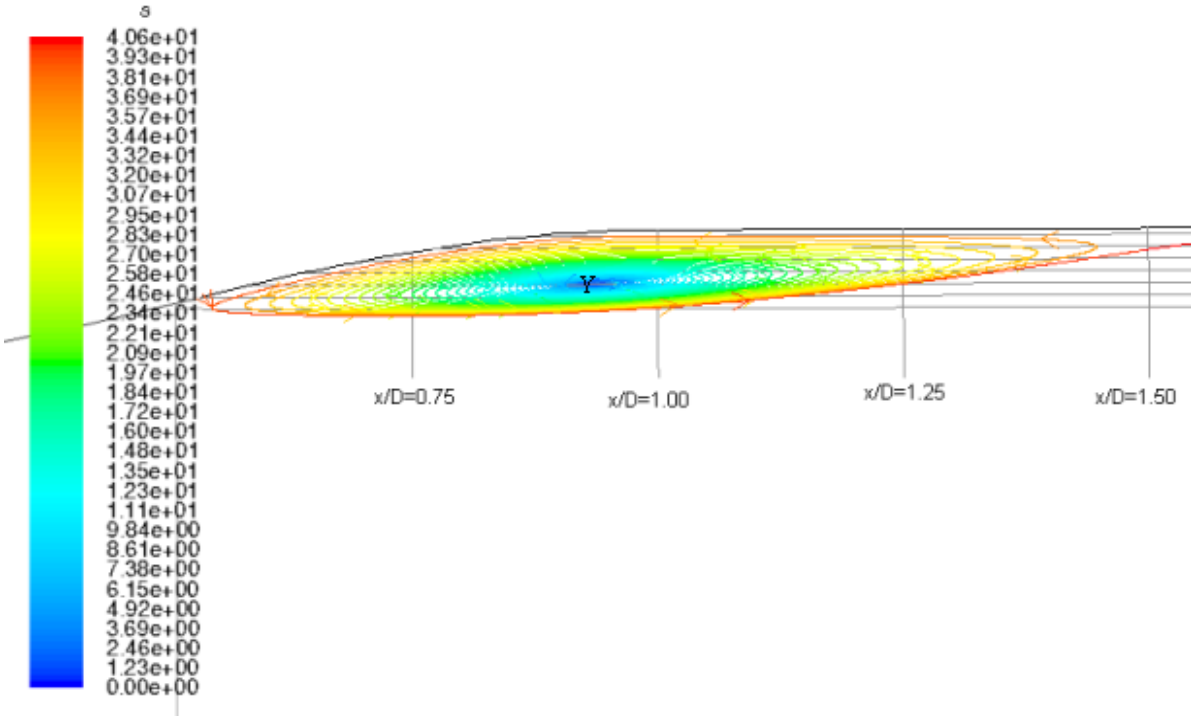

b. Re_i =320. The total PRT is 40.60s. Number of orbits is 40.

Figure 7.12 Trajectory of particles from the central vortex at a. Re_i =250 and b. Re_i=320.

7.4.6 **Conclusions**

For particle injection in steady flow conditions, the particle trajectory at selected locations was simulated to explain the accumulation behaviour in the recirculation zone observed in the experiment. The Saffman-Mei lift force had a negligible effect for particles circulating in the separation zone, but increased the particle residence time for particles traveling in the boundary region with the high shear zone. The particles at higher flow rates circulated for more orbits than those traveling at lower rates. However, the residence time to complete the orbits for the former was shorter.

7.5 Discussion

Particles were tracked using the transient fluid motion for a shorter integral time of 0.028s due to computing time and cost. The unsteady results indicate that the slip velocity $V_s=(V_p-V)$ at the expansion section was relatively higher in the recirculation zone than in the mainstream. In the equation of particle motion, the Saffman-Mei lift force and the drag force are a function of slip velocity.

The second method employed was to inject the particle into a steady fluid flow. The particle residence time and the final location of particles were monitored. In the experimental work using PIV in Chapter 5, the particle distribution was correlated with the light scattered by the particles. The light intensity was measured and normalized with the mean light intensity at the inlet. The light intensity was not uniform, with a relatively higher pixel count in the recirculation zone for flow rates at Re_i =250 and Re_i=320. The results were for a particle diameter of 20μm and the weight concentration was 0.07%, corresponding to the physical properties of monocytes. The light intensity for this case was shown in Figure 5.7b, which was greatest at the central vortex. This observation indicates that there are more particles residing in the recirculation region.

In the simulation study conducted, considering the particles from the boundary of the flow separation zone, particles R (x/D=0.652, r/R=0.855) and S (x/D=0.750, r/R=0.855) orbited inside the recirculation region. Particle R orbited and left the separation zone, finally reaching the reattachment point within 14.8s (Figure 7.8a), while Particle S took 21.1s (Figure 7.10). Other particles in the boundary (N, O, P and T) escaped the recirculation zone and reached the reattachment point in less than one second. Therefore, particles R and S, which orbited in the recirculation zone, resided respectively around 15 and 20 times longer than particles N, O, P and T.

Longer residence times may explain the high light intensity scattered by the particles in the recirculation zone. The intensity increment in this study indicates that the average particle distribution from the light scattered in 200 images of steady flow, and the particle residence time simulated defined as the time required for a particle to pass through a flow section. Therefore, when there is a higher light intensity observed, there are more particles present, because they reside in the recirculation zone longer.

However, when looking at the particle path, the particles at the flow separation boundary (R and S) did not reach the middle vortex. In the experiment, there was an intensity peak at the centre of the recirculation zone, which indicates that more particles resided in the central vortex. The forces considered in this study were not enough to drive the particles from the flow separation boundary to the central vortex. There are in addition, at least two main factors related to particle migration lift forces that was not considered in this simulation (Loth, 2008); the first are lift forces due to particle rotation, or Magnus force, and the second is the lift force due to solid-body rotation in a vortex, or Heron lift.

The effect of varying the flow rates was studied by injecting particles from the middle vortex. The residence time and the number of orbits they completed before leaving the recirculation zone was monitored. Particle W was introduced at Re_i=250 (Figure 7.12a) and Particle Y was tracked at Re_i=320 (Figure 7.12b). Particle W has twice the residence time of Particle Y. In the experiment, the light intensity scattered by the particles at these flow rates were shown in Figures 5.11 and 5.12. The intensity at the vortex centre for Re_i=250 was 50% higher than for Re_i=320. Generally, higher residence times in the simulation correspond to the higher light intensity measured by PIV for Re_i=250. However, the magnitude of the intensity increment measured when the flow rate was reduced was less than the simulated residence time increment by half. Further analysis was difficult, because the particle residence time simulated here does not indicate how long they spend in each location along their path.

It is important to note that in the dilute suspension model, using the Discrete-Phase-Model, the inter-particle forces are neglected. As highlighted in Chapter 5, inter-particle interaction may play a major role where the interaction within orbits may change the trajectories of neighbouring particles (Karino and Goldsmith, 1977).

7.6 Conclusions

The motion of particles distal to stenosis were tracked where the particle residence time were monitored. The slip velocity in the recirculation zone was significantly higher than in the mainstream, suggesting the importance of the lift force on the particle motion. The effect of linear shear lift, Saffman-Mei lift force was analysed by tracking the particle motion with and without the lift term. For the particle tracked from the high shear zone at the throat of the stenosis, the inclusion of the Saffman-Mei lift force term was observed to increase the residence time by 1.8%. This particle subsequently escaped the recirculation zone.

The residence time of particles introduced at the boundary of the recirculation zone and circulating at the outer orbits, was found to be almost not affected by the Saffman-Mei lift force. The lift force applied in this simulation was insufficient to cause the particle migration to the centre of recirculation. It was hypothesised that the lift that is due to solid body rotation in vortex, the 'Herron lift', and the lift that is due to particle rotation, may have more influence on the migration of particles in the recirculation zone. Other neglected force in the simulation was the particle-particle interaction that may plays a role in the particle migration.

Chapter 8

CONCLUSIONS AND FUTURE WORK

8.1 Conclusions

Cardiovascular diseases (CVD) account for nearly 30% of deaths worldwide. The World Health Organisation (WHO) projection statistics on the mortality due to CVD was predicted to increase from 17.1 million in 2004 to 23.4 million in 2030. For all CVDs the narrowing of artery or atherosclerosis was known to be the main factor. The critical stage of the disease leads to fatal or permanent debility occurred when atherothrombosis or blood clotting reaction occludes the arterial lumen.

The development and progression of atherosclerosis is strongly correlated with wall shear stress and blood cells interactions. The region of low wall shear stress has been identified as the site where the atherosclerosis begins. In stenotic artery the low wall shear stress region was in the separation zone distal to stenosis. The aim of this study was to investigate blood cell migration to the flow separation zone in a mild stenosed artery model. Particular interest was paid to the hydrodynamics mechanism that influenced the blood cell motion in blood plasma. Experimental studies followed by computer simulation were performed. To date, most of the research in the literature only focused on wall shear stress measurement without considering the cellular components in the blood. This study was performed beyond the macro scale measurement.

Blood cells in plasma can be regarded as solid particles suspended in fluid. The important flow parameters relevant to this study were the Reynolds numbers, Stokes number and the Peclet number. The relevant hydrodynamic forces that governed the particle migration were shown to be the drag and lift force.

Particle Image Velocimetry (PIV) system was employed to characterise the velocity of the flow and to measure the particle distribution. A 200mJ Nd:YAG laser was used to create a pulsed light sheet in a transparent 30% stenosed artery model manufactured using a ‘lost core’ technique. A blood mimic fluid was developed to match the conflicting requirements of an appropriate viscosity and density (blood) and refraction index for the PIV. To ensure transparency of the fluid suspension which was required for velocity measurement, the

number of particles were dilute. The particle concentrations of blood mimic solutions were 0.04%, 0.07% and 0.14% by weight.

The flow was steady to minimise the transient variable effect in order to establish the essential understanding of particle migration phenomena. The flow rates studied were within the physiological range; Re_i=250 and Re_i=320. The particle suspension concentration used was the most dilute; 0.04% by weight. The flow visualisation suggested a streamlined flow and flow separation were developed at the corner of the expansion region. The reattachment points were between 1.63*D* to 1.93*D* from the throat of the stenosis was depending on the Reynolds number. The results agreed with the laminar flow nature that the separation length increased with the flow rates. The Stokes number and Reynolds number yielded from the velocity measurement indicated the flow was governed by fluid inertia. There was a large variation in the velocity gradient. Distal to stenosis, the maximum high shear was sandwiched between recirculation zone and the jet. Non-uniform light scattered by particles suggested unequal particle distribution was observed in this area.

In Chapter 5 further investigation on the particle distribution in recirculation zone was made. The light scattered by the particles was correlated with the particle distribution. Two concentrations (0.07% and 0.14%), two particle diameters (10μm and 20μm) at three flowrates (Re_i=130, Re_i=250, Re_i=320) were varied. The migration of particles was found to depend on all of the parameters studied; the particle size, particle concentration and fluid flowrates. Particle concentrations as much as 3 times as high as the ambient concentration were observed in the recirculation zone.

At low flowrates (Re_i=130), a particle depleted layer of 0.35mm (5% of the tube diameter) was formed. A particle depleted layer in an artery has physiological implications such that the layer may become a barrier for oxygen transport and NO diffusivity from blood cells to the muscle tissues. These phenomena suggested that when blood flow at a certain site of artery is low and cell-free layer is formed, an efficient supply of oxygen to the area and normal physiological activity may be interrupted.

At the higher flowrates investigated, the particles tend to accumulate in the recirculation zone. Results for particles size of 20μm with a concentration of 0.07%, which resembles the physical properties of monocytes in blood, suggest that the monocytes will accumulate in the middle vortex of the recirculation zone. During the inflammatory process when the wall senses low shear stress, monocytes in the bloodstream migrating to the wall subsequently initiate the plaque formation that promotes atherosclerosis. The migration shown in the experiment suggests, even in the absence of biological forces, the monocytes will migrated

from the mainstream to the low wall shear stress area. The hydrodynamic forces may promote the progression of atherosclerosis in the recirculation region of a mildly stenosed artery.

A 3D finite element Computational Fluid Dynamic (CFD) method was used to simulate the flow and particle behaviour observed in the experimental work. Chapter 6 presented CFD simulations treating the suspension as a single-phase. The velocity field characterised from the experiments in Chapter 4 and 5 were compared. The reattachment length predicted was slightly shorter than the length measured by PIV which may be due experimental uncertainty at the wall boundary. It is possible that the particle interactions which occurred in the experiments results in the disparity of reattachment length determined from the single-phase simulation.

Chapter 7 extended the CFD simulations to consider the two-phase property where to consider particle motion within the fluid. The drag force and the lift force terms in the governing equations are functions of the slip velocity. The slip velocity in the recirculation zone was found to be three times higher than in the mainstream, suggesting that the drag and lift term are higher in the separation area. The effect of linear shear lift, Saffman-Mei lift force was analysed by tracking the particle motion with and without lift term. The particle residence time of particles distal to stenosis was monitored. The particle residence time was defined as the time taken by the particle to reach to a particular position. For particle tracked from the high shear zone at the throat of the stenosis, Saffman-Mei lift force was observed to increase the residence time by 1.8%. However, this particle escaped the recirculation zone. The particles residence time introduced at the boundary of the recirculation zone which circulated at the outer orbits was found almost not affected by the Saffman-Mei lift force.

In conclusion, both the theoretical drag and lift forces applied in this simulation were insufficient to cause the particle migration to the centre of recirculation observed in the experiments. It is hypothesised that lift due to solid body rotation in vortex, Herron lift and lift due to particle rotation may be having more influence on the migration of particles in the recirculation zone. In this simulation the Basset force and added mass force were not taken into account. The discrete phase method used in the simulation also ignored hydrodynamic inter-particle interaction. All of these neglected factors may have role in particle migration.

In the experimental study, the hydrodynamic forces has been shown important in the particle migration of monocytes, however, the simulation results suggested that the linear shear lift, Saffman-Mei lift model was insufficient to cause the particles migrated to the centre of recirculation zone.

In a review by Steinman and Taylor (2005), it was highlighted that research in this decade should address the understanding of micro-hydrodynamics at cellular level. On the same note, this study has emphasized the consideration of cells interaction in predicting the progression of atherosclerosis and the occurrence of atherothrombosis.

8.2 Limitations

There are several assumptions and simplifications in this study that limit the simulation of blood flow according to the physiological environment. This study was in in-vitro scale where the interest was to study the particle-fluid interaction. The use of an idealised model (axisymmetric stenosis geometry) was within the interest of investigating fluid mechanics factors. In this work, the vessel wall was assumed rigid and smooth. The stenosed artery model was made of silicon which was hard. In the simulation, slip velocity was specified and the wall property was set to non-penetrating. The effect of particle migration to the wall and the influence of wall movement were not considered. In earlier study by Li (2006), vessel wall movement was observed not to affect fluid velocities. Therefore the dynamics of particles from mainstream and high shear regions to the recirculation zone was valid. Movement of particles at the wall does not describe the actual blood cells behaviour. At the wall of artery, there are biological reactions that govern the migration of blood cells.

The particle concentrations used represented the concentration of monocytes which was 0.14% by weight. The presence of red blood cells was treated as a high viscous bulk fluid with viscosity of 6.23 mPas. In reality, red blood cells should be considered as cellular particles as well. Due to the nature of PIV which favour dilute particle suspension, the consideration of red blood cell as cellular particles could not be made. Other measurement techniques such as nuclear magnetic resonance and electrical impedance tomography that could measure velocity of concentrated particle suspension would be more suitable. Nevertheless, the results on particle migration behaviour presented in this work able to explain the influence of the bulk fluid flow on the motion of dilute particles similar to monocytes characteristics. Even though the presence of monoctytes in blood is small, the role in triggering atherosclerosis is important. Particle residence time observed in the recirculation region was relatively higher than the mainstream. If the presence of red blood cells are considered, the diffusion of monocytes towards the wall might be enhanced (Hund and Antaki,2009).

The morphology of blood cells in this work was taken as spherical and rigid where particles employed were a rough hard sphere. Actual blood cell has a certain degree of elasticity and the shape was varied depending on shear and biological environment. In this work, the effect

of elasticity on particle migration was not investigated. Elastic properties may impose different surrounding flow velocity structure and bulk viscosity. However, the effect of cell elasticity on flow in large artery is small compared to flow in capillary and arterioles (Ku, 1997). In large artery, blood cells concentration has a dominant influence on the flow compared to elasticity.

The blood flow in human is driven by a pulsatile heart beat but the flow carried out in this work was steady. The reason to consider steady flow was to minimise variables contributed by transient behaviour. Unlike experimental work, in CFD the variables could be separated easily. In order to verify the numerical model, the experiment was performed under steady mode where time-dependent factors were eliminated. It is important for future work to investigate the particle migration phenomena under unsteady flow.

The hydrodynamics model used in this study was validated with fundamental fluid mechanics theory in which some of the micro scale factors, geometry and flow nature discussed above have been simplified. Actual artery geometry in humans is tortuous, winding and non-uniform in shape. The findings from this model could be further employed in computational studies using suitable patient specific artery geometry. In-vivo validation using animal models could be use to verify the assumptions made in this work. Careful consideration of the difference between human and animal biology has to be made.

A simple method to determine particle concentration distribution was employed in this work. The incident laser light was assumed uniform and each particle supposedly scattered the same amount of light. The light intensity was normalised with the intensity at the inlet where the particle distribution is homogenous. Particle concentration inhomogeneity in this study was indicated by ratio of local light intensity to intensity at the inlet position. Based on this simplification, quantitative particle concentration measurement was not made. Robust method could be designed to improve the accuracy by considering the fact that each particle received and scattered light a varying degree. Incident laser light intensity could be measured to verify the uniformity. The noise from measured light intensity scattered by particles could be filtered by deducting the pixels from the light intensity of flow without particles. Detailed calibration of particle concentration with respect to the light intensity scattered in a straight channel could be established. This will be a basis for quantitative particle concentration characterisation in stenosed artery.

8.3 Future work

The main challenge in studying cell migration is the high concentration of RBCs present in blood flow. In imaged-based experimental measurement like PIV, a high concentration of scatterers results in significant noise such that the flow field information is lost. Further studies need to be performed at higher particle concentrations. This could be achieved by using 'ghost cells' – RBCs with the haemoglobin replaced by salt water to make them invisible. Also non-scattering spherical particles refractive index matched to the carrier fluid could be developed.

The numerical simulations were incapable of accurately modelling the high particle concentrations observed in the experiments. Further work is required to determine whether this is due to the theoretical lift models employed being insufficient to model particle flows in rapidly-shearing environments. Also, hydrodynamic particle-particle interaction mechanisms should be studied to determine whether they may be playing a role in the particle concentration patterns observed.

In CFD, the limitation is on the computing capability of the Lagrangian approach in considering cellular interactions. A dilute phase approach has the potential to address the consideration of high concentration of cells in blood plasma. Using this approach, the migration of dilute species such as white blood cells and platelets in the low WSS region can be predicted by treating red blood cells (45% concentration) and plasma as a single continuous phase. The interaction of red blood cell and dilute species can be represented by diffusion coefficient (Hund and Antaki, 2009) and this aspect has to be carefully validated. Research employed this method has been establish for a simple system such as in parallel plates and straight tube at non-physiological arterial flow rates (Sorensen et al., 1999; Wootton et al., 2001; Jordan et al., 2004; Hund and Antaki, 2009). For the systems considered in those works, the Brownian diffusion is significant. The findings in this work have suggested that for a complex geometry like a stenosed artery at physiological flow rates, the shear-induced diffusion is more significant than the Brownian motion. With correct physiological physics, a more accurate cell migration mechanism in disturbed flow could be established using dilute phase models.

In-line with the research direction recommended (Taylor and Steinman, 2010) which emphasized on the higher-order-effect to improve the level of CFD accuracy, a correct physics models has to be tested. In this work, only drag and linear shear-induced lift (Saffman-Mei model) are considered. These models only could explain the particle residence time but not the particle path. A detail lift model associated with fluid vorticity could be

addressed by considering Herron lift (Herron et al., 1975). Lift due to particle spin can be explained by applying Magnus lift (Rubinow and Keller, 1961). A combination expression of both lift models has been derived by Bagchi and Balachandar (2002). The important issues to verify will be in terms of the compliance of the models for blood flow system.

CFD simulations performed in this work indicated a demanding computing time and cost to model individual particles that can yield robust results in accurately predicting the particle migration mechanism. These studies shown that, to track few hundred particles in a domain of around 1.5 million mesh elements using a standard computing system would require several months to get even 10mm particles movement. An alternative particle model that is more practical and reliable has to be sought in studying the particle motion in large arteries. This might involve a multi-scale model taking account of the particle-particle interactions at the micro-scale and their dependence on and effect on the macro-scale flow.

'The development of clinically useful tools based on the integration of engineering, haemodynamics and physiological knowledge continues to be a primary goal, which requires improved translation of biofluid mechanical information into clinical application' (Lieber et al., 2005). Extension from this work could improve models and methodologies that take dynamic information in order to develop clinically acceptable tools.

BIBLIOGRAPHY

Aarts, P., S. A. T. Vandenbroek, et al. (1988). Blood-Platelets Are Concentrated Near The Wall And Red Blood-Cells, In The Center In Flowing Blood. *Arteriosclerosis* **8**(6): 819-824.

Abbas, M., E. Climent, et al. (2009). Shear-induced self-diffusion of inertial particles in a viscous fluid. *Physical Review E* **79**(3):036313.

Acrivos, A., G. K. Batchelor, et al. (1992). Longitudinal Shear-Induced Diffusion of Spheres in a Dilute Suspension. *Journal of Fluid Mechanics* **240**: 651-657.

Adrian, R. J. (1991). Particle-Imaging Techniques For Experimental Fluid-Mechanics. *Annual Review Of Fluid Mechanics* **23**: 261-304.

Ahmed, S. A. and D. P. Giddens (1983). Flow Disturbance Measurements through a Constricted Tube at Moderate Reynolds-Numbers. *Journal of Biomechanics* **16**(12): 955-963.

Ahmed, S. A. and D. P. Giddens (1983). Velocity-Measurements in Steady Flow through Axisymmetric Stenoses at Moderate Reynolds-Numbers. *Journal of Biomechanics* **16**(7): 505-516.

Alsheikh-Ali, A. A., G. D. Kitsios, et al. (2010). The Vulnerable Atherosclerotic Plaque: Scope of the Literature. *Annals of Internal Medicine* **153**(6): 387-W149.

Altobelli, S. A., E. Fukushima, et al. (1997). Nuclear magnetic resonance imaging of particle migration in suspensions undergoing extrusion. *Journal Of Rheology* **41**(5): 1105-1115.

Artoli, A. M., A. Sequeira, et al. (2007). Leukocytes rolling and recruitment by endothelial cells: Hemorheological experiments and numerical simulations. *Journal of Biomechanics* **40**(15): 3493-3502.

Asmolov, E. S. (2008). Shear-induced self-diffusion in a wall-bounded dilute suspension. *Physical Review E* **77**(6):066312.

Azarov, I., K. T. Huang, et al. (2005). Nitric oxide scavenging by red blood cells as a function of hematocrit and oxygenation. *Journal of Biological Chemistry* **280**(47): 39024-39032.

Bagchi, P. and S. Balachandar (2002). Shear versus vortex-induced lift force on a rigid sphere at moderate Re. *Journal of Fluid Mechanics* **473**: 379-388.

Barber, K. M., A. Pinero, et al. (1998). Effects of recirculating flow on U-937 cell adhesion to human umbilical vein endothelial cells. *American Journal of Physiology-Heart and Circulatory Physiology* **44**(2): H591-H599.

Barnea, E. and J. Mizrahi (1975). Generalized Approach to Fluid-Dynamics of Particulate Systems .2. Sedimentation and Fluidization of Clouds of Spherical Liquid Drops. *Canadian Journal of Chemical Engineering* **53**(5): 461-468.

Baskurt, O. K. and H. J. Meiselman (2003). Blood rheology and hemodynamics. *Seminars In Thrombosis And Hemostasis* **29**(5): 435-450.

Baskurt, O. K. and H. J. Meiselman (2003). Phatophysiology Significance of Blood Rheology *Turkish Journal Medical Sciences* **33**: 347-335.

Beech-Brandt, J. J., W. J. Easson, et al. (2005). Large-eddy simulation of flow in a tube with an axisymmetric stenosis. *Proceedings of the Third IASTED International Conference on BIOMECHANICS*: 145-150.

Benard, N., D. Coisne, et al. (2003). Experimental study of laminar blood flow through an artery treated by a stent implantation: characterisation of intra-stent wall shear stress. *Journal Of Biomechanics* **36**(7): 991-998.

Berger, S. A. and L. D. Jou (2000). Flows in stenotic vessels. *Annual Review of Fluid Mechanics* **32**: 347-382.

Bitsch, L., L. H. Olesen, et al. (2003). *Micro PIV on blood flow in a microchannel*. 7th International Conference on Miniaturized Chemical and Biochemical Analysis Systems, Squaw Valley, California, USA:825-828.

Blake, J. R. (2008). On the assessment of blood velocity and wall shear rate in arteries with Doppler ultrasound: a validation study. *School of Clinical Sciences and Community Health*. Edinburgh, The University of Edinburgh. **PhD**.

Blake, J. R., W. J. Easson, et al. (2009). A Dual-Phantom System for Validation of Velocity Measurements in Stenosis Models Under Steady Flow. *Ultrasound in Medicine & Biology* **35**(9): 1510-1524.

Bluestein, D., L. J. Niu, et al. (1997). Fluid mechanics of arterial stenosis: Relationship to the development of mural thrombus. *Annals of Biomedical Engineering* **25**(2): 344-356.

Buchanan, J. R., C. Kleinstreuer, et al. (2000). Rheological effects on pulsatile hemodynamics in a stenosed tube. *Computers & Fluids* **29**(6): 695-724.

Butler, A., I. Megson, et al. (1998). Diffusion of nitric oxide and scavenging by blood in the vasculature. *Biochimica et Biophsica Acta* **1425**: 168-176.

Caro, C. G. (1978). *The mechanics of the circulation*. Oxford, Oxford University Press.

Caro, C. G., J. M. Fitz-Gerald, et al. (1971). Atheroma and arterial wall shear. Observation, correlation and proposal of a shear dependent mass transfer mechanism for atherogenesis. *Proc Royal Soc Lond Biol Sci* **177**: 109-159.

Cebral, J. R., M. A. Castro, et al. (2005). Efficient pipeline for image-based patient-specific analysis of cerebral aneurysm hemodynamics: Technique and sensitivity. *Ieee Transactions on Medical Imaging* **24**(4): 457-467.

Chandran, K. B., M. J. Vonesh, et al. (1996). Computation of vascular flow dynamics from intravascular ultrasound images. *Medical Engineering & Physics* **18**(4): 295-304.

Cheng, C., F. Helderman, et al. (2007). Large variations in absolute wall shear stress levels within one species and between species. *Atherosclerosis* **195**(2): 225-235.

Chien, S. (1970). Shear Dependence of Effective Cell Volume as a Determinant of Blood Viscosity. *Science* **168**(3934): 977-979.

Cho, Y. I. and K. R. Kensey (1991). Effects of the Non-Newtonian Viscosity of Blood on Flows in a Diseased Arterial Vessel .1. Steady Flows. *Biorheology* **28**(3-4): 241-262.

Crowe, C., M. Sommerfeld, et al. (1998). *Multiphase flows with droplets and particles*. Boca Raton, Florida ; London :, CRC Press.

daCunha, F. R. and E. J. Hinch (1996). Shear-induced dispersion in a dilute suspension of rough spheres. *Journal of Fluid Mechanics* **309**: 211-223.

Davies, K. N. and P. R. Humphrey (1993). Complications of Cerebral-Angiography in Patients with Symptomatic Carotid Territory Ischemia Screened by Carotid Ultrasound. *Journal of Neurology Neurosurgery and Psychiatry* **56**(9): 967-972.

Davies, P. F., J. A. Spaan, et al. (2005). Shear stress biology of the endothelium. *Annals Of Biomedical Engineering* **33**(12): 1714-1718.

Deplano, V. and M. Siouffi (1999). Experimental and numerical study of pulsatile flows through stenosis: Wall shear stress analysis. *Journal Of Biomechanics* **32**(10): 1081-1090.

Deshpande, M. D. and D. P. Giddens (1980). Turbulence Measurements in a Constricted Tube. *Journal of Fluid Mechanics* **97**(MAR): 65-89.

Easthope, P. L. and D. E. Brooks (1980). A Comparison Of Rheological Constitutive Functions For Whole Human-Blood. *Biorheology* **17**(3): 235-247.

Feng, Z. G. and E. E. Michaelides (2003). Equilibrium position for a particle in a horizontal shear flow. *International Journal of Multiphase Flow* **29**(6): 943-957.

Ferziger, J. and M. Peric (1999). *Computational Methods for Fluid Dynamics*. Berlin, Springer-Verlag.

Fogelson, A. L. and R. D. Guy (2004). Platelet-wall interactions in continuum models of platelet thrombosis: formulation and numerical solution. *Mathematical Medicine and Biology-a Journal of the Ima* **21**(4): 293-334.

Fung, Y. C. (1993). *Biomechanics: Mechanical Properties of Living Tissues* Springer-Verlag New York Inc. (USA).

Gach, H. M. and I. J. Lowe (2000). Measuring flow reattachment lengths downstream of a stenosis using MRI. *Journal of Magnetic Resonance Imaging* **12**(6): 939-948.

Giddens, D. P., C. K. Zarins, et al. (1993). The Role Of Fluid-Mechanics In The Localization And Detection Of Atherosclerosis. *Journal Of Biomechanical Engineering-Transactions Of The Asme* **115**(4): 588-594.

Gijsen, F. J. H., E. Allanic, et al. (1999). The influence of the non-Newtonian properties of blood on the flow in large arteries: unsteady flow in a 90 degrees curved tube. *Journal of Biomechanics* **32**(7): 705-713.

Gijsen, F. J. H., A. Goijaerts, et al. (1997). A new method to determine wall shear stress distribution. *Journal Of Rheology* **41**(5): 995-1006.

Gijsen, F. J. H., F. N. van de Vosse, et al. (1998). Wall shear stress in backward-facing step flow of a red blood cell suspension. *Biorheology* **35**(4-5): 263-279.

Glor, F. P., B. Ariff, et al. (2005). Operator dependence of 3-D ultrasound-based computational fluid dynamics for the carotid bifurcation. *Ieee Transactions on Medical Imaging* **24**(4): 451-456.

Glor, F. P., Q. Long, et al. (2003). Reproducibility study of magnetic resonance image-based computational fluid dynamics prediction of carotid bifurcation flow. *Annals of Biomedical Engineering* **31**(2): 142-151.

Goldsmith, H. L. and V. T. Turitto (1986). Rheological Aspects of Thrombosis and Hemostasis - Basic Principles and Applications - Icth-Report - Subcommittee on Rheology of the International Committee on Thrombosis and Hemostasis. *Thrombosis and Haemostasis* **55**(3): 415-435.

Gray, J. D. (2002). Non-Newtonian scaling of blood flow in a femoral bypass., University of Liverpool. **PhD**.

Guy, R. D. and A. L. Fogelson (2002). Probabilistic modeling of platelet aggregation: Effects of activation time and receptor occupancy. *Journal of Theoretical Biology* **219**(1): 33-53.

Hankey, G. J., C. P. Warlow, et al. (1990). Cerebral Angiographic Risk in Mild Cerebrovascular-Disease. *Stroke* **21**(2): 209-222.

Hathcock, J. J. (2006). Flow effects on coagulation and thrombosis. *Arteriosclerosis Thrombosis and Vascular Biology* **26**(8): 1729-1737.

Herron, I. H., S. H. Davis, et al. (1975). On the sedimentation of a sphere in a centrifuge. *Journal of Fluid Mechanics* **68**(2): 209-234.

Hinds, M. T., Y. J. Park, et al. (2001). Local hemodynamics affect monocytic cell adhesion to a three- dimensional flow model coated with E-selectin. *Journal Of Biomechanics* **34**(1): 95-103.

Hoskins, P. R. (2008). Simulation and validation of arterial ultrasound imaging and blood flow. *Ultrasound in Medicine and Biology* **34**(5): 693-717.

Hoskins, P. R. and D. Hardman (2009). Three-dimensional imaging and computational modelling for estimation of wall stresses in arteries. *British Journal of Radiology* **82**: S3-S17.

Host-Madsen, A. and D. R. McCluskey (1994). *On the Accuracy and Reliability of PIV measurements*. Proceedings of the Seventh International Symposium on Applications of Laser Techniques to Flow Measurements, Lisbon.

Hund, S. J. and J. F. Antaki (2009). An extended convection diffusion model for red blood cell-enhanced transport of thrombocytes and leukocytes. *Physics in Medicine and Biology* **54**(20): 6415-6435.

Hyun, S., C. Kleinstreuer, et al. (2000). Hemodynamics analyses of arterial expansions with implications to thrombosis and restenosis. *Medical Engineering & Physics* **22**(1): 13-27.

Hyun, S., C. Kleinstreuer, et al. (2004). Particle-hemodynamics simulations and design options for surgical reconstruction of diseased carotid artery bifurcations. *Journal Of Biomechanical Engineering-Transactions Of The Asme* **126**(2): 188-195.

Ishii, M. and N. Zuber (1979). Drag Coefficient and Relative Velocity in Bubbly, Droplet or Particulate Flows. *Aiche Journal* **25**(5): 843-855.

Ishikawa, T., L. F. R. Guimaraes, et al. (1998). Effect of non-Newtonian property of blood on flow through a stenosed tube. *Fluid Dynamics Research* **22**(5): 251-264.

Jin, B. and A. Acrivos (2004). Theory of particle segregation in rimming flows of suspensions containing neutrally buoyant particles. *Physics of Fluids* **16**(3): 641-651.

Johnston, B. M., P. R. Johnston, et al. (2004). Non-Newtonian blood flow in human right coronary arteries: steady state simulations. *Journal of Biomechanics* **37**(5): 709-720.

Jordan, A., T. David, et al. (2004). The effects of margination and red cell augmented platelet diffusivity on platelet adhesion in complex flow. *Biorheology* **41**(5): 641-653.

Jung, J. and A. Hassanein (2008). Three-phase CFD analytical modeling of blood flow. *Medical Engineering & Physics* **30**(1): 91-103.

Jung, J. H., A. Hassanein, et al. (2006). Hemodynamic computation using multiphase flow dynamics in a right coronary artery. *Annals Of Biomedical Engineering* **34**(3): 393-407.

Jung, J. W., R. W. Lyczkowski, et al. (2006). Multiphase hemodynamic simulation of pulsatile flow in a coronary artery. *Journal of Biomechanics* **39**(11): 2064-2073.

Kagadis, G. C., E. D. Skouras, et al. (2008). Computational representation and hemodynamic characterization of in vivo acquired severe stenotic renal artery geometries using turbulence modeling. *Medical Engineering & Physics* **30**(5): 647-660.

Kamm, R. D. (2002). Cellular fluid mechanics. *Annu Rev Fluid Mech* **34**: 211-232.

Karino, T. and H. L. Goldsmith (1977). Flow Behavior Of Blood-Cells And Rigid Spheres In An Annular Vortex. *Philosophical Transactions Of The Royal Society Of London Series B-Biological Sciences* **279**(967): 415-445.

Karino, T. and H. L. Goldsmith (1979). Aggregation of Human-Platelets in an Annular Vortex Distal to a Tubular Expansion. *Microvascular Research* **17**(3): 217-237.

Keane, R.D. and R.J. Adrian (1992). Theory of cross-correlation analysis of PIV images. *Applied Science Research* **49**: 191-215.

Kim, S., P. K. Ong, et al. (2009). The cell-free layer in microvascular blood flow. *Biorheology* **46**(3): 181-189.

Kim, Y. H., J. E. Kim, et al. (2008). Hemodynamic analysis of a compliant femoral artery bifurcation model using a fluid structure interaction framework. *Annals of Biomedical Engineering* **36**(11): 1753-1763.

Kleinstreuer, C. (2006). *Biofluid dynamics :principles and selected applications*. Boca Raton, FL, CRC/Taylor & Francis.

Krams, R., J. J. Wentzel, et al. (1997). Evaluation of endothelial shear stress and 3D geometry as factors determining the development of atherosclerosis and remodeling in human coronary arteries in vivo - Combining 3D reconstruction from angiography and IVUS (ANGUS) with computational fluid dynamics. *Arteriosclerosis Thrombosis and Vascular Biology* **17**(10): 2061-2065.

Ku, D. N. (1997). Blood flow in arteries. *Annual Review Of Fluid Mechanics* **29**: 399-434.

Kuharsky, A. L. and A. L. Fogelson (2001). Surface-mediated control of blood coagulation: The role of binding site densities and platelet deposition. *Biophysical Journal* **80**(3): 1050-1074.

Kumar, A. and S. Hartland (1985). Gravity Settling in Liquid Liquid Dispersions. *Canadian Journal of Chemical Engineering* **63**(3): 368-376.

Kunov, M. J., D. A. Steinman, et al. (1996). Particle volumetric residence time calculations in arterial geometries. *Journal of Biomechanical Engineering-Transactions of the Asme* **118**(2): 158-164.

Kupeli, S., T. Hazirolan, et al. (2010). Evaluation of Coronary Artery Disease by Computed Tomography Angiography in Patients Treated for Childhood Hodgkin's Lymphoma. *Journal of Clinical Oncology* **28**(6): 1025-1030.

Lei, M., D. P. Giddens, et al. (2001). Pulsatile flow in an end-to-side vascular graft model: Comparison of computations with experimental data. *Journal Of Biomechanical Engineering-Transactions Of The Asme* **123**(1): 80-87.

Leighton, D. and A. Acrivos (1987). The Shear-Induced Migration Of Particles In Concentrated Suspensions. *Journal Of Fluid Mechanics* **181**: 415-439.

Lemson, M. S., J. H. M. Tordoir, et al. (2000). Intimal hyperplasia in vascular grafts. *European Journal of Vascular and Endovascular Surgery* **19**(4): 336-350.

Levick, J. R. (2003). *An introduction to cardiovascular physiology*. London, Arnold.

Li, M. (2006). Numerical simulation of blood flow and vessel wall stresses in stenosed arteries. *School of Engineering and Electronics*. Edinburgh, University of Edinburgh. **PhD**.

Li, M. X., J. J. Beech-Brandt, et al. (2007). Numerical analysis of pulsatile blood flow and vessel wall mechanics in different degrees of stenoses. *Journal of Biomechanics* **40**(16): 3715-3724.

Libby, P., P. M. Ridker, et al. (2002). Inflammation and Atherosclerosis. *Circulation* **105**(9): 1135-1143.

Lieber, B. B., M. Siebes, et al. (2005). Correlation of hemodynamic events with clinical and pathological observations. *Annals of Biomedical Engineering* **33**(12): 1695-1703.

Liepsch, D. (2002). An introduction to biofluid mechanics - basic models and applications. *Journal of Biomechanics* **35**(4): 415-435.

Lima, R., T. Ishikawa, et al. (2008). Radial dispersion of red blood cells in blood flowing through glass capillaries: The role of hematocrit and geometry. *Journal of Biomechanics* **41**(10): 2188-2196.

Lima, R., S. Wada, et al. (2006). Confocal micro-PIV measurements of three-dimensional profiles of cell suspension flow in a square microchannel. *Measurement Science & Technology* **17**(4): 797-808.

Long, D. S., M. L. Smith, et al. (2004). Microviscometry reveals reduced blood viscosity and altered shear rate and shear stress profiles in microvessels after hemodilution. *Proceedings of the National Academy of Sciences of the United States of America* **101**(27): 10060-10065.

Long, Q., X. Y. Xu, et al. (2000). Reconstruction of blood flow patterns in a human carotid bifurcation: A combined CFD and MRI study. *Journal of Magnetic Resonance Imaging* **11**(3): 299-311.

Long, Q., X. Y. Xu, et al. (2001). Numerical investigation of physiologically realistic pulsatile flow through arterial stenosis. *Journal of Biomechanics* **34**(10): 1229-1242.

Longest, P. W. and C. Kleinstreuer (2003a). Comparison of blood particle deposition models for non-parallel flow domains. *Journal of Biomechanics* **36**(3): 421-430.

Longest, P. W. and C. Kleinstreuer (2003b). Numerical simulation of wall shear stress conditions and platelet localization in realistic end-to-side arterial anastomoses. *Journal of Biomechanical Engineering-Transactions of the Asme* **125**(5): 671-681.

Longest, P. W. and C. Kleinstreuer (2003c). Particle-hemodynamics modeling of the distal end-to-side femoral bypass: effects of graft caliber and graft-end cut. *Medical Engineering & Physics* **25**(10): 843-858.

Longest, P. W., C. Kleinstreuer, et al. (2004). Efficient computation of micro-particle dynamics including wall effects. *Computers & Fluids* **33**(4): 577-601.

Loth, E. (2008). Lift of a solid spherical particle subject to vorticity and/or spin. *Aiaa Journal* **46**(4): 801-809.

Malek, A. M., S. L. Alper, et al. (1999). Hemodynamic shear stress and its role in atherosclerosis. *Jama-Journal of the American Medical Association* **282**(21): 2035-2042.

Matas, J.-P., J. F. Morris, et al. (2004). Inertial migration of rigid spherical particles in Poiseuille flow. *Journal Of Fluid Mechanics* **515**(-1): 171-195.

Matas, J. P., J. F. Morris, et al. (2003). Transition to turbulence in particulate pipe flow. *Physical Review Letters* **90**(1):014501.

Matas, J. P., J. F. Morris, et al. (2004). Inertial migration of rigid spherical particles in Poiseuille flow. *Journal of Fluid Mechanics* **515**: 171-195.

McLaughlin, J. B. (1991). Inertial Migration of a Small Sphere in Linear Shear Flows. *Journal of Fluid Mechanics* **224**: 261-274.

McLaughlin, J. B. (1993). The Lift on a Small Sphere in Wall-Bounded Linear Shear Flows. *Journal of Fluid Mechanics* **246**: 249-265.

Meagher, S., J. Blake, et al. (2005). *Validation of Ultrasound Velocity Measurements against Particle Image Velocimetry*. Second IASTED International Conference on Biomechanics, Benidorm, Spain ACTA Press

Meagher, S., T. L. Poepping, et al. (2007). Anatomical flow phantoms of the nonplanar carotid bifurcation, part II: Experimental validation with Doppler ultrasound. *Ultrasound in Medicine and Biology* **33**(2): 303-310.

Mei, R. W. and R. J. Adrian (1992). Flow Past a Sphere with an Oscillation in the Free-Stream Velocity and Unsteady Drag at Finite Reynolds-Number. *Journal of Fluid Mechanics* **237**: 323-341.

Moraczewski, T. and N. C. Shapley (2007). Pressure drop enhancement in a concentrated suspension flowing through an abrupt axisymmetric contraction-expansion. *Physics of Fluids* **19**(10):103304.

Moraczewski, T., H. Y. Tang, et al. (2005). Flow of a concentrated suspension through an abrupt axisymmetric expansion measured by nuclear magnetic resonance imaging. *Journal of Rheology* **49**(6): 1409-1428.

Morbiducci, U., R. Ponzini, et al. (2009). In Vivo Quantification of Helical Blood Flow in Human Aorta by Time-Resolved Three-Dimensional Cine Phase Contrast Magnetic Resonance Imaging. *Annals of Biomedical Engineering* **37**(3): 516-531.

Morris, L., P. Delassus, et al. (2005). 3-D numerical simulation of blood flow through models of the human aorta. *Journal of Biomechanical Engineering-Transactions of the Asme* **127**(5): 767-775.

Morsi, S. A. and A. J. Alexander (1972). Investigation of Particle Trajectories in 2-Phase Flow Systems. *Journal of Fluid Mechanics* **55**(SEP26): 193-208.

Neofytou, P. (2004). Comparison of blood rheological models for physiological flow simulation. *Biorheology* **41**(6): 693-714.

Neofytou, P. and D. Drikakis (2003). Non-Newtonian flow instability in a channel with a sudden expansion. *Journal Of Non-Newtonian Fluid Mechanics* **111**(2-3): 127-150.

Neofytou, P. and S. Tsangaris (2006). Flow effects of blood constitutive equations in 3D models of vascular anomalies. *International Journal for Numerical Methods in Fluids* **51**(5): 489-510.

Nichols, W. W. and M. F. O'Rourke (2005). *McDonald's Blood Flow in Arteries* Hodder Arnold

O'Callaghan, S., M. Walsh, et al. (2006). Numerical modelling of Newtonian and non-Newtonian representation of blood in a distal end-to-side vascular bypass graft anastomosis. *Medical Engineering & Physics* **28**(1): 70-74.

Oseen, C. W. (1910). Über die Stokes'sche formel, und über eine verwandte Aufgabe in der Hydrodynamik. *Arkiv för matematik, astronomi och fysik* **29**.

Pal, R. (2003). Rheology of concentrated suspensions of deformable elastic particles such as human erythrocytes. *Journal Of Biomechanics* **36**(7): 981-989.

Papanastasiou, T. C. (1987). Flows Of Materials With Yield. *Journal Of Rheology* **31**(5): 385-404.

Patankar, S. V. (1980). *Numerical Heat Transfer and Fluid Flow*. New York, USA, McGraw Hill.

Perktold, K., M. Resch, et al. (1991). Pulsatile Non-Newtonian Flow Characteristics In A 3-Dimensional Human Carotid Bifurcation Model. *Journal Of Biomechanical Engineering-Transactions Of The Asme* **113**(4): 464-475.

Prasad, A. K. (2000). Particle image velocimetry. *Current Science* **79**(1): 51-60.

Pries, A. R., A. Fritzsche, et al. (1992). Redistribution Of Red-Blood-Cell Flow In Microcirculatory Networks By Hemodilution. *Circulation Research* **70**(6): 1113-1121.

Pritchard, W. F., P. F. Davies, et al. (1995). Effects of wall shear stress and fluid recirculation on the localization of circulating monocytes in a three-dimensional flow model. *Journal Of Biomechanics* **28**(12): 1459-1469.

Quemada, D. (1978). Rheology Of Concentrated Disperse Systems .3. General Features Of The Proposed Non-Newtonian Model - Comparison With Experimental-Data. *Rheologica Acta* **17**(6): 643-653.

Raffel, M., C. E. Willert, et al. (1998). *Particle image velocimetry :a practical guide*. Berlin, Springer.

Rayz, V. L., L. Boussel, et al. (2010). Flow Residence Time and Regions of Intraluminal Thrombus Deposition in Intracranial Aneurysms. *Annals of Biomedical Engineering* **38**(10): 3058-3069.

Raz, S., S. Einav, et al. (2007). DPIV prediction of flow induced platelet activation - Comparison to numerical predictions. *Annals of Biomedical Engineering* **35**(4): 493-504.

Reneman, R. S., T. Arts, et al. (2006). Wall shear stress - an important determinant of endothelial cell function and structure - in the arterial system in vivo. *Journal of Vascular Research* **43**(3): 251-269.

Richardson, L. F. and J. A. Gaunt (1927). The deferred approach to the limit. Part I. Single lattice. Part II. Interpenetrating lattices. *Philosophical Transactions of the Royal Society of London Series a-Containing Papers of a Mathematical or Physical Character* **226**: 299-361.

Roache, P. J. (1994). Perspective - a Method for Uniform Reporting of Grid Refinement Studies. *Journal of Fluids Engineering-Transactions of the Asme* **116**(3): 405-413.

Rubinow, S. I. and J. B. Keller (1961). The Transverse Force on a Spinning Sphere Moving in a Viscous Fluid. *Journal of Fluid Mechanics* **11**(3): 447-459.

Saffman, P. G. (1965). Lift on a Small Sphere in a Slow Shear Flow. *Journal of Fluid Mechanics* **22**: 385-400.

Sankar, D. S. and U. Lee (2008). Two-fluid Casson model for pulsatile blood flow through stenosed arteries: A theoretical model. *Communications in Nonlinear Science and Numerical Simulation* **15**(8): 2086-2097.

Santiago, J. G., S. T. Wereley, et al. (1998). A particle image velocimetry system for microfluidics. *Experiments In Fluids* **25**(4): 316-319.

Schiller, L. and Z. Naumann (1935). A Drag Coefficient Correlation. *Zeitschrift des Vereines Deutscher Ingenieure* **77**: 318-320.

Segre, G. , et al. (1962). Behaviour of macroscopic rigid spheres in Poiseuille flow Part 2. Experimental results and interpretation. *Journal of Fluid Mechanics Digital Archive* **14**(01): 136-157.

Segre, G. and A. Silberberg (1961). Radial Particle Displacements in Poiseuille Flow of Suspensions. *Nature* **189**(476): 209-210.

Sharma, G. C., M. Jain, et al. (2004). Performance modeling and analysis of blood flow in elastic arteries. *Mathematical And Computer Modelling* **39**(13): 1491-1499.

Shin, S., Y. Ku, et al. (2004). Blood flow resistance with vibration and its effect on blood cell migration. *Clinical Hemorheology And Microcirculation* **30**(3-4): 353-358.

Skalak, R. and S. Chien (1987). *Handbook of bioengineering*. New York, McGraw-Hill.

Skilbeck, C. A., P. G. Walker, et al. (2004). Disturbed flow promotes deposition of leucocytes from flowing whole blood in a model of a damaged vessel wall. *British Journal of Haematology* **126**(3): 418-427.

Slager, C. J., J. J. Wentzel, et al. (1995). The role of shear stress in the destabilization of vulnerable plaques and related therapeutic implications. *Nature Clinical Practice Cardiovascular Medicine* **2**(9): 456-464.

Slager, C. J., J. K. Wentzel, et al. (1995). The role of shear stress in the generation of rupture-prone vulnerable plaques. *Nature Clinical Practice Cardiovascular Medicine* **2**(8): 401-407.

Sorensen, E. N., G. W. Burgreen, et al. (1999). Computational simulation of platelet deposition and activation: I. Model development and properties. *Annals of Biomedical Engineering* **27**(4): 436-448.

Srivastava, V. P. and R. Srivastava (2009). Particulate suspension blood flow through a narrow catheterized artery. *Computers & Mathematics with Applications* **58**(2): 227-238.

Steinberg, D. (2002). Atherogenesis in perspective: Hypercholesterolemia and inflammation as partners in crime. *Nature Medicine* **8**(11): 1211-1217.

Steinman, D. A., J. S. Milner, et al. (2003). Image-based computational simulation of flow dynamics in a giant intracranial aneurysm. *American Journal of Neuroradiology* **24**(4): 559-566.

Steinman, D. A. and C. A. Taylor (2005). Flow imaging and computing: Large artery hemodynamics. *Annals of Biomedical Engineering* **33**(12): 1704-1709.

Stickel, J. J. and R. L. Powell (2005). Fluid mechanics and rheology of dense suspensions. *Annual Review Of Fluid Mechanics* **37**: 129-149.

Stokes, G. G. (1845). On the theories of the internal friction in fluids in motion. *Transaction of the Cambridge Philosophical Society* **8**(22): 287-319.

Strickman, N. E. and P. Loyalka (2005). Carotid artery stenosis - An endovascular specialist's perspective. *Texas Heart Institute Journal* **32**(3): 318-322.

Stroev, P. V., P. R. Hoskins, et al. (2007). Distribution of wall shear rate throughout the arterial tree: A case study. *Atherosclerosis* **191**(2): 276-280.

Sugii, Y., R. Okuda, et al. (2005). Velocity measurement of both red blood cells and plasma of *in vitro* blood flow using high-speed micro PIV technique. *Measurement Science and Technology* **16**(5): 1126-1130.

Taylor, C. A., C. P. Cheng, et al. (2002). In vivo quantification of blood flow and wall shear stress in the human abdominal aorta during lower limb exercise. *Annals of Biomedical Engineering* **30**(3): 402-408.

Taylor, C. A. and D. A. Steinman (2010). Image-Based Modeling of Blood Flow and Vessel Wall Dynamics: Applications, Methods and Future Directions. *Annals of Biomedical Engineering* **38**(3): 1188-1203.

Tiwari, P., S. P. Antal, et al. (2009). Modeling shear-induced diffusion force in particulate flows. *Computers & Fluids* **38**(4): 727-737.

Walburn, F. J. and D. J. Schneck (1976). Constitutive Equation For Whole Human-Blood. *Biorheology* **13**(3): 201-210.

Walsh, M., T. McGloughlin, et al. (2003). On using experimentally estimated wall shear stresses to validate numerically predicted results. *Proceedings Of The Institution Of Mechanical Engineers Part H- Journal Of Engineering In Medicine* **217**(H2): 77-90.

Weissberg, P. (2007). Imaging of inflammation in atherosclerotic plaques. *Inflammation Research* **56**: S156-S156.

Weissberg, P. L. (2000). Coronary disease: Atherogenesis: current understanding of the causes of atheroma *Heart* **83**(2): 247-252

Wells, R. E. and E. W. Merrill (1962). Influence Of Flow Properties Of Blood Upon Viscosity-Hematocrit Relationships. *Journal Of Clinical Investigation* **41**(8): 1591-1598.

Westerweel, J. (1997). Fundamentals of digital particle image velocimetry. *Measurement Science & Technology* **8**(12): 1379-1392.

WHO (2002). *The World Health Report 2002: Reducing Risks to Health, Promoting Healthy Life* Geneva, World Health Organization.

Willert, C. E. and M. Gharib (1991). Digital Particle Image Velocimetry. *Experiments in Fluids* **10**(4): 181-193.

Wootton, D. M. and D. N. Ku (1999). Fluid mechanics of vascular systems, diseases, and thrombosis. *Annual Review Of Biomedical Engineering* **1**: 299-329.

Wootton, D. M., C. P. Markou, et al. (2001). A mechanistic model of acute platelet accumulation in thrombogenic stenoses. *Annals of Biomedical Engineering* **29**(4): 321-329.

Xu, X. Y., Q. Long, et al. (1999). Reconstruction of blood flow patterns in human arteries. *Proceedings of the Institution of Mechanical Engineers Part H-Journal of Engineering in Medicine* **213**(H5): 411-421.

Yilmaz, F. and M. Y. Gundogdu (2008). A critical review on blood flow in large arteries; relevance to blood rheology, viscosity models, and physiologic conditions. *Korea-Australia Rheology Journal* **20**(4): 197-211.

Yilmaz, F. and M. Y. Gundogdu (2009). Analysis of conventional drag and lift models for multiphase CFD modeling of blood flow. *Korea-Australia Rheology Journal* **21**(3): 161-173.

Zarraga, I. E. and D. T. Leighton (2002). Measurement of an unexpectedly large shear-induced self-diffusivity in a dilute suspension of spheres. *Physics of Fluids* **14**(7): 2194-2201.

Zhang, J. M., L. P. Chua, et al. (2008). Validation of numerical simulation with PIV measurements for two anastomosis models. *Medical Engineering & Physics* **30**(2): 226-247.

Zhao, R., J. N. Marhefka, et al. (2008). Micro-flow visualization of red blood cell-enhanced platelet concentration at sudden expansion. *Annals of Biomedical Engineering* **36**(7): 1130-1141.